Fall 2012

Organic and composite aerogels through ring opening metathesis polymerization (ROMP)

Dhairyashil Mohite

ORGANIC AND COMPOSITE AEROGELS THROUGH RING OPENING
METATHESIS POLYMERIZATION (ROMP)

by

DHAIRYASHIL P. MOHITE

A DISSERTATION

Presented to the Faculty of the Graduate School of the

MISSOURI UNIVERSITY OF SCIENCE AND TECHNOLOGY

In Partial Fulfillment of the Requirements for the Degree

DOCTOR OF PHILOSOPHY

in

CHEMISTRY

2012

Approved

Dr. Nicholas Leventis, Advisor
Dr. Chariklia Sotiriou-Leventis, Co-Advisor
Dr. Philip Whitefield
Dr. Manashi Nath
Dr. K. Chandrashekhara

..

PUBLICATION DISSERTATION OPTION

This dissertation consists of the following three manuscripts for publication:

Pages 44-106 have been submitted to *Chemistry of Materials.*

Pages 107-147 have been published in *Chemistry of Materials* **2011**, 23, 2250-2261.

Pages 148-225 have been submitted to *Chemistry of Materials.*

ABSTRACT

Aerogels are open-cell nanoporous materials, unique in terms of low density, low thermal conductivity, low dielectric constants and high acoustic attenuation. Those exceptional properties stem from their complex hierarchical solid framework (agglomerates of porous, fractal secondary nanoparticles), but they also come at a cost: low mechanical strength. This issue has been resolved by crosslinking silica aerogels with organic polymers. The crosslinking polymer has been assumed to form a conformal coating on the surface of the skeletal framework by covalent bridging elementary building blocks. However, "assuming" is not enough: for correlating nanostructure with bulk material properties, it is important to know the exact location of the polymer on the aerogel backbone. For that investigation, we synthesized a new norbornene derivative of triethoxysilane (**Si-NAD**) that can be attached to skeletal silica nanoparticles. Those norbornene-modified silica aerogels were crosslinked with polynorbornene by ring opening metathesis polymerization (ROMP). The detailed correlation between nanostructure and mechanical strength was probed with a wide array of characterization methods ranging from molecular to bulk through nano. Subsequently, it was reasoned that since the polymer dominates the exceptional mechanical properties of polymer crosslinked aerogels, purely organic aerogels with the same nanostructure and interparticle connectivity should behave similarly. That was explored and confirmed by: (a) synthesis of a difunctional nadimide monomer (**bis-NAD**), and preparation of robust polyimide aerogels by ROMP of its norbornene end-caps; and, (b) synthesis of dimensionally stable ROMP-derived polydicyclopentadiene aerogels by grafting the nanostructure with polymethylmethacrylate (PMMA) via free radical chemistry.

ACKNOWLEDGEMENTS

First and foremost, I want to express my sincere thanks to my advisor, Prof. Nicholas Leventis and Co-advisor Prof. Chariklia Sotiriou-Leventis for their continuous guidance and support throughout my graduate studies at Missouri S & T. Their advice and words of wisdom, technical as well as profession and personal, have helped me not only to be successful academically, but also to be a better human being. I really admire their imagination which taught me the fact that you need to be passionate about your work apart from being smart and hard-working. I am grateful to them for the things they have taught me, directly and indirectly. I look at them as my real role models.

I would like to thank my advisory committee members, Dr. Philip Whitefield, Dr. Manashi Nath and Dr. K. Chandrashekhara for serving on my committee and advising me throughout the completion of my dissertation. I thank the Department of Chemistry of Missouri S & T for teaching assistantships and resources. I want to thank Mr. Joe Counsil for his timely help with all the instruments and Mr. Mike Myers and Mr. Dean Lenz for their help at various occasions.

I would like to thank the past and present group members for their help, guidance and more importantly their friendship. I also want to thank all my friends in India who believed in me and supported my decisions time to time. The warm support and friendship of the friends I met in Rolla is unforgettable.

The most importantly, I want to thank my parents, Mr. Prataprao Mohite and Mrs. Kamal Mohite, my brothers Suhas and Sharad, sisters-in-law Deepa and Vinaya for their unconditional love and support. Words alone cannot express my feelings for how much I owe them. To them, I dedicate this thesis.

TABLE OF CONTENTS

LIST OF ILLUSTRATIONS

LIST OF SCHEMES

PAPER III

LIST OF TABLES

Supporting Information

1. INTRODUCTION

1.1 AEROGELS

Aerogels are open-cell nanoporous solids and comprise one of the lowest-density man-made solid materials.[1] Typically, aerogels consist of more than 90% v/v of empty space. Conversely, their skeletal framework is an intricate matrix of an organic or inorganic polymer. The finely structured skeletal framework and the vast empty space provide aerogels with high surface areas, low thermal conductivities and dielectric constants, and high acoustic attenuation.[2] In particular, extremely low thermal conductivities are the result of mesopores (i.e., pores in the 2 to 50 nm range), which are smaller than the mean free path of air (68 nm at standard temperature-pressure (STP)).[3]

Aerogels were invented by S. Kistler in the 1930s. He replaced the pore-filling solvent in wet-gels with air without destroying the gel structure, by converting the liquid into a supercritical fluid (SCF).[4] Besides silica, Kistler successfully prepared other aerogels that include alumina, tungstic, ferric, or stannic oxide and nickel tartrate along with some organic aerogels based on cellulose, nitrocellulose, gelatin, agar or egg albumin.[5] Silica aerogels are the most common and most well-studied materials in this class. The silica wet-gel precursors were made from aqueous sodium silicate solutions in which the gelation solvent (water) was replaced with copious solvent extractions by ethanol. Kistler perceived the potential industrial applications of aerogels and eventually ended up commercializing the first silica aerogels through Monsanto Chemical Company. The main drawback in the preparation of silica aerogels from aqueous sodium silicate solutions was the time-consuming solvent exchange steps. Peri improved that process by using sol-gel chemistry with metal alkoxides as precursors.[6] Subsequent research efforts

have extended this class of materials to non-silicate inorganic oxides, natural and synthetic organic polymers, carbon, metal and ceramic materials.[7]

The unique properties of aerogels result from the structure of their solid network, which for a typical silica aerogel, is shown in Figure 1.1. The solid network consists of a complex hierarchical structure comprising agglomerates of porous secondary particles which in turn are aggregates of smaller primary particles. The generation and agglomeration of the particles is controlled by the chemistry of gelation. The physical properties of aerogels are effectively derived by the shape and size of pores created by the solid network.[8] Consequently, a significant effort has been directed to better understand and control the nanoporous structure. Aerogels have now reached a stage where the focus is on their applications and commercialization.
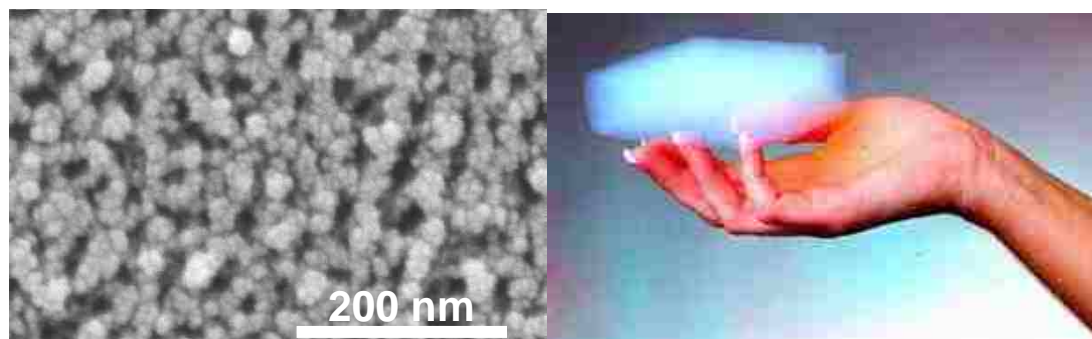
Figure 1.1 The typical nanostructure of a silica aerogel on left and its macroscopic appearance on right.[9]

1.2 THE THREE DIMENSIONAL STRUCTURAL NETWORK IN SILICA AEROGELS

The formation of three dimensional porous networks of nanoparticles is one of the key steps in the preparation of aerogels. Figure 1.2 shows the preparation of silica aerogels via the so-called sol-gel process, which involves mixing of precursors to form nanoparticles through polymerization and phase separation of colloidal primary nanoparticles. When enough primary nanoparticles are formed, they are connected to one another to form fractal secondary particles. Those secondary particles agglomerate, forming a network that grows in three dimensions to yield a wet-gel.

Typical alkoxy silane precursors used for the synthesis of silica aerogels include tetramethylorthosilicate ($Si(OCH_3)_4$, abbreviated as TMOS) or tetraethylorthosilicate ($Si(OC_2H_5)_4$, abbreviated as TEOS). Those precursors are dissolved in their respective alcohol, which acts as a co-solvent for the silane and water needed for hydrolysis. Thus, the first step of the process is either an acid- or a base-catalyzed hydrolysis of the alkoxy silane to form silanols, which undergo a condensation reaction in situ to form Si-O-Si linkages that grow in 3D to form a silica network that in turn yields sequentially primary particles, secondary particles and higher aggregates, as above.[10] The resulting solvent-filled wet-gels are solvent-exchanged with alcohol to remove water from the network before drying. Silica wet-gels can be dried in two different ways: (a) by allowing entrapped solvent to evaporate at atmospheric pressure to form a collapsed porous structure with extensive shrinkage that is referred to as a xerogel; or, (b) by using a supercritical fluid (SCF) such as CO_2 to form an aerogel whereas the volume and the porous structure of the original wet-gel are retained. In practice, supercritical drying involves use of an autoclave to replace the gelation solvent with liquid CO_2, which is then

converted to SCF that is vented off isothermally (critical point of CO_2: 31.1 ^{o}C at 1072 psi).[11]
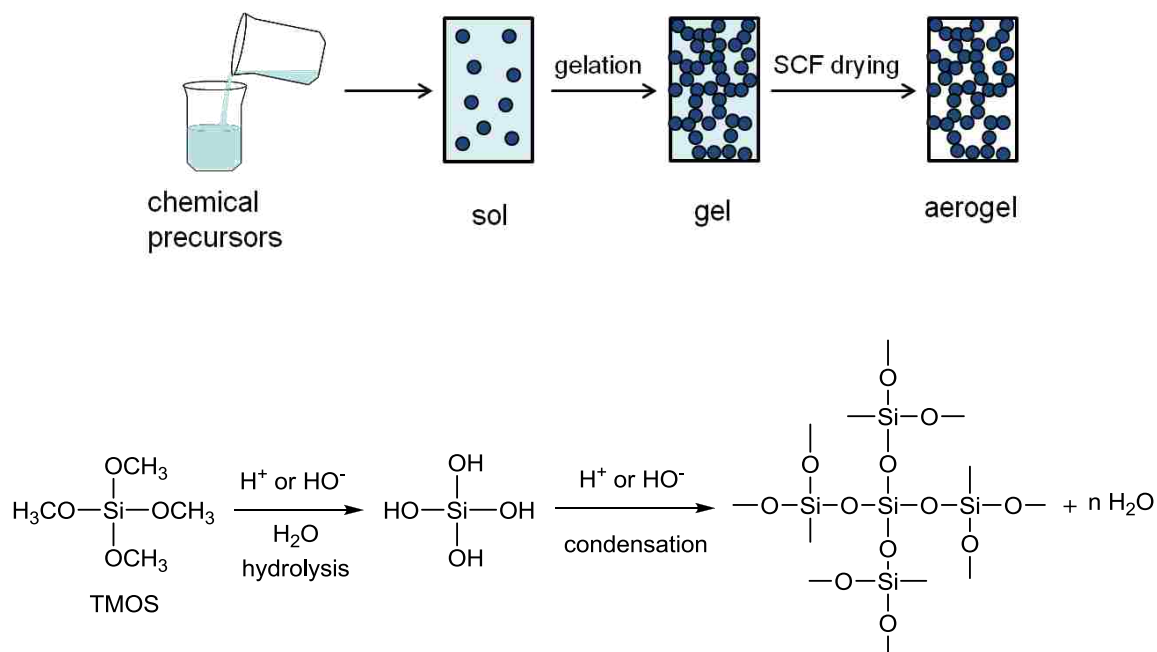
Figure 1.2 Preparation of silica aerogel via the sol-gel process.

1.3 CROSSLINKED SILICA AEROGELS (X-AEROGELS)

Because of their attractive bulk properties, aerogels have been proposed for many applications including thermal and acoustic insulation,[12] dielectrics,[13] catalyst supports[14] and as hosts for functional guests in chemical, electronic and optical applications.[15] However, silica aerogels have been actually used only in specialized environments, like as Cerenkov radiation detectors in certain nuclear reactors, aboard spacecraft as collectors for cosmic particles (NASA's Stardust program),[16] and for thermal insulation in planetary vehicles on Mars. Despite their attractive properties and potential applications,

commercialization of silica aerogels has been slow, because of their fragility and poor mechanical properties. The poor mechanical properties of silica aerogels are generally attributed to the well defined narrow interparticle necks.[17] In our past research work, we have resolved the fragility issue by crosslinking aerogels with organic polymers.[18]

For this, it was realized that chemically, silica particles possess hydroxy functional groups on their surface, which were reacted with isocyanate groups from polyisocyanates to form polyurethane tethers that bridge chemically (crosslink) the nanoparticles, reinforcing the interparticle necks. The entire skeletal framework is coated conformally with a polymer while maintaining open pores (Figure 1.3), and the resulting materials have been referred to as polymer-crosslinked aerogels (X-aerogels). X-aerogels are exceptionally strong in comparison not only with their non-crosslinked counterparts (native aerogels), but also with other materials that are usually considered strong, such as steel, Kevlar and silicon carbide.[19] Importantly, other bulk properties of X-aerogels such as the internal void space or the specific surface area are not compromised significantly by crosslinking, while the flexural strength of a typical X-aerogel monolith is increased by 300 times for a nominal increase in density by only factor of 3.

The functional groups on the surface of nanoparticles used as anchors for polymer bridges can be altered by careful choice of the molecular precursors. More versatile surface modification of silica particles can be easily achieved by using trialkoxysilanes as precursors. Figure 1.4 shows the surface functionalization of silica aerogels with amines using 3-aminopropytriethoxysilane (APTES).[20] Because of lower reactivity, APTES undergoes slower hydrolysis compared to TMOS, so the core structure of silica particles
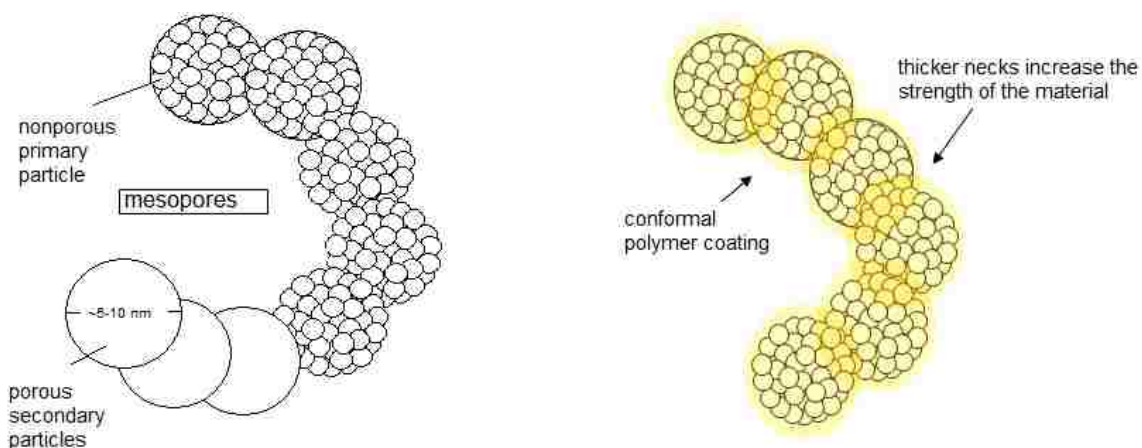
Figure 1.3 A thin polymer layer is formed conformally on the skeletal silica nanoparticles.

is formed from TMOS while $-NH_2$ groups from APTES remain on the surface of the TMOS-derived nanoparticles, and are available to carry out further polymerization (crosslinking) processes. Thus APTES-originating amines have been utilized for attachment of epoxy resins,[21] polyurea,[18b] or polystyrene.[18c]

Another polymer chemistry that has been widely studied and is used recently with an accelerating space for the preparation of new polymeric materials is ring opening metathesis polymerization (ROMP). ROMP-derived polymers such as polynorbornene and polydicyclopentadiene are extremely robust and have been commercially successful.[22] With the advent of new, highly active, functional group tolerant catalysts for ROMP and by appropriate surface modification of silica particles, ROMP can be used for the crosslinking of silica aerogels to yield new class of mechanically strong X-aerogels.
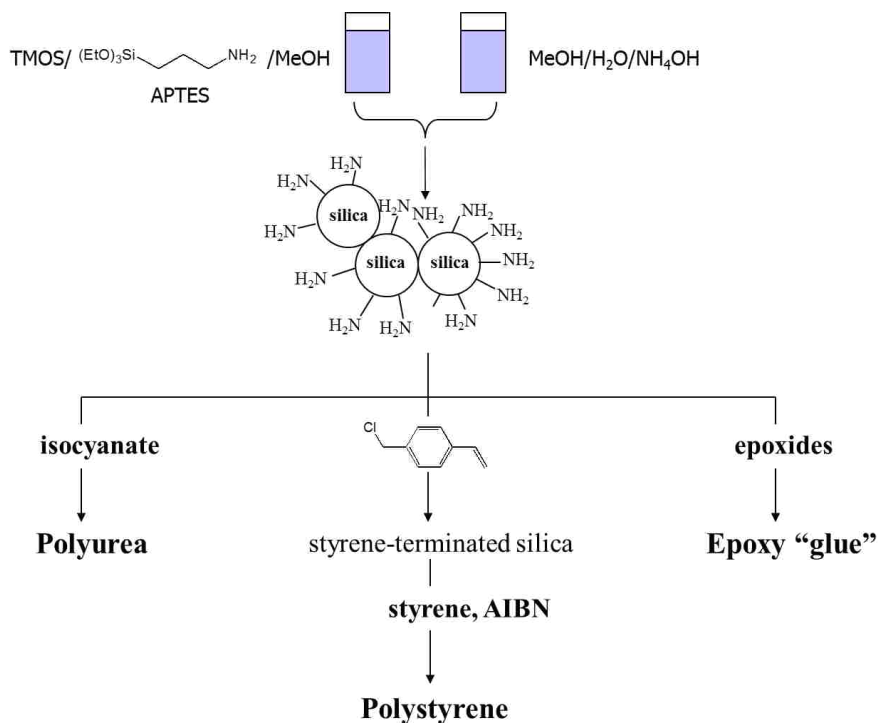
Figure 1.4 Surface modification of silica with amines for polymer crosslinking.

1.4 RING OPENING METATHESIS POLYMERIZATION (ROMP)

In recent years, a lot of interest is shown by many synthetic organic and polymer chemists in olefin metathesis reactions (Scheme 1).

Scheme 1. Olefin metathesis
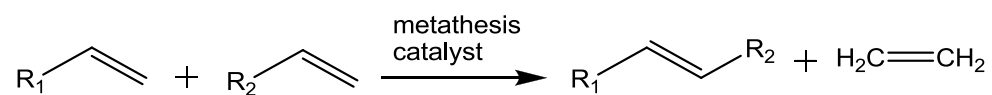
Scheme 2. Ring opening metathesis polymerization (ROMP)
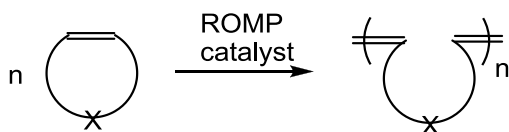
Application of the olefin metathesis to cyclic olefins led to the development of new and versatile materials through ring opening metathesis polymerization (Scheme 2). ROMP has made it possible to synthesize a variety of functionalized polymers by direct incorporation of functional groups from the monomer. Also, the unsaturation in the polymer backbone allows carrying out different reactions to externally incorporate functional groups for backbone modification. Incorporation of different functional groups from the monomer itself is the main area of interest as it gives leverage to modify material properties. Further, the functional group tolerance of ruthenium catalysts has made ROMP available to new and a more diverse set of monomers. Before going to the recent advances in development of new polymeric materials through ROMP from these new monomers, it is important to understand the evolution of olefin metathesis catalysts.

Most of the catalytic processes have been found by accident, and the same is true for olefin metathesis. It was discovered through the outgrowing studies of Zeigler polymerization with different metal systems.[23] Karl Zeigler discovered in 1953 the $TiCl_3$/ Et_2AlCl as a heterogeneous catalytic system for the polymerization of ethylene.[24] Other metal salts were also investigated in combination with alkyl aluminum compounds. Natta in 1954 demonstrated the synthesis of stereoregular polypropylene using similar catalysts.[23] On one occasion, the reaction produced 1-butene from ethylene instead of

polymer. Subsequently, it was found that the presence of Ni in the autoclave was responsible for 1-butene, and that discovery has since become the foundation of olefin metathesis.[23] Later, a group at DuPont observed that polymerization of norbornene produced unsaturated polymer in which one ring had been opened.[25] Natta observed similar results with the polymerization of cyclopentene using W and Mo halides.[26] Another group at Philips Petroleum Co. observed formation of ethylene and 2-butene during attempted polymerization of propylene.[27] All those observations together indicated a fundamentally new olefin metathesis reaction.[28]

Initially, a pairwise mechanism was proposed involving a quasicyclobutane-metal complex as shown in Scheme 3.[29] Chauvin proposed a new non-pairwise mechanism that

Scheme 3. The pairwise mechanism of olefin metathesis (proved incorrect)
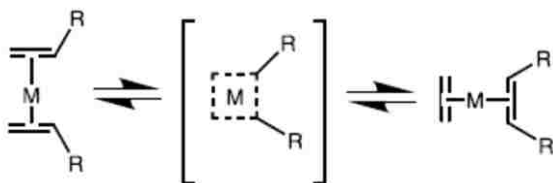
involved fragmentation of olefin to form a 4-membered metallacyclobutane as intermediate by alternating [2+2] cycloadditions and cycloreversions (Scheme 4). This mechanism has now become known as the "carbene" mechanism.[30]

Scheme 4. Carbene (non-pairwise) mechanism of olefin metathesis
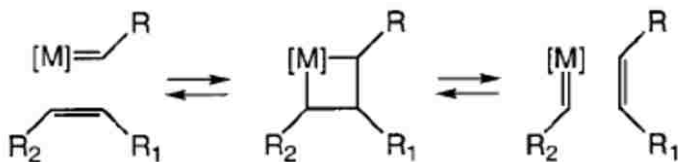
During early stages of olefin metathesis studies, metathesis catalysts were prepared by the alkylation of high oxidation state early metal halides (W and Mo). These are referred to as the "classical" metathesis catalysts. The first high oxidation state alkylidene complexes (Ta) (**1**) were prepared by Schrock, but it was shown that those catalysts did not induce olefin metathesis.[31] On the other hand, Fischer carbenes (**2**) which are low oxidation state carbenes, showed low activity towards olefin metathesis.[32]

1   **2**
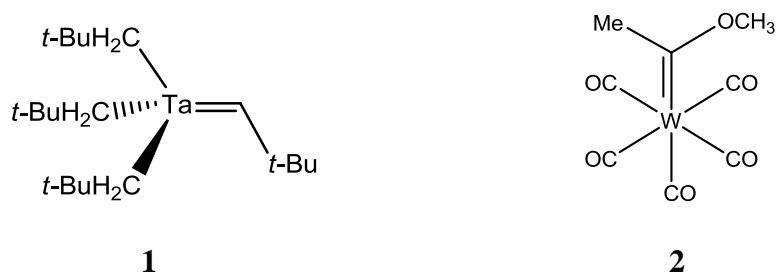
The first "well-defined" metathesis catalysts were developed by Tebbe, Schrock and Osborn from high oxidation state late metal complexes.[33-35] The catalyst developed by Tebbe which is now known as "Tebbe reagent" in a "Wittig-type" reaction (Scheme 5) served as an excellent model for the mechanistic study of olefin metathesis.[36]

Scheme 5. Tebbe reagent in a Wittig-type reaction
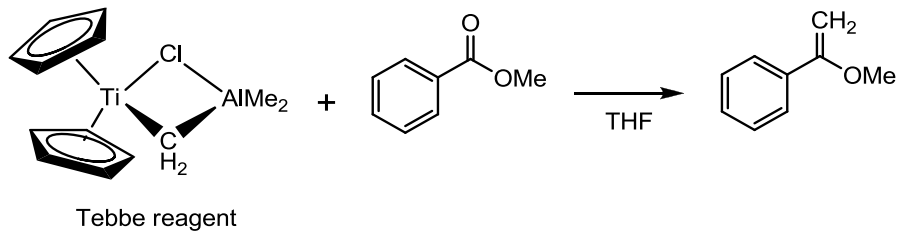
Tebbe reagent

In a mechanistic study, the Tebbe reagent was used to determine the structure of metallacycle intermediate, and it was shown that addition of pyridine to the reaction system formed a metallacycle intermediate as a stable complex (Scheme 6).[37] Further experiments on this study established that the formation of metallacyclobutane is the intermediate complex in olefin metathesis. Identification of the key intermediate in olefin metathesis influenced the work of catalyst development based on rational design for further catalyst optimization.

Scheme 6. Formation of metallacycle intermediate as a stable complex

metallacycle intermediate
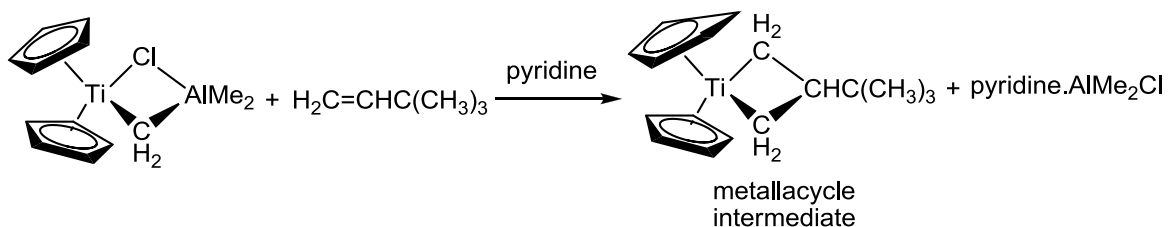
Schrock's highly active tungsten and molybdenum alkylidene complexes containing bulky imido ligands were the first efficient and controlled catalysts for metathesis. That was a breakthrough in olefin metathesis reactions as Schrock's alkylidene complexes made the foundation for work in organic and controlled polymer synthesis.[38] During those initial stages in controlled polymer synthesis, it was found that Tebbe complex forms a stable metallacycle with norbornene which on heating with more norbornene forms a polymer. Further studies showed that norbornene would be polymerized using this stable metallacycle only at higher temperature whereas it would be inactive for polymerization after cooling to room temperature. The resulting polymer would contain an active titanacyclobutane at the end of polymer that can be reactivated on heating, giving rise to living polymerization (Scheme 7).[39]

Scheme 7. Living polymerization of norbornene
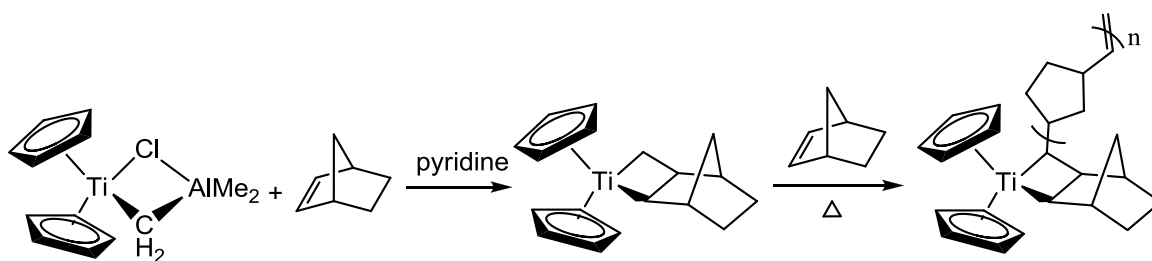
Subsequently, Schrock developed a number of very efficient molybdenum and tungsten metathesis catalysts. But the oxophilicity of the metal center in those early transition metal catalysts led to poor functional group tolerance making the handling and

preparation of catalysts to be carried out under inert atmosphere.[40] The necessity to develop a new, functional group tolerant catalyst led to the ruthenium (II) based catalyst. Nguyen and Grubbs prepared the ruthenium based catalyst **3** which was active towards polymerization of norbornene and also stable in presence of protic solvents.[41]

$$
\begin{array}{c}
\text{PPh}_3 \\
\text{Cl}_{\textit{/////}} | \qquad\qquad\qquad \text{Ph} \\
\text{Ru}=\\
| \quad \text{Cl} \qquad\qquad \\
\text{PPh}_3 \qquad\qquad \text{Ph}
\end{array}
$$

3
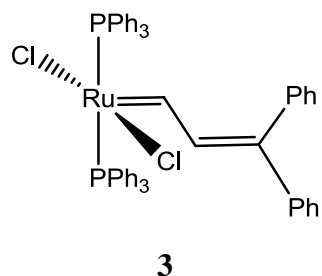
The basic structure of bis(triphenylphosphine)dichloro ruthenium alkylidene complex **3** has remained the same in even most recently developed highly active metathesis catalysts. This catalyst was only active for metathesis with strained and electron rich olefins. In the beginning, based on conclusions drawn from Schrock-type (early transition metal) catalysts, it was assumed that the activity increased with more electron-withdrawing ligands, and it was believed that ruthenium-based catalyst activity and tolerance to ligands were inversely related. However, it was found out that the larger in size and more basic the phosphine ligand, the higher the metathesis activity and the more tolerant to functional groups. In that regard, Nguyen and Grubbs developed catalyst **4** by exchanging triphenylphosphine (PPh$_3$) ligands with more basic and bulky tricyclohexylphosphine (PCy$_3$) ligands. Catalyst **4** will polymerize unrestrained olefins (e.g., cyclopentene) and induce reactions with acyclic olefins.[42]

Those ruthenium based systems have greater functional group tolerance and can be handled using standard organic techniques whereas handling early transition metal catalysts required vacuum line and dry box conditions. Synthesis of **4** also involved the
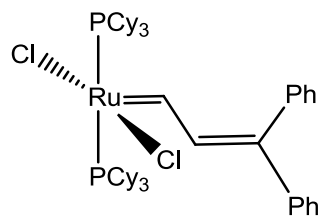
4

difficult synthesis of diphenylcyclopropene and thus limited availability of these complexes. Alternatively, alkylidene complexes were synthesized (**5**) in good yield using alkyl- and aryl-diazoalkanes (Scheme 8).[30] Also, it was found that the reactivity of alkylidene derivatives was higher than diphenylvinyl derivative.

Scheme 8. Synthesis of **4** and **5**[30]
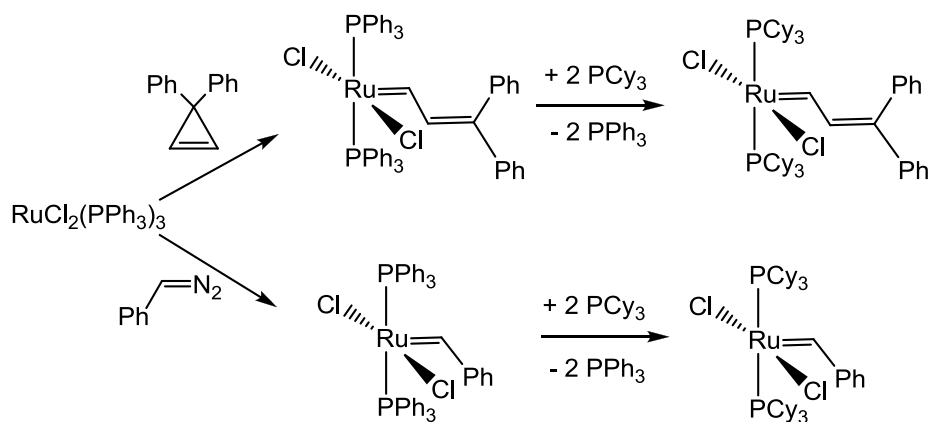
Ruthenium's preference for soft Lewis bases and π-acids, such as olefins, over hard bases such as oxygen-based ligands, is responsible for its high tolerance to air and water. Early studies based on the mechanism of olefin metathesis using well-defined Ru-alkylidene complexes had established that phosphine dissociation is the crucial step in

catalytic reaction.[43] Substitution of one phosphine ligand with olefin can happen by either associative or dissociative pathway (Scheme 9). Associative pathway (A) involves initial binding of olefin to the metal center to form 18e⁻ complex followed by loss of phosphine. On the other hand, dissociative pathway (B) proceeds by initial loss of phosphine.

Scheme 9. Substitution of phosphine with olefin in catalytic activity[43]
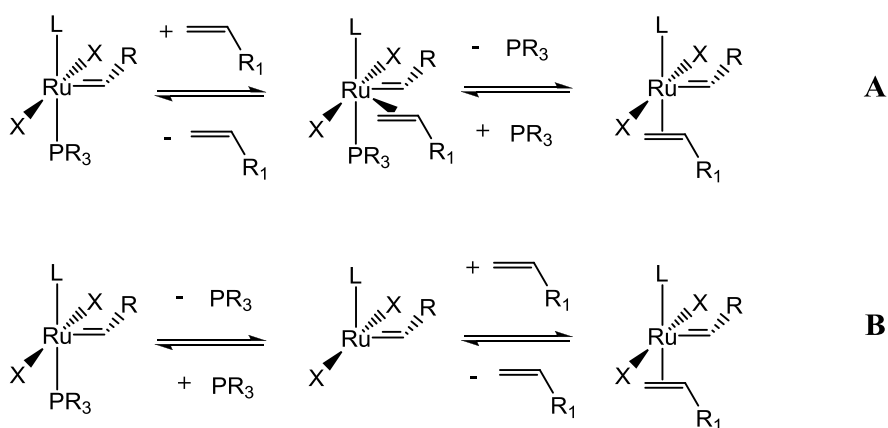
Detailed mechanistic study catalyzed by different Ru-complexes with varying ligands concluded that substitution of phosphine with olefin occurs in a dissociative fashion through first formation of a 14e⁻ intermediate as active species. However, the re-coordination of free phosphine is competitive with the olefin binding and the active species carries out few catalytic turnovers before getting 'quenched' with free phosphine. Coordination of olefin to the metal center involves two possibilities (Scheme 10). In one possibility, alkylidene rotation occurs to give an intermediate where olefin remains cis to the alkylidene. This intermediate then forms a metallacyclobutane cis to the bound

phosphine, followed by cleavage to yield metathesis products. In second possibility, olefin rearranges during coordination followed by metallacyclobutane formation trans to the bound phosphine.[30] Different metathesis catalysts show different stereoselectivity based on metal center as well as coordinated ligands to yield stereoregular polymers or metathesis products.

Scheme 10. Mechanism of olefin metathesis[30]
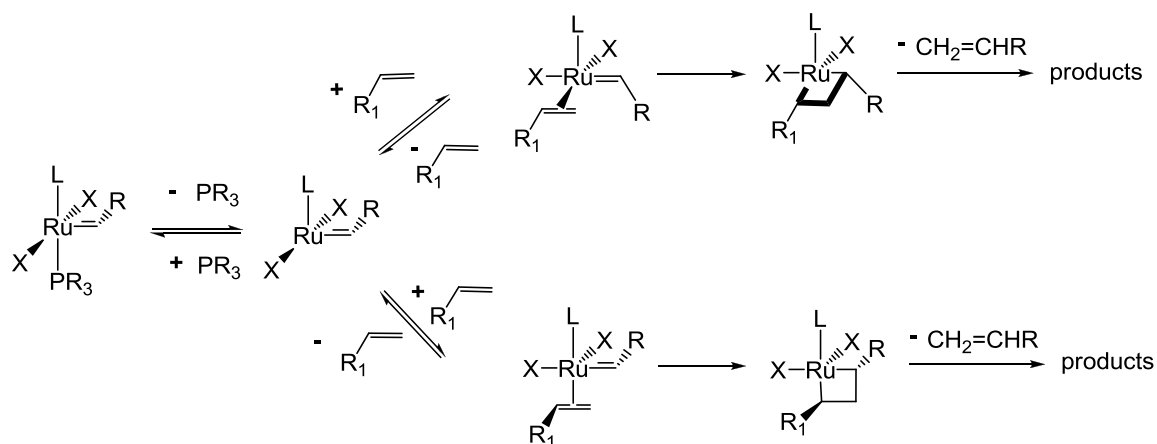
Thus, the catalyst activity depends on olefin binding, phosphine dissociation and the stability of the intermediate. For olefin metathesis to begin, one of the phosphine ligands must be labile enough for dissociation and activate the catalysis by forming a metallacyclobutane intermediate. The contribution of the second phosphine ligand is through σ-donation to the metal center and stabilizes the intermediate. Previously, N-heterocyclic carbene ligands were found to be stronger σ-donors and less labile compared to phosphine. In mixed-ligand complex **6**, N-heterocyclic ligand enhanced the

dissociation of phosphine and also stabilized the electron-deficient intermediate by virtue of its bulky and σ-donating properties.[44] Complex 6 is referred to as the 2nd generation Grubbs' catalyst, and demonstrates exceptional activity in large number of ROMP reactions. However, it yields polymers with un-controlled molecular weight and broad polydispersities, because of its relatively slow initiation rate and secondary chain-transfer reactions. Further catalyst tuning by weakly coordination pyridine ligands has resulted into a new class of Ru-based catalyst (compound **7**). Those catalysts exhibit fast initiation kinetics and the resulting polymers show low polydispersity.[44]

1st generation
Grubbs' catalyst (**GC-I**)

2nd generation
Grubbs' catalyst (**GC-II**)

3rd generation
Grubbs' catalyst (**GC-III**)

5   **6**   **7**
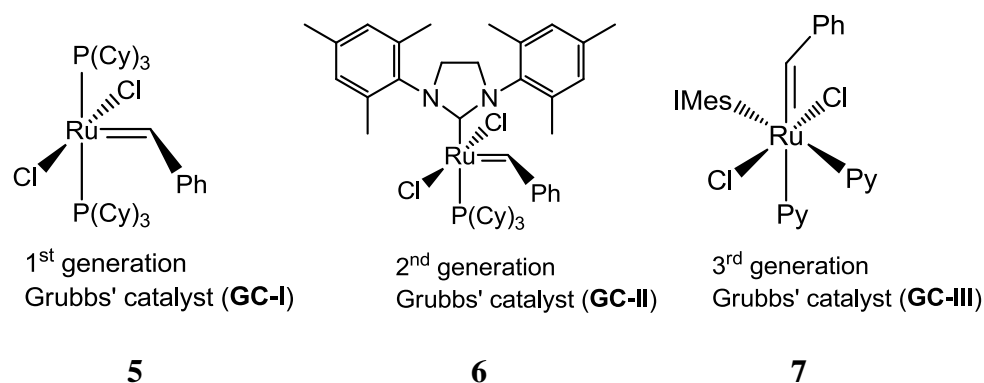
1.5 APPLICATIONS OF ROMP IN POLYMER SYNTHESIS

The properties of polymeric materials can be tuned by proper selection of functional groups as part of the polymeric chains. A lot of research is being carried out to synthesize new polymeric materials with different properties by incorporating appropriate functional groups through norbornene and oxanorbornene derivatives. At the same time, well-defined and tuned active catalysts are also being developed, which are tolerant to different functional groups, thus broadening the choice of monomers. Some of the earliest commercial applications of olefin metathesis involved the production of

polydiclopentadiene (pDCPD) through ROMP of dicyclopentadiene (DCPD).[40] DCPD polymerizes at room temperature with ruthenium catalysts to give tough and highly cross-linked polymer networks (Scheme 11). Currently, polydicyclopentadiene is a commercial material made by reaction injection molding (RIM) even at low temperatures, and is used to manufacture large parts with good structural characteristics such as stiffness and impact strength as well as moisture resistance.

Scheme 11. Polymerization and crosslinking of DCPD by ROMP
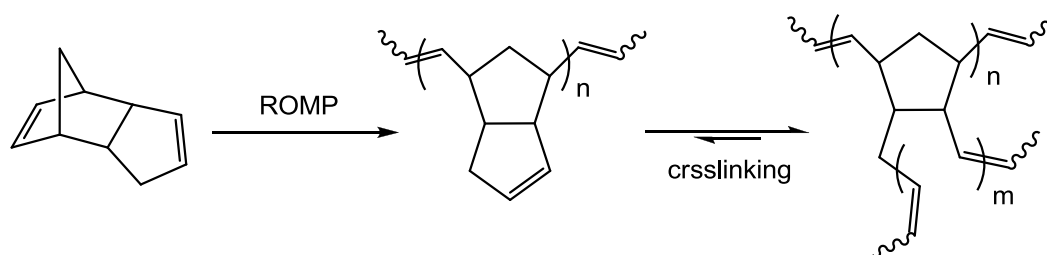
The mechanism of crosslinking in pDCPD, however, has been controversial. The conventionally accepted crosslinking reaction has been attributed to an equilibrium metathesis reaction of the pendant cyclopentene ring of DCPD (Scheme 8). However, Wagener and co-workers have studied the polymerization mechanism of DCPD using both classical (WCl_6/$(C_2H_5)_2AlCl$) and the well-defined Schrock's alkylidene catalyst **8**.[45] In their study, they have used two model monomers 8,9-dihydrodicyclopentadiene (**9**) and 5,6-dihydrodicyclopentadiene (**10**). Polymerization of **9** using the classical catalyst (WCl_6/$(C_2H_5)_2AlCl$) produced the polymer through ROMP of strained norbornene ring

with a small amount of olefin addition. On the other hand, polymerization of **10** using

WCl$_6$/(C$_2$H$_5$)$_2$AlCl produced a linear polymer exclusively through olefin addition with no

8   **9**   **10**
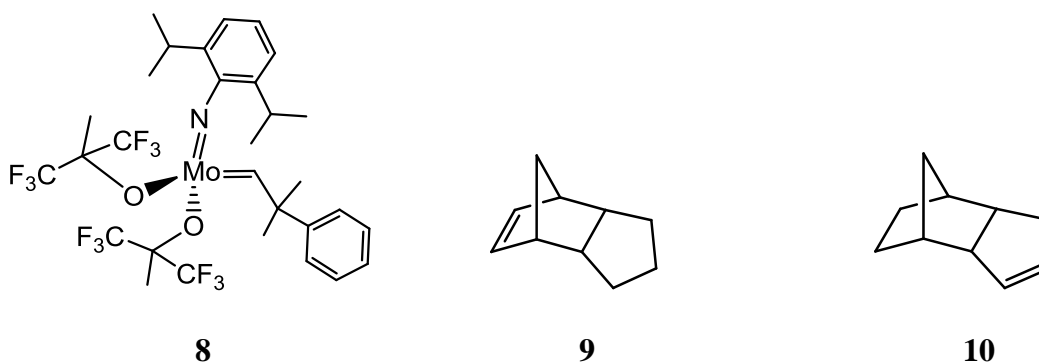
signs of ROMP. Attempted reaction of **10** using Schrock's catalyst **8** did not induce any

polymerization indicating that **10** is completely inert to metathesis. Also the

polymerization of DCPD in high concentrations using **8** produced highly crosslinked

insoluble polymer while low concentrations of DCPD produced linear and soluble

polymer. Based on those observations, it was concluded that crosslinking in pDCPD does

not take place through the widely accepted mechanism that involves ROMP of the

pendant cyclopentene ring, but instead the pendant cyclopentene is inert to the metathesis

reaction and crosslinking takes place through olefin addition into the cyclopentene ring

(Scheme 12) induced by heat released during the highly exothermic ROMP reaction of

the norbornene moiety.

One of the recent and technologically advanced applications of ROMP of DCPD

involves autonomic healing of polymer composites. S. R. White and co-workers

developed a composite system of epoxy by incorporating DCPD-filled microcapsules

(50-200 μm) with a urea-formaldehyde shell, which were prepared by standard

microencapsulation techniques.[46] The microcapsule shell provides a protective barrier

between the ROMP Grubbs' catalyst embedded in the composite matrix and DCPD,

Scheme 12. Crosslinking in pDCPD through olefin addition[45]
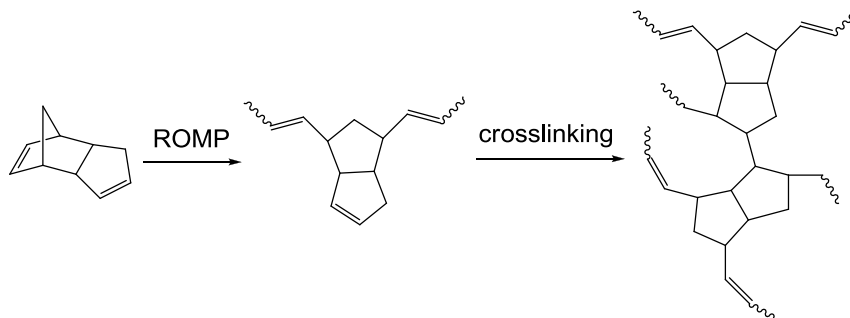
which prevents polymerization during preparation of composite. Propagating cracks caused by thermal or mechanical fatigue, rupture microcapsules along the path, releasing by capillary action DCPD in matrix. DCPD comes in contact with the catalyst and induces polymerization of DCPD bonding the crack faces (Figure 1.5).
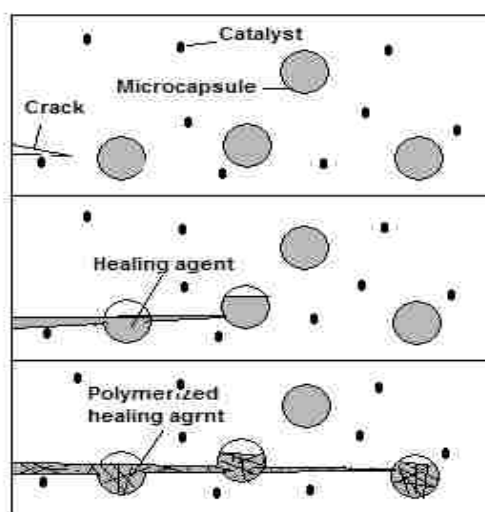
Figure 1.5 Autonomical healing of polymers using pDCPD.[46]

1.5.1 Block Copolymers and Hyper-branched Structures. The living nature of ROMP yields polymers with narrow polydispersity, whereas the polymer length can be controlled by inducing chain termination (vinyl ethers are used as chain terminating agents), or by adjusting the monomer/catalyst ratio.[30] Since the catalyst remains attached at the end of the polymer chain even after complete consumption of the monomer, synthesis of block copolymers can be achieved easily by just adding a second monomer. Thus, T. M. Swager and co-workers have reported the synthesis and the electrochemical properties of block copolymers prepared by ROMP copolymerization of three different norbornene derivatives having phenylene-thiophene, phenylene-bithiophene and phenylene-furan linked to either norbornene or 7-oxonorbornene.[47] The block copolymers were further cross-linked by anodic electropolymerization to give conducting polymers.

Synthesis of amphiphilic block copolymers with two covalently bonded incompatible blocks is of special interest for the design of highly ordered and nanostructured materials.[48] When a block copolymer is dissolved in a selective solvent, which is a good solvent for one block and poor for the other, it self-assembles to form micelles leading to many applications.[49] Trimmel et al. have presented a comprehensive series of block copolymers synthesized with ROMP, allowing precise tuning of micelle, core and shell size (Scheme 13).[50]

In another venue, the design of highly ordered and nanostructured polymeric materials is one of the challenges facing materials chemistry. In that regard, a variety of macromolecular architectures including dendronized, cylindrical, star, hyperbranched and cyclic polymers have all been considered due to recent breakthroughs in polymer syntheses.[51-53] Dendritic macromolecules in particular are a special class of polymers

Scheme 13. Synthesis of block copolymers via ROMP[50]
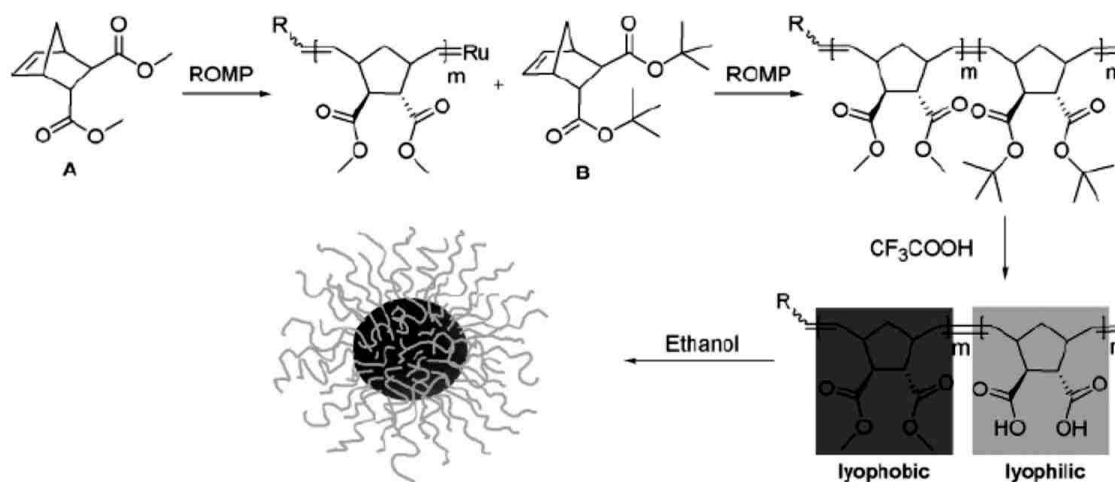
characterized by hyperbranched and well defined three dimensional architectures, which provide properties desirable for many potential applications. For example, dendrimers are promising as additives, viscosity modifiers or nanoscale building blocks. Another group of potential applications of dendrimers is as drug delivery vesicles, stimuli sensitive molecules or catalysts.[54] Living polymerization techniques are of special interest for the synthesis of dendronized polymers due to superior control over placement of dendrons along the backbone.[55] In that regard, ring opening metathesis polymerization has been utilized for the polymerization of dendronized macromonomer bearing norbornenyl group to produce cyclic organic nanostructures[56] as well as polynorbornene dendronized polymers.[57] ROMP-synthesis of nanoporous materials from a self-organizing star-shaped copolymer that creates a nanosized domain through selective collapse as a result of a solvent stimulus has also been reported.[58]

Branched polymeric structures play a vital role in the design of nanoscopic polymeric materials with potential application in drug delivery.[59] The application of dendrimers is limited by the synthetic difficulty. Similar nanoscale structures can be formed from brush-polymers, which are unique type of macromolecules with high density of side chains grafted to the polymer backbone.[60] One of the approaches to the synthesis of brush-polymers is the "grafting through" method, which involves polymerization of well-defined monofunctional macromonomers.[61] ROMP of norbornenyl functional macromonomers has been reported for the synthesis of brush polymers (Scheme 14) for use in chemotherapy delivery.[62]

Scheme 14. Schematic of bivalent macromonomer and bivalent-brush polymers[62b]
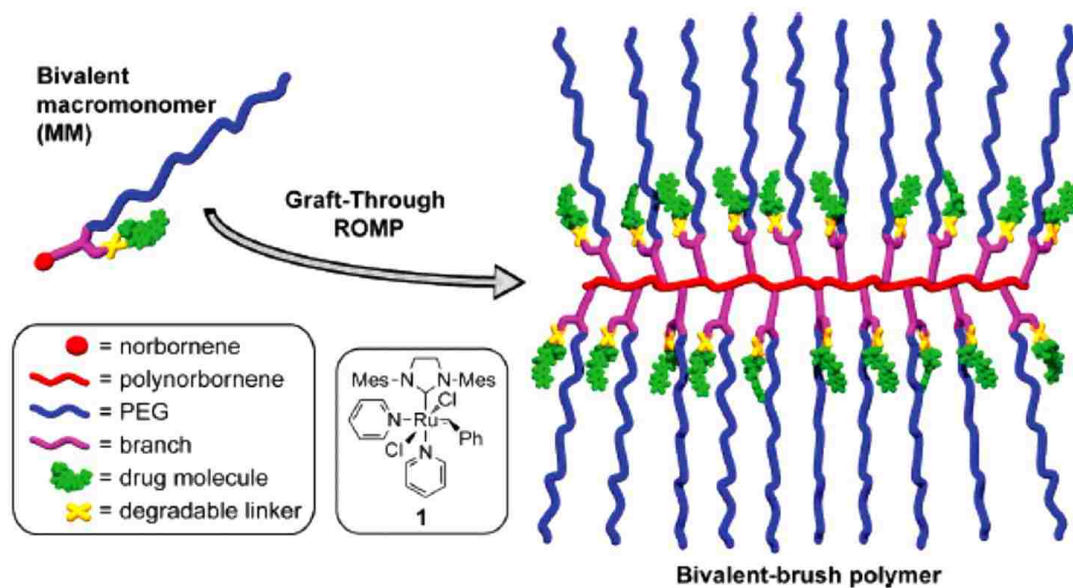
1.5.2 Aqueous ROMP. In recent years a lot of research is focused on the development of Synthetic Mimics of Antimicrobial Peptides (SMAPs).[63] Positive charge and amphiphilicity are the two most common features of antimicrobial peptides. Thus, Tew and co-workers recently reported poly(norbornenes) with pendant quaternary pyridinium groups (**11**) as SMAPs, but they were proved less selective for bacteria.[64]
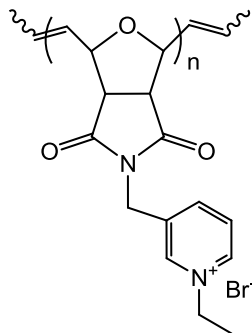
11

The same authors reported also the easy and versatile synthesis of a broad variety of amphiphilic oxonorbornene derivatives, which after ROMP and deprotection (Scheme 15) provide several series of SMAPs that are highly selective towards bacteria.[65] The hydrophilic NH_3^+ group was introduced in its protected *t*-butyl carbamate (NHBoc) form, because ROMP does not usually tolerate unprotected amines due to their ligating properties. It is also noted that the polymerization of monomers was carried out using the third generation Grubbs' catalyst.

There are many environmental and processing advantages by carrying out industrial polymerizations in aqueous media. For example, many commodity polymers and latexes are prepared by emulsion or suspension polymerization techniques.[66] ROMP of 7-oxanorbornene derivatives in aqueous media using simple ruthenium indium, and osmium salts are well documented.[67] These polymerizations are not living and their

Scheme 15. Synthesis of SMAPs though ROMP[65]
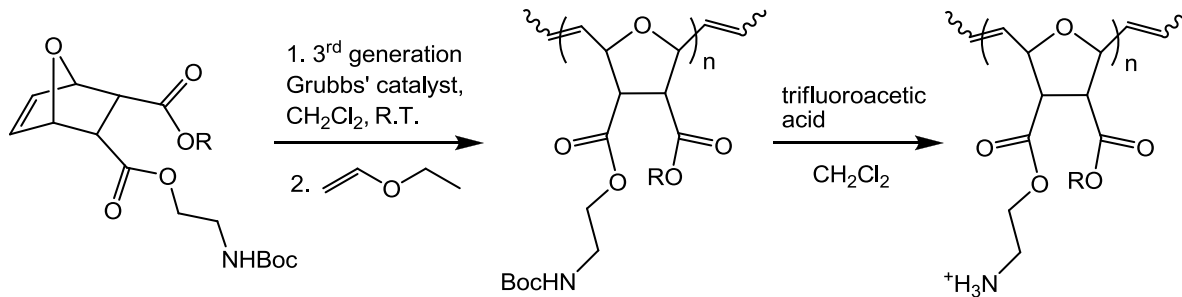
initiation is inefficient (less than 1% of metal centers are converted to catalytically active species). However, David Lynn and co-workers have reported the living ring opening metathesis polymerization of norbornene and 7-oxanorbornene derivatives in aqueous media by using Ru-based catalysts **4** and **5** in the presence of dodecyltrimethylammonium bromide (DTAB) as surfactant. The catalyst was dissolved in a small amount of organic solvent in order to achieve controlled initiation.[68] That emulsion system gave a polymeric latex, nevertheless, both the polymer yield and the molecular weight were reported to be lower than those obtained by solution polymerization. The same authors have further reported water-soluble catalysts **12** and **13** for living ROMP. Using these catalysts, water soluble monomers can be homogeneously polymerized in water in the presence of Bronsted acids without any surfactant or organic solvents.[69]
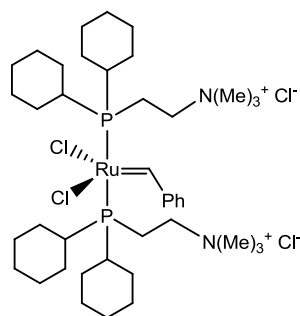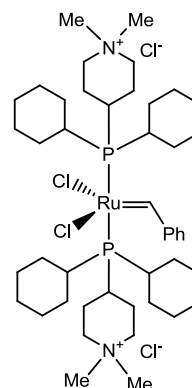
12   **13**

1.5.3 Surface-initiated ROMP. Surface-initiated polymerization is a relatively recent approach for growing polymeric thin films on silicon and gold substrates using cationic, anionic and radical polymerization methods.[70] The advantage of ROMP over other surface-initiated polymerization methods lies in the mild conditions involved and the short reaction times. Thus, ROMP has been used as a surface polymerization process at room temperature to form uniform, covalently bonded polymeric films, patterned polymer overlayers, as well as polymer brushes on silicon and gold substrates.[71,72]

Polymerization of monomers on a substrate is initiated by decorating the surface with a Ru catalyst through norbornenyl groups (Scheme 16).[73] Further, new synthetic methods developed for the preparation of nanostructured materials consisting of inorganic cores and organic polymer shells yield a versatile class of hybrid nanocomposites. There are also reports on synthesis of both silica and gold hybrid core-shell nanostructures through surface-initiated ROMP, by taking advantage of the recently developed Ru-based ROMP catalysts **5** and **6**.[74,75]

Scheme 16. Schematic for surface-initiated ROMP[71]
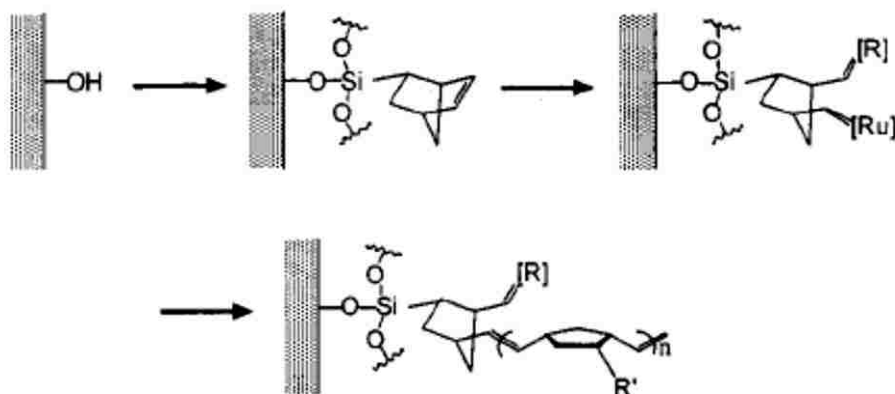
1.5.4 Porous Polymeric Materials through ROMP. Dense macroporous polymers with structural rigidity in the form of polymeric microglobules were introduced in the 1950s for chromatographic applications, and utilize extensive crosslinking at the molecular level.[76] Such macroporous polymers are often prepared in the form of polymeric beads by suspension polymerization from polystyrene-divinylbenzene (PS-DVB) and acrylic polymers.[77] Monolithic separation media on the other hand are becoming more important due to their beneficial properties such as high throughput at comparably low back pressures.[78] Thus, monolithic capillary columns show completely different flow characteristics as stationary phases compared to packed-column stationary phases, as monoliths are one single piece of highly porous material. Also simple, one-step *in-situ* preparation procedures allow for almost no limitation in column dimensions.[79] In that regard, ROMP has been also used for the preparation of polymeric monoliths based on norbornene and its derivatives.[80] The advantage of using ROMP is that the resulting polymer is highly unsaturated, and the backbone double bonds can be used for

introducing functional groups that modify and tailor the selectivity towards specific analytes.

At this point it is noted that porous polymeric monoliths used as separation media are basically synthesized via sol-gel methods, which are conceptually and practically similar to the bottom-up approach used for the synthesis of aerogels. In that bottom-up approach, phase-separation and the pore structure can be controlled by using non-solvents as porogens.[81] Specifically, using solvents miscible with the monomer but insoluble in the polymer can yield an array of structures: Low solvent concentrations (closer to neat monomer) create closed pores, while higher solvent concentrations induce phase separation of the polymer and the structure consists of hierarchical primary/secondary particle structures. The phase diagram shown in Figure 1.6 summarizes the phenomena observed across the entire solvent/monomer/polymer range. It has been noted that bicontinuous structures corresponding to spinodal decomposition expected in a narrow range of intermediate solvent/monomer concentrations have not been observed. Along those lines, homogeneous, as well as porosity-gradient macroporous monoliths of crosslinked polydicyclopentadiene have been reported by *in situ* phase separation in non-solvents.[82] In terms of backbone modification, the polymerization of methyl methacrylate from the surface of crosslinked pDCPD by grafting the atom transfer radical polymerization initiator on their surface has been also reported.[83] Based on these advances, porous pDCPD monolithic wet-gels prepared using the 1st generation Grubbs' catalyst via the bottom-up approach have been dried supercritically to yield pDCPD aerogels of varying densities and thermal conductivities.[84] Specifically, lower thermal conductivity values with increasing concentration of the monomer (DCPD) have been
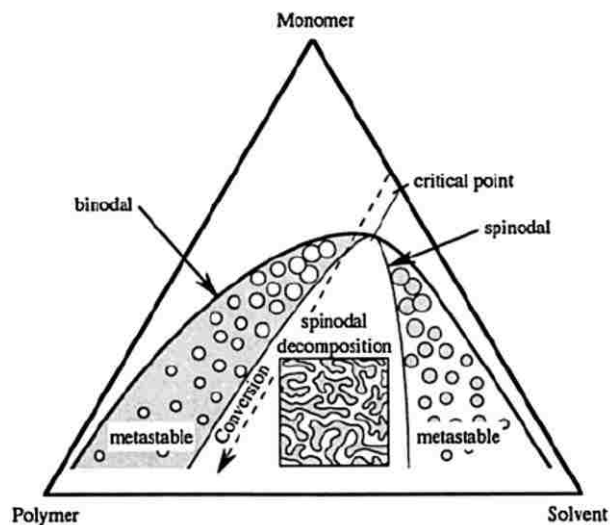
Figure 1.6 General phase-diagram of solvent/monomer/polymer system.[82a]

reported (Figure 1.7). The authors have attributed the lower thermal conductivities at higher densities to the lower gas and radiation contributions relative to the increasing contribution of the solid network to the thermal conductivity. It was further observed in that study that higher concentration sols caused an increase in larger pores, which resulted in increased pore volume, but the overall pore size distribution was not affected significantly. Authors have reported that, "most of the pDCPD aerogel monoliths were produced with regular shape and appearance (Figure 1.8). However, it should be also noted that pDCPD aerogel samples prepared with lower target densities (i.e., 0.02 g/cm3) became significantly shrunken after processing and did not show regular shape and appearance, generating dust due to their structural weaknesses. On the other hand, pDCPD aerogel monoliths prepared with relatively high target density (i.e., 0.2 g/cm3) were also shrunken non-uniformly in the radial direction, exhibiting some warpage of the
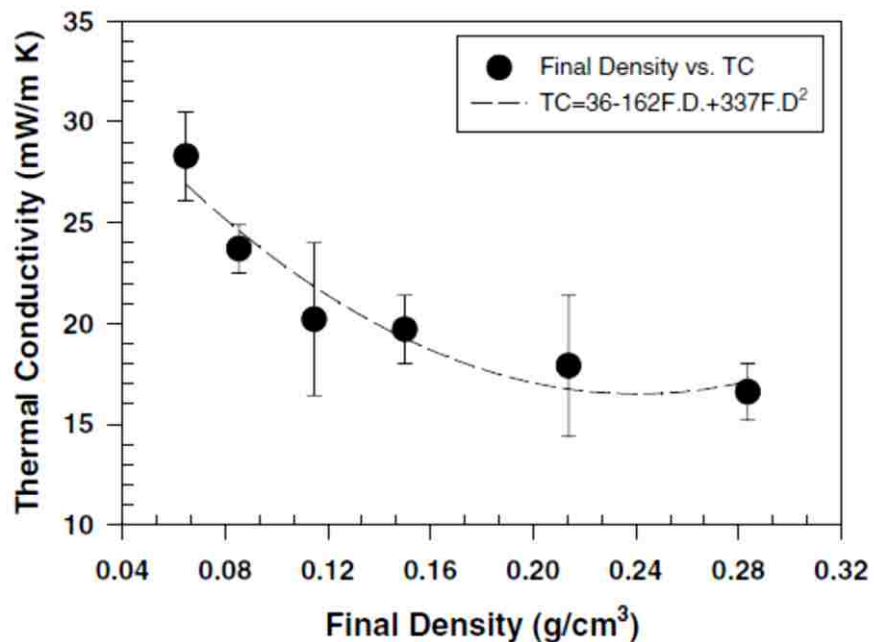
Figure 1.7 Thermal conductivity of pDCPD aerogels as a function of density.[84]

sample surface. This is probably due to the different crosslinking reaction rates locally, inducing non-uniform structural stresses during aging."
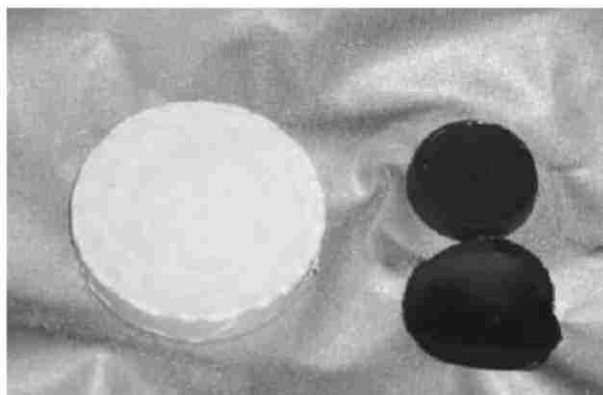
Figure 1.8 pDCPD aerogel on left and xerogel on right.[84]

DSC and solvent extraction studies indicated the presence of both linear and crosslinked pDCPD in aerogel materials. They have also reported higher thermal conductivity of pDCPD xerogels than corresponding aerogels due to higher solid conduction. More recently, a similar approach has been applied by the LLNL for making low-density aerogels films through ROMP-copolymerization of DCPD and norbornene. The gelation behavior of pDCPD was manipulated by reducing the amount of crosslinking through copolymerization with norbornene (Scheme 17) to improve the uniformity of gel-films formed under shear forces.[85]

Scheme 17. ROM-co-P of DCPD and norbornene using 1st generation Grubbs' catalyst[85]
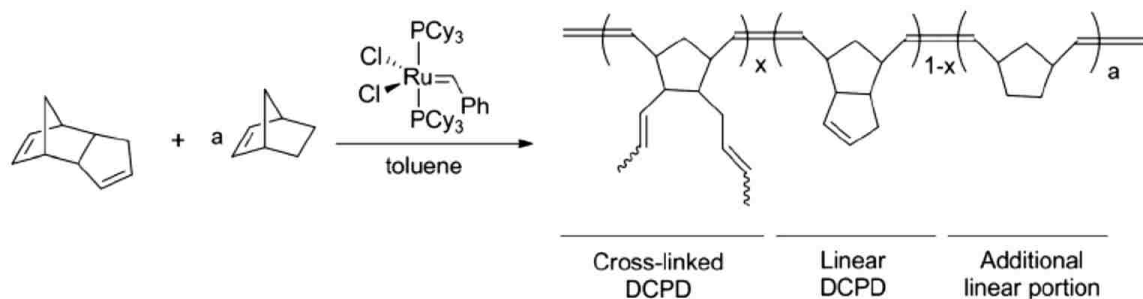
1.6 SILICA AEROGELS CROSSLINKED WITH POLYNORBORNENE VIA ROMP

The crosslinking process of aerogels is similar to grafting polymers onto surfaces, which essentially can be carried out using either the "grafting from" or the "grafting to" method, whereas both methods require appropriate surface modification.[18d] In the "grafting form" method, polymerization starts form the surface, which has to be modified

with appropriate initiator. The process is referred to as surface-initiated polymerization (SIP). On the other hand, the "grafting to" method is based on solution polymerization of monomers in the presence of surface functional groups that can be engaged in the polymerization process.

In the work described in this thesis, we used the "grafting to" ROMP method for crosslinking silica aerogels with polynorbornene. For this purpose, we synthesized a new norbornene derivative, **Si-NAD**, which was incorporated in the sol-gel silica network by co-gelation with TMOS and provided the pore surfaces of silica aerogels with the norbornene functionality.

Si-NAD
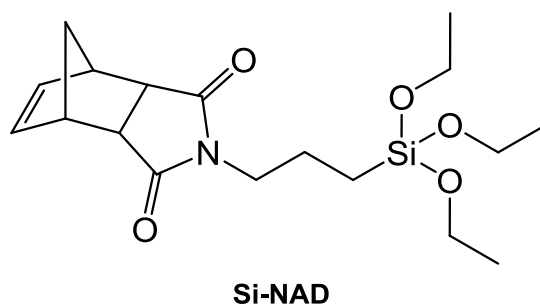
Subsequently, the pore-filling solvent was exchanged with a norbornene (NB) solution and ROMP was initiated at room temperature using the 2nd generation Grubbs' catalyst **GC-II** - see above. Subsequently, unbound polynorbornene was removed from the pores by typical solvent exchanges and samples were dried using supercritical CO_2 to yield mechanically strong **X-SiNAD** aerogels. Those polynorbornene (pNB) crosslinked aerogels (**X-SiNAD**) were used in fundamental studies of the nature of crosslinking in X-aerogels and it was determined that for greatly improved mechanical strength, the polymer needs just to fill secondary particles. Thus, the use of the term "conformal polymer coating" to describe X-aerogels is rather a misnomer stemming from the

inability of the main characterization tool (scanning electron microscopy - SEM) to see what is happening inside secondary particles.

1.7 ORGANIC AEROGELS VIA ROMP

Preparation of organic aerogels through the sol-gel process involves polymerization of monomer(s) with simultaneous phase separation. Many polymeric solutions gel, but only a sub-set can be dried into aerogels. In order to form an aerogel, it is necessary to develop chemical (covalent) bonding between the particles. Solutions of polymers with continuously increasing molecular weights either build sufficiently high viscosity and appear as gels, or undergo phase separation due to insolubility to form colloidal particles. If phase-separated colloidal particles are stabilized by interparticle covalent bonds, they form 3D networks, which can retain their form even in the dry state after removing the solvent. The formation of covalently stabilized 3D network of colloidal particles is more often possible in crosslinked polymers. Linear polymers on the other hand either give polymeric gels due to high viscosity, or form precipitates in non-solvents for the polymer. In the case of most linear polymer gels, during drying, polymer chains try to achieve their lowest energy[86] by maximizing their Van Der Waals interactions. That causes structural collapse and extensive shrinkage. Therefore, phase separation and 3D bonding are essential, and can be induced by choosing monomer precursors able to crosslink.

Most of the work in organic aerogels has been concentrated on resorcinol-formaldehyde (RF) aerogels, which upon pyrolysis yield carbon aerogels.[87] Subsequently, several other types of organic aerogels were reported based on similar phenolic-type resins, polyurethane, polyurea, polybenzoxazine, and more recently polyimides. The

targeted practical applications have always been in the area of thermal insulation. In that regard, high temperature thermal insulation is especially desirable.

Owing to the high thermal stability and exceptional mechanical properties of polyimides, aerogels of that type concentrate significant recent attention for their potential application in high temperature thermal insulation. Polyimides are generally synthesized by reaction of dianhydrides with diamines. The most commercially successful polyimide is referred to as Kapton® (trade name of DuPont Chemical Company) and is synthesized from pyromellitic dianhydride (PMDA) and oxydianiline (Scheme 18).

Scheme 18. Synthesis of Kapton® polyimide
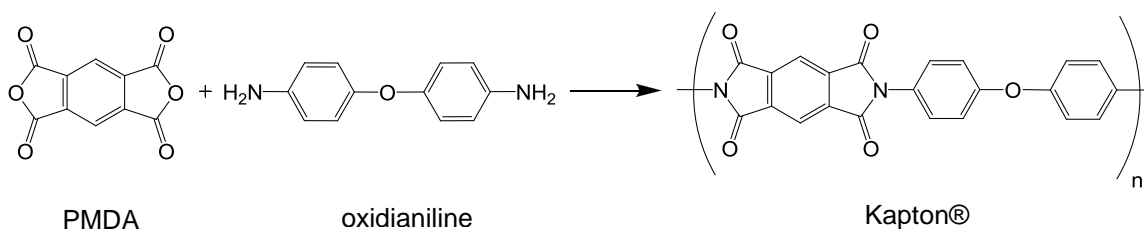
There is also another type of polyimide that has emerged as an aerospace industry standard, is referred to as PMR-15, and is based on ~1,500 molecular weight imidized oligomers, end-capped with two norbornene moieties (**14**), whose high temperature (>300 ºC) crosslinking yields the thermoset resin.
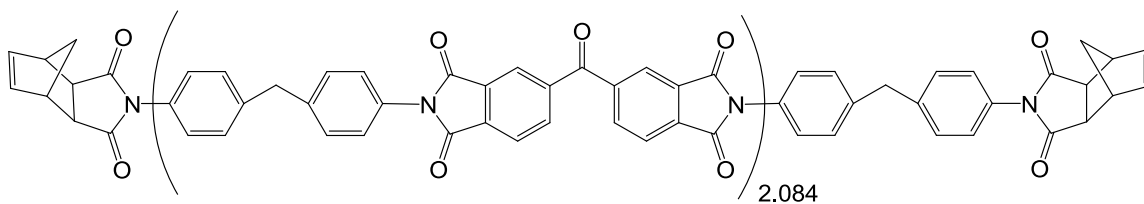
14

There are obvious advantages if PMR-type polymers could be prepared at lower temperatures. That can potentially be accomplished by ring opening metathesis polymerization (ROMP) of the end caps. Thus, inspired by the demonstrated success of the PMR-type polyimides, we synthesized mechanically strong polyimide aerogels by crosslinking through ROMP of a bisnadimide bifunctional monomer (**bis-NAD**) using the second generation Grubbs' catalyst **GC-II**.
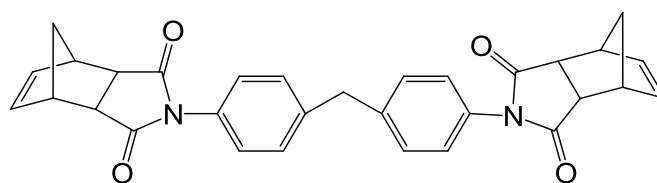
bis-NAD

Polydicyclopentadiene (pDCPD) and polynorbornene (pNB) are the two commercially successful polymers prepared through ROMP. pDCPD, which is obtained by ROMP of the monomer DCPD, an inexpensive and readily available petroleum byproduct, gives mechanically strong crosslinked polymeric structures. For example, Figure 1.9 shows a pDCPD block with two 9 mm bullets embedded in it.[88]

PolyDCPD-9mm Ballistic Protection

Figure 1.9 pDCPD composite with two 9 mm bullets embedded in it.[88]

In that regard, we attempted the synthesis of pDCPD based aerogels via Grubbs' catalyst (**GC-II**) induced ROMP of DCPD, only to receive non-uniform and highly deformed samples. That problem was resolved by crosslinking pDCPD with polymethylmethacrylate (PMMA) using free radical chemistry (Scheme 19) to yield uniform and mechanically strong polydiclopentadiene aerogels.

Scheme 19. Crosslinking pDCPD with PMMA
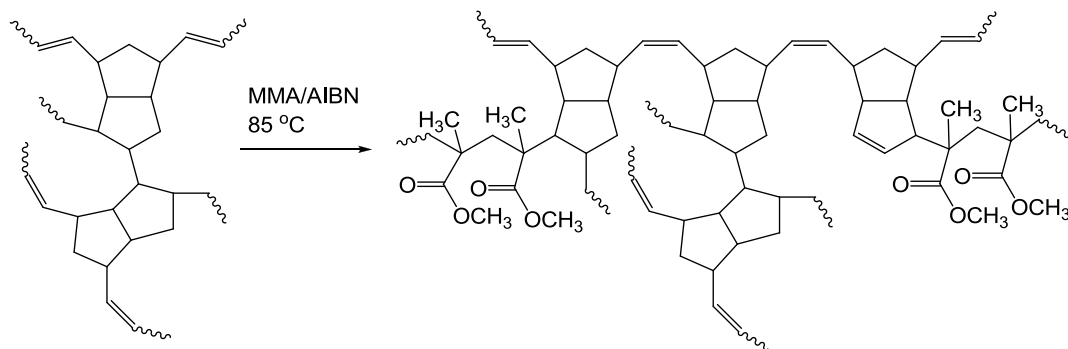
Polynorbornene on the other hand is a linear polymer, which may gel due to increase in viscosity and cannot be dried into aerogels. Here we resort to the use of a non-solvent (isopropanol) as a porogen to induce phase separation of PNB and hence form colloidal particles. Thus, this work includes synthesis of open-cell macroporous monoliths of polynorbornene by the Grubbs' catalyst (**GC-II**) induced ROMP of norbornene in toluene using isopropanol (*i*PrOH) as a non-solvent and we studied the effect of the toluene:*i*PrOH ratio on their microscopic structure.

REFERENCES

1. Tillotson, T. M.; Hrubesh, L. W. *J. Non-Cryst. Solids* **1992**, *145*, 44-50.

2. (a) Rolison, D. R.; Dunn, B. *J. Mater. Chem.* **2001**, *11*, 963–980. (b) Pierre, A. C.; Pajonk, G. M. *Chem. Rev.* **2002**, *102*, 4243–4265. (c) Al-Muhtaseb, S. A.; Ritter, J. A. *Adv. Mater.* **2003**, *15*, 101–114.

3. (a) Kistler, S. S. *J. Phys. Chem.* **1935**, *39*, 79-86. (b) Lu, X.; Caps, R.; Fricke, J.; Pekala, R. W. *J. Non-Cryst. Solids* **1995**, *188*, 226-234.

4. Kistler, S. S. *Nature* **1931**, *127*, 741.

5. (a) Kistler, S. S. *J. Phys. Chem*. **1932**, *36*, 52-64. (b) Kistler, S. S.; Sherlock, S.; Appel, E. G. *Ind. Eng. Chem.* **1934**, *26*, 388-391.

6. Peri, J. B. *J. Phys. Chem.* **1966**, *70*, 2937-2945.

7. Pierre, A. C. History of Aerogels. In *Aerogels Handbook*; Agerter, M. A., Leventis, N., Koebel, M. M., Eds.; Springer: New York, 2011, pp 3-18.

8. Kanamori, K; Nakanishi, K. *Chem. Soc. Rev.* **2011**, *40*, 754-770.

9. http://stardust.jpl.nasa.gov/photo/aerogel.html (07-12-2012).

10. Livage, J.; Sanchez, C. *J. Non-Cryst. Solids* **1992**, *145*, 11-19.

11. (a) Zarzycki, J.; Prassas, M.; Phalippou, J. *J. Mat. Sci.* **1982**, *17*, 3371-3379. (b) Tewari, P. H.; Hunt, A. J.; Lofftus, K. D. *Mater. Lett.* **1985**, *3*, 363-367.

12. (a) Wittwer, V. *J. Non-Cryst. Solids* **1992**, *145*, 233–236. 16. (b) Gerlach, R.; Kraus, O.; Fricke, J.; Eccardt, P. C.; Kroemer, N.; Magori, V. *J. Non-Cryst. Solids* **1992**, *145*, 227–232.

13. Jo, M. H.; Park, H. H. *Appl. Phys. Lett.* **1998**, *72*, 1391.

14. Pajonk, G. M. *Appl. Catal.* **1991**, *72*, 217–266.

15. Morris, C. A.; Anderson, M. L.; Stroud, R. M.; Merzbacher, C. I.; Rolison, D. R. *Science* **1999**, *284*, 622-624.

16. daCunha, J. P.; Neves, P.; Lopes, M. *Nucl. Instrum. Methods Phys. Res., Sect. A* **2000**, *452*, 401–421.

17. Woignier, T.; Phalippou, J. *J. Rev. Phys. Appl.* **1989**, *24*, 179-184.

18. (a) Katti, A.; Shimpi, N.; Roy, S.; Lu, H.; Fabrizio, E. F.; Dass, A.; Capadona, L. A.; Leventis, N. *Chem. Mater.* **2006**, *18*, 285–296. (b) Meador, M. A.; Capadona, L. A.; McCorkle, L.; Papadopoulos, D. S.; Leventis, N. *Chem. Mater.* **2007**, *19*, 2247–2260. (c) Ilhan, U. F.; Fabrizio, E. F.; McCorkle, L.; Scheiman, D. A.; Dass, A.; Palczer, A.; Meador, M. A. B.; Johnston, J. C.; Leventis, N. *J. Mater. Chem.* **2006**, *16*, 3046–3054. (d) Mulik, S.; Sotiriou-Leventis, C.; Churu, G.; Lu, H.; Leventis, N. *Chem. Mater.* **2008**, *20*, 5035–5046.

19. (a) Leventis, N. *Acc. Chem. Res.* **2007**, *40*, 874-884. (b) Leventis, N.; Mulik, S.; Wang, X.; Dass, A.; Sotiriou-Leventis, C.; Lu, H. *J. Am. Chem. Soc.* **2007**, *129*, 10660-10661. (c) Leventis, N.; Sotiriou-Leventis, C.; Zhang, G.; Rawashdeh, A.-M. M. "Nano Engineering Strong Silica Aerogels," *NanoLetters* **2002**, *2,* 957-960.

20. Husing, N.; Schubert, U.; Mezer, R.; Fratzl, P.; Riegel, B.; Kiefer, W.; Kohler, D.; Mader, W. *Chem. Mater.* **1999**, *11*, 451-457.

21. Meador, M. A. B.; Fabrizzio, E. F.; Ilhan, F.; Dass, A.; Zhang, G.; Vassilaras, P.; Johnston, J. C.; Leventis, N. *Chem. Mater.* **2005**, *17*, 1085–1098.

22. Mol, J. C. *J. Mol. Catal. A: Chemical* **2004**, *213*, 39-45.

23. Grubbs, R. H. *Tetrahedron* **2004**, *60*, 7117-7140.

24. Bohm, L. L *Angew. Chem. Int. Ed.* **2003**, *42*, 5010-5030.

25. Eleuterio, H. S. *J. Mol. Catal.* **1991**, *65*, 55-61.

26. Natta, G.; Dall'Asta, G.; Bassi, I. W.; Giovanna, C. *Makromol. Chem.* **1966**, *91*, 87-106.

27. Banks, R. L.; Bailey, G. C. *Ind. Eng. Chem. Prod. Res. Dev.* **1964**, *3*, 170-173.

28. Truett, W. L.; Johnson, D. R.; Robinson, I. M. *J. Am. Chem. Soc.* **1960**, *82*, 2337-2340.

29. Calderon, N.; Chen, H. Y.; Scott, K. W. *Tetrahedron Lett.* **1967**, 3327.

30. Trnka, T. M.; Grubbs, R. H. *Acc. Chem. Res.* **2001**, *34*, 18-29.

31. Schrock, R. R. *Acc. Chem. Res.* **1979**, *12*, 98-104.

32. Katz, T. J.; Lee, S. J.; Acton, N. *Tetrahedron Lett.* **1976**, *47*, 4247-4250.

33. Tebbe, F. N.; Parshall, G. W.; Ovenall, D. W. *J. Am. Chem. Soc.* **1979**, *101*, 5074-5075.

34. Wengrovius, J.; Schrock, R. R.; Churchill, M. R.; Missert, J. R.; Youngs, W. J. *J. Am. Chem. Soc.* **1980**, *102*, 4515-4516.

35. Kress, J. R. M.; Russell, M. J.; Wesolek, M. G.; Osborn, J. A. *J. Chem. Soc. Chem. Commun.* **1980**, *10*, 431-432.

36. Pine, S. H.; Zalher, R.; Evans, D. A.; Grubbs, R. H. *J. Am. Chem. Soc.* **1980**, *102*, 3270-3272.

37. Howard, T. R.; Lee, J. B.; Grubbs, R. H. *J. Am. Chem. Soc.* **1980**, *102*, 6876-6878.

38. (a) Schrock, R. R.; DePue, R. T.; Feldman, J.; Schaverien, C. J.; Dewan, J. C.; Liu, A. H. *J. Am. Chem. Soc.* **1988**, *110*, 1423-1435. (b) Schrock, R. R. *Angew. Chem. Int. Ed.* **2006**, *45*, 3748-3759.

39. Gilliom, L. R.; Grubbs, R. H. *J. Am. Chem. Soc.* **1986**, *108*, 733-742.

40. Grubbs, R. H. *Angew. Chem. Int. Ed.* **2006**, *45*, 3748-3759.

41. Nguyen, S. T.; Johnson, L. K.; Grubbs, R. H.; Ziller J. W. *J. Am. Chem. Soc.* **1992**, *114*, 3974-3975.

42. Nguyen, S. T.; Grubbs, R. H.; Ziller, J. W. *J. Am. Chem. Soc.* **1993**, *115*, 9858-9859.

43. Dias, E. L.; Nguyen, S. T.; Grubbs, R. H. *J. Am. Chem. Soc.* **1997**, *119*, 3887-3897.

44. (a) Bielawski, C. W.; Grubbs, R. H. *Prog. Polym. Sci.* **2007**, *32*, 1-29. (b) Choi, T.-L.; Grubbs, R. H. *Angew. Chem. Int. Ed.* **2003**, *42*, 1743-1746.

45. Davidson, T. A.; Wagener, K. B.; Priddy, D. B. *Macromolecules*, **1996**, *29*, 786-788.

46. White, S. R.; Sottos, N. R.; Geubelle, P. H.; Moore, J. S.; Kessler, M. R.; Sriram. S. R.; Brown, E. N.; Viswanathan, S. *Nature* **2001**, 409, 794-797.

47. Kang, H. A.; Bronstein,H. E.; Swager, T. M. *Macromolecules* **2008**, *41*, 5540-5547.

48. Forster, S.; Plantenberg, T. *Angew. Chem. Int. Ed*. **2002**, *41*, 689-714.

49. Gohy, J.-F. *Adv. Polym. Sci.* **2005**, *190*, 65-136.

50. Stupenrauch, K.; Moitzi, C.; Fritz, G.; Glatter, O.; Trimmel, G.; Stelzer, F. *Macromolecules* **2006**, *39*, 5865-5874.

51. Matyjaszewski, K.; Xia, J. *Chem. Rev*. **2001**, *101*, 2921-2990. 44. Fischer, M.; Vogtle, F. *Angew. Chem. Int. Ed.* **1999**, *38*, 884-905.

52. Frechet, J. M. J. *Science* **1994**, 263, 1710-1715.

53. Grayson, S. M.; Frechet, J. M. J. *J Am. Chem. Soc.* **2000**, *122*, 10335-10344.

54. Bosko, J. T. *Macromolecules* **2011**, *44*, 660-670.

55. Frechet, J. M. J. *J. Polym. Sci. Part A: Polym. Chem.* **2003**, *41*, 3713-3725.

56. Boydston, A. J.; Holcombe, T. W.; Unruh, D. A.; Frechet, J. M. J.; Grubbs, R. H. *J. Am. Chem. Soc.* **2009**, *131*, 5388-5389.

57. Nystrom, A.; Malcoch, M.; Furo, I.; Nystrom, D.; Unal, K.; Antoni, P.; Vamvounis, G.; Hawker, C.; Wooley, K.; Malmstrom, E.; Hult, A. *Macromolecules* **2006**, *39*, 7241-7249.

58. Connor, E. F.; Sundberg, L. K.; Kim, H.-C.; Cornelissen, J. J.; Magbitang, T.; Rice, P. M.; Lee, V. Y.; Hawker, C. J.; Volksen, W.; Hedrick, J. L.; Miller, R. D. *Angew. Chem. Int. Ed.* **2003**, *42*, 3785-3788.

59. (a) Gref, R.; Minamitake, Y.; Peracchia, M. T.; Trubetskoy, V.; Torchilin, V.; Langer, R. *Science* **1994**, *263*, 1600-1603. (b) Gref, R.; Domb, A.; Quellec, P.; Blunk, T.; Mueller, R. H.; Verbaratz, J. M.; Langer, R. *Adv. Drug Delivery Rev.* **1995**, *16*, 215-233.

60. (a) Hadjichristidis, N.; Pitsikalis, M.; Pispas, S.; Latrous, H. *Chem. Rev.* **2001**, *101*, 3747-3792. 53. (b) Zhang, M.; Muller, A. H. E. *J. Polym. Sci., Part A: Polym. Chem.* **2005**, *43*, 3461-3481.

61. Johnson, J. A.; Lu, Y. Y.; Burts, A. O.; Lim, Y.-H.; Finn, M. G.; Koberstein, J. T.; Turro, N. J.; Tirrell, D. A.; Grubbs, R. H. *J. Am. Chem. Soc.* **2011**, *133*, 559-566.

62. (a) Xia, Y.; Kornfield, J. A.; Grubbs, R. H. *Macromolecules* **2009**, *42*, 3761-3766. (b) Johnson, J. A.; Lu, Y. Y.; Burts, A. O.; Xia, Y.; Durrell, A. C.; Tirrell, D. A.; Grubbs, R. H. *Macromolecules* **2010**, *43*, 10326-10335.

63. (a) Kuroda, K.; DeGrado, W. F. *J. Am. Chem. Soc*. **2005**, *127*, 4128. (b) Mouery, B. P.; Lee, S. E.; Kissounko, D. A.; Epand, R. F.; Epand, R. M.; Weisblum, B.; Stahl, S. S.; Geliman, S. H. *J. Am. Chem. Soc.* **2007**, *129*, 15474.

64. Eren, T.; Som, A.; Rennie, J. R.; Nelson, C. F.; Urgina, Y.; Nusslein, K.; Coughlin, E. B.; Tew, G. N. *Macromol. Chem. Phys.* **2008**, *209*, 516-524.

65. Lienkamp, K.; Madkour, A. E.; Musante, A.; Nelson, C. F.; Nusslein, K.; Tew, G. N. *J. Am. Chem. Soc.* **2008**, *130*, 9826-9843.

66. Odian, G. Principles of Polymerization, 4th ed.; John Wiley and Sons, Inc.; New York, 2004.

67. (a) Novak, B.M.; Grubbs, R.H. *J. Am. Chem. Soc.* **1988**, *110*, 7542-7543. (b) Hillmayer, M. A.; Lepetit, C.; McGrath, D. V.; Novak, B. M.; Grubbs, R. H. *Macromolecules* **1992**, *25*, 3345-3350. (c) Feast, W. J.; Harrison, D. B. *J. Mol. Catal.* **1991**, *65*, 63-72.

68. Lynn, D.M.; Kanaoka, S.; Grubbs, R.H. *J. Am. Chem. Soc.* **1996**, *118*, 784-790.

69. Lynn, D.M.; Mohr, B.; Grubbs, R.H. *J. Am. Chem. Soc.* **1998**, *120*, 1627-1628.

70. See for example: (a) Prucker, O.; Ruhe, J. *Macromolecules* **1998**, *31*, 602-613. (b). Matyjaszewsi, K.; Miller, P. J.; Shukla, N.; Immaraporn, B.; Gelman, A.; Luokala, B. B.; Siclovan, T. M.; Kickelbick, G.; Vallant, T.; Hoffmann, H.; Pakula, T. *Macromolecules* **1999**, *32*, 8716-8724.

71. Kim, N. Y.; Jeon, N. L.; Choi, I. S.; Takami, S.; Harada, Y.; Finnie, K. R.; Girolani, G. S.; Nuzzo, R. G.; Whitesides, G. M.; Laibinis, P. E. *Macromolecules* **2000**, *33*, 2793-2795.

72. Kong, B.; Lee, J. K.; Choi, I. S. *Langmuir* **2007**, *23*, 6761-6765.

73. (a) Weck, M.; Jackiw, J. J.; Rossi, R. R.; Weiss, P. S.; Grubbs, R. H. *J. Am. Chem. Soc.* **1999**, *121*, 4088-4089. (b) Rutenberg, I. M.; Scherman, O. A.; Grubbs, R. H.; Jiang, W.; Garfunkel, E.; Bao, Z. *J. Am. Chem. Soc.* **2004**, *126*, 4062-4063. (c) Juang, A.; Scherman, O. A.; Grubbs, R. H.; Lewis, N. S. *Langmuir* **2001**, *17*, 1321-1323. (d) Harada, Y.; Girolami, G. S.; Nuzzo, R. G. *Langmuir* **2003**, *19*, 5104-5114.

74. Mingotaud, A.-F.; Reculusa, S.; Mingotaud, C.; Keller, P.; Sykes, C.; Duguet, E.; Ravaine, S. *J. Mater. Chem.* **2003**, *13*, 1920-1925.

75. Watson, K. J.; Zhu, J.; Nguyen, S. T.; Mirkin, C. A. *J. Am. Chem. Soc.* **1999**, *121*, 462-463.

76. Cong, Y. U.; Mingcheng, X. U.; Frantisek, S.; Jean, M. J. F. *J. Poly. Sci. Part A: Poly. Chem.* **2002**, *40*, 755-769.

77. (a) Sherrington, D. C. *Chem. Commun.* **1998**, 2275-2286. (b) Santora, B. P.; Gagne, M. R. *Macromolecules* **2001**, *34*, 658-661.

78. Svec, F. *J. Chromatogr. A* **2012**, *1228*, 250-262.

79. Fretag, R. *J. Chromat. A* **2004**, *1033*, 267-273.

80. (a) Buchmeiser, M. R. *J. Sep. Sci.* **2008**, *31*, 1907-1922. (b) Gatschelhofer, C.; Mautner, A.; Reiter, F.; Pieber, T. R.; Buchmeiser, M. R.; Sinner, F. M. *J. Chromatogr. A.* **2009**, *1216*, 2651-2657. (c) Sinner, F. M.; Gatschelhofer, C.; Mautner, A.; Magnes, C.; Buchmeiser, M. R.; Pieber, T. R. *J. Chromatogr. A.* **2008**, *1191*, 274-281. (d) Buchmeiser, M. R. Rigid polymers, *J. Chromatogr.* **2003**, *67*, 104-118.

81. (a) Yang, X.-Y.; Li, Y.; Lemaire, A.; Yu, J.-G.; Su, B.-L. *Pure Appl. Chem.* **2009**, *81*, 2265-2307. (b) Svec, F.; Frechet, J. M. J. *Science* **1996**, *273*, 205-211. (c) Scheler, S. *J. Appl. Polm. Sci.* **2007**, *105*, 3121-3131.

82. (a) Martina, A. D.; Hilborn, J. G.; Mhlebach, A. *Macromolecules,* **2000**, *33*, 8, 2916-2921. (b) Martina, A. D.; Garamszegi, L.; Hilborn, J. G. *J. Poly. Sci. Part A: Poly. Chem.* **2003**, *41*, 2036-2046. (c) Martina, A. D.; Hilborn, J. G. *J. Mater. Res.* **2001**, *16*, 2045-2051.

83. Martina, A. L.; Garamszegi, L.; Hilborn, J. G. *React. Funct. Polym.* **2003**, *57*, 49-55.

84. Lee, J. K.; Gould, G. L. *J. Sol-Gel Sci. Technol.* **2007**, *44*, 29-40.

85. Dawedeit, C.; Kim, S. H.; Braun, T.; Worsley, M. A.; Stephan, A. L.; Wu, K. J.; Walton, C. C.; Chernov, A. A.; Satcher, J. H. Jr.; Hamza, A. V.; Biener, J. *Soft Matter* **2012**, *8*, 3518-3521.

86. Everett, D. H. Basic Principles of Colloid Science Royal Society of Chemistry: London, U.K. 1988.

87. Pekala, R.W. *Low Density Resorsinol-Formaldehyde Aerogels*, U.S. Patent No. 4,873,218, 1989.

88. http://nobelprize.org/nobel_prizes/chemistry/laureates/2005/grubbs-slides.pdf (07-09-2012).

PAPER

I. Monolithic Hierarchical Fractal Assemblies of Silica Nanoparticles Crosslinked with Polynorbornene via ROMP:

A Structure-Property Correlation from Molecular to Bulk through Nano

Dhairyashil P. Mohite[1], Zachary J. Larimore[1], H. Lu[*,2], Joseph T. Mang[*,3], Chariklia Sotiriou-Leventis[*,1] and Nicholas Leventis[*,1]

1. *Department of Chemistry, Missouri University of Science and Technology, Rolla, MO 65409, U.S.A. leventis@mst.edu, cslevent@mst.edu*

2. *Department of Mechanical Engineering, The University of Texas at Dallas, Richardson, TX 75080, U.S.A. hongbing.lu@utdallas.edu*

3. *Los Alamos National Laboratory, Los Alamos, NM 87545, U.S.A. jtmang@lanl.gov*

Abstract: Monolithic hierarchical fractal assemblies of silica nanoparticles are referred to as aerogels and despite an impressive collection of attractive macroscopic properties, fragility has been the primary drawback to applications. In that regard, polymer-crosslinked silica aerogels have emerged as strong lightweight nanostructred alternatives rendering new applications unrelated to aerogels before, as in ballistic protection, possible. In polymer-crosslinked aerogels skeletal nanoparticles are connected covalently with a polymer. However, the exact location of the polymer on the elementary structure of silica and, therefore, critical issues, such as how much is enough, have remained ambiguous. To address those issues, the internal nanoporous surfaces of silica wet-gels were modified with norbornene (NB) by co-gelation of tetramethylorthosilicate (TMOS) with a newly synthesized derivative of nadic acid (**Si-NAD**: *N*-(3-triethoxysilylpropyl)-5-norbornene-2,3-dicarboximide). As inferred by both rheological and liquid ^{29}Si NMR data, **Si-NAD** reacts more slowly than TMOS, yielding a TMOS-derived skeletal silica network surface-derivatized with NB via monomer-cluster aggregation. Then, ring

opening metathesis polymerization (ROMP) of free NB in the nanopores engages surface-bound NB moieties and bridges skeletal nanoparticles either through cross-metathesis, or a newly described stitching mechanism. After solvent exchange and drying with supercritical fluid CO_2 into aerogels (bulk densities in the range 0.27-0.63 g cm^{-3}, versus 0.20 g cm^{-3} of the native network), the bridging nature of the polymer is inferred by a >10-fold increase in mechanical strength and a 4-fold increase in the energy absorption capability relative to the native samples. The cross-linking polymer was freed from silica by treatment with HF and it was found by GPC that it consists of a long and a short component, with around 400 and 10 monomer units, respectively. No evidence (by SAXS) was found for the polymer coiling up into particles, consistent with the microscopic similarity (by SEM) of both native and crosslinked samples. Most importantly, the polymer does not need to spill over higher aggregates for greatly improved mechanical strength; mechanical properties begin improving after the polymer coats primary particles. Extremely robust materials are obtained when the polymer fills most of the fractal space within secondary particles.

1. Introduction

Low-density, open-cell, nanoporous solids consisting of three-dimensional (3D) assemblies of nanoparticles are referred to as aerogels, and have been pursued for their bulk properties, such as high surface areas, low thermal conductivities, low dielectric constants, and high acoustic attenuations.[1] The most well-studied of those materials are silica aerogels; they are synthesized either by an acid-catalyzed gelation of aqueous sodium silicate solutions[2] or by acid- or base-catalyzed hydrolysis and polycondensation

of silicon alkoxides into wet-gels that subsequently are dried by converting the pore-filling solvent into a supercritical fluid (SCF) that is vented off isothermally.[1] Conveniently, prior to the SCF drying, gelation solvents are extracted in an autoclave with liquid CO_2 whose low critical point (31.1 ^{o}C, 7.38 MPa) renders the process safer.

The most serious impediment against the practical (commercial) use of aerogels has been poor mechanical strength.[1] That issue was addressed successfully ten years ago, by using the innate surface functionality of silica (-OH groups) for the covalent post-gelation anchoring and accumulation of a polymer coating on the nanoscopic skeletal framework. The mechanical properties of the composite improved dramatically over those of the native silica framework while most of the porosity and, therefore, the desirable bulk aerogel properties, were preserved.[3] This process has been referred to as crosslinking and has been extended to over 30 different metal and semi-metal aerogels in addition to silica.[4] The mechanical strength of such polymer-crosslinked aerogels far surpasses not only that of native aerogels, but also that of other materials considered strong.[5] Selected polymer crosslinked networks are strong enough to withstand stresses during ambient pressure drying from low vapor pressure solvents, e.g., pentane.[6] Others are suitable for applications typically unrelated to aerogels, e.g., in ballistic protection (armor).[3c] Further, as suggested by a recent quantitative (100% efficient) conversion of polyacrylonitrile-crosslinked silica aerogels to isomorphic SiC aerogels,[7] emerging applications include the carbothermal synthesis of a wide array of monolithic, highly porous, metals and ceramics.

The crosslinking process is akin to grafting polymers onto surfaces. It has been demonstrated with both grafting to and grafting from methods. Generally, both require a

modification of the skeletal nanoparticles by co-gelation of tetramethyl orthosilicate (TMOS) with a trialkoxy silane derivative of the modifier.[8] In grafting from crosslinking, polymerization begins at the surface of the skeletal nanoparticles, which are modified either with free radical,[9] atom transfer radical,[10] or anionic polymerization initiators. This process has been conducted both in the wet-gel state with polystyrene, polymethylmethacrylate and polyacrylonitrile, and in the dry aerogel state by the vapor deposition of suitable monomers (e.g., cyanoacrylates).[11] Grafting to has been more versatile. It is based on solution polymerization of monomers in the pores that engages the surface functional groups. It includes aerogels crosslinked with isocyanate-derived polyurea using for backbone attachment either the innate hydroxyl surface functionality of silica,[12] or amine-modified silica obtained by co-gelation of TMOS with 3-aminopropyltriethoxysilane (APTES).[13] Amine-modified silica has also been used for crosslinking with epoxides.[14] A reaction of dangling amine groups with chloromethylstyrene has led to crosslinking with polystyrene.[15] Crosslinking with polystyrene has also been successfully conducted by a direct surface modification with olefins via co-gelation of TMOS with vinyltrimethoxysilane.[16]

Despite the rather intense activity in this area, the nature of crosslinking at the fundamental building block level (primary and secondary nanoparticles) has remained ambiguous. As inferred by SEM, the microstructure is not affected visibly by the crosslinkng process. Hence, the crosslinkng polymer has been assumed to follow the contour surface of the skeletal framework and, therefore, has been referred to as conformal. However, the exact location of the polymer on the backbone is important for correlating nanostructure with bulk material properties, such as porosity, surface area,

and mechanical strength; also, for the synthesis of new porous materials that rely on intimate contact of skeletal inorganic nanoparticles with for example a carbonizable polymer.

Specifically, a first key question to be answered addresses the amount of polymer required for maximum mechanical strength with a minimum penalty in surface area, density, and porosity. In addition, noting that interpenetrating organic/inorganic networks in the much more compact xerogel form react carbothermally towards metals and carbides much more efficiently (at up to 400 ^{o}C lower temperatures) than aerogels,[17] it is expected that core-shell structures, such as polymer crosslinked aerogels, would be more attractive than interpenetrating networks, therefore knowledge of the exact location of the polymer is also key.

That investigation must rely on a polymerization process yielding a rather well-defined, soluble polymer that can be readily washed off if unbound. For this, we turned to crosslinking of silica aerogels with norbornene by ring opening metathesis polymerization (ROMP).[18] ROMP-derived polymers, such as both polynorbornene and polydicyclopentadiene, are extremely robust, use inexpensive monomers, and have been commercially successful. ROMP-derived all-organic aerogels have also been recently described.[19] Closer to our purposes, ROMP has been used in the surface-initiated mode by immobilizing suitable catalysts on surfaces to produce, in a grafting from fashion, polymeric thin films,[20] polymer brushes,[21] and core-shell type structures on both silica and gold.[22] Our process, however, was related to grafting to ROMP. The latter has been used with carbon nanotubes (CNTs) functionalized with norbornene to produce both CNT/polydicyclopentadiene composites,[23] and surface-grafted polymer supports.[24]

Si-NAD   **GC-II**
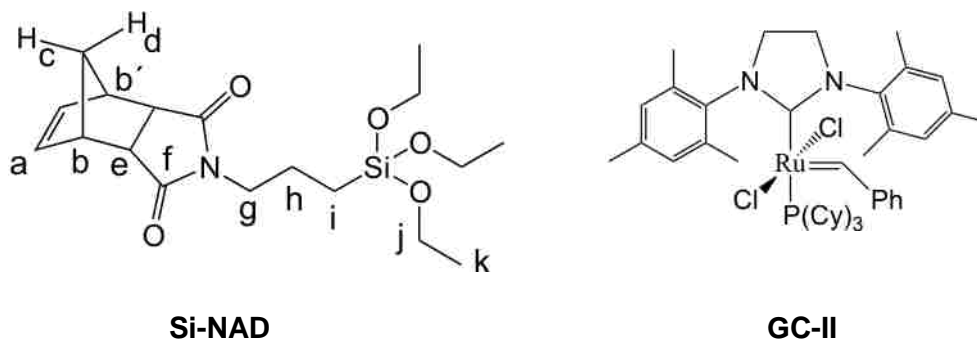
Here, the norbornene functionality on the pore surfaces of silica aerogels was provided by a co-gelation of TMOS with a new norbornene derivative, **Si-NAD**. The pores were filled with a norbornene (NB) solution. ROMP was then conducted at room temperature using a water-tolerant, second generation Grubbs' catalyst (**GC-II**). Unbound polynorbornene was washed off during typical solvent exchanges. Probing the location of the polymer was a complex issue; no single characterization method was sufficient to address by itself. Hence, the nanostructure was probed chemically both at the molecular level by IR, ^{13}C, and ^{29}Si solids NMR and at the nanoscopic level by SAXS, SANS, TEM and SEM. Porosity was investigated using N_2 sorption. All results were correlated with the macroscopic mechanical strength using quasi-static compression. Control materials included both the native (non-crosslinked) NB-modified silica (**n-SiNAD**) which, in turn, was referenced against native TMOS-derived silica (**n-TMOS**), and silica obtained by a co-gelation of TMOS with APTES (**n-TMOS-co-APTES**). Overall, the polymer first coated the primary particles. In that regard, a mild degree of crosslinking was sufficient for improving the mechanical properties to a level that silica aerogels are no longer fragile materials. Complete filling of the fractal space within the secondary particles is essential, however, for ultimate mechanical strength.

2. Experimental

2.1. Materials. All reagents and solvents were used as received, unless noted otherwise. Dicyclopentadiene was purchased from Fluka. Maleic acid, thionyl chloride, 3-aminopropyltriehoxysilane (APTES), tetramethylorthosilicate (TMOS), a 14.8 N ammonium hydroxide solution, norbornene, second generation Grubbs' catalyst **GC-II** ((1,3-bis(2,4,6-trimethylphenyl)-2-imidazolidinylidene) dichloro(phenylmethylene) (tricyclo-hexylphosphine) ruthenium), and anhydrous toluene were purchased from Aldrich Chemical Co. HPLC grade tetrahydrofuran (THF) was purchased from Fisher and was distilled from lithium aluminum hydride. Cyclopentadiene was obtained via a reverse Diels-Alder reaction by distillation of dicyclopentadiene (bp 170 $^{\circ}$C).[25] Nadic acid was synthesized according to literature procedures[25] by a Diels-Alder reaction between cyclopentadiene and maleic acid, (mp 182-186 $^{\circ}$C; Sigma-Aldrich: *endo-*, 175 $^{\circ}$C (dec.); *endo-/exo-*, 185-189 $^{\circ}$C).

Scheme 1. Synthesis of **Si-NAD**
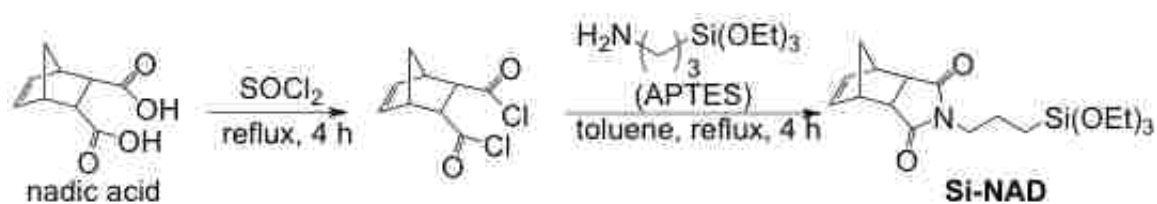
2.2. Synthesis of *N*-(3-triethoxysilylpropyl)-5-norbornene-2,3-dicarboximide (Si-NAD). The process is summarized in Scheme 1: nadic acid (7.8 g, 0.0428 mol) was added under magnetic stirring at room temperature to an excess of thionyl chloride (25.0 mL, 0.3441 mol) in a 2-neck round-bottom flask, and the mixture was refluxed for 4 h under N$_2$. At the end of the period, the reaction mixture was first allowed to cool to room temperature, the reflux apparatus was converted to a distillation set-up and the excess of

thionyl chloride was removed under reduced pressure using an aspirator connected through a drying tube. The solid product was used without further purification. First, it was dissolved in anhydrous toluene (25 mL) added with a syringe through a septum at room temperature. Then, APTES (10.0 mL, 0.0428 mol) was added to the solution under N_2 with a syringe, and the mixture was refluxed for 4 h under magnetic stirring. At the end of the period, the reaction mixture was allowed to cool to room temperature and toluene was removed by distillation under reduced pressure, again using an aspirator connected through a drying tube, to yield a viscous liquid, which was further dried under vacuum to yield a waxy yellow solid of **Si-NAD**. Received: 13.0 g (75%); mp 40-45 $^\circ$C; ^{1}H-NMR (400 MHz, CDCl$_3$) δ (ppm): 6.09 (dd, 2H, J_{ab}=4.00 Hz, $J_{ab'}$=2.00 Hz, H$_a$), 3.80 (q, 6H, J_{jk} = 6.80 Hz, H$_j$), 3.36-3.40 (m, 2H, H$_b$), 3.32 (t, 2H, J_{gh} = 7.40 Hz, H$_g$), 3.23 (dd, 2H, J_{eb} = 3.00 Hz, $J_{eb'}$ = 1.40 Hz, H$_e$), 1.73 (dt, 1H, J_{cd} = 8.40 Hz, J_{cb} = 1.40 Hz, H$_c$), 1.50-1.58 (m, 3H, H$_d$ & H$_h$), 1.21 (t, 9H, J_{kj} = 6.80 Hz, H$_k$), 0.50-0.60 (m, 2H, H$_i$); ^{13}C NMR (100 MHz, CDCl$_3$) δ (ppm): 177.9, 134.6, 58.6, 52.4, 45.9, 45.1, 41.2, 21.5, 18.5, 8.1; ^{29}Si NMR (79.415 MHz, CDCl$_3$) δ (ppm): -46.26; HRMS calcd for $C_{18}H_{29}NO_5SiNa^+$ 390.17072, found 390.17045. **Si-NAD** is moisture-sensitive and to increase its shelf-life, facilitate handling and standardize procedure, it was stored as a 0.5 M solution in dry THF under N_2 at 10 $^\circ$C.

2.3. Preparation of Native Silica Aerogels Incorporating Si-NAD (n-SiNAD). Native silica aerogels were formulated with 10% mol:mol of silicon coming from **Si-NAD** (the balance from TMOS). The stock solution of **Si-NAD** in THF (0.5 M) was allowed to warm to room temperature, and an aliquot (5.2 mL, 0.0026 mol) was transferred into a round-bottom flask. The solvent was removed at 40 $^\circ$C under reduced

pressure, and the resulting viscous liquid was dissolved in a mixture of methanol (4.5 mL) and TMOS (3.45 mL, 0.0235 mol) (Solution A). A second solution (Solution B) consisting of methanol (4.5 mL), distilled water (1.5 mL), and 80 μL of 14.8 N aq. NH_4OH was added to Solution A, the resulting sol was shaken vigorously for 30 s and was poured either into polypropylene molds (Wheaton polypropylene OmniVials, Part No. 225402, 1 cm in diameter), or into 10 cm^3 polyethylene syringes (Nonsterile BD Luer-Lok Tip, Part No. 301029, 14 mm in diameter). The latter molds were used for samples intended for compression testing. All sols gelled within 10-15 min at room temperature. The resulting wet-gels were aged in their molds for 24 h at room temperature, and solvent-exchanged first with THF and then with acetone using 4 washes per solvent, 8 h per wash cycle and 4× the volume of the gel for each wash. Acetone-filled wet-gels were dried in an autoclave to native aerogels with liquid CO_2, which was removed at the end as a SCF.

2.4. Preparation of Norbornene-crosslinked Silica Aerogels (X-SiNAD). THF-filled wet-gels (see above) were equilibrated for 24 h at room temperature in 10% w/w (0.93 M), 20% w/w (1.83 M) or 30% w/w (2.71 M) solutions of norbornene in THF with frequent swirling. The volume of each norbornene solution was 4 times the volume of each gel. Subsequently, wet-gels together with the surrounding norbornene solutions were cooled in a freezer for 2 h at -5 ^{o}C. A THF solution of the Grubbs' catalyst **GC-II** (1.0 mL, containing 0.025, 0.020 or 0.015 % mol:mol relative to the amount of NB in the 10%, 20% or 30% crosslinking solutions, respectively) was added to the cold monomer solution and the vials were immediately placed back in a freezer for equilibration over another 12 h with intermittent swirling. At the end of that period, the wet-gels in the

monomer/**GC-II** solutions were allowed to warm to room temperature. As the temperature increased, the monomer solution began to build up viscosity. The wet-gels were taken out of the viscous polymer solution just before it gelled (0.5 to 2 h), the remaining viscous liquid on the surface of the gels was wiped off with a Kimwipe[TM] tissue (Kimberly-Clark), and were placed in tightly closed vials (20 mL) with a small amount of THF to keep the environment inside saturated with THF vapors. After 4 h, wet-gels were washed with THF (4 washes, 8 h per wash, using 4× the gel volume per wash) to remove loose polymer. Subsequently, wet-gels were solvent-exchanged with acetone (4 washes, 8 h per wash cycle, using 4× the gel volume per wash) and dried in an autoclave with CO_2 to yield **X-SiNAD**. Meanwhile, the viscous crosslinking solution surrounding the silica wet-gels was let itself to gel, and the polymer gel was aged in parallel with the crosslinked wet silica gels for 4 h. At the end of the period, the polymer was dissolved in a large excess of THF, was precipitated with methanol and analyzed by modulated differential scanning calorimetry and gel permeation chromatography (see Methods section below).

Control native silica and amine-modified silica aerogels were prepared according to literature procedures: for native silica aerogels (**n-TMOS**), Solution A consisting of 3.85 mL TMOS (0.0261 mol) and 4.5 mL CH_3OH was mixed at room temperature with Solution B consisting of 4.5 mL CH_3OH, 1.5 mL H_2O and 40 μL of concentrated aqueous NH_4OH;[26] for native amine-modified silica aerogels (**n-TMOS-co-APTES**), Solution A consisting of 2.887 mL TMOS (0.0196 mol), 0.963 mL APTES (0.0041 mol) and 4.5 mL CH_3CN was cooled in dry ice/acetone, and mixed with a similarly cold Solution B consisting of 4.5 mL CH_3CN and 1.5 mL of H_2O.[13a] The sol was poured into

molds to gel. Wet **n-TMOS** silica gels were washed once with CH_3OH, 4× with acetone and dried with CO_2 taken out as a SCF. Wet, amine-modified silica gels (**n-TMOS-co-APTES**) were washed 4× with CH_3CN and were dried with CO_2 taken out again as a SCF.

2.5. Methods. Supercritical fluid CO_2 drying was conducted using an autoclave (SPI-DRY Jumbo Supercritical Point Dryer, SPI Supplies, Inc. West Chester, PA). Bulk densities (ρ_b) were calculated from the weight and the physical dimensions of the samples. Skeletal densities (ρ_s) were determined using helium pychnometry with a Micromeritics AccuPyc II 1340 instrument. Porosities, Π, were determined from ρ_b and ρ_s. Surface areas and pore size distributions were measured by nitrogen sorption porosimetry using a Micromeritics ASAP 2020 surface area and porosity analyzer. In preparation for surface area and skeletal density determination, samples were outgassed for 24 h under vacuum at 80 ^{o}C. (A separate series of samples was also outgassed at 50 ^{o}C - in order to remain below the glass transition temperature of the polymer. Data were practically identical for samples outgassed at either temperature.) Average pore diameters were determined by the $4 \times V_{Total}/\sigma$ method, where V_{Total} is the total pore volume per gram of sample and σ, the surface area determined by the Brunauer-Emmett-Teller (BET) method from the N_2 adsorption isotherm. The value of V_{Total} can be calculated either from the single highest volume of N_2 adsorbed along the adsorption isotherm, or from the relationship $V_{Total} = (1/\rho_b)-(1/\rho_s)$. Average pore diameter values were calculated by both methods and are cited herewith; if those values converge, it is considered as indication that the material is mesoporous. If average pore diameters calculated using $V_{Total} = (1/\rho_b)-(1/\rho_s)$ are significantly higher, that is taken as evidence for macroporosity.

Liquid ^{1}H, ^{13}C and ^{29}Si NMR were recorded with a 400 MHz Varian Unity Inova NMR instrument (100 MHz carbon frequency and 79.415 MHz silicon frequency).

High resolution, accurate mass analysis was conducted by direct infusion electrospray ionization (ESI) mass spectrometry using an LTQ OrbitrapXL hybrid mass spectrometer (Thermo Scientific, San Jose, CA). Using the on-board syringe pump, a THF sample of **Si-NAD**, diluted in methanol, was infused into the source at a flow rate of 5 μL min^{-1}. The ESI voltage was 5 kV, the sheath gas flow rate was 8 (arbitrary units in the software), and the capillary temperature was 275 °C. Mass analysis was done in the Orbitrap FT mass analyzer with resolution set to 100,000. One hundred sixty four (164) individual scans were acquired and averaged.

Chemical characterization of native and crosslinked silica aerogels was conducted with infrared (IR) and solid-state ^{13}C NMR spectroscopy. IR spectra were obtained in KBr pellets with a Nicolet-FTIR Model 750 Spectrometer. Solid-state ^{13}C NMR spectra were obtained with samples ground into fine powders on a Brucker Avance 300 Spectrometer with a 75.475 MHz carbon frequency using magic angle spinning (at 7 kHz) with broadband proton suppression and the CPMAS TOSS pulse sequence for spin sideband suppression.

Thermogravimetric analysis (TGA) was conducted in air with a TA Instruments model Hi-Res-TGA 2950 analyzer at a heating rate of 10 ^{o}C min^{-1}.

Modulated Differential Scanning Calorimetry (MDSC) was conducted under N_2 with a TA Instruments Differential Scanning Calorimeter Model Q2000 at a heating rate of 10 °C min^{-1} in the modulated T4P mode, using 60 s as the modulation period and 1 °C as the modulation amplitude. Samples were subjected to two heating scans and one

cooling scan from 0 ^{o}C to 280 °C. Glass transition temperatures were determined from the second heating scan.

The structure of the fundamental building blocks of the materials was probed with both small-angle X-ray scattering (SAXS) and small-angle neutron scattering (SANS), using 2-3 mm-thick disks, 0.7-1.0 cm in diameter. SAXS was carried out with a PANalytical X'PertPro Multipurpose Diffractometer (MPD) configured for SAXS, using Cu Kα radiation (λ= 1.54 Å) and a 1/32° SAXS slit together with a 1/16° anti-scatter slit on the incident beam side, and 0.1 mm anti-scatter slit and Ni 0.125 mm automatic beam attenuator on the diffracted beam side. Samples were placed in circular holders between thin Mylar^{TM} sheets and scattering intensities were measured with a point detector in the transmission geometry by 2 Theta scans ranging from -0.1 up to 5°. SANS was conducted with a time-of-flight, low-Q diffractometer (LQD) at the Manuel Lujan, Jr. Scattering Center of the Los Alamos National Laboratory.[27] SANS scattering data were recorded in absolute units (cm^{-1}), while SAXS data are reported in arbitrary units as a function of Q, the momentum transferred during a scattering event. Data analysis was conducted with the Irena SAS tool for modeling and analysis of small angle scattering within the commercial Igor Pro software package (WaveMetrics, Inc. Lake Oswego, OR).[28]

Scanning electron microscopy (FESEM) was conducted with samples coated with Au using a Hitachi S-4700 field emission microscope. Transmission Electron Microscopy (TEM) was conducted with a FEI Tecnai F20 instrument employing a Schottky field emission filament operating at a 200 kV accelerating voltage. For TEM, samples were ground to fine powder by hand in a mortar with a pestle and the smallest particles were selected and placed on a 200 mesh copper grid bearing a lacey Formvar/carbon film for

microscopy. At least six different areas/particles were examined on each sample to ensure that the results were representative of the material.

For molecular weight determinations of polynorbornene, **X-SiNAD(xx)** samples were ground to coarse powders, ~0.5 g of which was treated with 5 mL of an aqueous HF solution (1 M) for 1 h, with intermittent vigorous mixing. The polymer was extracted in chloroform by multiple washes, chloroform extracts were combined, the solvent was removed at 40 ^{o}C under reduced pressure and the polymer was further dried in a vacuum oven at 40 ^{o}C for 12 h. The residue was dissolved in THF and was analyzed by gel permeation chromatography (GPC) using a Shodex GPC KH-803L column connected to a Schimadzu liquid chromatograph (LC-10AD) equipped with a UV-Vis detector (SPD-10AV). HPLC grade THF was used as eluent at 1 mL min^{-1}. Linear polystyrene standards from Varian (Polystyrene Low EasiVials; Part No. PL2010-0400 and PL2010-0403) were used for calibration. Multiple Gaussian curves were fitted within the experimental chromatograms using OriginLab's data analysis and graphing software version OriginPro 8. Number- and weight-average molecular weights (M_n and M_w, respectively) and polydispersity indexes (M_w/M_n) were calculated using the fitted chromatograms.[29]

Compression testing was performed according to the ASTM D695-02a standard on cylindrical specimens using a Instron 4469 universal testing machine frame. According to the ASTM standard, the height-to-diameter ratio of the specimen was 2:1; typical samples were machined to about 2.0 cm in length and 1.0 cm in diameter.

The rheological behavior of TMOS and TMOS/**Si-NAD** sols was recorded with a TA Instruments AR 2000ex Rheometer using an aluminum cone (60 mm diameter, 2° angle) and a Peltier plate geometry with a 1 mm gap between them. The instrument was

operated in the continuous oscillation mode and time-sweep experiments were performed with a fixed strain amplitude either from the beginning (case of TMOS), or 10 min after mixing of Solution A with Solution B (case of TMOS/**Si-NAD**), till gelation. The Peltier plate was set at 20 $^{\circ}$C. The gel point was determined using a dynamic multiwave method with three superimposed harmonics with frequencies 1, 4, and 8 rad s^{-1}. The strain of the fundamental oscillation (1 rad s^{-1}) was set at 5%.

The relative rates of incorporation of TMOS and **Si-NAD** in the **n-SiNAD** gel network were determined using liquid ^{29}Si NMR on the 400 MHz Varian Unity Inova NMR instrument. A teflon liner inside a 5 mm glass tube was used as sample holder. The field-frequency was locked to deuterium (CD$_3$OD). Broad-band proton decoupling was applied to suppress possible nuclear Overhauser effects. Chromium acetylacetonate (0.015 M) and tetramethylsilane (TMS) were added in the sol to reduce the spin-lattice relaxation time, and as an internal standard, respectively. Spectra were collected in regular intervals during gelation and beyond, using 256 scans and a relaxation delay of 1 s. A receiver gating time of 500 μs following a pulse of 7.8 μs was also applied in order to eliminate the broad background signal from the borosilicate glass in the NMR tube and probe.

3. Results and Discussion

3.1. Synthesis and Characterization of Native n-SiNAD Aerogels. The monomer **Si-NAD** can be considered an APTES derivative. Like the latter, **Si-NAD** does not gel by itself.[13-15] Thus, in both and analogy to APTES and as summarized in Scheme 2, silica wet-gels and aerogels incorporating norbornyl moieties were prepared by

replacing 10 mol % of the TMOS with **Si-NAD** from a typical NH_4OH-catalyzed TMOS-gelation process. Extensive prior work with APTES-modified silica has relied on a 17.3 mol % APTES.[13-15] Here, however, it was deemed appropriate to use a lower **Si-NAD**:TMOS mol ratio in order to capture crosslinked materials at earlier stages of crosslinking and thus explore the evolution of mechanical properties closer to the native network.

Scheme 2. Preparation of both native and crosslinked aerogels incorporating **Si-NAD**
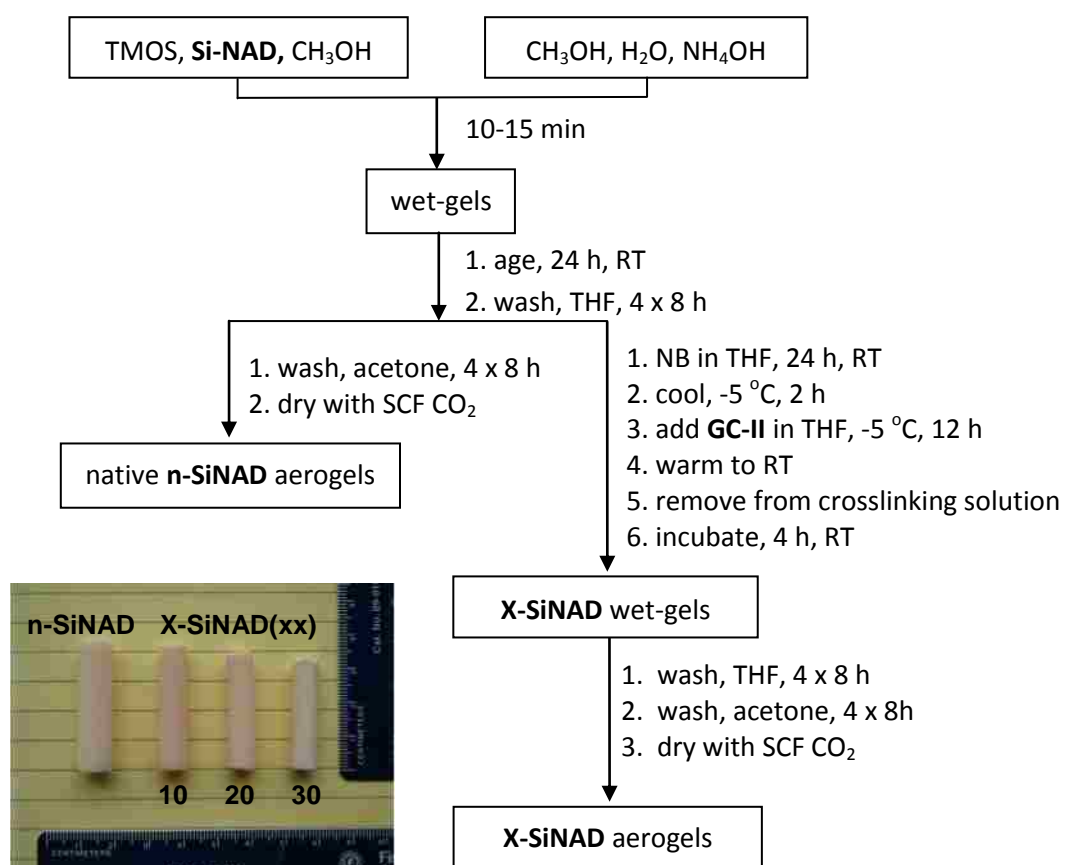
The co-gelation of **Si-NAD** with TMOS was followed in comparison with the gelation of TMOS with itself. That was accomplished by monitoring both the rheological properties of the sol as well as the ^{29}Si NMR signal of the monomers. Figure 1A shows

the typical evolution of the storage (G') and the loss (G'') moduli of the sol as a function of time from mixing the sol. These curves cross, as expected, near the gelation point, where the elastic properties of the newly formed, rigid gel become dominant. (For corresponding data regarding gelation of TMOS only, refer to Figure S.1 in Supporting Information.) The actual gelation point (a physical property of the system) is given by the inflection point of the $\tan\delta$ ($=G''/G'$) versus time plot at a given frequency (included in Figure 1A). This point can alternatively be given as the common (independent of frequency) crossing point of all $\tan\delta$ versus time curves (Figure 1B).[30] This common crossing point is also located at the minimum of the statistical variable $\log(s/\langle\tan\delta\rangle)$ versus time-after-mixing plot (see Inset in Figure 1B. s: standard deviation of the three $\tan\delta$ obtained at specified times during gelation, at three different oscillatory frequencies of the cone, operated in the multiwave mode).[31] Results are summarized in Table 1. At equal catalyst concentrations, TMOS gels faster than the TMOS/**Si-NAD** system, suggesting that **Si-NAD** interferes with the gelation of TMOS. At the gelation point, the $\tan\delta$ value is related to the gel relaxation exponent 'n' via eq. 1.[32]

$$\tan\delta=\tan(n\pi/2) \tag{1}$$

In turn, considering the excluded volume of the (primary) particles forming the clusters, 'n' is related via eq. 2 to the fractal dimension, D_f, of the clusters existing at the gel point (for three-dimensional non-fractal clusters, $D=3$).[33]

$$n = \frac{D\left(D+2-2D_f\right)}{2\left(D+2-D_f\right)} \tag{2}$$

At two different catalyst concentrations and, therefore, different gelation times, the D_f values calculated via eq 2 for the native **n-SiNAD** gels are in the [2,3] interval

suggesting a reaction-limited cluster-cluster aggregation mechanism for network formation.[34] Additionally, the D_f values of **n-SiNAD** are sufficiently close to those of **n-TMOS** gels (Table 1), suggesting that the space filling pattern in the two types of wet-gels is similar.

Table 1. Rheological data for the gelation of TMOS and of TMOS/**Si-NAD**

alkoxide catalyst amount [a]	gelation point, t_g (s) [b]	$\tan\delta$ at t_g	n [c]	D_f [d]
TMOS				
40 μL	690	0.33	0.203	2.32
TMOS/**Si-NAD**				
40 μL	2175	0.06	0.038	2.47
80 μL [e]	355	0.20	0.126	2.39

[a]All other parameters remaining the same as in the basic formulation described in the Experimental section. [b]Identified at the minimum of the statistical function as shown in Figure 1B-Inset. [c]From eq 1. [d]From eq. 2. [e]Actual amount of catalyst used in gel synthesis, as described in the Experimental section.

A preeminent tool for the elucidation of the sol-gel chemistry of silicon alkoxides is ^{29}Si NMR.[35] Here (Figure 2A), the ^{29}Si signal is not lost after gelation. Additionally, the transient appearance of a resonance peak at -76 ppm corresponds to hydrolysis products from TMOS [$(MeO)_{4-x}Si-(OH)_x$].[35] That resonance disappears after gelation, in contrast to the TMOS resonance (-78.52 ppm) that remains present and keeps decreasing. Overall, it is noted that: (a) a significant amount of TMOS is still unreacted at the gel point, when nanoparticles reach their bond-percolation threshold;[36] (b) **Si-NAD** (at -46.26 ppm) is still in the pores after all signal from TMOS is gone; and, (c) in the absence of **Si-NAD**, TMOS is incorporated in the gel framework faster (see Figure 2B). Eventually, both TMOS and **Si-NAD** are incorporated in the network: (a) TGA in the air (Figure 3) shows that **n-SiNAD** leaves a ~76% w/w residue, versus 75.4% expected

stoichiometrically if all **Si-NAD** is incorporated in the network with all alcoxides hydrolyzed; (b) the solids CPMAS ^{13}C NMR of **n-SiNAD** aerogels (Figure 4) is dominated by the -$(CH_2)_3$-NAD moiety, showing only very small residual signals from the ethoxy groups (peaks marked "j" and "k"); and finally, (c) the solids ^{29}Si NMR of **n-SiNAD** (Figure 5) shows both the Q and T resonances expected from TMOS and **Si-NAD**, respectively. The Q^1-Q^4 distribution of intensities in both **n-TMOS** and **n-SiNAD** aerogels is the same. The most intense signal is at -98.78 ppm, corresponding to the Q^3 silicon participating in three Si-O-Si bridges. That fact, together with the small amount of residual ethoxy groups in the ^{13}C NMR spectrum, supports further that almost all of the original Si-OR groups have been hydrolyzed, most have been incorporated into the silica network in the form of Si-O-Si bridges, while some remain as dangling OHs, a fact supported by the OH stretches in the IR spectra of all samples (see Figure S.2 in Supporting Information).

Both the rheology and the liquid ^{29}Si NMR data considered together suggest that, in both cases, **n-TMOS** and **n-SiNAD**, the primary gel network was formed by TMOS. Presumably, either more TMOS or **Si-NAD** kept adding onto the network after its initial formation according to a monomer-cluster aggregation model. This conclusion is supported by the gradual and eventual disappearance of all ^{29}Si signals after gelation. That model also suggests that **Si-NAD** decorates the surfaces of the skeletal silica framework with NB, as intended, and agrees with previous speculation to that effect[3b] based on slower reaction rates expected from: (a) ethoxy versus methoxy silanes; and, (b) alkyltrialcoxy versus tetraalcoxy silanes.[8,37] Within that monomer-cluster aggregation model, the slower gelation of the TMOS/**Si-NAD** system may be reconciled by assuming

that elementary particles formed at early stages get capped by **Si-NAD**, which sterically hinders interparticle bond formation. However, Si-O-Si bridges are hydrolyzed off continuously and **Si-NAD** re-precipitates on the network during the particle aggregation process.

To gather further support for a TMOS-like network, we turned to small angle X-ray scattering (SAXS), comparing native **n-SiNAD** with both **n-TMOS** and **n-TMOS-co-APTES** aerogels (Figure 6). Small angle neutron scattering (SANS) data when available agreed quite well with those from SAXS (see for example Figure S.3 in Supporting Information). That together with the high porosity of the samples suggests that all scattering information in SAXS arises from the particles, not from the pores. Results are summarized in Table 2. The high-Q region (Region I, Figure 6) of the **n-SiNAD** aerogels follows a power law, with a slope equal to 4.22±0.03. The slopes for **n-TMOS** and **n-TMOS-co-APTES** aerogels are 3.97±0.03 and 4.37±0.02, respectively. At ~4.0, the high-Q slope of **n-TMOS** indicates primary particles with abrupt interfaces. In **n-SiNAD** and **n-TMOS-co-APTES**, values >4.0 indicate density-gradient (fuzzy) interfaces. The interfacial layer thickness, t, can be calculated via eq 3, assuming a Gaussian distribution

$$t = (2\pi)^{0.5} s \tag{3}$$

of matter at the nanoparticle interfaces with standard deviation s. In turn, s is obtained by fitting the scattering intensity to the suitably modified Porod's law (eq 4), whereas $I(Q)$ is

$$I(Q) = 2\pi N (\Delta\rho)^2 S Q^{-4} \exp[-s^2 Q^2] \tag{4}$$

the scattering intensity as a function of Q, N the number of scatterers per unit volume, $\Delta\rho$ the difference in scattering-length density between scatterers and the surrounding

medium, and S the surface area of the scatterer.[38] The surface layer thickness, t, was found equal to 3.8±0.3 Å and 5.0±0.3 Å for **n-TMOS-co-APTES** and **n-SiNAD**, respectively (Table 2). These values agree well with both the trends in the fully-extended length of the -$(CH_2)_3NH_2$ group of APTES (3.86 Å) and of the -$(CH_2)_3$-NAD group of **Si-NAD** (8.09 Å), both by molecular modeling. The lower SAXS thickness of -(CH_2)-NAD implies some bending. The radius of the primary particles, R_1, is calculated via $R_g=0.77\times R$,[39] where R_g is the radius of gyration, obtained from the Guinier knee (Region II) in the Log-Log plot of $I(Q)$ versus Q of either the SAXS or the SANS data (Figure 6). The radii of the primary particles in **n-SiNAD** fall within the range of 7.1-7.7 nm and, therefore, are similar to those for **n-TMOS** (5.7 nm, by SAXS only, see Table 2). Both the presence and the size of primary particles in **n-SiNAD**, as detected by SAXS, were confirmed by TEM (Figure 7). Additionally, particles in the dimensions suggested by SAXS/TEM for primary particles are the smallest entities discernible in FESEM (Figure 8, whereas the primary particles are pointed at with arrows). Primary nanoparticles aggregated in 3D into mass fractal secondary particles with fractal dimension D_f given by the slope of the second power-law region at lower Q-values (Region III, Figure 6). D_f was found equal to 1.94±0.28 for **n-TMOS** (by SAXS), and 2.07±0.02 for **n-SiNAD** (both by SANS and SAXS; see Table 2). (It is noted that the aggregation of primary particles of **n-TMOS-co-APTES** with a radius of 5.16 nm was beyond the Q-range of our SAXS capability.) The radius of the secondary particles, R_2, was calculated again via the second radius of gyration, $R_g(2)$, which was obtained from the second Guinier knee (Region IV, Figure 6) by fitting the entire scattering profile according to the Beaucage

Table 2. SAXS and SANS data for **Si-NAD** derived aerogels and controls (native **n-TMOS** and **n-TMOS-co-APTES**)

	Primary Particles				Secondary Particles			
	high-Q slope [a]	thickness t (Å) [b]	$R_g(1)$ (nm) [c]	R_1 [d] (nm)	D_f [e]	$R_g(2)$ [f] (nm)	R_2 [d] (nm)	empty space [g] (% v/v)
n-TMOS								
SAXS	3.97±0.02	h	4.2±0.1	5.5±0.2	1.9±0.3	17.6±0.6	22.9±0.8	85
n-TMOS-co-APTES								
SAXS	4.37±0.02	3.8±0.3	3.97±0.06	5.16±0.08	i	i	i	
n-SiNAD								
SAXS	4.22±0.03	5.0±0.3	5.94±0.05	7.71±0.06	2.07±0.02	22.1±0.2	28.7±0.3	78
SANS	j	N/A	5.5±0.2	7.1±0.3	2.07±0.00$_2$	19.3±0.5	25.1±0.6	77
X-SiNAD(10)								
SAXS	4.25±0.05	6.0±0.3	5.9±0.1	7.7±0.1	2.01±0.03	16.1±0.3	20.9±0.4	70
SANS	j	N/A	5.5±0.3	7.1±0.4	1.93±0.03	14.0±0.4	18.2±0.5	69
X-SiNAD(20)								
SAXS	4.26±0.04	6.8±0.3	6.3±0.2	8.2±0.3	2.47±0.02	16.5±0.1	21.4±0.1	70
SANS	j	N/A	5.2±0.4	6.8±0.5	2.25±0.00$_4$	12.5±0.5	16.2±0.6	67
X-SiNAD(30)								
SAXS	4.30±0.06	6.3±0.5	7.2±0.1	9.4±0.1	1.55±0.01	22.4±0.3	29.1±0.4	74
SANS	j	N/A	5.8±0.2	7.5±0.3	0.82±0.00$_2$	28.3±5.0	36.$_8$±6.$_5$	83

Referring to Figure 6: [a]From power law Region I. [b]Via eq 3. [c]From Guinier Region II. [d]Particle radius = R_g/0.77. [e]From power law Region III. [f]From Guinier Region IV. [g]Within secondary particles. Calculated as described in Appendix I of Supporting Information. [h]Abrupt interface (Porod slope = 4.0). [i]No higher aggregates could be probed within the low-Q region accessible. [j]High-Q region not accessible.

Unified Model.[40] R_2 fell within the 25-29 nm range for **n-SiNAD** and ~23 nm for **n-TMOS**. The secondary particles, by comparison with FESEM, are the entities enclosed by the *dark* dashed circles in Figure 8. The number of primary particles, $N(R_2)$, within the secondary particles can be calculated via eq 5, whereas $\zeta = \pi/3\sqrt{2} = 0.7405$ is the fill-factor in cubic or hexagonal closely packed spheres,[41] and R_1, R_2 and D_f have the same meaning as above.

$$N(R_2) = \zeta \left(\frac{R_2}{R_1} \right)^{D_f} \tag{5}$$

In turn, $N(R_2)$ can be used to calculate the percentage of empty space within secondary particles (see Appendix I in Supporting Information). Thus, with R_1=7.71 nm, R_2=28.7 nm, and D_f=2.07, the secondary particles of **n-SiNAD** consist of 78% v/v empty space.

Finally, it is noted that the fractal dimensions of the secondary particles of both **n-SiNAD** and **n-TMOS** (2.07±0.02 and 1.9±0.3, respectively) are different (lower) than the fractal dimensions of the particles forming the gel network as indentified by rheology (2.47 and 2.32, respectively, refer to Table 1). That difference strongly suggests that the gel network is not formed by secondary particles, but by higher aggregates of the latter. That aggregation can be clearly seen in FESEM (entities enclosed by *white* dashed circles, Figure 8). Overall, both neutron and X-ray scattering data further support a TMOS-derived fractal network of nanoparticles whose surface is decorated with NB moieties. That model is consistent with the macroscopic mechanical properties of the entire structure under quasi-static compression (Figure 9 and Table 3).

Table 3. Quasi-static compression data for **Si-NAD** derived aerogels and controls (native **n-TMOS** and **n-TMOS-co-APTES**)

sample	bulk density, (ρ_b, g cm^{-3})	Young's Modulus, (E, MPa)	yield stress at 0.2% offset strain (MPa)	ultimate strength (MPa)	ultimate strain (%)	Poisson ratio	specific energy abs.[b] (J g^{-1})
n-TMOS	0.200	2.9±0.3	0.13±0.01	3.3±0.7	49.7±3.6		2.7±0.6
n-TMOS-co-APTES	0.196	12.8±1.5	0.37±0.09	11.9±6.8	60.8±6.7		10.3±4.7
n-SiNAD	0.197	5.3±0.3	0.21±0.02	4.5±0.4	57.2±5.8		5.7±1.9
X-SiNAD(10)	0.273	108±22	2.9±0.4	18.8±1.7	35.6±3.2	0.08±0.03	14.5±1.3
X-SiNAD(20)	0.382	187±18	5.6±1.1	22.5±0.1	39.0±1.5	0.15±0.02	13.8±0.1
X-SiNAD(30)	0.632	386±25	5.5±0.9	59.3±8.6	43.9±5.9	0.27±0.05	23.2±2.9

[a]Average of 3 samples at strain rate=0.005 s^{-1}. [b]Calculated from the area under the stress-strain curves at ultimate strain.

Thus, while in terms of ultimate strength and within error **n-TMOS** and **n-SiNAD** aerogels behave similarly (ultimate compressive strengths at 3.3±0.7 MPa versus 4.5±0.4 MPa, respectively), suggesting a similar interparticle connectivity, on the other hand **n-SiNAD** are stiffer than **n-TMOS** (Young's modulii at 5.3±0.3 MPa and 2.9±0.3 MPa, respectively) consistent with a surface layer that gets on the way to bending of particles around their interparticle necks.[9] (It is also noted in passing that, in terms of ultimate strain, both native aerogels (**n-TMOS** and **n-SiNAD**) are capable of reaching unusually high values: ~50% and ~57%, respectively. Such supercompressibility for silica at those high densities has not previously been observed.[42] We speculate that this overlooked property of those materials is usually masked by macroscopic defects leading to premature failure. The matter is being investigated further.)

3.2. X-SiNAD Aerogels and the Topology of Crosslinking. Scheme 3 summarizes the crosslinking process from a chemical design perspective. ROMP initiated in the pores engages surface **Si-NAD** moieties. Interparticle bridging (crosslinking) takes place via either cross-metathesis or a stitching mechanism. Experimentally, the process was implemented as shown in Scheme 2. The pore-filling gelation solvent was first equilibrated with variable concentration solutions of NB in THF. A cold (-5 $^{\circ}$C) THF-solution of the **GC-II** catalyst was added to the also cold (-5 $^{\circ}$C) NB bath surrounding the NB-equilibrated gels. Subsequently, samples were incubated at -5 $^{\circ}$C to allow infusion of the catalyst into the gels without significant reaction, the criterion for which is increasing viscosity and ultimately gelation of the crosslinking bath itself. The crosslinking process was completed by allowing the system to warm-up to room temperature. Both short oligomers and loose polymer were removed using four THF washes according to

procedures followed before.[3-8,12-17] Next, wet-gels were solvent-exchanged with acetone and dried in an autoclave with liquid CO_2 taken out supercritically. NB-crosslinked aerogels are referred to as **X-SiNAD(xx)**, where 'xx' takes the values of 10, 20, or 30 denoting the weight percent concentration of NB in the crosslinking baths.

Scheme 3. Crosslinking Mechanisms

A. Cross-metathesis
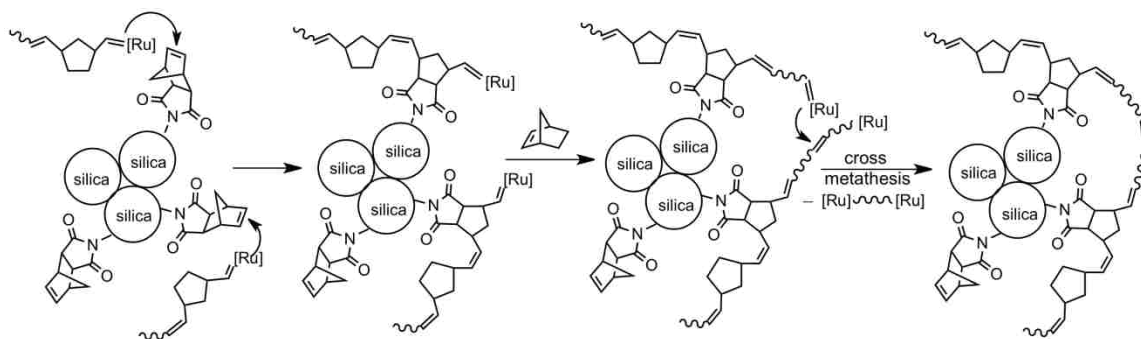
B. Stitching
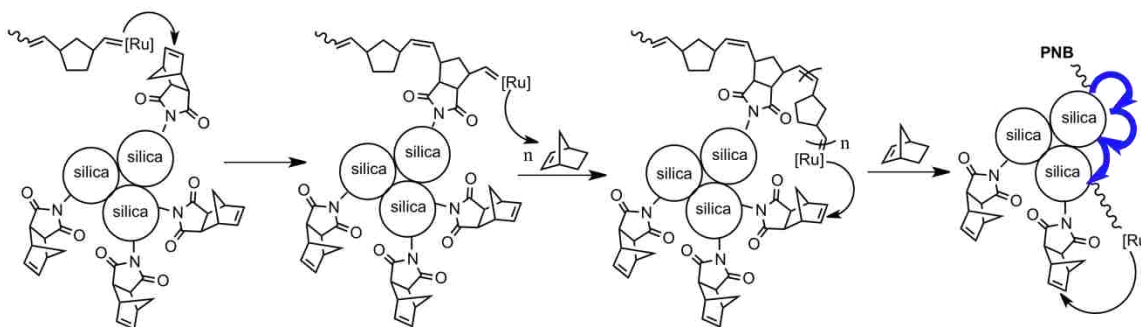
The ^{13}C NMR spectra of all **X-SiNAD(xx)** are dominated by polynorbornene (Figure 4). The ^{29}Si NMR spectra (Figure 5) are identical to that of native **n-SiNAD**, indicating no adverse effect by the crosslinking process upon the chemical make-up of the skeletal framework. General materials properties of **X-SiNAD(xx)** aerogels are summarized in Table 4. The polymer uptake by TGA (Figure 3) increases for more concentrated crosslinking solutions: from 16% to 26% and, ultimately, to 38% w/w,

roughly in proportion to the monomer concentration in the crosslinking bath (Table 4). (For the calculation method of the weight percent of polymer from TGA data, see Appendix II in Supporting Information). Skeletal densities, ρ_s, decrease as the amount of polymer increases. However, the ρ_s values are also consistently lower than the ρ_s calculated from the skeletal densities of the native framework ($\rho_{\textbf{n-SiNAD}}=1.811$ g cm^{-3}, Table 4) and the density of free polynorbornene formed and isolated from the crosslinking bath ($\rho_{PNB}=1.129$ g cm^{-3}, by He pycnometry). That discrepancy can be attributed to closed pores (CP), whose volume, V_{CP}, can be estimated via eq 6, and in turn be used to calculate the percent closed void space, %V_{CP}, on the skeletal framework. ($f_{\textbf{n-SiNAD}}$ and f_{PNB} are the mass fractions of the skeletal framework and polymer, respectively.) The %V_{CP} values are cited in Table 4 and vary from 1.6 % v/v in **X-SiNAD(10)** to 5.6 % v/v in **X-SiNAD(30)**.

$$V_{CP} = \frac{1 - \left(\dfrac{f_{\textbf{n-SiNAD}}}{\rho_{\textbf{n-SiNAD}}} + \dfrac{f_{PNB}}{\rho_{PNB}} \right)\rho_{\textbf{X-SiNAD}}}{\rho_{\textbf{X-SiNAD}}} \qquad (6)$$

On the contrary, due to shrinkage, bulk densities, ρ_b, increased more than expected from simple polymer uptake. Native **n-SiNAD** shrank the least relative to the molds (6.0±0.7% in linear dimensions), shrinking less than both **n-TMOS** and **n-TMOS-co-APTES** aerogels (8-13%). **X-SiNAD** shrank progressively more from 13±1% [**X-SiNAD(10)**] to 27±1% [**X-SiNAD(30)**] as the polymer content increased – see photograph in Scheme 2. The additional shrinkage of the X-samples is attributed to a pulling effect exerted by the polymer on the skeletal framework as it tries to contract in order to maximize its inter-strand van der Waals forces. That additional shrinkage of the X-samples is taken as indirect evidence of bridging skeletal nanoparticles. The effect of

shrinking is evident in FESEM (Figure 8): the microstructure of **n-SiNAD** includes larger voids in the macropore range (>50 nm). Those voids are not present in the X-samples, although the major morphostructural features of the native framework have been preserved. A more quantitative evaluation of the porous structure follows.

Open porosity, via $\Pi=100\times[(1/\rho_b)-(1/\rho_s)]/(1/\rho_b)$, decreased from approximately 89% in **n-SiNAD** to 55% v/v of void space in the most dense crosslinked samples. A more detailed evaluation of the porous structure was conducted with N_2-sorption porosimetry. Internal surface areas, σ, calculated by the BET method, applied on the early part of the adsorption isotherms (Figure 8), decreased as the polymer uptake increased (Table 4). Qualitatively, macroporosity created a divergence of the average pore sizes calculated via the $4\times V_{Total}/\sigma$ method, whereas the total volume of N_2 adsorbed, V_{Total}, either is taken from the highest point of the adsorption isotherm at $P/P_o\sim1$), or is calculated via eq 6. $V_{Total}=(1/\rho_b)-(1/\rho_s)$. With regards to both the n- and all X-samples, the average pore sizes calculated by the two methods are equally close to one another (Table 4). This finding suggests that we are dealing, primarily with mesoporous materials (i.e., pore sizes in the 2-50 nm range). Indeed, all N_2-sorption isotherms (Figure 8) showed desorption hysteresis loops. Those isotherms can be classified as Type IV characterizing mesoporous materials. Upon closer examination though, the isotherms of **n-SiNAD** do not reach saturation, in agreement with the macroporosity noted in FESEM. On the other hand, the isotherms of all X-samples did reach saturation, suggesting that macroporosity had been eliminated. Furthermore, as the amount of polymer increased the desorption branch turns from H1-type (unobstructed adsorption-desorption, **X-SiNAD(10)** and **X-Si-NAD(20)** samples) into H2-type (ink-bottle like pores, **X-SiNAD(30)** samples).

Table 4. Materials properties of the **Si-NAD** derived aerogels and the controls (native **n-TMOS** and **n-TMOS-co-APTES**)

sample	polymer % w/w [a]	skeletal density, ρ_s (g cm^{-3}) [b]	closed skeletal porosity, $\%V_{CP}$ (v/v) [c]	monolith linear shrinkage (%) [d,e]	bulk density, ρ_b (g cm^{-3}) [d]	open bulk porosity, Π (% void space)	BET surface area, σ (m^2 g^{-1})	average pore diameter (nm) [f]	BJH pore diameter (nm) [g]	particle radius, r (nm) [h]
n-SiNAD	i	1.811 ± 0.007	-	6 ± 0.7	0.197 ± 0.005	89.1	590	25.4[30.7]	41.5[24.0]	2.8
X-SiNAD(10)	16	$1.60_9\pm0.01_3$	1.6	13 ± 1	0.273 ± 0.009	83.0	368	25.3[33.1]	38.6[13.0]	5.1
X-SiNAD(20)	26	1.505 ± 0.003	3.8	20 ± 0.5	$0.38_2\pm0.01_1$	74.6	243	18.9[32.2]	22.2[6.9]	8.2
X-SiNAD(30)	38	1.391 ± 0.004	5.6	27 ± 1	$0.63_2\pm0.02_0$	54.6	124	14.2[27.8]	16.1[3.2]	17.4
n-TMOS	i	1.970 ± 0.007	-	13.0	0.200	89.8	724	19.6[24.8]	20.7[2.8]	2.1
n-TMOS-co-APTES	i	1.835 ± 0.003	-	8 ± 0.5	0.196 ± 0.002	89.3	491	12.4[37.1]	13.4[3.6]	3.3

[a]By TGA (Figure 3); For calculations, see Appendix II in Supporting Information. [b]Single sample, average of 50 measurements. [c]Via eq 6. [d]Average of three samples. [e]Linear shrinkage $= 100 \times$ (sample diameter – mold diameter)/(mold diameter). [f]By the $4\times V_{Total}/\sigma$ method. For the first number, V_{Total} was calculated by the single-point adsorption method; For the number in brackets, V_{Total} was calculated via $V_{Total} = (1/\rho_b)-(1/\rho_s)$. [g]From the desorption branch of the isotherm. The first number is the peak maxima; the number in brackets is the full width at the half maxima. [h]Calculated via $r=3/\rho_s\sigma$. [i]Not applicable.

The samples, however, remained mesoporous, as the t-plot analysis shows no indication for open microporosity (pore diameters<2 nm) in any sample. By the same token, however, along the process of ink-bottle pore formation, it is reasonable that some bottle-necks might get closed. That could explain the small amount of closed porosity identified via skeletal density considerations above.

Pore size distributions were evaluated by the BJH method applied on the desorption branch of the isotherms. (Plots are given as insets in Figure 8.) The maxima of the BJH plots are in good agreement with those from the $4 \times V_{\text{Total}}/\sigma$ method applied to the maximum volume of N_2 adsorbed (see Table 4). The native **n-SiNAD** samples also show a shoulder at the smaller pore side of the BJH curve (~30 nm, indicated with an arrow in Figure 8), suggesting two kinds of mesopores. That shoulder is progressively eliminated in the X-samples, suggesting a closing of the smaller pores. The elimination of smaller pores should have shifted average pore sizes to larger values. The opposite, however, was observed, presumably as the result of a contraction (shrinking) of the entire structure.

As previously discussed, the simple accumulation of polymer on the skeletal framework of **X-SiNAD(xx)** samples would increase the stiffness (resistance to bending). As opposed to simple polymer accumulation, bridging skeletal nanoparticles covalently would increase the ultimate strength of the whole structure.[9] Indeed, under compression, all NB-crosslinked **X-NB-Si-NAD** aerogels were not only much stiffer (108-386 MPa vs. 5.3 MPa), but also much stronger (19-59 MPa vs. 4.5 MPa) and tougher (14.5-23.2 J g^{-1} vs. 5.7 J g^{-1}) than **n-SiNAD**. The elastic (Young's) modulus, E, increases exponentially with the bulk density, ρ_b, according to a power law of the form $E \sim \rho_b^{1.5}$ (see Figure 9). (It is noted though that the power-law exponent is lower than what has been reported for

silica (3.7),[43] thus underlining the efficiency of low polymer loadings for increasing stiffness.) Even more intriguing is the behavior of both the ultimate compressive strength (UCS) and the energy absorption as functions of bulk density (both shown by Log-Log plots in Figure 9); after an initial jump from **n-SiNAD** to **X-SiNAD(10)**, these properties remained nearly constant for **X-SiNAD(20)**, increasing drastically thereafter for **X-SiNAD(30)**. The slopes of the Log-Log plots between **X-SiNAD(20)** and **X-SiNAD(30)** are 1.92 and 1.03 for the UCS and energy absorption, respectively, in line with silica (2.6 and 1.6, respectively, albeit in a 3–point bending configuration).[43] The discontinuity in the Log-Log plots for both UCS and energy absorption suggests that not all polymer is equivalent: polymer accumulating at the early stages of crosslinking has a different effect from that accumulating later. Hence, both indentifying possible chemical differences and locating the two kinds of polynorbornene on the silica nanostructure are important.

As inferred by the microscopic similarity of **n-SiNAD** to all three **X-SiNAD(xx)** (Figure 8), the polymer is always closely associated with silica. That fact, in combination with covalent bonding between the two, should restrict segmental motion of polymeric strands, and therefore raise the glass transition temperature, T_g, relative to the bulk polymer as the thickness of the polymeric crosslinker decreases.[44] Indeed, as shown in Figure 10, **X-SiNAD(10)** had the highest T_g (73.8 ^{o}C). That value decreased sharply to 63.9 ^{o}C for **X-SiNAD(20)**, eventually reaching 60.6 ^{o}C for **X-SiNAD(30)**. This temperature is still higher than the T_g of free polymer formed and collected from the crosslinking bath (50.4 ^{o}C). Clearly, the polymer in all three X-samples never reached a thickness high enough to behave as bulk NB. In a careful comparison of grafted brushes versus cast PMMA films, Yamamoto demonstrated that a 10 ^{o}C higher T_g [an analogous

situation to **X-SiNAD(30)**] corresponds to layers of brushes approximately 10 nm thick.[44c] In terms of the **n-SiNAD** nanostructure, this thickness is within secondary particles. Finally, the full width at half maxima of the heat exchange profiles of the three X-samples was much broader (42-67 $^{\circ}$C) than that of the free polymer (12 $^{\circ}$C), reflecting the variable lengths between points of attachment of the polymer to the silica backbone.

The crosslinking polymer was freed from the silica framework of all three X-samples by treatment with HF. The free polymer was extracted with CHCl$_3$, and its size was investigated with gel permeation chromatography (GPC) in THF using polystyrene standards. Results were compared to free polymer formed outside the gels in the surrounding crosslinking bath. (Owing to similar hydrodynamic radii in THF of both polynorbornene and polystyrene at equal molecular weights, the latter was a good model for the former.[45]) Typical GPC data are given in Figure 11. All results are summarized in Table S.1 in Supporting Information. By inspection, peaks corresponding to individual polymers/oligomers were placed in both a lower retention time group (R$_f$~6.5 min, higher molecular weight polymer) and a higher R$_f$ group (~9.7 min, smaller oligomers). Those two groups were fitted to Gaussian profiles (indicated with dashed lines in Figure 11). Average molecular weights were calculated by standard procedures.[29] The long component varied from 379 to 505 monomer units; its weight percent contribution increases from 32% in **X-SiNAD(10)** to 41% in **X-SiNAD(20)** to 50% in **X-SiNAD(30)**, while the polydispersity remained relatively low, in the 1.88-2.28 range. The short component, however, had only 8-11 monomer units and a polydispersity of 1.74-2.53. The make-up of the polymer formed in the crosslinking bath was somewhat different from that formed on the skeletal framework; that polymer included a third major fraction

(50% w/w), with intermediate retention time (R_f~8.4 min) corresponding to ~100 monomer units with very high polydispersity (7-10). In contrast to the X-samples, the distribution of the three fractions in the polymer from the crosslinking bath did not change with the concentration, advocating for the role of surface-NB in modulating the polymer length in the gels through the stitching mechanism of Scheme 3. The radii of gyration, R_g, of the polymer fractions freed from the network were calculated both for good (swelling) solvents via eq. 7,[46] and for theta solvents via eq 8,[47] where the number

$$R_{g\_swelling} = \frac{a}{(6)^{1/2}} N^{3/5} \tag{7}$$

$$R_{g\_theta} = \frac{a}{(6)^{1/2}} N^{1/2} \tag{8}$$

of monomer units, N, is taken from Table S.1 in Supporting Information and the length of the monomer repeat unit, α, was found by simulation equal to 4.85 Å.

Three models are thus consistent with the data (Scheme 4). Model I is based on the polymerization chemistry outlined in Scheme 3, which is expected to form a polymer shell around NB-modified silica cores. Model II expands on Model I by considering that the polymer may form lumps distributed within the empty space (see Table 2) of secondary particles. In Model III, an alternative to Model II, most of the space within the secondary particles is filled evenly by polymer; some void space, in the form of closed pores, is consistent with the polymer content/skeletal density considerations above.

If the polymer coils-up (Model II), the radius of gyration calculated for theta solvents, R_{g_theta}, may be considered an upper bound for the radius of gyration of possible dry spherical lumps. Those radii of gyration are included in Table S.1. They were used to

Scheme 4. Models for secondary particles in **X-SiNAD(xx)** aerogels[a]
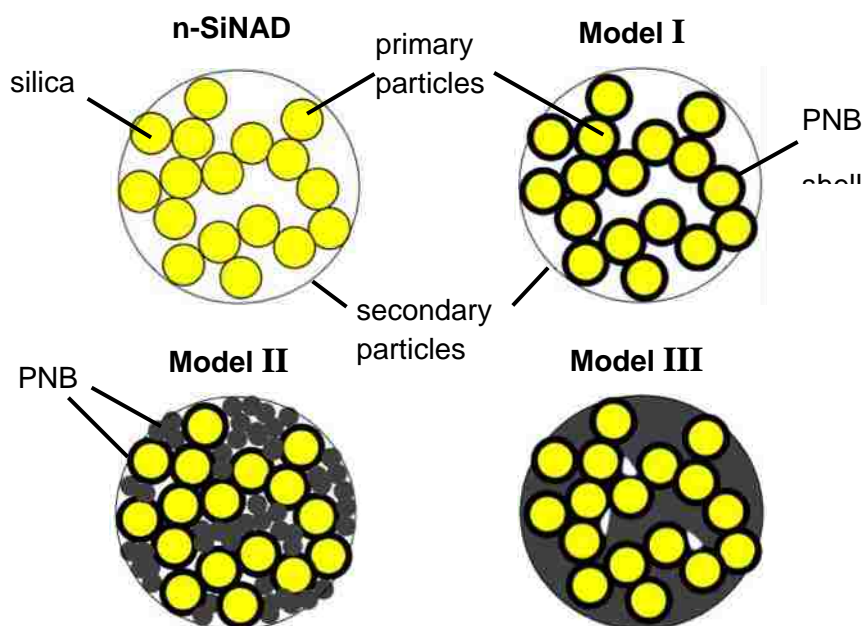
[a]Model I: secondary particles consist of silica-core/polymer-shell primary particles; Model II: in addition to Model I, secondary particles include lumps of polynorbornene; Model III: an alternative to Model II, whereas polymer is evenly distributed around core/shell primary particles. (The illustration emphasizes also the fact that secondary particles may include closed pores.)

calculate the actual radii of the hypothetical lump which, for the short polymer component, were 0.73-0.86 nm, and for the long component in the range of 5.0-5.8 nm. TEM as a tool to look directly inside secondary particles in hopes to see those polymer spheres was inconclusive, probably because of the small Z-attenuation difference between silica and polymer:[48] according to Figure S.4 in Supporting Information, upon polymer uptake images get blurry, the sharp definition of silica particles is lost, but yet they appear surrounded by a unstructured sort of matrix. Thus, to glimpse inside the secondary particles, we resorted back to SAXS/SANS (Figure 6 and Table 2) in combination with some selected general material characterization data from Table 4.

By SANS/SAXS, all three crosslinked samples continued to demonstrate the same hierarchical primary/fractal-secondary particle structure of **n-SiNAD**. Of major importance is the fact that primary particles were discernible at all. Thus, those particles were embedded in a medium of different density ($\Delta\rho\neq0$, refer to eq 4). The radius of the primary particles increased monotonically with the degree of crosslinking from **X-SiNAD(10)** to **X-SiNAD(30)**. The radius of the secondary particles first decreased from 28.7±0.3 nm in **n-SiNAD** to ~21 nm in **X-SiNAD(10)** and **X-SiNAD(20)**, and then increased to 29.1± 0.4 nm in **X-SiNAD(30)**. The uncertainties (error) in the radii of gyration of the primary particles were less than 4% in SAXS, 7% in SANS, and, in most cases, less than 2%. Hence, we are dealing with only one kind of primary particles. Should the polymer have coiled into 5.0-5.8 nm lumps, those lumps would have interfered with the scattering profile of the silica primary particles, yielding bimodal particle size distributions. The latter were not detected. Therefore, discrete polymeric lumps (Model II, Scheme 4) were not formed at any level. On the contrary, primary particles in the crosslinked samples still show fuzzy (density-gradient) interfaces (high-Q slopes >4.0), and the thicknesses of the fuzzy zones are very similar to those of the native **n-SiNAD** samples (6.0-6.8 Å, versus 5.0 Å, respectively).

To this point in the study, the SAXS/SANS data have been consistent with polymer building into a tight, dense conformal shell (coating) around the silica core primary particles comprising the native **n-SiNAD** network. That coating covalently bridges, as designed, primary particles, pulling them together so that secondary particles contract. As outlined in Appendix III of the Supporting Information, the radius of the core-shell primary particles can be calculated from the radius of the native primary

particles (7.71 nm by SAXS), the skeletal density of the silica core (1.811 g cm^{-3}), and the density of the polynorbornene isolated from the crosslinking bath (ρ_{PNB}=1.129 g cm^{-3}). It was thus found for the ratio, (experimental radius by SAXS/calculated radius, nm/nm): 7.7/8.7 for **X-SiNAD(10)**; 8.2/9.4 for **X-SiNAD(20)**; and, 9.4/10.6 for **X-SiNAD(30)**. The values in the pairs are close, providing support for the formation of polynorbornene shells around the primary silica core particles of the native **n-SiNAD** framework.

The medium surrounding the primary core-shell particles within the secondary particles may be either air, or looser polymer of different density from that forming the core-shell structure around primary particles (Model III). The GPC analysis above corroborates with this model, suggesting a succession of events: NB moieties on primary particles are engaged early, leading to a conformal coating of shorter, closely held (denser) polymer. Longer polymer fills the empty space within secondary particles. The immediate question then is whether or not secondary particles are completely filled with polymer. As discussed in Section 3.1, owing to their fractal structure, secondary particles of **n-SiNAD** consist of 78% empty space. Similarly, "empty" space within secondary particles of X-samples can also be calculated from the experimental radii of gyration of the core-shell primary particles and is cited in Table 2. Owing to the uncertainties involved, for that calculation we assumed that the fractal dimension of all secondary particles remained equal to that of **n-SiNAD** (D_f=2.07). At first approximation, i.e., by ignoring closed pores, an assessment of whether that "empty" space is filled with polynorbornene can be obtained by comparing the experimental skeletal densities of the X-samples (Table 4) with those calculated as the weighted average of silica and polymer,

and assuming that all the space surrounding primary particles is occupied by polymer. Additional assumptions are: (a) secondary particles consist of primary silica particles of the same dimensions found in **n-SiNAD** (7.71 nm by SAXS); and, (b) space is filled by one kind of polymer, that obtained from the crosslinking bath. We thus find for the ratio (experimental/calculated skeletal densities, g cm^{-3}/g cm^{-3}): 1.609/1.327 for **X-SiNAD(10)**; 1.505/1.327 for **X-SiNAD(20)**; and, 1.391/1.279 for **X-SiNAD(30)**. The two skeletal densities converge for **X-SiNAD(30)**. Looking at the issue from a different perspective, the smallest particle radii, r, calculated from both skeletal densities and BET surface areas (values included in Table 4) agree reasonably well with the radii of the core-shell primary particles estimated from SAXS for **X-SiNAD(10)** and **X-SiNAD(20)**, but they jump to higher values for **X-SiNAD(30)**, consistent with mostly polymer-filled secondary particles. Overall, data converge towards Model III.

4. Conclusion

The experimental implementation in 2002 of Mackenzie's 1992 conjecture calling for polymer/sol-gel composites consisting of polymeric tethers bridging inter-connected silica particles,[49] produced polymer-crosslinked aerogels, a class of extremely strong, yet lightweight materials.[3b] However, given the complex hierarchical structure of silica (agglomerates of porous, fractal secondary nanoparticles), the exact location of the polymer, and therefore application-specific questions such as how much is enough, had not been addressed yet. Here, by designing a system whereas crosslinking takes place by a well-defined process (grafting to ROMP), loose polymer can be removed easily. Then, by using a wide array of characterization methods, it is concluded that accumulation of

the crosslinking polymer follows the hierarchical structure of silica (Model III, Scheme 4). The polymer stays close forming a conformal coating around primary particles. Subsequently, it fills secondary particles without formation of globules or lumps. Along that process, only a very small amount of closed porosity is created (<5% v/v of the skeletal network). Most importantly, however, a small amount of polymer (e.g., 16% w/w) that coats only primary particles with minimal compromise in the overall porosity (from 89% to 83% v/v) and the porosity-related properties (e.g., BET surface areas, from 590 to 368 m^2 g^{-1}) is enough to increase stiffness by a factor of 20×, and ultimate compressive strength by a factor of 4×. At that point, silica aerogels are quite robust materials, making them easy to handle. Additional polymer continues to accumulate, mostly on and around primary particles, so that properties such as porosity and BET surface area begin decreasing noticeably without any gain in either ultimate compressive strength, or specific energy absorption. The point where mechanical properties start improving drastically again is when secondary particles are almost completely filled with polymer. The subject matter of this paper, i.e., the detailed correlation of structure-mechanical strength at the early stages of crosslinking, raises obvious questions about the opposite end of the strength-density continuum, namely for materials classified as polymer-matrix composites.[50]

of the SANS instrument, LQD at the Manuel Lujan, Jr. Neutron Scattering Center of the Los Alamos National Laboratory, supported by the DOE office of Basic Energy Sciences and utilized facilities supported in part by the National Science Foundation under Agreement No. DMR-0454672.

Supporting Information. Rheology during base-catalyzed gelation of TMOS (Figure S.1); IR spectra of representative aerogel samples (Figure S.2); Overlaid SAXS and SANS data for **n-SiNAD** (Figure S.3); TEM data for **X-SiNAD(xx)** (Figure S.4); GPC analysis data (Table S.1); Calculation of empty space in secondary particles (Appendix I); Calculation of polymer content in X-samples from TGA data (Appendix II); Calculation of the thickness of a polymer shell around silica core from experimental skeletal density data (Appendix III). This information is available free of charge via the Internet at http://pubs.acs.org.

5. References

1. (a) Pierre, A. C.; Pajonk, G. M.; *Chem. Rev.* **2002**, *102*, 4243-4265. (b) Morris, C. A.; Anderson, M. L.; Stroud, R. M.; Merzbacher, C. I.; Rolison, D. R. *Science*, **1999**, *284*, 622-624.

2. (a) Kistler, S. S. *Nature*, **1931**, *127*, 741. (b) Kistler, S. S. *J. Phys. Chem.* **1932**, *36*, 52-64. (c) Gurav, J. L.; Rao, A. V.; Rao, A. P.; Nadargi, D. Y.; Bhagat, S. D. *J. Alloy Compd.* **2009**, *476*, 397-402. (d) Rao, A. V.; Bangi, U. K. H.; Kavale, M. S.; Imai, H.; Hirashima, H. *Micropor. Mesopor. Mat.* **2010**, *134*, 93-99.

3. (a) Leventis, N.; Sotiriou-Leventis, C.; Zhang, G.; Rawashdeh, A-M. M. *Nano Lett.* **2002**, *2*, 957-960. (b) Leventis, N. *Acc. Chem. Res.* **2007**, *40*, 874-884. (c) Leventis, N.; Lu, H. Polymer-Crosslinked Aerogels. In *Aerogels Handbook*; Aegerter, M. A., Leventis, N., Koebel, M. M., Eds.; Springer: New York, 2011, pp 251-285.

4. (a) Leventis, N.; Vassilaras, P.; Fabrizio, E. F.; Dass, A. *J. Mater. Chem.* **2007**, *17*, 1502-1508. (b) Leventis, N.; Sotiriou-Leventis, C.; Mulik, S.; Dass, A.; Schnobrich, J.; Hobbs, A.; Fabrizio, E. F.; Luo, H.; Churu, G.; Zhang, Y.; Lu, H. *J. Mater. Chem.* **2008**, *18*, 2475-2482. (c) Leventis, N.; Chandrasekaran, N.; Sotiriou-Leventis, C.; Mumtaz, A. *J. Mater. Chem.* **2009**, *19*, 63-65. (d) Leventis, N. Interpenetrating Organic/Inorganic Networks of Resorsinol-Formaldehyde/Metal Oxide Aerogels. In *Aerogels Handbook*; Aegerter, M. A., Leventis, N., Koebel, M. M., Eds.; Springer: New York, 2011, pp 287-313.

5. Lu, H.; Luo, H.; Leventis, N. Mechanical Characterization of Aerogels. In *Aerogels Handbook*; Aegerter, M. A., Leventis, N., Koebel, M. M., Eds.; Springer: New York, 2011, pp 499-535.

6. Leventis, N.; Palczer, A.; McCorkle, L.; Zhang, G.; Sotiriou-Leventis, C. *J. Sol-Gel Sci. Tech.* **2005**, *35*, 99-105.

7. Leventis, N.; Sadekar, A.; Chandrasekaran, N.; Sotiriou-Leventis, C. *Chem. Mater.* **2010**, *22*, 2790-2803.

8. Hüsing, N.; Schubert, U. *Angew. Chem. Int. Ed.* **1998**, *37*, 22-45.

9. Mulik, S.; Sotiriou-Leventis, C.; Churu, G.; Lu, H.; Leventis, N. *Chem. Mater.* **2008**, *20*, 5035-5046.

10. Boday, D. J.; Keng, P. Y.; Muriithi, B.; Pyun, J.; Loy, D. A. *J. Mater. Chem.* **2010**, *20*, 6863-6865.

11. Boday, D. J.; DeFriend, K. A.; Wilson, K. V.; Coder, D.; Loy, D. A. *Chem. Mater.* **2008**, *20*, 2845-2847.

12. Zhang, G.; Dass, A.; Rawashdeh, A-M. M.; Thomas, J.; Counsil, J. A.; Sotiriou-Leventis, C.; Fabrizio, E. F.; Ilhan, F.; Vassilaras, P.; Scheiman, D. A.; McCorkle, L.; Palczer, A.; Johnson, J. C.; Meador, M. A. B.; Leventis, N. *J. Non-Cryst. Solids* **2004**, *350*, 152-164.

13. (a) Katti, A.; Shimpi, N.; Roy, S.; Lu, H.; Fabrizio, E. F.; Dass, A.; Capadona, L. A.; Leventis, N. *Chem. Mater.* **2006**, *18*, 285-296. (b) Meador, M. A. B.; Capadona, L. A.; McCorkle, L.; Papadopoulos, D. S.; Leventis, N. *Chem. Mater*. **2007**, *19*, 2247-2260.

14. Meador, M. A. B.; Fabrizio, E. F.; Ilhan, F.; Dass, A.; Zhang, G.; Vassilaras, P.; Johnston, J. C.; Leventis, N. *Chem. Mater.* **2005**, *17*, 1085-1098.

15. See for example: Ilhan, F.; Fabrizio, E. F.; McCorkle, L.; Scheiman, D.; Dass, A.; Palczer, A.; Meador, M. A. B.; Johnston, J. C.; Leventis, N. *J. Mater. Chem.* **2006**, *16*, 3046-3054.

16. (a) Guo, H.; Nguyen, B. N.; McCorkle, L. S.; Shonkwiler, B.; Meador, M. A. B. *J. Mater. Chem.* **2009**, *19*, 9054-9062. (b) Nguyen, B. N.; Meador, M. A. B.; Tousley, M. E.; Shonkwiler, B.; McCorkle, L.; Sceiman, D. A.; Palczer, A. *ACS Appl. Mater. Interfaces* **2009**, *1*, 621-630.

17. (a) Leventis, N.; Chandrasekaran, N.; Sadekar, A. G.; Sotiriou-Leventis, C.; Lu, H. *J. Am. Chem. Soc.* **2009**, *131*, 4576-4577. (b) Leventis, N.; Chandrasekaran, N.; Sadekar, A. G.; Mulik, S.; Sotiriou-Leventis, C. *J. Mater. Chem.* **2010**, *20*, 7456-7471.

18. Grubbs, R. H. *Angew. Chem. Int. Ed*. **2006**, *45*, 3760-3765.

19. (a) Lee, J. K.; Gould, G. L. *J. Sol-Gel Sci. Technol.* **2007**, *44*, 29-40. (b) Dawedeit, C.; Kim, S. H.; Braun, T.; Worsley, M. A.; Letts, S. A.; Wu, K. J.; Walton, C. C.; Chernov, A. A.; Satcher, J. H. Jr.; Hamza, A. V.; Biener, J. *Soft Matter* **2012**, DOI: 10.1039/c2sm07396j.

20. (a) Juang, A.; Scherman, O. A.; Grubbs, R. H.; Lewis, N. S. *Langmuir* **2001**, *17*, 1321-1323. (b) Harada, Y.; Girolami, G. S.; Nuzzo, R. G. *Langmuir* **2003**, *19*, 5104-5114. (c) Kim, N. Y.; Jeon, N. L.; Choi, I. S.; Takami, S.; Harada, Y.; Finnie, K. R.; Girolami, G. S.; Nuzzo, R. G.; Whitesides, G. M.; Laibinis, P. E. *Macromolecules* **2000**, *33*, 2793-2795.

21. (a) Kong, B.; Lee, J. K.; Choi, I. S. *Langmuir* **2007**, *23*, 6761-6765. (b) Weck, M.; Jackiw, J. J.; Rossi, R. R.; Weiss, P. S.; Grubbs, R. H. *J. Am. Chem. Soc*. **1999**, *121*, 4088-4089.

22. Watson, K. J.; Zhu, J.; Nguyen, S. T.; Mirkin, C. A. *J. Am. Chem. Soc*. **1999**, *121*, 462-463.

23. Jeong, W.; Kessler, M. R. *Chem. Mater*. **2008**, *20*, 7060-7068.

24. Buchmeiser, M.; Sinner, F.; Mupa, M.; Wurst, K. *Macromolecules* **2000**, *33*, 32-39.

25. Pavia, D. L.; Lampman, G. M.; Kriz, G. S.; Engel, R. G. A Small Scale Approach to Organic Laboratory Techniques 3rd Edition, Brooks Cole: Independence, KY, 2010, pp 405-409.

26. Leventis, N.; Elder, I. A.; Rolison, D. R.; Anderson, A. L.; Merzbacher, C. I. *Chem. Mater.* **1999**, *11*, 2837-2845.

27. Seeger, P. A.; Hjlem, R. P. Jr. *J. Appl. Crystallogr*. **1991**, *24*, 467-478.

28. Ilavsky, J.; Jemian, P. R. *J. Appl. Cryst*. **2009**, *42*, 347-353.

29. (a) Harmon, D. J. *J. Polym. Sci*. **1965**, *C8*, 243-251. (b) May, J. A. Jr.; Smith, W. B. *J. Phys. Chem*. **1968**, *72*, 216-221.

30. Winter, H. H. *Polym. Eng. Sci.* **1987**, *27*, 1698-1702.

31. Kim, S.-Y.; Choi, D.-G.; Yang, S.-M. *Korean J. Chem. Eng*. **2002**, *19*, 190-196.

32. Raghavan, S. R.; Chen, L. A. ; McDowell, C.; Khan, S. A., Hwang, R.; White, S. *Polymer* **1996**, *37*, 5869-5875.

33. Muthukumar, M. *Macromolecules* **1989**, *22*, 4656-4658.

34. Kolb, M.; Botet, R.; Julien, J. *Phys. Rev. Lett.* **1983**, *51*, 1123-1126.

35. See for example: (a) Mazúr, M.; Mlynárik, V.; Valko, M.; Pelikán, P. *Appl. Magn. Reson.* **1999**, *16*, 547-557. (b) Corminbœuf, C.; Heine, T.; Weber, J. *Chem. Phys. Lett.* **2002**, *357*, 1-7. (c) El hadad, A. A.; Carbonell, D.; Barranco, V.; Jiménez-Morales, A.; Casal, B.; Galván, J. C. *Colloid Polym. Sci.* **2011**, *289*, 1875-1883.

36. Hench, L. L.; West, J. K. *Chem. Rev.* **1990**, *90*, 33-72.

37. Hüsing, N.; Schubert, U.; Mezei, R.; Fratzl, P.; Riegel, B.; Kiefer, W.; Kohler, D.; Mader, W. *Chem. Mater.* **1999**, *11*, 451–457.

38. Koberstein, J. T.; Morra, B.; Stein, R. S. *J. Appl. Crystallogr.* **1980**, *13*, 34-45.

39. Guinier, A.; Fournet, G. Small-Angle Scattering of X-rays, John Wiley and Sons: New York, NY, 1955.

40. (a) Beaucage, G. *J. Appl. Cryst*. **1995**, *28*, 717-728. (b) Beaucage, G. *J. Appl. Cryst*. **1996**, *29*, 134-146. (c) Mang, J. T.; Son, S. F.; Hjelm, R. P.; Peterson, P. D.; Jorgensen, B. S. *J. Mater. Res.* **2007**, *22*, 1907-1920.

41. Lee, D. G.; Bonner, J. S.; Garton, L. S.; Ernest, A. N. S.; Autenrieth, R. L. *Wat. Res.* **2000**, *34*, 1987-2000.

42. Kucheyev, S. O.; Stadermann, M.; Shin, S. J.; Satcher, J. H. Jr.; Gammon, S. A.; Letts, S. A.; van Buuren, T.; Hamza, A. V. *Adv. Mater.* **2012**, *24*, 776-780.

43. Woignier, T.; Phalippou, J. *Rev. Phys. Appl.* **1989**, *24*, 179-184.

44. See for example: (a) Vyazovkin, S.; Dranca, I.; Fan, X.; Advincula, R.; *J. Phys. Chem. B* **2004**, *108*, 11672-11679. (b) Blum, F. D.; Young, E. N.; Smith, G.; Sitton, O. C. *Langmuir* **2006**, *22*, 4741-4744. (c) Yamamoto, S.; Tsujii, Y.; Fikuda, T. *Macromolecules* **2002**, *35*, 6077-6079.

45. Jordi, M. A.; Seery, T. A. P. *J. Am. Chem. Soc.* **2005**, *127*, 4416-4422.

46. Ken, T.; Mays, J. W. *Eur. Polym. J.* **2004**, *40*, 1623-1627.

47. Peterson, K. A.; Zimmt, M. B.; Linse, S.; Dominique, R. P.; Fayer, M. D. *Macromolecules* **1987**, *20*, 168-175.

48. See for example: (a) Ribbe, A.; Prucker, O.; Rühe, J. *Polymer*, **1996**, *37*, 1087-1093. (b) Midgley, P. A.; Ward, E. P. W.; Hungría, A. B.; Thomas, J. M. *Chem. Soc. Rev.* **2007**, *36*, 1477-1494. (c) Chen, Z.; Gang, T.; Zhang, K.; Zhang, J.; Chen, X.; Sun, Z.; Yang, B. *Coll. Surf. A: Physicochem. Eng. Aspects* **2006**, *272*, 151-156. (d) Hao, L.; Zhu, C.; Chen, C.; Kang, P.; Hu, Y.; Fan, W.; Chen, Z. *Synth. Met.* **2003**, *139*, 391-396.

49. Hu, Y.; Mackenzie, J. D. *J. Mater. Sci.* **1992**, *27*, 4415–4420.

50. Leventis, N.; Sotiriou-Leventis, C.; Mulik, S.; Patil, V.; Mohite, D.; Zhang, Y.; Lu, H. *Polymer Preprints* **2008**, *49*, 504-506.

6. Figures
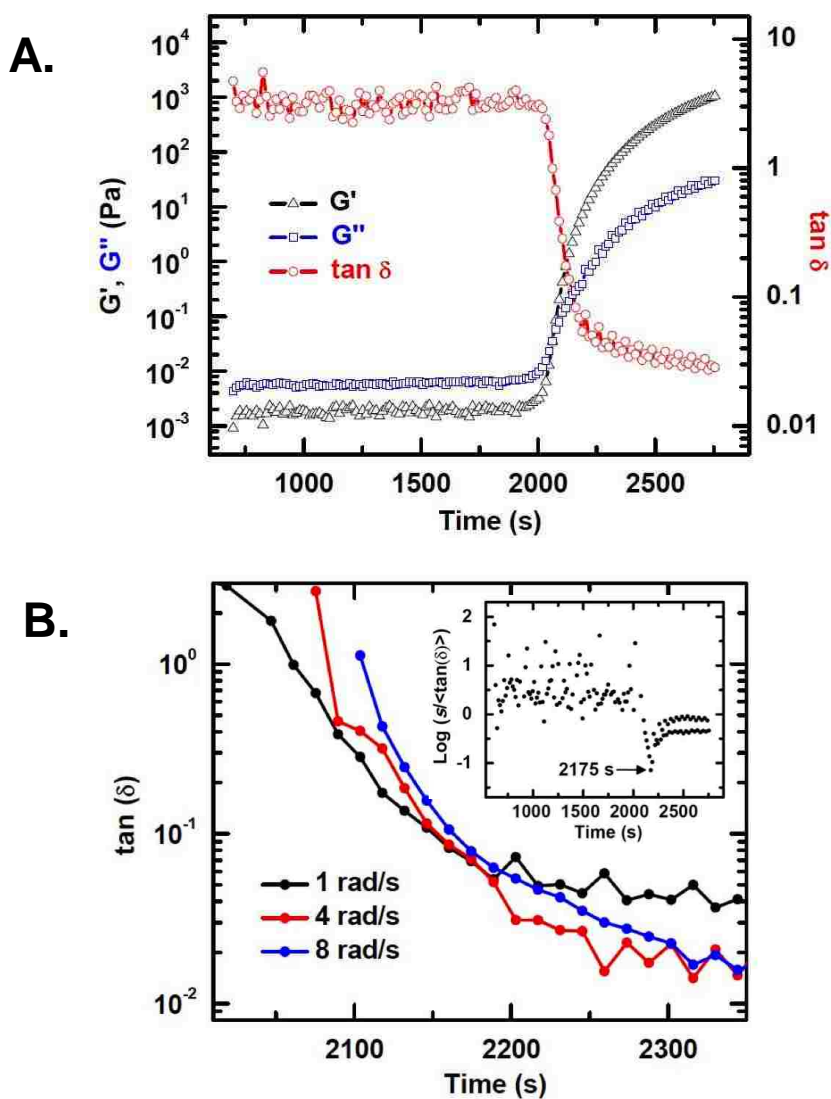
Figure 1. Rheology during the base-catalyzed (NH$_4$OH, 40 mL) co-gelation of **Si-NAD** with TMOS (1:9 mol/mol) at 20 ^{o}C, according to the procedure described in the Experimental section. A. Evolution of the storage (G´) and loss (G´´) modulii as well as of tan*d* versus time from mixing the sol. Data shown at 1 rad s^{-1} oscillation frequency. (For other parameters, see Experimental section.) B. Tan*d* versus time from mixing the sol, close to the gelation point, at three different oscillation frequencies. Inset: Statistical variable versus time (see text). The gelation point is defined at the minimum.
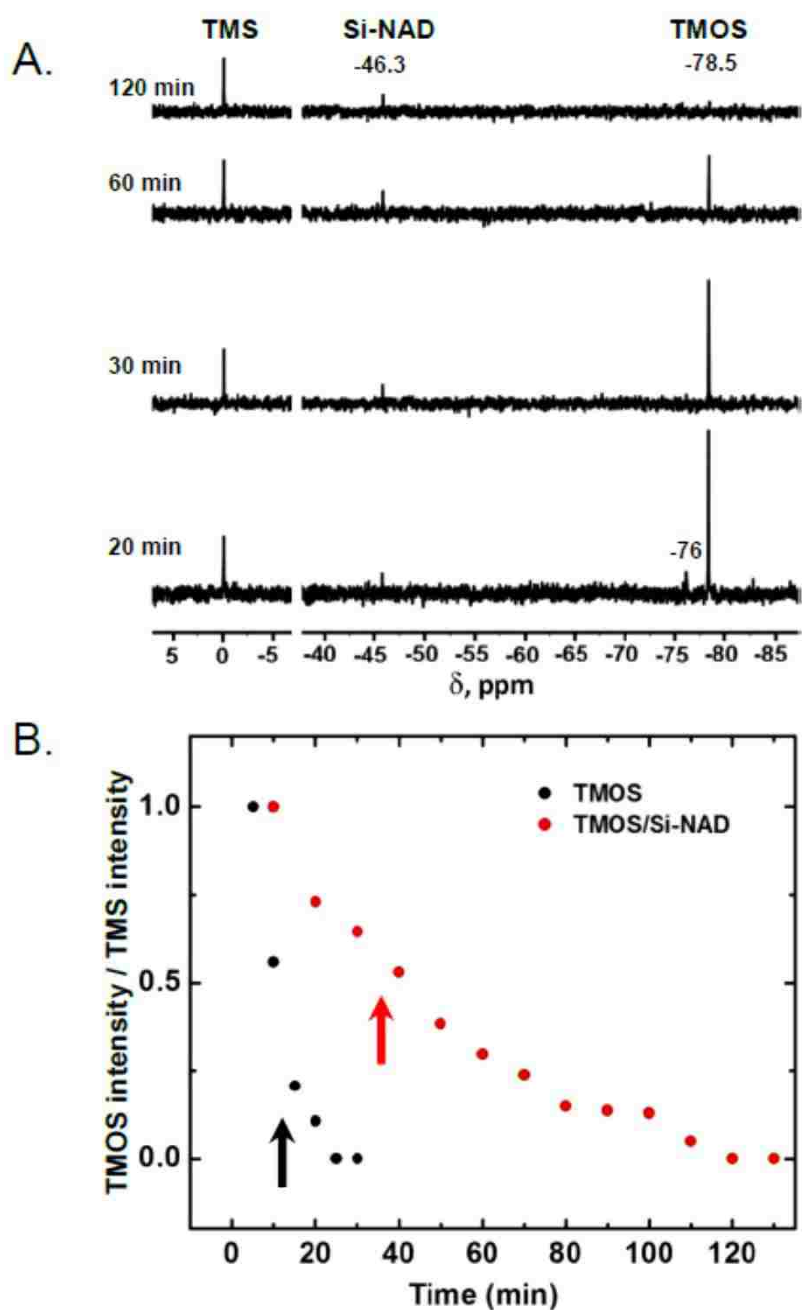
Figure 2. A. Liquid ^{29}Si NMR of a **Si-NAD**/TMOS sol (using 40 mL catalyst – see Experimental) as a function of time from mixing. (Solution stops flowing at ~25 min from mixing; formal gelation point by rheology at 36.25 min.) B. Comparative loss of TMOS signal (-78.5 ppm) in a TMOS versus a **Si-NAD**/TMOS sol at the same catalyst concentration. Arrows mark respective gelation points.
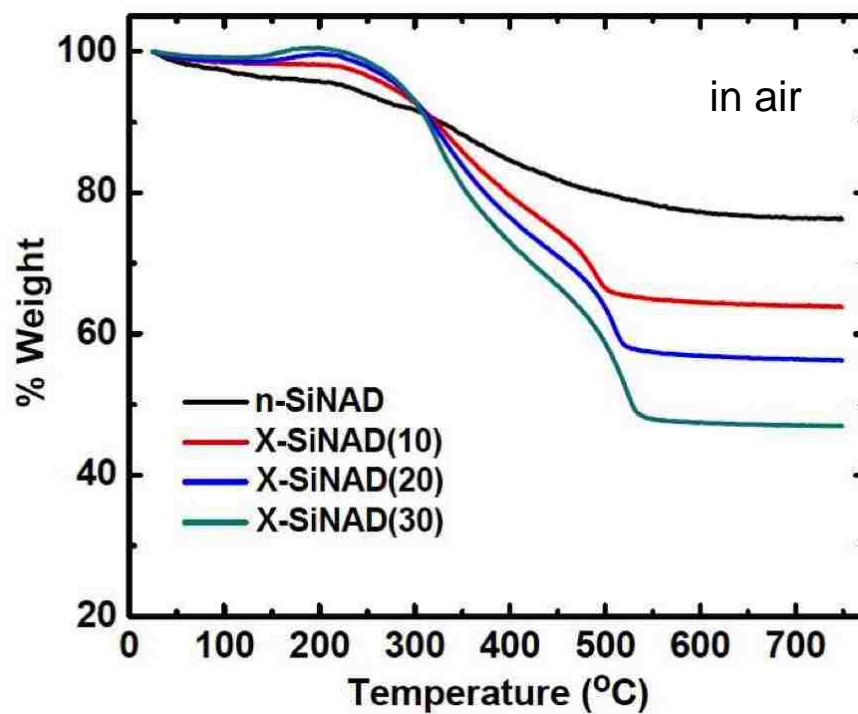
Figure 3. Thermogravimetric analysis (TGA) in air of samples as shown. The increase in mass at ~200 $^{\circ}$C is attributed to the initial epoxidation of backbone double bonds.
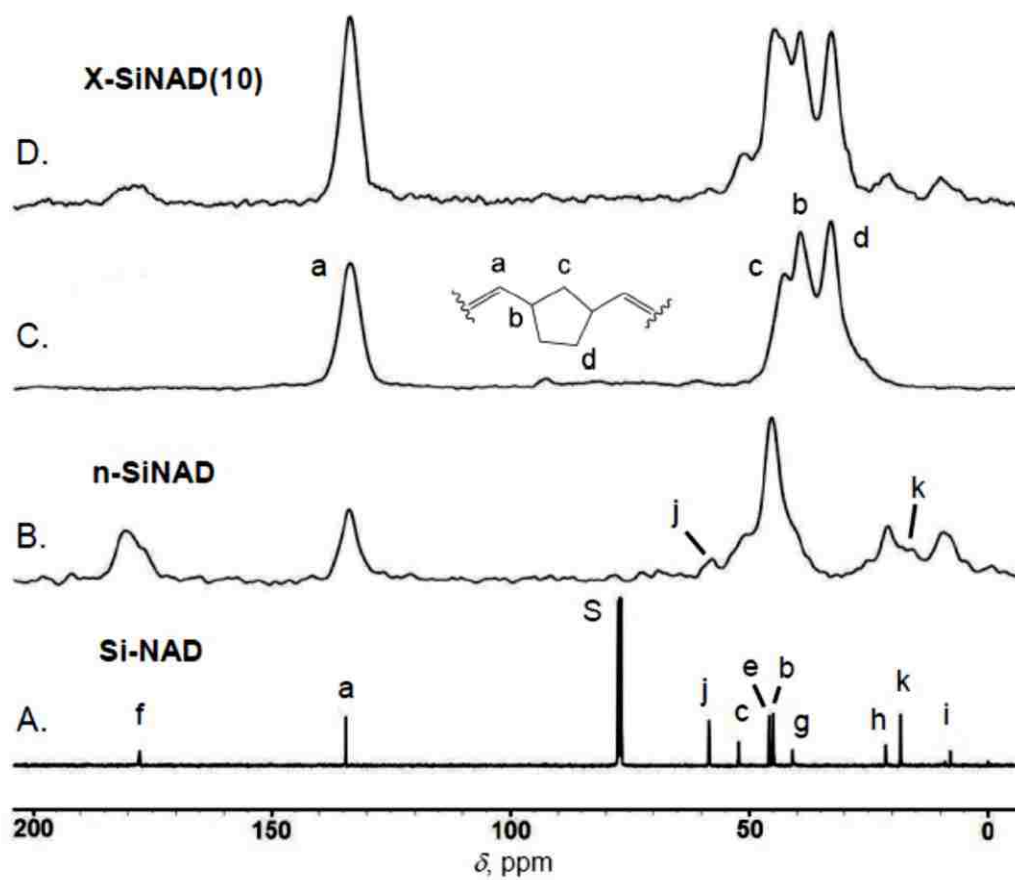
Figure 4. ^{13}C CPMAS NMR of solids samples, in comparison to the liquid ^{13}C NMR of **Si-NAD** (CDCl$_3$). Polynorbornene (frame C) was isolated from the crosslinking bath. For peak assignments, see structures in text.
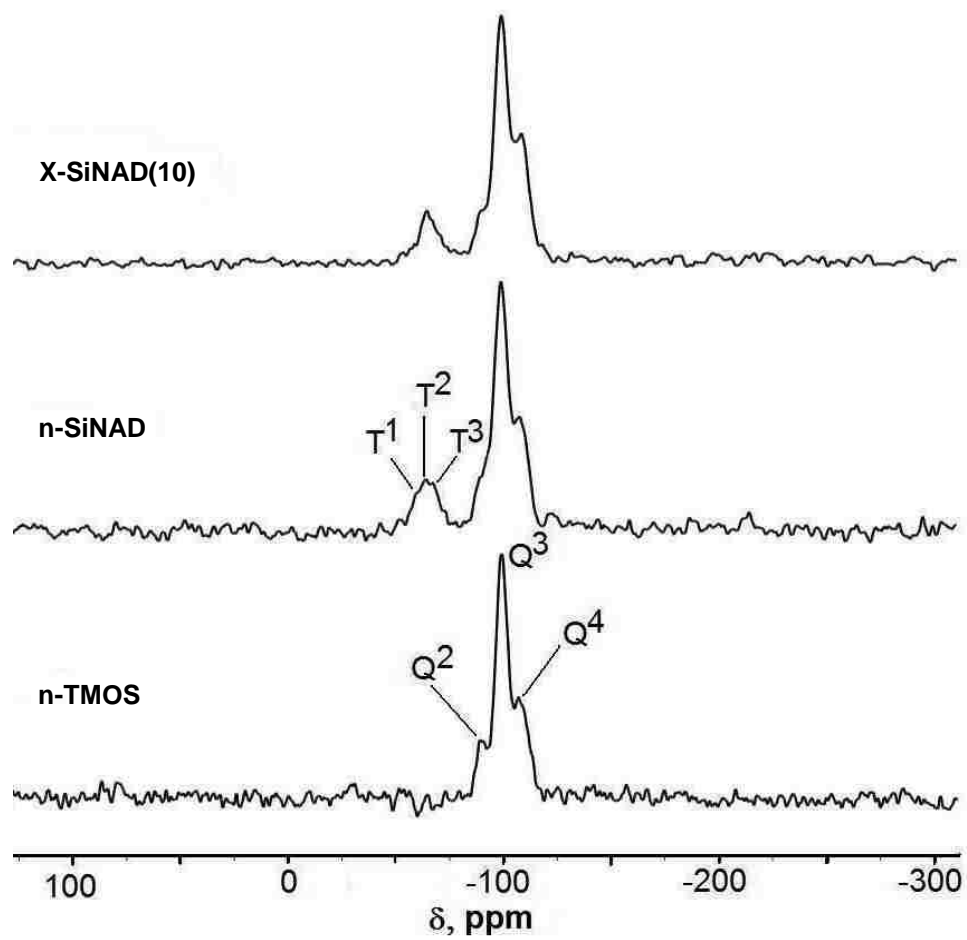
Figure 5. Solid ^{29}Si CPMAS NMR data.
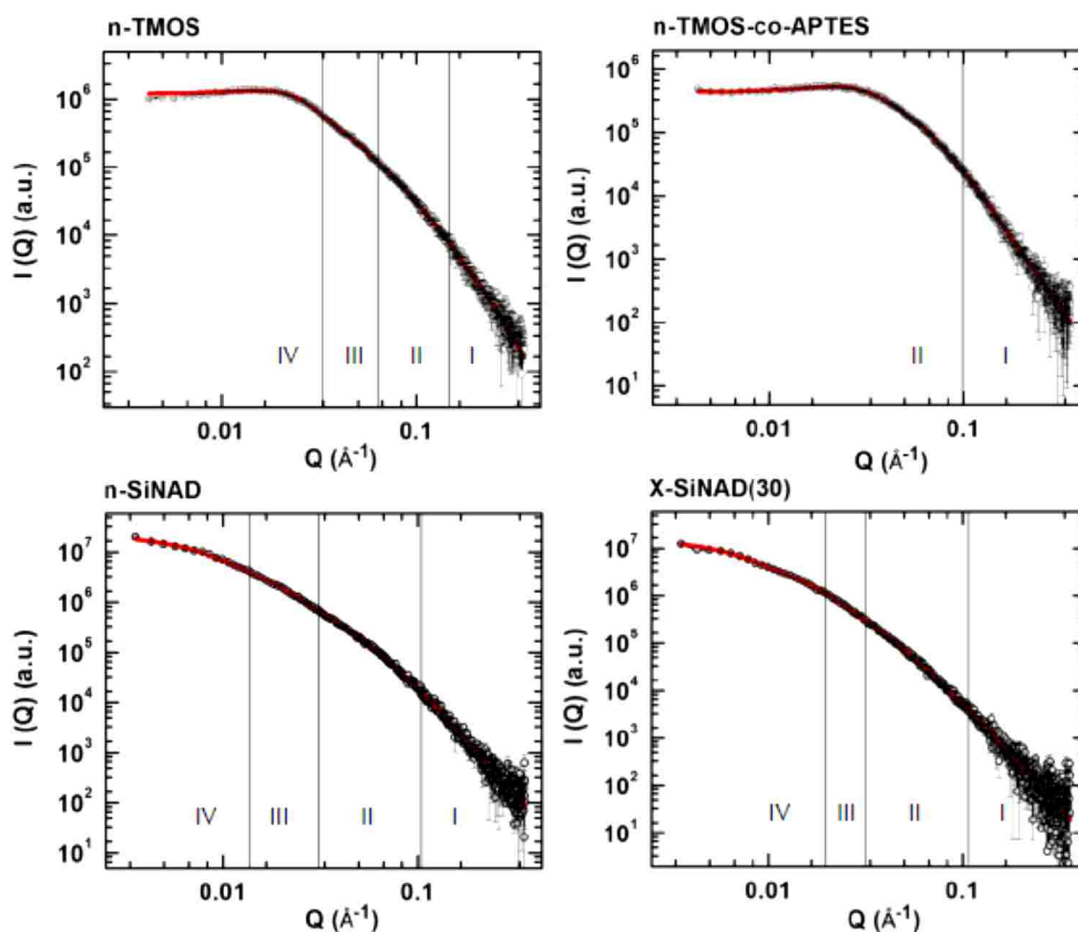
Figure 6. Small angle X-ray scattering (SAXS) data for aerogel samples. (Data are summarized in Table 2; for additional sample information, refer to Table 4.) Primary particle radii were extracted from Guinier Region II. Secondary particle radii from Region IV. Fractal dimensions of secondary particles from Region III. Fitting power-law Region I to modified Porod's law (eq 4) yielded the surface layer thickness of primary particles. **n-TMOS-co-APTES** did not yield information beyond the radius of primary particles (Region II) in the *Q*-range available.
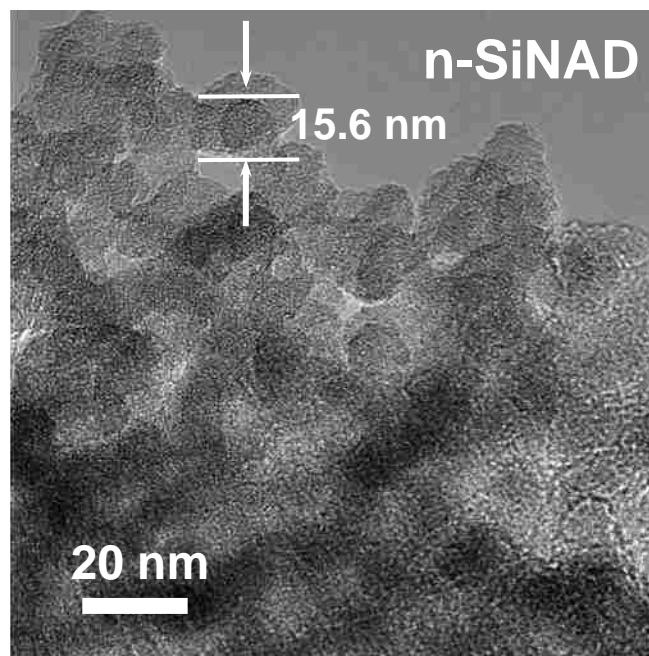
Figure 7. Transmission electron micrograph (TEM) of **n-SiNAD**. The primary particle diameter (15.6 nm) matches with that found using SAXS (15.4 nm – see Figure 6 and Table 2). For TEM of the **X-SiNAD(xx)** samples see Figure S.4 in Supporting Information.
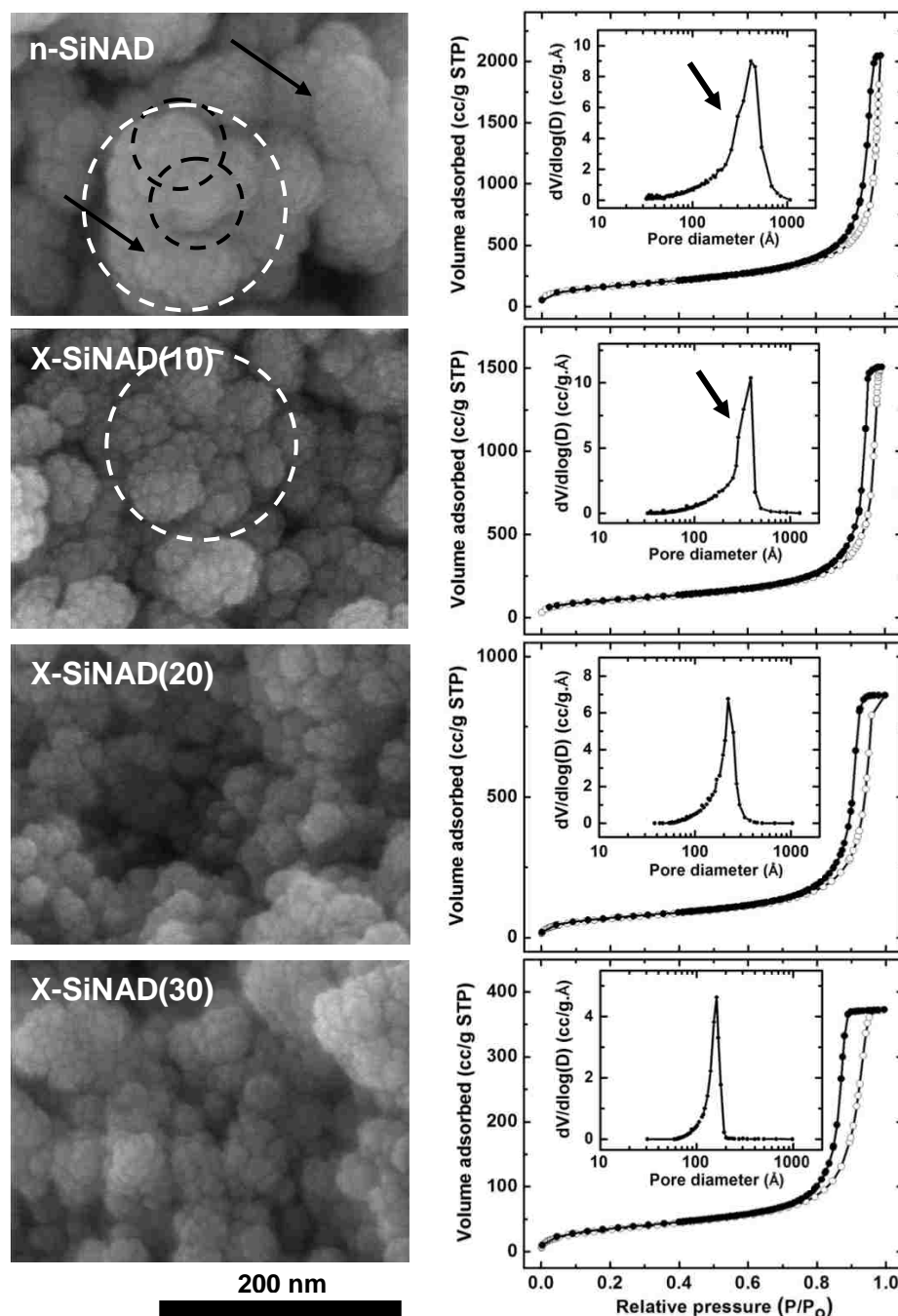
Figure 8: Scanning electron microscopy (SEM), N_2-sorption isotherms, and BJH plots (insets). Pertinent data, including bulk and skeletal densities, porosities, pore sizes, and pore size distributions are summarized in Table 4. In SEM, primary particles, as identified by both SAXS/SANS and TEM, are indicated with arrows. Dashed dark circles delineate secondary particles, as identified by SAXS/SANS. Dashed white circles delineate aggregates of secondary particles forming the network, as suggested by rheology. In BJH plots, arrows point at the low pore size shoulder that decreases in size, eventually disappearing as polymer uptake increases.
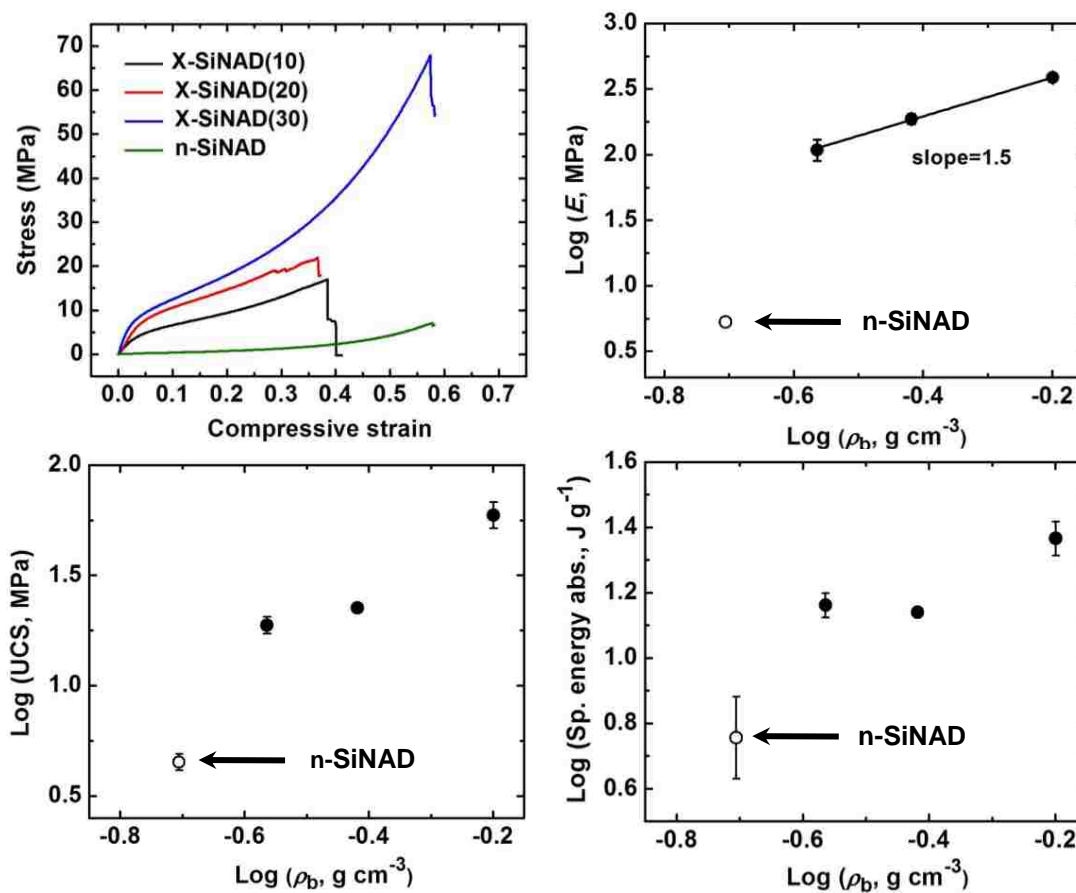
Figure 9. Mechanical characterization data under quasi-static compression (strain rate: 0.005 s^{-1}). In the Log-Log plots of Young's modulus (*E*), ultimate compressive strength (UCS) and specific energy absorption versus density, open circles show the corresponding property of the **n-SiNAD** network and dark circles those of the **X-SiNAD(xx)** samples. Results are summarized in Table 3.
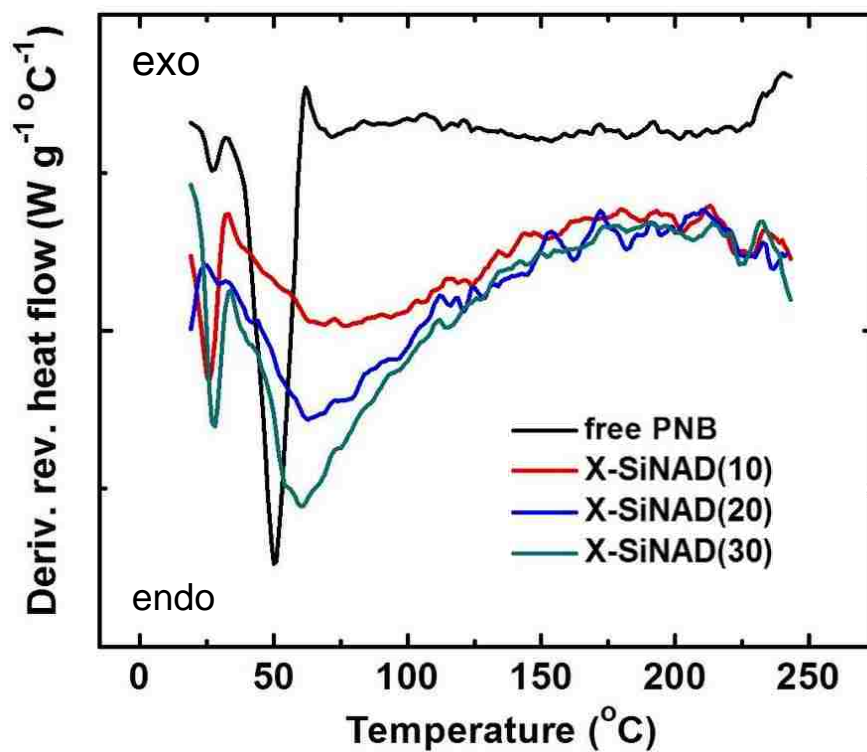
Figure 10. Modulated differential scanning calorimetry (MDSC) data under N_2 at 10 ^{o}C min^{-1}. (For additional parameters, see Experimental section.)
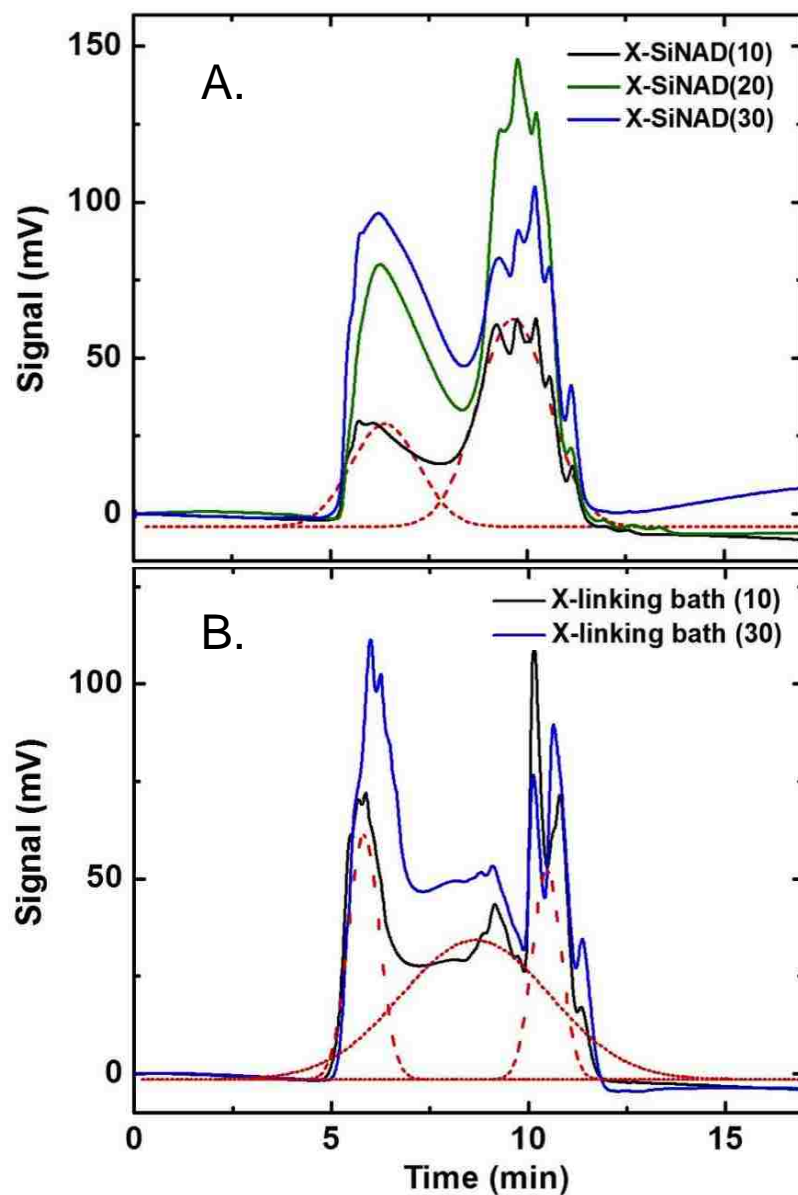
Figure 11. Gel permeation chromatographic (GPC) analysis of polymer extracted from crosslinked samples (A), and of polymer formed and isolated from two crosslinking baths, as indicated (B). For details, refer to the Experimental section. Eluted peaks are segregated into a low and a high retention time cluster, which are fitted to Gaussian profiles, as indicated by the dashed curves. Complete data analysis is available in Table S.1 of Supporting Information.

7. Supporting Information
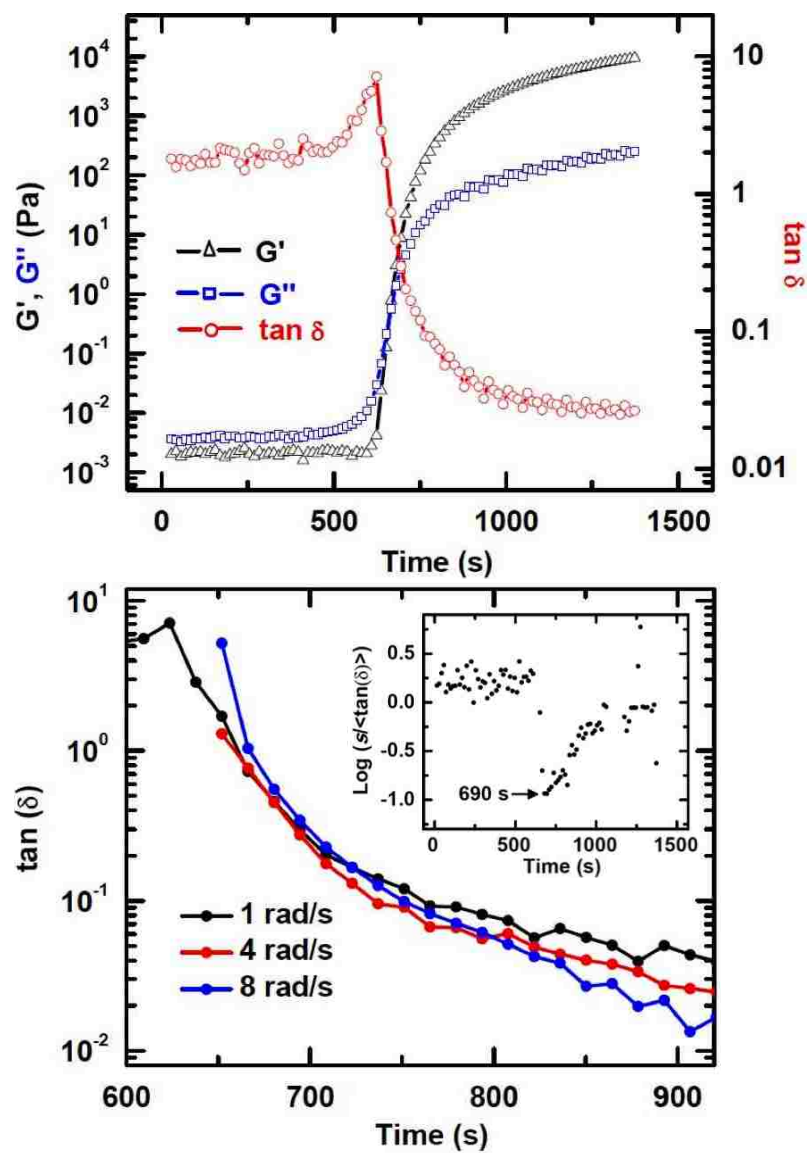
Figure S.1. Rheology during the base-catalyzed (NH_4OH, 40 μL) gelation of TMOS at 20 ^{o}C, according to the procedure described in the Experimental section.
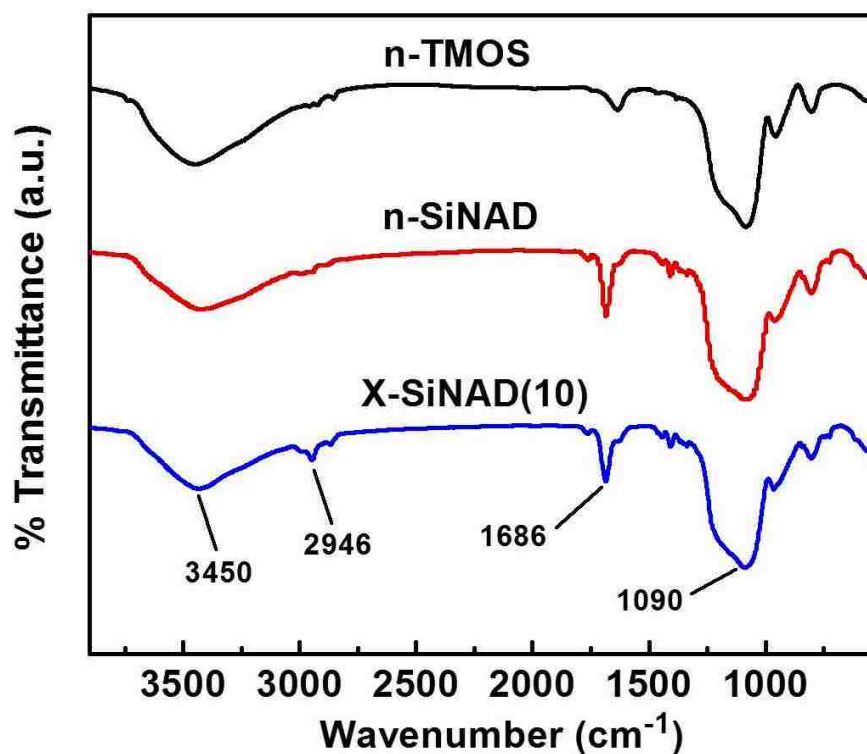
Figure S.2 Representative IR data (in KCl) of selected aerogel samples. All IR spectra are dominated by the characteristic Si-O stretch of silica at 1090 cm^{-1} and the broad absorption of remaining unreacted surface –OH groups in the 3500 cm^{-1} region. The absorption at 1686 cm^{-1} is assigned to the imide C=O stretch of **Si-NAD**, while the absorption bands in the 2870-2960 cm^{-1} range are due to C-H stretches from both **Si-NAD** and polynorbornene.
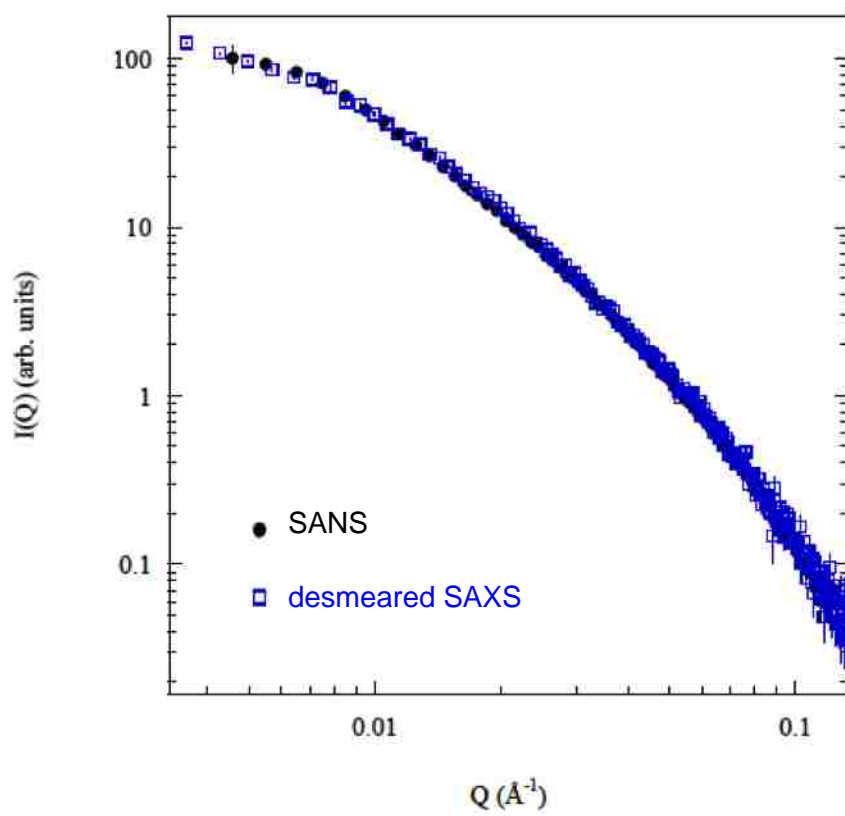
Figure S.3 Overlaid SAXS and SANS data for **n-SiNAD**.
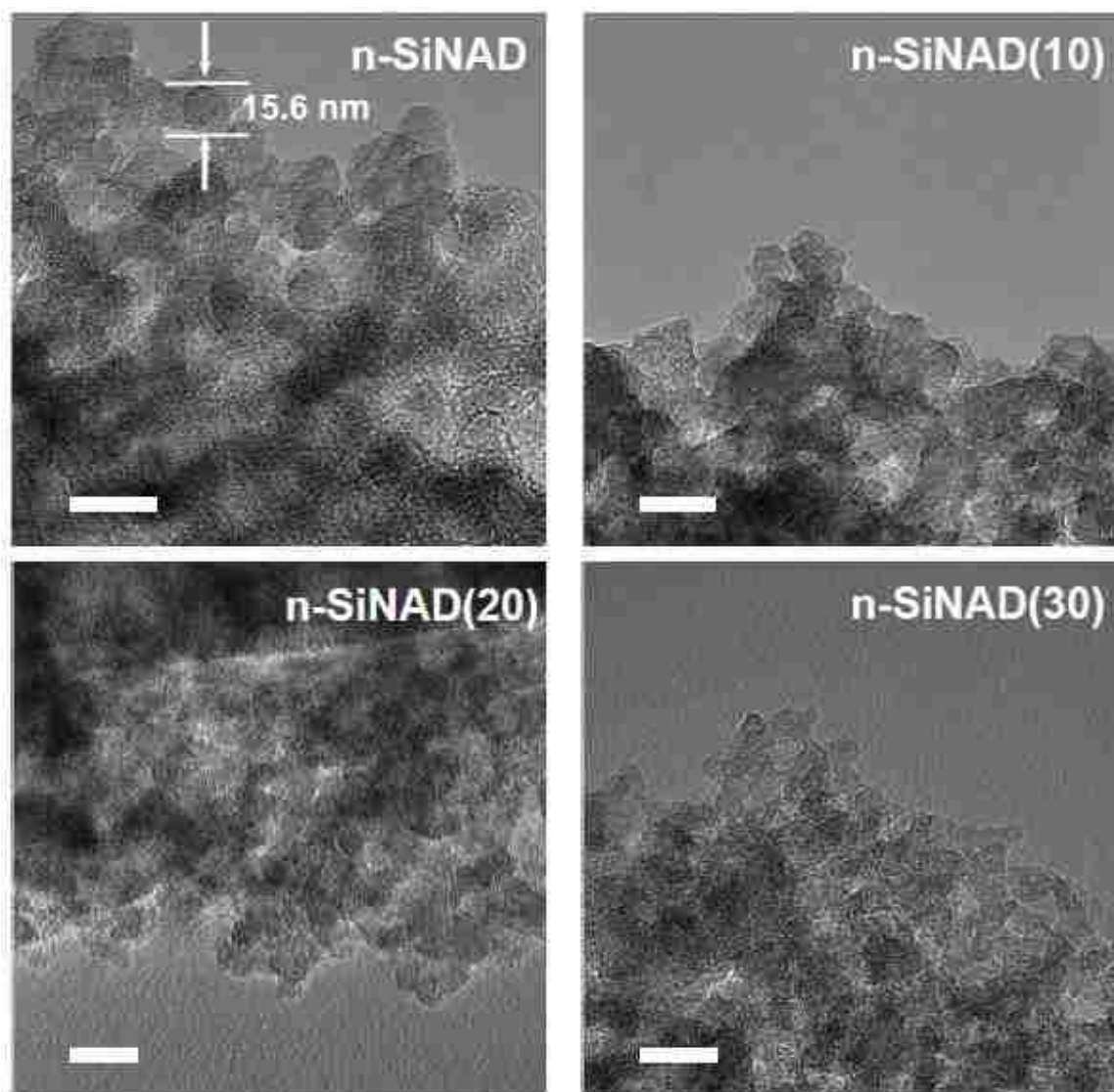
Figure S.4 Transmission electron microscopy (TEM) data for the three **X-SiNAD(xx)** samples in comparison to **n-SiNAD**, as the latter is shown in Figure 7 of the main article. Images of the **X-SiNAD(xx)** samples are blurred due to the small Z-attenuation difference between silica and polymer, and are not conclusive in terms of particles and sizes. All scale bars at 20 nm.

Table S.1. GPC analysis of **X-SiNAD** samples as well as their crosslinking baths[a]

	R_{time}[b] (min)	area[c] %	M_n	M_w	M_w/M_n[d]	N[e]	R_{g_S}[f] (nm)	R_{g_theta}[g] (nm)
X-SiNAD(10)	6.40	32.0	25209	47467	1.88	505	8.29	4.45
	9.65	68.0	457	1033	2.26	11	0.83	0.66
X-SiNAD(20)	6.70	41.2	16583	35661	2.15	379	6.98	3.85
	9.80	58.8	438	763	1.74	8	0.70	0.56
X-SiNAD(30)	6.60	50.2	18064	41244	2.28	439	7.62	4.15
	9.75	49.8	380	961	2.53	10	0.79	0.63
X-link_bath(10)	5.80	23.9	61258	73989	1.20	784	10.80	5.54
	8.4	49.5	1024	10492	10.25	112	3.36	2.10
	10.5	26.6	229	293	1.28	3	0.38	0.34
X-link_bath(30)	6.10	28.3	43780	55839	1.28	594	9.14	4.83
	8.35	52.6	1230	8985	7.30	96	3.06	1.94
	10.7	19.1	176	226	1.28	2.4	0.33	0.31

a. Using a Shodex GPC KH-803L column connected to a Schimadzu liquid chromatograph (LC-10AD) equipped with a UV-Vis detector (SPD-10AV). HPLC grade THF was used as eluent at 1 mL min^{-1}. Linear polystyrene standards from Varian (Polystyrene Low EasiVials; Part No. PL2010-0400 and PL2010-0403) were used for calibration.

b. Retention time

c. Area under groups of peaks as shown in Figure 10 of the main article

d. Polydispersity

e. Number of monomer units $= M_w/M_{w,monomer}$ ($M_{W,monomer}=94$)

f. R_{g_S}: radius of gyration in good swelling solvents (via eq. 6 of the main article)

g. R_{g_theta}: radius of gyration in theta solvents (via eq. 7 of the main article)

Appendix I. Calculation of the fraction of empty space in secondary particles from SAXS data (radii of the primary and secondary particles and the mass fractal dimension)

The number of spherical primary particles, $n(r)$, of radius r_o in a larger sphere (e.g., a secondary particle) of radius r is given by:

$$n(r) = \zeta \left[\frac{r}{r_o} \right]^{D_f}, \text{ where}$$

ζ: packing factor, indicating how primary particles are packed. For Euclidian space and cubic or hexagonal close-packing, $\zeta = \pi/3\sqrt{2} = 0.7405$ [S.1].

Also,

$$\text{volume of secondary particle } = \frac{4}{3}\pi r^3$$

$$\text{volume of primary particles } = \frac{4}{3}\pi r_o^3$$

therefore,

volume of empty space in secondary particles =

$$= \frac{4}{3}\pi r^3 - n(r)\frac{4}{3}\pi r_o^3 = \frac{4}{3}\pi \left[r^3 - \zeta \left(\frac{r}{r_o} \right)^{D_f} r_o^3 \right] = \frac{4}{3}\pi r_o^3 \left[\left(\frac{r}{r_o} \right)^3 - \zeta \left(\frac{r}{r_o} \right)^{D_f} \right] = \frac{4}{3}\pi r^3 \left[1 - \zeta \left(\frac{r}{r_o} \right)^{D_f - 3} \right]$$

or,

$$\text{volume of empty space in secondary particles} = \frac{4}{3}\pi r^3 \left[1 - \zeta \left(\frac{r}{r_o} \right)^{D_f - 3} \right]$$

For $D_f=3$, this formula reproduces the volume fraction of empty space in close-packed spheres, that is (1-ζ)≈0.26

For native **n-SiNAD** from SAXS (Table 2 in the main article):

$r_o = 7.71$ nm (primary particles)

$r = 28.7$ nm (secondary particles)

$D_f=2.07$

Therefore, volume of empty space in secondary particles = 78 %

[S.1] Lee, D. G.; Bonner, J. S.; Garton, L. S.; Ernest, A. N. S.; Autenrieth, R. L. *Wat. Res.* **2000**, *34*, 1987-2000.

Appendix II. Calculation of the polymer content in the X-SiNAD(xx) samples

Table S.2 TGA data for the native and crosslinked aerogel samples

Sample	% wt loss from TGA in air	% residue from TGA in air	% polymer
n-SiNAD	24	76	N/A
X-SiNAD(10)	36	64	16
X-SiNAD(20)	44	56	26
X-SiNAD(30)	53	47	38

Consider 1 g of any **X-SiNAD(xx)** sample. It has two components, silica and organic.

Therefore:

1 g of **X-SiNAD** = Mass (Silica) + Mass(Organic Component)

In turn, the Organic Component has also two contributing components: (a) from the native skeletal framework (due to the **Si-NAD** moieties); and, (b) from the accumulated polymer (polynorbornene). Therefore:

1 g of **X-SiNAD** = Mass(Silica) + Mass(Organic from native network) + Mass(Polymer)

Always,

Mass(Silica) = TGA residue

Also,

Mass(Organic from native network)/Mass(Silica) = 0.24/0.76 (from the TGA analysis of the native **n-SiNAD**)

Or,

Mass(Organic from native network) = (0.24/0.76) × (TGA residue)

Therefore,

1 g of **X-SiNAD** = (TGA residue) + (0.24/0.76) × (TGA residue) + Mass(Polymer)

For **X-SiNAD(10)** for example:

From TGA in air, TGA residue = 0.64 g, therefore Mass(Polymer) = 0.16 g

Similarly for **X-SiNAD(20)** and **X-SiNAD(30)**.

Appendix III. Calculation of the thickness of a polymer shell from experimental skeletal density data
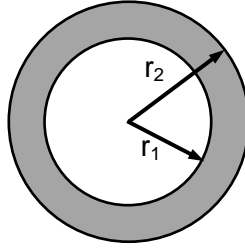
Volume of core $= \dfrac{4}{3}\pi r_1^3$

Volume of shell $= \dfrac{4}{3}\pi\left(r_2^3 - r_1^3\right)$

$Mass_{Total} = Mass_{core} + Mass_{shell} = \dfrac{4}{3}\pi r_1^3 \rho_{core} + \dfrac{4}{3}\pi\left(r_2^3 - r_1^3\right)\rho_{shell}$

Density of the entire assembly =

$= \dfrac{Mass_{Total}}{Volume_{Total}} = \dfrac{\dfrac{4}{3}\pi\left[r_1^3\rho_{core} + (r_2^3 - r_1^3)\rho_{shell}\right]}{\dfrac{4}{3}\pi r_2^3} = \left(\dfrac{r_1}{r_2}\right)^3 \rho_{core} + \left[1 - \left(\dfrac{r_1}{r_2}\right)^3\right]\rho_{shell}$

whereas here,

Density of the entire assembly = ρ_s (experimental skeletal density for each **X-SiNAD**(xx))

$\rho_{core} = \rho_{silica}$ skeletal density of the native **n-SiNAD** aerogels, measured at 1.811 g cm^{-3})

$\rho_{shell} = \rho_{polymer}$ (density of polynorbornene, measured by He pycnometry at 1.129 g cm^{-3})

Now, let $\dfrac{r_1}{r_2} = x$

Then, $\rho_s = \rho_{silica}x^3 + (1 - x^3)\rho_{polymer}$, hence $x = \dfrac{r_1}{r_2} = \sqrt[3]{\dfrac{\rho_s - \rho_{polymer}}{\rho_{silica} - \rho_{polymer}}}$

For **X-SiNAD(10)**

$\rho_s = 1.609$ g cm^{-3} (Table 4 in main article), therefore $\dfrac{r_1}{r_2} = 0.89 \Rightarrow r_2 = \dfrac{r_1}{0.89}$

Since the radius of the primary particle r_1=7.71 nm (by SAXS, Table 2 in main article), then $r_{core\text{-}shell\_particle}$=8.7 nm (found by SAXS 7.7±0.1 nm, with a surface density-gradient layer thickness of 0.6 nm)

For **X-SiNAD(20)**

ρ_s = 1.505 g cm^{-3} (Table 4 in main article), therefore $\dfrac{r_1}{r_2} = 0.82 \Rightarrow r_2 = \dfrac{r_1}{0.82}$

Since the radius of the primary particle r_1=7.71 nm (by SAXS, Table 2 in main article), then $r_{core\text{-}shell\_particle}$=9.4 nm (found by SAXS 8.2±0.3 nm, with a surface density-gradient layer thickness of 0.7 nm)

And, for **X-SiNAD(30)**

ρ_s = 1.391 g cm^{-3} (Table 4 in main article), therefore $\dfrac{r_1}{r_2} = 0.73 \Rightarrow r_2 = \dfrac{r_1}{0.73}$

Since the radius of the primary particle r_1=7.71 nm (by SAXS, Table 2 in main article), then $r_{core\text{-}shell\_particle}$=10.6 nm (found by SAXS 9.4±0.1 nm, with a surface density-gradient layer thickness of 0.63 nm)

II. Polyimide Aerogels by Ring Opening Metathesis Polymerization (ROMP)

Nicholas Leventis[*,a], Chariklia Sotiriou-Leventis[*,a], Dhairyashil P. Mohite[a], Zachary J. Larimore[b], Joseph T. Mang[*,c], Gitogo Churu[d] and Hongbing Lu[*,d]

a. *Department of Chemistry, Missouri University of Science and Technology, Rolla, MO 65409, U.S.A.*

b. *Department of Mechanical Engineering, Missouri University of Science and Technology, Rolla, MO 65409, U.S.A.*

c. *Los Alamos National Laboratory, Los Alamos, NM 87545, U.S.A.*

d. *Department of Mechanical Engineering, The University of Texas at Dallas, Richardson, TX 75080, U.S.A.*

Abstract: Polyimide aerogel monoliths are prepared by ring opening metathesis polymerization (ROMP) of a norbornene end-capped diimide, **bis-NAD**, obtained as the condensation product of nadic anhydride with 4,4´-methylenedianiline. The density of the material was varied in the 0.13-0.66 g cm^{-3} range by varying the concentration of **bis-NAD** in the sol. Wet-gels experience significant shrinkage relative to their molds (28-39% in linear dimensions), but the final aerogels retain high porosities (50-90% v/v), high surface areas (210-632 m^2 g^{-1}, of which up to 25% is traced to micropores) and pore size distributions in the mesoporous range (20-33 nm). The skeletal framework consists of 16-17 nm in diameter primary particles assembling to 60-85 nm in diameter secondary aggregates (by SANS and SEM). At lower densities (e.g., 0.26 g cm^{-3}) secondary particles are mass fractals (D_m=2.34±0.03) turning to closed-packed surface fractal objects (D_S=3.0) as the bulk density increases ($\geq$0.34 g cm^{-3}), suggesting a change in the network forming mechanism from diffusion-limited aggregation of primary particles to a space-filling bond percolation model. The new materials combine facile one-step synthesis with heat resistance up to 200 ^{o}C, high mechanical compressive strength and

specific energy absorption (168 MPa and 50 J g^{-1}, respectively, at 0.39 g cm^{-3} and 88% ultimate strain), low speed of sound (351 m s^{-1} at 0.39 g cm^{-3}) and Styrofoam-like thermal conductivity (0.031 W m^{-1} K^{-1} at 0.34 g cm^{-3} and 25 $^{\circ}$C), hence they are reasonable multifunctional candidate materials for further exploration as thermal/acoustic insulation at elevated temperatures.

1. Introduction

Aerogels are low-density nanoporous solids with high surface area, low thermal conductivity and high acoustic attenuation.[1,2] They are prepared by converting and removing the pore-filling solvents of suitable wet-gels as supercritical fluids (SCF).[3,4] Inorganic aerogels are mostly based on silica and have been studied more extensively. They are fragile materials and confirmed applications have been only in specialized environments, for example as thermal insulators aboard planetary vehicles and as Cherenkov radiation detectors in certain nuclear reactors. Other oxide aerogels are evaluated as energetic materials, or starting materials for porous metals and ceramics.[5,6,7]

On the other hand, organic aerogels were first reported together with the inorganic counterparts,[3,4] however, early emphasis on the latter delayed their systematic investigation for almost 60 years, till R. Pekala reported the bottom-up synthesis a phenolic resin-type aerogels by condensation of resorcinol with formaldehyde (RF).[8] Subsequently, several other types of bottom-up polymer aerogels were reported, first by variation of the phenolic resin chemistry (phenol-furfural,[9] cresol-formaldehyde,[10] melamine-formaldehyde[11]), and then based on polyurethane,[12] polyurea,[13] and more recently on polybenzoxazine,[14] poly(bicyclopentadiene) synthesized via ring opening

metathesis polymerization (ROMP) of the monomer,[15] and polyimides.[16,17] Several other types of aerogels based on soluble polymers such as polystyrene,[18] polyacrylonitrile[19] and cellulose[20] are prepared by inducing phase-separation of preformed polymers. The accelerated interest in organic aerogels is driven by the facile tailoring of their properties by choosing the polymer, the straightforwardness of the polymerization process that facilitates synthesis, and the fact that inorganic aerogels whose skeletal framework has been coated conformally and crosslinked covalently with polymers demonstrate dramatically increased mechanical strength rendering this class of materials suitable for applications inconceivable for aerogels before, as for example in ballistic protection (armor).[21] Since the mechanical properties of the latter materials are dominated by the polymer, purely polymeric aerogels with the structure and interparticle connectivity of polymer-crosslinked aerogels should have similar mechanical properties.

In that context, interest in polyimide aerogels stems from the high mechanical strength and high thermal stability of the polymer[22] that would render this class of aerogels suitable for high temperature thermal and acoustic insulation. In general, there are two classic routes to consider for polyimide aerogel synthesis: the first (DuPont process) yields linear polyimides and involves reaction of dianhydrides with diamines,[23] while the second one, referred to as the PMR-route (PMR: polymerization of monomeric reactants) yields thermoset resins and involves synthesis and polymerization of norbornene-capped imide oligomers.[24] The DuPont route proceeds through a linear polyamic acid that is dehydrated to the imide either chemically (e.g., with sacrificial reagents like acetic anhydride/pyridine), or thermally at high temperatures. The PMR

route has been strictly a high-temperature process involving crosslinking of the norbornene end-caps.

The first polyimide aerogels were prepared via the DuPont process using both chemical dehydration and high temperature treatment to complete imidization.[16,17,25] Those conditions compound the inherent economic disadvantage of supercritical fluids in the aerogel synthesis. In that regard, recently we introduced an alternative route whereas polyimide aerogels can be obtained at room temperature via reaction of dianhydrides with diisocyanates; thus, aerogels prepared from pyromellitic dianhydride and 4,4´-methylenedianiline are chemically identical to those prepared from the same anhydride and methylene diphenyl-*p*-diisocyanate.[26] Here we introduce a second low-temperature process to polyimide aerogels via the PMR-route whereas the norbornene end caps of a suitable bisnadimide, **bis-NAD**, are polymerized via ROMP using the second generation Grubbs' catalysts **GC-II**.[27] Evidently, **bis-NAD**-derived polyimide aerogels are extremely robust multifunctional materials, combining Styrofoam-like thermal conductivity and mechanical properties comparable to those of polymer-crosslinked silica aerogels.[21]
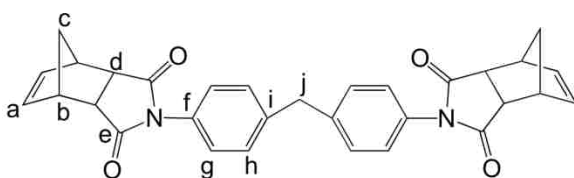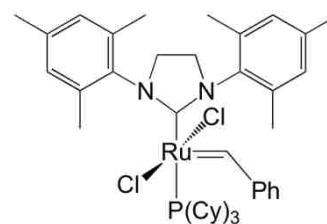
bis-NAD   **GC-II**

2. Experimental

2.1. Materials. All reagents and solvents were used as received unless noted otherwise. Dicyclopentadiene (DCPD), 2nd generation Grubbs' catalyst, **GC-II**, and anhydrous *N*-methyl-2-pyrrolidone (NMP) were purchased from Aldrich Chemical Co. Maleic anhydride, 4,4´-methylenedianiline (MDA), and 1,4-dioxane were purchased from Acros Organics. Methanol and laboratory grade NMP were purchased from Fisher.

2.2. Synthesis of bis-NAD. Bis-NAD [IUPAC name: 2,2'-(methylenebis(4,1-phenylene))bis(3a,4,7,7a-tetrahydro-1*H*-4,7-methanoisoindole-1,3(2*H*)-dione)] was prepared from nadic anhydride and MDA by a modification of literature procedures.[28] In turn, nadic anhydride was prepared via a Diels-Alder reaction of fresh cyclopentadiene with maleic anhydride. Cyclopentadiene was prepared via a reverse Diels-Alder reaction by refluxing DCPD at 180 ^{o}C. Cyclopentadiene was collected in an ice-cooled receiver and used for further reaction with maleic anhydride. The latter (4.00 g, 0.0408 mol) was first dissolved in ethyl acetate (15.0 mL) at room temperature under magnetic stirring. The solution was cooled for 15 minutes in an ice-bath, and freshly prepared cyclopentadiene (4.0 mL) was added in the solution. The reaction mixture was stirred for another 20 minutes and 15.0 mL of hexane was added to complete precipitation of the crude product. The precipitate was separated by vacuum filtration and purified by recrystallization from ethyl acetate/hexane. Subsequently, nadic anhydride (1.656 g, 0.0101 mol) was dissolved in anhydrous NMP (15.0 mL) at room temperature under magnetic stirring. MDA (1.000 g, 0.005 mol) was added and the reaction mixture was stirred at room temperature for 24 h under N_2. At the end of the period, acetic anhydride (6.180 g, 0.0606 mol) and pyridine (1.0 mL) were added and the reaction mixture was

heated at 100 ^{o}C for 6 h. The mixture was allowed to cool at room temperature, and the precipitate was washed with methanol followed by drying under vacuum at 70 ^{o}C for 24 h: yield 2.0 g (75%); mp 243-245 °C (lit.[28a] mp 244 °C for the *endo,endo-* isomer) ^{1}H NMR (400 MHz, CDCl$_3$) δ 7.22 (d, J = 8.4 Hz, 4H), 7.05 (d, J = 8.4, 4H), 6.24 (t, J = 1.8, 4H), 3.98 (s, 2H), 3.49 (m, 4H), 3.41 (dd, J = 1.5 Hz, J=2.9 Hz, 4H), 1.75 (dt, J = 1.6 Hz, J=8.8 Hz, 2H), 1.58 (dt, J = 1.6 Hz, J=8.8 Hz, 2H); ^{13}C NMR (100 MHz, CDCl$_3$) δ 176.78, 140.76, 134.49, 129.88, 129.56, 126.56, 52.13, 45.66, 45.38, 41.01; IR (KBr) 2990, 1770, 1710, 1510, 1380, 1180, 840, 745, 620 cm^{-1}. Elemental Analysis, (CHN % w/w). Found: C: 75.47; H: 5.04; N: 5.71. Theoretical: C: 75.92; H: 5.31; N: 5.71.

2.3. Synthesis of polyimide aerogels from bis-NAD via ROMP. Polyimide aerogels were prepared by mixing two solutions, one containing **bis-NAD** in NMP and one with moisture-tolerant Grubbs' catalyst **GC-II** in toluene. Different sets of samples with different bulk densities were obtained by varying the concentration of **bis-NAD**. Aerogel samples are abbreviated as **bis-NAD-xx**, where the extension -**xx** stands for the weight percent of **bis-NAD** in the **bis-NAD** plus NMP mixture. All formulations are summarized in Table 1. Because **bis-NAD** has limited solubility in NMP at room temperature, heating at 60 ^{o}C was required in order to make the 2.5 and 5% w/w **bis-NAD** solutions, while the 10%, 15%, and 20% w/w **bis-NAD** solutions were heated at 90 ^{o}C. **GC-II** in 50 μL toluene (see Table 1) was added to the **bis-NAD** solution and the mixture was shaken vigorously and was poured into molds (Wheaton polypropylene OmniVials, Part No. 225402, 1 cm in diameter, or 15 cm^3 Fisherbrand Class B Amber Glass Threaded Vials, 1.8 cm inner diameter, Part No. 03-339-23D; the latter molds were used for samples prepared for compression testing). All solutions gelled within 10-20

Table 1. Formulations of **bis-NAD-xx** aerogels

sample	**bis-NAD** (% w/w versus NMP)	**GC-II** (% w/w versus **bis-NAD**)	**GC-II** (% mol versus **bis-NAD**)	**bis-NAD** : **GC-II** (mol:mol)
bis-NAD-2.5	2.5	4.0	2.30	43.3
bis-NAD-5	5.0	2.0	1.15	86.6
bis-NAD-10	10.0	1.0	0.58	173.2
bis-NAD-15	15.0	0.75	0.43	231.0
bis-NAD-20	20.0	0.50	0.29	346.4

minutes except the 20% w/w **bis-NAD** sol, which gelled within 1 minute. The resulting wet gels were aged in their molds for 12 h at 90 ^{o}C, washed with NMP (4 washes, 8 h per wash), 1,4-dioxane (4 washes, 8 h per wash), acetone (4 washes, 8 h per wash) and dried in an autoclave with liquid CO_2 to yield **bis-NAD-xx** polyimide aerogels.

2.4 Methods. Drying with liquid CO_2, taken out as a supercritical fluid (SCF) was conducted in an autoclave (SPI-DRY Jumbo Supercritical Point Dryer, SPI Supplies, Inc. West Chester, PA). Bulk densities (ρ_b) were calculated from the weight and the physical dimensions of the samples. Skeletal densities (ρ_s) were determined with helium pycnometry using a Micromeritics AccuPyc II 1340 instrument. Porosities, Π, were determined from ρ_b and ρ_s via $\Pi = 100 \times [(1/\rho_b) - (1/\rho_s)] / (1/\rho_b)$. Surface areas and pore size distributions were measured by N_2 sorption porosimetry using a Micromeritics ASAP 2020 Surface Area and Porosity Analyzer. Samples for surface area and skeletal density determination were outgassed for 24 h at 80 ^{o}C under vacuum before analysis. Average pore diameters were determined by the $4 \times V_{Total}/\sigma$ method, where V_{Total} is the total pore volume per gram of sample and σ, the surface area determined by the Brunauer-Emmett-Teller (BET) method. V_{Total} can be calculated either from the single

highest volume of N_2 adsorbed along the adsorption isotherm or from the relationship

$V_{Total} = (1/\rho_b) - (1/\rho_s)$. If the two average pore diameters coincide, it is taken as proof that

the material lacks macroporosity. Liquid ^1H and ^{13}C NMR of **bis-NAD** were obtained

with a 400 MHz Varian Unity Inova NMR instrument (100 MHz carbon frequency).

Elemental analysis was conducted using a Perkin Elmer Elemental Analyzer, Model 2400

CHN. Infrared (IR) spectra were obtained in KBr pellets using a Nicolet-FTIR Model 750

Spectrometer. Solid-state ^{13}C NMR spectra were obtained with samples ground into fine

powders on a Brucker Avance 300 Spectrometer with 75.475 MHz carbon frequency

using magic angle spinning (at 7 kHz) with broadband proton suppression and the

CPMAS TOSS pulse sequence for spin sideband suppression. Thermogravimetric

analysis (TGA) was conducted under N_2 or air with a TA Instruments Model TGA Q50

thremogravimetric analyzer, using a heating rate of 10 ^0C min^{-1}. Scanning electron

microscopy (SEM) was conducted with Au-coated samples on a Hitachi S-4700 field

emission microscope. The crystallinity of the polyimide samples was determined by x-ray

diffraction (XRD) using a Scintag 2000 diffractometer with Cu K_α radiation and a

proportional counter detector equipped with a flat graphite monochromator. The identity

of the fundamental building blocks of the two materials was probed with small angle

neutron scattering (SANS) using ~2 mm thick discs cut with a diamond saw from

cylinders similar to those used for mechanical testing, on a time of flight, low-Q

diffractometer, LQD, at the Manuel Lujan Jr. Scattering Center of the Los Alamos

National Laboratory.[29] The scattering data are reported in the absolute units of

differential cross section per unit volume (cm^{-1}) as a function of Q, the momentum

transferred during a scattering event. Quasi-static mechanical testing under compression

was conducted on an Instron 4469 universal testing machine frame, following the testing procedures and specimen length (2.0 cm) to diameter (1.0 cm) ratio specified in ASTM D1621-04a (Standard Test Method for Compressive Properties of Rigid Cellular Plastics). The recorded force as a function of displacement (machine-compliance corrected) was converted into stress as a function of strain. The thermal diffusivity, R, of the **bis-NAD-xx** aerogels was measured at 23 ^{o}C with a Netzsch NanoFlash Model LFA 447 Flash diffusivity instrument using disk samples ~1 cm in diameter, 2.0-2.2 mm thick (the thickness of each sample was measured with 0.01 mm resolution and was entered as required by the data analysis software). Heat capacities at 23 ^{o}C of powders of the same samples (4-8 mg), needed for the determination of their thermal conductivity, l, were measured using a TA Instruments Differential Scanning Calorimeter Model Q2000 calibrated against a sapphire standard and run from -10 ^{o}C to 40 ^{o}C at 0.5 ^{o}C min^{-1} in the modulated T4P mode, using 60 s modulation period and 1 ^{o}C as modulation amplitude. The raw data with **bis-NAD-xx** were multiplied by the calibration factor (0.920±0.028) determined with rutile, KCl, Al, graphite, and corundum just before our experiments.

3. Results and Discussion

3.1. Synthesis and characterization of bis-NAD. The monomer, **bis-NAD**, was prepared in high yield (75%) via the DuPont route from nadic anhydride and 4,4´-methylenedianiline (MDA) via chemical dehydration of the intermediate diamic acid (Scheme 1), and was characterized by elemental analysis, IR, ^{1}H and ^{13}C NMR. The IR spectrum (Figure 1) is dominated by the imide C=O symmetric and asymmetric stretches

at 1710 cm^{-1} and 1770 cm^{-1}, respectively, and by the C-N stretch at 1380 cm^{-1}. The absorption at 1510 cm^{-1} is assigned to the C=C stretch, while the absorption at 1170 cm^{-1}

Scheme 1. Synthesis of **bis-NAD**
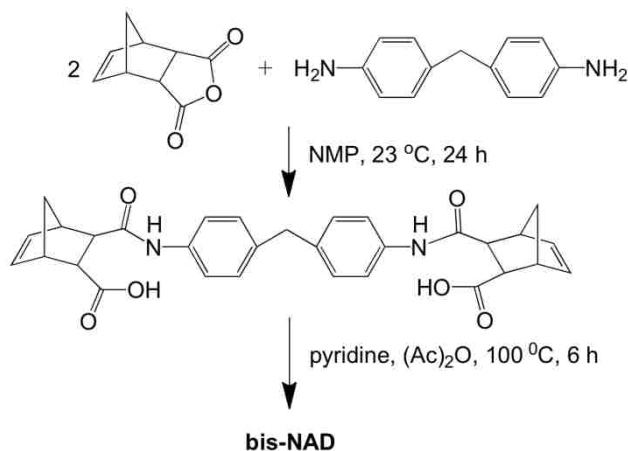
is attributed to the =C-H in-plane bending from both the nadic and aromatic rings. In ^{13}C NMR (Figure 2, peak assignment by simulation) all carbons of **bis-NAD** are resolved. No impurities are visible, consistently with the elemental analysis data (see Experimental). The resonance at 177 ppm is assigned to the imide carbonyl, the one at 134 ppm to the sp^2-carbons of the norbornene moieties and the several resonances between 125 and 145 ppm to the aromatic carbons. The peak at 41 ppm is due the –CH$_2$- group of MDA, while the peaks between 43 and 55 ppm are assigned to the aliphatic carbons of the norbornene end caps. By TGA (Figure 3A), **bis-NAD** is thermally stable up to about 220 $^{\circ}$C, undergoing a 16% mass loss between 220 $^{\circ}$C and 350 $^{\circ}$C owing to a reverse Diels-Alder reaction (loss of cyclopentadiene was confirmed by mass spectrometry). The observed mass loss corresponds to loss of one end-cap per **bis-NAD** molecule (Scheme 2), which

Scheme 2. Primary thermal decomposition mechanism of **bis-NAD**
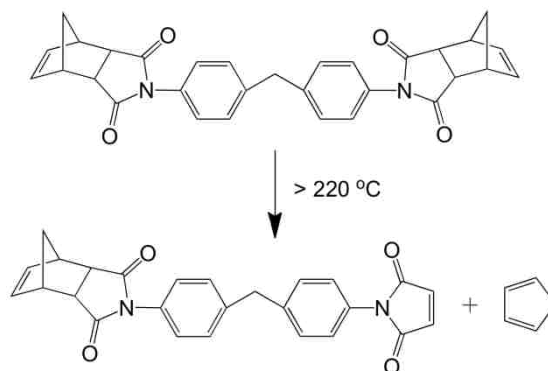
in turn may imply that the newly created maleimide reacts with the norbornene end-cap of another molecule to a more stable adduct. This matter was not investigated further, however, the TGA data of Figure 3A become important in assessing whether all norbornene end caps react during the ROMP gelation process, as discussed below.

3.2. Synthesis of bis-NAD-xx polyimide aerogels. Bis-NAD related molecules (e.g., with 4,4′-dioxyaniline bridges) have been crosslinked before thermally or with microwaves.[30] Crosslinking of **bis-NAD** itself via ROMP is summarized in Scheme 3. Monoliths with different densities were obtained by varying the monomer concentration. The amount of the **GC-II** catalyst was varied inversely to the monomer concentration in order to keep the gelation time under 20 min. Wet-gels were aged in their molds for 12 h at 90 $^\circ$C to ensure that all monomer is consumed and incorporated in the gels.[31] This was confirmed in two ways: first, by analyzing the washes for unreacted monomer, and second by the mass balance between the aerogels and the amount of **bis-NAD** used for their preparation. Nevertheless, aging has not been optimized time-wise. Wet-gels were solvent-exchanged from NMP, through 1,4-dioxane, to acetone before they were dried with liquid CO_2 taken out superscritically at the end. Right after gelation wet-gels are

yellowish-brown; they look off-white after NMP washes because of remaining traces of the catalyst, and completely white after 1,4-dioxane and acetone. Dry aerogels were opaque-white (see photograph in Scheme 3).

3.3. Characterization of bis-NAD-xx aerogels.

3.3.a. Chemical characterization. Polymerization of **bis-NAD** proceeds according to Scheme 4. ROMP does not alter the identity of the functional groups, and elemental analysis of **bis-NAD-xx** gives similar results as for the monomer

Scheme 3. Flow-chart for the preparation of polyimide aerogels from **bis-NAD**
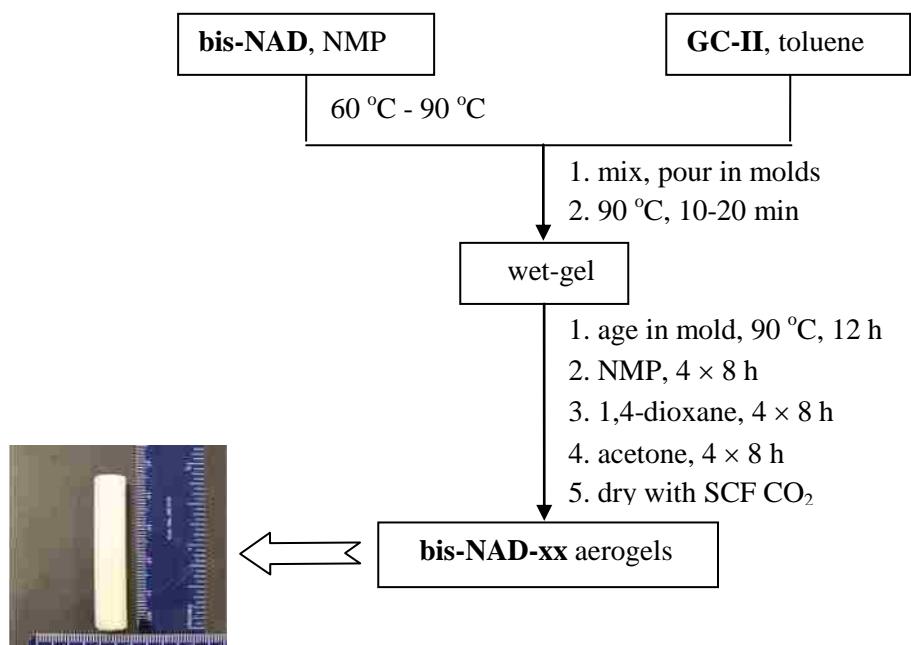
Scheme 4. Polymerization of **bis-NAD** via ROMP
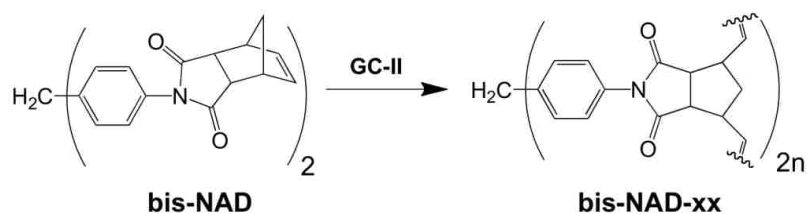
(%w/w: C, 75.47; H, 5.04; N, 5.71; versus C, 73.99; H, 5.21; N, 5.61 for the monomer). Similarly, in IR (Figure 1) the most prominent differences between **bis-NAD** and **bis-NAD-xx** are associated with the CH_2 and CH stretches that move to lower frequencies after ring-opening of the nadimide (from the 2987-2871 cm^{-1} range to the 2937-2855 cm^{-1} range), and an increase from 750 cm^{-1} to 805 cm^{-1} in the absorption frequency of the =C-H out-of-plane bending. In CPMAS ^{13}C NMR of **bis-NAD-xx**, after ring opening the alkene carbon resonance moves upfield (from 134 ppm originally), merging with the aromatic carbons. The resonance of the bridgehead carbon (labeled as "c") moves also upfield from 52 to the 30-42 ppm range, merging with the MDA methylene bridge (Figure 2). After ring opening the "b" and "d" aliphatic carbons of the norbornene ring move slightly downfield from 45.66 to 48.50 ppm and from 45.38 to 45.66 ppm, respectively. Those spectroscopic changes, however, do not warrant that all norbornene moieties have been crosslinked. TGA of **bis-NAD-xx** in N_2 (Figure 3B) shows a small initial mass loss (~3%) below 100 ^{o}C (owing to residual solvents), and a second small mass loss (~3%) in the 190-240 ^{o}C range consistent with a reverse Diels-Alder reaction of a small amount of dangling unreacted norbornene moieties according to Scheme 2. Those moieties may have become inaccessible to the catalyst in closely packed polymer. In that regard, XRD shows that all samples have a high degree of crystallinity (up to 53%, Figure 4) suggesting regular packing of the polymer chains within the fundamental building blocks of the skeletal framework. In turn, that implies early phase separation of a polymer with substantial linearity.

3.3.b. Microstructural characterization. Porosity and pore structure are reported as a function of the bulk density, ρ_b, that in turn is related to the monomer

concentration in the sol. Results are summarized in Table 2. The morphology of the pore walls (i.e., the skeletal framework) was inspected with SEM and their composition was investigated at the fundamental building block level with SANS.

Although all **bis-NAD** is incorporated in the final aerogels, ρ_b does not vary linearly with the concentration of the monomer in the sol: e.g., r_b of **bis-NAD-20** is 0.660 g cm^{-3} but that of **bis-NAD-2.5** is 0.134 g cm^{-3}, not 8× less as expected from the relative concentrations of the monomer. This is because all samples shrink in reverse order to the concentration of **bis-NAD** in the sol: **bis-NAD-2.5** samples shrink 39% relative to the molds, while **bis-NAD-20** samples shrink less (28%, Table 2). Minimal shrinking (1-3% in linear dimensions) is observed during gelation and aging (syneresis), no further shrinkage takes place during NMP and 1,4-dioxane washes, while the majority of shrinkage is observed during the final acetone washes. No shrinking is observed during SCF drying. Therefore, most probably, exhibiting typical gel-like semi-permeable membrane behavior, **bis-NAD-xx** wet-gels swell until the internal pressure created by stretching of the framework –which, therefore must be quite flexible– is balanced by the osmotic pressure of the internal "solution."[32] Thus, changing the polarity of the solvent changes the degree of swelling. Interparticle covalent bonding is more prevalent in higher-density samples, hence they stretch less, swell less and therefore shrink less.

All skeletal densities, ρ_s, fall in the 1.26-1.36 g cm^{-3} range, the variation is significant, but since there is no systematic trend with the monomer concentration, it is rather attributed to random error. Porosities, P, calculated from the ρ_b and ρ_s values, decrease from 90% to 48% as the bulk density increases (Table 2). N_2-sorption porosimetry (Figure 5) suggests that the most dense samples are strictly mesoporous.

Specifically, at lower densities ($\leq$0.34 g cm^{-3}) the N_2 absorption isotherms rise above

P/P$_o$=0.9 and do not reach a well-defined saturation plateau, indicating that a significant

portion of the porosity is due to macropores (defined as pores above 50 nm in diameter);

on the other hand, the same isotherms do show narrow hysteresis, an indication of some

mesoporosity. As the bulk density increases ($\geq$0.5 g cm^{-3}) the onset of the quick rise in

the volume of N_2 adsorbed moves to lower P/P$_o$ values (to around P/P$_o$~0.8), the

isotherms reach saturation and they show large H2-type hysteresis loops all consistent

with mostly mesoporous materials and "ink-bottle" type of pores.[33] Quantitatively,

average pore diameters calculated by the $4 \times V_{Total}/\sigma$ method using V_{Total} either from the

maximum volume adsorbed from the isotherms (captures mesopores), or from $V_{Total} =$

$(1/\rho_b)$-$(1/\rho_s)$ (captures all pores) diverge significantly at lower densities (signifying

macroporosity), but converge for the more dense samples (signifying mesoporosity;

Table 2). Similarly, BJH-desorption plots (shown as insets in Figure 5) give broad (with

hints for bimodal) pore-size distributions for the lower density samples, but they are quite

narrow and monomodal at higher densities. (It is noted that although BJH maxima are

also summarized in Table 2, they should not be considered quantitatively, because all

adsorption-desorption isotherms are consistently open-looped, indicating swelling of non-

rigid pores[33,34] in agreement with conclusions reached above from shrinkage data.) At the

low P/P$_o$ end of the isotherms, the significant quick rise of the volume of N_2 adsorbed

indicates the presence of a significant fraction of micropores. Data analysis within the

0.05<P/P$_o$<0.3 range according to the BET model (Table 2) shows that at low densities

the surface area is quite high (up to 632 m^2 g^{-1} for **bis-NAD-2.5**) decreasing (but

remaining quite significant) to 210 m^2 g^{-1} at ρ_b=0.660 g cm^{-3} (**bis-NAD-20** samples). *t-*

Plot analysis of the isotherms within the 0.05<P/P$_o$<0.5 range using the Harkins and Jura method[35] shows that at low densities up to 35% of the surface area comes from micropores, decreasing to less than 10% in the more dense samples (**bis-NAD-15** and **bis-NAD-20**).

By SEM (Figure 6), all samples consist of particles agglomerating together to larger clusters. Lower density samples (< 0.5 g cm^{-3}) show clearly the presence of macropores, consistently with the N$_2$-sorption analysis above. The minimum particle diameter observed by SEM, around 20 nm, is rather uniform throughout all densities. Those smallest particles assemble to larger aggregates, 50-100 nm in diameter, but they are best defined (discernible) in the lowest and highest density samples (**bis-NAD-5** and bis-**NAD-20**, respectively). The medium density samples (**bis-NAD-10**) are fuzzier and the smallest particles look as if they are fused together into larger clusters. The smallest particles in the highest density samples (**bis-NAD-20**) are rather uniformly dispersed in space rendering hard to identify the larger aggregates. A quantitative assessment of the make up of the skeletal framework was obtained with SANS; the data are included in Figure 6, and the results obtained by applying the Beaucage Unified Model analysis,[36] which models the samples as having multiple levels of structure, each with a distinct characteristic length, corresponding hierarchically (starting from high Qs) to a particle, aggregate, agglomerate, are summarized in Table 3. Further, the Unified Model allows analysis of such hierarchical structures over the full range of *Q*, the momentum transferred in a scattering event, allowing deconvolution of overlapping length scales that can lead to subtle changes in the data, such as a change in slope. Over all densities and

Table 2. Selected properties of polyimide aerogels via ROMP

sample	diameter (cm)[a]	shrinkage (%)[a,b]	bulk density, ρ_b (g cm^{-3})[a]	skeletal density, ρ_s (g cm^{-3})[c]	porosity Π(% void space)	surface area, (m^2 g^{-1})[d]	average pore diameter (nm)[e]	average pore diameter (nm)[f]
bis-NAD-2.5	0.609 ± 0.005	39 ± 1	0.134 ± 0.002	1.360 ± 0.014	90.1	632 [180]	13.8 [42.6]	33.4 [69.7]
bis-NAD-5	0.639 ± 0.005	36 ± 1	0.261 ± 0.005	1.325 ± 0.008	80.3	524 [124]	16.7 [23.5]	42.8 [67.6]
bis-NAD-10	0.685 ± 0.005	32 ± 1	0.341 ± 0.011	1.260 ± 0.003	72.9	438 [72]	16.4 [19.6]	42.6 [44.2]
bis-NAD-15	0.705 ± 0.007	30 ± 1	0.507 ± 0.014	1.292 ± 0.004	60.7	298 [29]	14.8 [16.1]	30.7 [12.8]
bis-NAD-20	0.725 ± 0.005	28 ± 1	0.660 ± 0.019	1.260 ± 0.002	47.6	210 [19]	12.9 [13.7]	20.4 [5.0]

[a]. Average of 3 samples. (Mold diameter: 1.0 cm) [b]. Shrinkage = 100 × (sample diameter – mold diameter)/(mold diameter). [c]. Single sample, average of 50 measurements. [d]. BET [micropore (by *t*-plot using the Harkins and Jura method)]. [e]. By the 4 ×V_{Total}/σ method. For the first number, V_{Total} was calculated by the single-point adsorption method; for the number in brackets, V_{Total} was calculated via $V_{Total} = (1/\rho_b)-(1/\rho_s)$. [f]. From the BJH desorption plot. First numbers are the peak maxima; numbers in brackets are the widths at half maxima.

the entire range of the scattering Q, SANS shows two Guinier regions (knees) indicative of characteristic length scales and two power-law regions (which appear linear on the log-log plots of Figure 6). Plots of the SANS data found in Figure 6 have been divided into four regions (in Q) for ease in identifying the different structural levels. The Unified Model provides the radii of gyration, R_G, from the Guinier knees (Regions II and IV in the data of Figure 6) and the fractal dimensions of the secondary particles from the linear Region III. The slope of the data in Region I provides information about the surface characteristics of the primary particles themselves. Matching and comparing the SANS data of Table 3 with the SEM data of Figure 6 identifies the minimum SEM particles as polydisperse, but monomodal primary particles, 16-17 nm in diameter, with smooth (non-fractal) interfaces (the slopes in Region I are all uniformly equal to 4.0). The size of the primary particles does not change with density (i.e., the concentration of **bis-NAD** in the sol), in analogy to silica.[37] Secondary aggregates are larger for medium density samples (85.2 nm in diameter for **bis-NAD-10**), but their size decreases as the density increases (60 nm for **bis-NAD-20**). The Guinier Region IV for **bis-NAD-5** was at the edge of the accessible Q-range and the secondary particle size could not be measured. Nevertheless, in those lower bulk density samples primary particles assemble into the secondary aggregates fractally (mass fractal dimension, $D_m=2.34\pm0.03$) suggesting diffusion limited aggregation as the growth mechanism.[38] As the bulk density increases (**bis-NAD-10** and **bis-NAD-20** samples) the Region III exponent increases and falls at the limit between mass and surface fractals. The level of uncertainty associated with the large size of both the primary and secondary particles causes significant overlap of the Guinier Regions II and IV with the linear Region III, from which the fractal dimension is estimated, making

assessment by SANS alone, inconclusive. However, combining the SANS and SEM results suggests that we are dealing with surface fractals of non-fractal objects. With the Region III slope being attributed to surface fractals with D_S=3.0, secondary particles of **bis-NAD-10** and **bis-NAD-20** are then classified as surface fractal closed-packed objects. Transition from the more-open fractal structure to the more-dense non-fractal one justifies the drop of the percent micropore surface area from 35% in the lower density samples, to <10% in the higher density ones.

Table 3. Small angle neutron scattering (SANS) data for polyimide aerogels via ROMP

| sample | Primary Particles | | Secondary Particles | | |
	Porod slope [a]	R_G (nm) [b] [c]	R_G (nm) [d] [c]	D_m [e]	D_S [e]
bis-NAD-5	4.0±0.1	6.3±1.1 [16.4]	[f]	2.34±0.03	
bis-NAD-10	4.0±0.1	6.5±1.2 [16.9]	32.8±2.5 [85.2]		2.9±0.1
bis-NAD-20	4.0±0.1	6.1±1.7 [15.8]	23.1±1.1 [60]		3.0±0.5

Referring to Figure 6: a. From Regions I. b. From Regions II. c. In brackets, particle diameter=2×R, where the particle radius R=0.77R_G (R_G, radius of gyration). d. From Regions IV. e. From Regions III. f. Region IV in this sample was beyond the experimentally accessible range of the scattering vector Q and thus R_G could not be estimated.

Considering the XRD and SANS data together, namely the closed packing of the polymeric strands implied by XRD and the invariance of the primary particle size revealed by SANS, supports fast polymerization to mostly linear oligomers that reach their solubility limit always at the same point, irrespective of the concentration of **bis-NAD** in the sol, and get phase-separated into uniform-sized primary particles, which are surface-active through dangling norbornene moieties, or catalyst-terminated polymer strands. At the lowest concentrations (e.g., **bis-NAD-5** samples) primary particles react with one another via a diffusion-limited mechanism to form fractal secondary particles

that in turn form a gel. D_S=3.0 at higher concentrations (e.g., **bis-NAD-10** and **bis-NAD-20** samples) might be associated with fast ROMP, which fills the sol with primary particles that react with their next neighbor through a bond percolation model yielding non-(mass) fractal secondary objects.[39] Crosslinking of the polymer strands most probably continues throughout those gel-forming processes. In the case of the **bis-NAD-20** samples, extremely fast ROMP consumes all monomer quickly (recall for example that gelation takes place in less than 1 min in those samples). Somewhat slower ROMP in the more dilute **bis-NAD-10** samples is followed by accumulation of monomer on the secondary particles (a monomer-cluster growth like process) explaining the fuzziness in SEM.

3.3.c. Application-related bulk properties. Polyimides are thermally stable polymers and therefore appropriate applications for **bis-NAD-xx** aerogels include high temperature thermal and acoustic insulation. Relevant properties to monitor include thermal stability, mechanical strength and thermal conductivity.

Thermal stability. Despite resemblance to PMR-type polyimides (both materials are prepared from the same norbornene end-capped oligomers),[24] ROMP-derived **bis-NAD-xx** aerogels have unsaturated backbones (Scheme 4). Therefore, their use in air might be problematic. Indeed, by TGA (Figure 3B) **bis-NAD-xx** show a mass increase above about 200 ^{o}C, presumably by reaction with oxygen. PMR-type polyimides are rated for operation up to ten thousand hours at 290 ^{o}C,[24] which is obviously not possible with as-prepared **bis-NAD-xx**. Increasing the molecular weight of the monomer, or post-gelation saturation of the double bonds might be approaches around this issue. Conveniently, that

process could be coupled with increasing the hydrophobicity and reducing the flammability of the material.

Mechanical properties. As stated in the Introduction, organic aerogels are pursued partly as alternatives to polymer crosslinked silica aerogels for their facile one-step synthesis and for their mechanical properties. In that regard, ROMP-derived polyimides were investigated under quasi-static compression. The stress-strain curves (Figure 7) show very short nearly-elastic ranges up to approximately 3% strain, followed by plastic deformation and hardening up to 70% strain owing to pore collapse. The fact that the early part of the stress-strain curves is nearly elastic was confirmed by conducting loading and unloading tests (Figure 7, inset); it was found that the unloading curve after loading to 3% strain, nearly follows the loading curve with 0.2% remaining strain. (By comparison, loading up to 5.5% strain results to 2% unrecovered strain and loading up to 8% strain gives 4% unrecovered strain.) Interestingly, after reaching the 0.2% offset yield stress, a conventional measure of the incipient of plastic deformation, the stress continues to increase with strain. This phenomenon is different from plastic foams[40] in which, after reaching the yield strength, the stress-strain curve shows a plateau associated with the collapse of pores due to cell-wall buckling. It is likely that the small ratio of pore size to wall thickness (refer to SEM) prevents pore walls from buckling during compression of the sample. As a result, hardening at strains prior to 70% are attributed to nano-bending deformations.

Macroscopically, in no case samples buckle during compression and all Poisson's ratios are in the 0.27-0.30 range reflecting little lateral expansion unless during the late stages of the test, when pores have been substantially closed and samples start to expand

radially. Ultimately, lower density samples ($\leq$0.5 g cm^{-3}) undergo compressive failure at >80% strain, but the most dense samples (**bis-NAD-20**, ρ_b=0.6 g cm^{-3}) fail catastrophically by fragmentation at much lower strains (~40%, see Figure 7). The ultimate compressive strains follow roughly the corresponding porosities of the samples (compare Tables 2 and 4). The Young's modulus (E, calculated from the slope of the early linearly elastic range), the speed of sound (calculated from the Young's modulus and the bulk density via $(E/\rho_b)^{0.5}$) and the yield stress at 0.2% offset strain all increase as the bulk density increases. Specifically, the Young's modulus follows a power law relationship with bulk density (Figure 8A) of the type $E\sim(\rho_b)^{3.35}$. The sensitivity (exponent) is higher than that observed with native silica aerogels (~3.0),[41] crosslinked silica aerogels (3.10),[42] crosslinked vanadia aerogels (1.87)[41c] and polyurea organic aerogels[43] signifying the vastly different nature of the interparticle bridging: in **bis-NAD-xx** the neck zones are purely polymeric while in polymer-crosslinked aerogels they are mixed organic-inorganic. On the other hand, the ultimate strength as well as the ability of the material to store energy (referred to as toughness and quantified by the integral of the stress-strain curve) vary non-monotonically with density: as shown in Figures 8B and 8C, they both increase with density in the beginning, they reach a maximum and afterwards they decline. That decline in strength and toughness coincides with both the change in the failure mode (see photographs in Figure 7), and the decline in the ultimate strain at failure (see data in Table 4).

Table 4. Mechanical characterization data under quasi-static compression of polyimide aerogels[a]

sample	bulk density, ρ_b (g cm^{-3})	strain rate (s^{-1})	Young's Modulus, E (MPa)	speed of sound (m s^{-1})	yield stress at 0.2% offset strain (MPa)	ultimate strength, UCS (MPa)	ultimate strain (%)	Poisson's ratio	specific energy abs. (J g^{-1}) [J cm^{-3}] [b]
bis-NAD-5	0.240	0.035	NA	NA	0.36 ± 0.02	45.0 ± 21.6	85.1 ± 2.1	0.267 ± 0.037	16.7 ± 3.9 [4]
bis-NAD-10	0.390	0.035	48 ± 8	350.8	2.25 ± 0.12	168.4 ± 18.6	88.1 ± 1.6	0.269 ± 0.041	50.2 ± 2.4 [20]
bis-NAD-15	0.528	0.035	173 ± 13	572.4	6.05 ± 0.17	127.4 ± 14.1	79.6 ± 3.1	0.286 ± 0.006	50.1 ± 2.0 [27]
bis-NAD-20	0.625	0.035	288 ± 0.5	678.7	11.2 ± 0.079	27.7 ± 0.8	40.6 ± 6.8	0.299 ± 0.008	14.7 ± 1.6 [9]

a. Average of 2 samples. b. In brackets: per unit volume energy absorption, calculated from the energy absorption per unit mass multiplied by bulk density.

A monotonic variation of the Young's modulus with density and a simultaneous non-monotonic variation of the ultimate strength and toughness (Figure 8) have been also observed with polymer crosslinked silica aerogels, and that behavior is independent of the crosslinking polymer.[44,45] In those materials the reinforcing polymeric tethers are placed on a pre-formed inorganic framework, and while all accumulated polymer contributes to stiffness,[46] only bridging tethers between nanoparticles contribute to strength and toughness.[44,45] In agreement with conclusions reached with silica aerogels,[47] changes in the fractal dimension, and therefore the connectivity within secondary particles, should not be relevant with the decline of the strength and toughness as the density increases. Indeed, the higher connectivity within the secondary particles of **bis-NAD-10** and **bis-NAD-20**, as indicated by their fractal dimension (Table 3), is not associated with an identifiable trend in their mechanical properties (Table 4). Therefore, the trends in Figure 8 should be traceable to the inter-secondary particle connectivity. Based on the microscopic characterization data, it was concluded that the growth mechanism of medium-density **bis-NAD-xx** samples does remind the crosslinking process of silica aerogels in that gelation is followed by a monomer-cluster growth process whereas particles continue to grow in size by continual reaction with remaining monomer. That reinforces the inter-secondary particle necks (in a crosslinked aerogel fashion) yielding stronger materials. At even higher monomer concentrations, reactions proceed fast consuming all monomer quickly and yield smaller particles with weaker interparticle necks, leading to a decline in ultimate strain and a concomitant decrease in ultimate strength and energy absorption.

Overall, at their best (i.e., at the medium density range) **bis-NAD-10** and **bis-NAD-15** aerogels compete favorably with, and in many aspects they are better than polymer crosslinked silica aerogels. For example, polyurea crosslinked silica at ρ_b=0.304 g cm^{-3}, process-optimized by statistical design of experiments (DoE) methods, are 77% porous with σ=147 m^2 g^{-1}, a Young's modulus of 32 MPa, a yield stress at 0.2% offset strain of 1.12 MPa and an ultimate strength of 237 MPa.[45] By comparison, **bis-NAD-10** samples (ρ_b=0.341 g cm^{-3}) are 73% porous, with σ=438 m^2 g^{-1} (Table 2), a Young's modulus of 48 MPa, a yield stress at 0.2% offset strain of 2.25 MPa, an ultimate strength of 168 MPa and they can absorb up to 50 J g^{-1} of energy (Table 4). The latter figure renders them better than strong materials typically used for ballistic protection, such as 4130 steel (15 J g^{-1} at 7.84 g cm^{-3}), Kevlar-49 epoxy composites (11 J g^{-1} at 1.04 g cm^{-3}) and SiC ceramics (20 J g^{-1} at 3.02 g cm^{-3}).[48] Now, from an engineering design perspective, a fair comparison with standard materials should also extend from energy absorption per unit mass (J g^{-1}) to energy absorption per unit volume (J cm^{-3}). Using the latter metric, steel and silicon carbide (117.6 J cm^{-3} and 60.4 J cm^{-3}, respectively) remain superior to **bis-NAD-xx** aerogels (27 J cm^{-3} at their best, Table 4), but the latter still surpass Kevlar-49 fiber-epoxy composites (11.4 J cm^{-3}). However, since fiber-epoxy composites fast replace steel and ceramics in armor,[49] it is concluded that the additional volume requirement for absorbing a fixed amount of energy by Kevlar composites is easily accounted for in practice. Therefore, by and large **bis-NAD-xx** aerogels are reasonable, and in fact better alternatives.

Thermal Conductivity (l). This was calculated from the thermal diffusivity, *R*, and the heat capacity, c_p, of ~2.0 mm thick **bis-NAD-xx** disks using eq 1. The thermal diffusivity

$$1 = \rho_b \times c_p \times R \qquad (1)$$

was measured using a Flash Method (see Experimental Section),[50] whereas the sample is heated from one side and the temperature rise is observed as a function of time at the other. Coating the samples on both sides with gold and carbon ensures absorption of the heat pulse and minimizes radiative pathways and pulse "bleed through."[51] Typical data are shown in Figure 9. The data analysis software employs the pulse-corrected Cowan model[52] to approximate the heat transfer equation using an initial value for the thermal diffusivity estimated by the time it takes for the detector voltage to reach its half-maximum value (marked as t_{50} in Figure 9). Subsequently, a least-squares fit is iteratively performed in a defined time range ($10 \times t_{50}$), and the value for thermal diffusivity, R, is obtained. (Ten times t_{50} has been found a suitable measure of the initial cooling event after the heat pulse.) Table 5 summarizes the data. Owing to the small variation of the thermal diffusivity with density and the constant value of the heat capacity, thermal conductivity scales linearly with the bulk density within the limits investigated, and expresses the contribution of the through-lattice heat transfer. The thermal conductivity of the **bis-NAD-10** samples is found equal to 0.031 W m^{-1} K^{-1}, which compares favorably with that of polyurea crosslinked silica aerogels (0.041 W m^{-1} K^{-1} at 0.451 g cm^{-3}),[42] glass wool (0.040 W m^{-1} K^{-1}), Styrofoam (0.030 W m^{-1} K^{-1}), and polyurethane foam (0.026 W m^{-1} K^{-1}).[53]

Table 5. Thermal conductivity data for selected **bis-NAD-xx** samples at 23 $^{\circ}$C [a]

Sample	bulk density ρ_b (g cm^{-3})	heat capacity c_p (J g^{-1} K^{-1}) [b]	thermal diffusivity R (mm^2 s^{-1}) [b]	thermal conductivity λ (W m^{-1} K^{-1}) [b]
bis-NAD-10	0.338±0.003	0.995±0.030	0.091±0.005	0.031±0.00$_1$
bis-NAD-15	0.568±0.003	1.088±0.033	0.085±0.001	0.053±0.00$_2$
bis-NAD-20	0.622±0.002	1.062±0.032	0.096±0.004	0.063±0.00$_3$

a. Average of three samples. b. At 23 $^{\circ}$C.

4. Conclusions

Bis-NAD-xx aerogels considered together with other organic aerogels from the recent literature,[8-17] exemplifies the design parameters for the bottom-up synthesis of polymeric gels that can be dried into aerogels. The key requirement seems to be phase separation of surface-reactive nanoparticles that can crosslink with one another into a three dimensional network. Phase separation is induced by reduced solubility of the growing polymer, which in turn is introduced by crosslinking at the molecular level.

Significant shrinking (in the present case up to 40%) seems to be encountered more frequently with organic aerogels rather than their inorganic counterparts. And while that is typically a problem with the latter, leading to cracking, the more flexible organic framework seems to accommodate stresses better, and the materials come out as perfect monoliths. More importantly though, desirable properties such as high surface area, porosity and pore structure do not seem to be affected detrimentally, and in that regard shrinkage may be difficult to predict, but most certainly is reproducible and therefore can be engineered into the final object. As demonstrated herewith, ROMP-derived polyimide aerogels can be prepared in one-step as mesoporous materials over a wide density range with high porosities, high surface areas, high modulus, high strength and high toughness.

Combining one-step synthesis with mechanical strength, manageable thermal stability, relatively-low thermal conductivity and low speed of sound wave propagation render **bis-NAD-xx** reasonable multifunctional candidates for further investigation into thermal and acoustic insulation at elevated temperatures. From a theoretical perspective, **bis-NAD-xx** underline the fact that nucleation and network growth in organic aerogels is a complicated process that may not be knowable *a priori*, but it has definite effects on the materials performance. It can be influenced by typical reaction conditions, such as solvent, temperature, monomer and catalyst concentration, and most certainly predictability can be gained through multivariable optimization studies.

5. References

1. Pierre, A. C.; Pajonk, G. M. *Chem. Rev.* **2002**, *102*, 4243-4265.

2. Morris, C. A.; Anderson, M. L.; Stroud, R. M.; Merzbacher, C. I.; Rolison, D. R. *Science* **1999**, *284*, 622-624.

3. Kistler, S. S. *Nature* **1931**, *127*, 741.

4. Kistler, S. S. *J. Phys. Chem.* **1932**, *36*, 52-63.

5. Gash, A. E.; Pantoya, M.; Satcher, J. H.; Simpson, R. L. *Polym. Prepr. (Am. Chem. Soc. Div. Polym. Chem.)* **2008**, *49*, 558-559.

6. Leventis, N.; Chandrasekaran, N.; Sadekar, A. G.; Mulik, S.; Sotiriou-Leventis, C. *J. Mater. Chem.* **2010**, *20*, 7456-7471.

7. Baumann, T. F.; Gash, A. E.; Chinn, S. C.; Sawvel, A. M.; Maxwell, R. S.; Satcher, J. H., Jr. *Chem. Mater.* **2005**, *17*, 395-401.

8. Pekala, R. W. "Low Density Resorsinol-Formaldehyde Aerogels," U.S. Patent No. 4873218, 1989.

9. Pekala, R. W.; Alviso, C. T.; Lu, X.; Gross, J.; Frickle, J. *J. Non-Cryst. Solids* **1995**, *188*, 34-40.

10. Li, W.-C.; Lu, A.-H.; Guo, S.-C. *J. Colloidal Interface Sci.* **2002**, *254*, 153-157.

11. Pekala, R. W. "Melamine-Formaldehyde Aerogels," U.S. Patent No. 5086085, 1992.

12. Biesmans, G.; Martens, A.; Duffours, L.; Woignier, T.; Phalippou, J. *J. Non-Cryst. Solids* **1998**, *225*, 64-68.

13. Lee, J. K.; Gould, G. L.; Rhine, W. L. *J. Sol-gel Sci. Technol.* **2009**, *49*, 209-220.

14. Lorjai, P.; Chaisuwan, T.; Wongkasemjit, S. *J. Sol-gel Sci. Technol.* **2009**, *52*, 56-64.

15. Lee, J. K.; Gould, G. L. *J. Sol-gel Sci. Technol.* **2007**, *44*, 29-40.

16. Rhine, W.; Wang, J.; Begag, R. "Polyimide Aerogels, Carbon Aerogels, and Metal Carbide Aerogels and Methods of Making Same," U.S. Patent No. 7074880, 2006.

17. (a) Kawagishi, K.; Saito, H.; Furukawa, H.; Horie, K. *Macromol. Rapid Commun.* **2007**, *28*, 96-100. (b) Meador, M. A. B.; Malow, E. J.; He, Z. J.; McCorkle, L.; Guo, H.; Nauyen, B. N. *Polym. Prepr. (Am. Chem. Soc. Div. Polym. Chem.)* **2010**, *51*, 265-266.

18. Daniel, C.; Giudiee, S.; Guerra, G. *Chem. Mater.* **2009**, *21*, 1028-1034.

19. Goueree, P.; Talbi, H.; Miousse, D.; Tran-van, F.; Dao, L. H.; Lee, K. H. *J. Electrochem. Soc.* **2001**, *148*, A94-A101.

20. (a) Fischer, F.; Rigacci, A.; Pirard, R.; Berthon-Fabry, S.; Achard, P. *Polymer* **2006**, *47*, 7636-7645. (b) Gavillon, R.; Budtova, T. *Biomacromolecules* **2008**, *9*, 269-277. (c) Surapolchai, W.; Schiraldi, D. A. *Polym. Bull.* **2010**, *65*, 951-960.

21. (a) Leventis, N.; Sotiriou-Leventis, C.; Zhang, G.; Rawashdeh, A.-M. M. *Nano Lett.* **2002**, *2*, 957-960. (b) Zhang, G.; Dass, A.; Rawashdeh, A.-M. M.; Thomas, J.; Counsil, J. A.; Sotiriou-Leventis, C.; Fabrizio, E. F.; Ilhan, F.; Vassilaras, P.; Scheiman, D. A.; McCorkle, L.; Palczer, A.; Johnston, J. C.; Meador, M. A. B.; Leventis, N. *J. Non-Cryst. Solids* **2004**, *350*, 152-164. (c) Leventis, N.; Palczer, A.; McCorkle, L.; Zhang, G.; Sotiriou-Leventis, C. *J. Sol-Gel Sci. Technol.* **2005**, *35*, 99-105. (d) Leventis, N. *Acc. Chem. Res.* **2007**, *40*, 874-884. (e) Leventis, N.; Vassilaras, P.; Fabrizio, E. F.; Dass, A. *J. Mater. Chem.* **2007**, *17*, 1502-1508. (f) Leventis, N.; Mulik, S.; Sotiriou-Leventis *Chem. Mater.* **2008**, *20*, 6985-6997.

22. Sroog, C. E.; Endrey, A. L.; Abrmo, S. V.; Berr, C. E.; Edward, W. M.; Oliver, K. L. *J. Polym. Sci. Part A* **1965**, *3*, 1373-1390.

23. (a) Edward, W. M.; Robinson, I. M. "*Polyimides of Pyromellitic Acid,*" U.S. Patent No. 2710853, 1955. (b) Edwards, W. M.; Robinson, I. M. "Preparation of Pyromellitimides," U.S. Patent No. 2867609, 1959.

24. (a) Woodfine, B.; Soutar, I.; Preston, P. N.; Jigajinni, V. B.; Stewart, N. J.; Hay, J. N. *Macromolecules* **1993**, *26*, 6330-6334. (b) Baugher, A. H.; Espe, M. P.; Goetz, J. M.; Schaefer, J.; Pater, R. H. *Macromolecules* **1997**, *30*, 6295-6301. (c) Hu, A. J.; Hao, J. Y.; He, T.; Yang, S. Y. *Macromolecules* **1999**, *32*, 8046-8051. (d) Xie, W.; Pan, W.-P.; Chuang, K. C. *Thermochimica Acta* **2001**, *367-368*, 143-153.

25. Sroog, C. E. *Prog. Polym. Sci.* **1991**, *16*, 561-694.

26. Chidambareswarapattar, C.; Larimore, Z.; Sotiriou-Leventis, C.; Mang, J. T.; Leventis, N. *J. Mater. Chem.* **2010**, *20*, 9666-9678.

27. Grubbs, R. H. *Angew. Chem. Int. Ed.* **2006**, *45*, 3760-3765.

28. (a) Laguitton, B.; Mison, P.; Sillion, B.; Brisson, J. *Macromolecules* **1998**, *31*, 7203-7207. (b) Chen, C.-F.; Qin, W.-M.; Huang, X.-A. *Polym. Eng. Sci.* **2008**, *48*, 1151-1156.

29. Seeger, P. A.; Hjelm, R. P., Jr. *J. Appl. Cryst.* **1991**, *24*, 467-478.

30. Liu, Y.; Sun, X. D.; Xie, X.-Q.; Scola, D. A. *J. Polym. Sci.: Part A: Polym. Chem.* **1998**, *36*, 2653-2665.

31. Polymerization of **bis-NAD** via ROMP is expected to be a living process that proceeds till all monomer is consumed. For example see: Bielawski, C. W.; Grubbs, R. H. *Prog. Polym. Sci.* **2007**, *32*, 1-29.

32. (a) Everett, D. H. "*Basic Principles of Colloid Science,*" The Royal Society of Chemistry, London, U.K., 1988, p 189. (b) Ilmain, F.; Tanaka, T.; Kokufuta, E. *Nature* **1991**, *349*, 400-401.

33. Sing, K. S. W.; Everett, D. H.; Haul, R. A. W.; Moscou, L.; Pierotti, R. A.; Rouquerol, J.; Siemieniewska T. *Pure and Appl. Chem.* **1985**, 57, 603-619.

34. Lowell, S.; Shields, J. E.; Thomas, M. A.; Thommes, M. "*Characterization of Porous Solids and Powders: Surface Area, Pore Size and Density,*" Kluwer Academic Publishers, Norwell, MA, 2004, pp 44-45.

35. Webb, P. A.; Orr, C. *Analytical Methods in Fine Particle Technology*, Micromeritics Instrument Corporation, Norcross, GA, 1997 pp 67-68.

36. (a) Beaucage, G. *J. Appl. Cryst.* **1995**, *28*, 717-728. (b) Beaucage, G. *J. Appl. Cryst.* **1996**, *29*, 134-146. (c) Mang, J. T.; Son, S. F.; Hjelm, R. P.; Peterson, P. D.; Jorgensen, B. S. *J. Mater. Res.* **2007**, *22*, 1907-1920. (d) Tappan, B. C.; Huynh, M. H.; Hiskey, M. A.; Chavez, D. E.; Luther, E. P.; Mang, J. T.; Son, S. F. *J. Am. Chem. Soc.* **2006**, *128*, 6589-6594.

37. Orcel, G.; Gould, R. W.; Hench, L. L. In *Better Ceramics Through Chemistry II;* Brinker, C. J., Clark, D. E., Ulrich, D. R., Eds.; Materials Research Society: Pittsburgh, PA, 1986; Vol. 73, p 289.

38. Hench, L. L.; West, J. K. *Chem. Rev.* **1990**, *90*, 33-72.

39. (a) Zallen, R. *The Physics of Amorphous Solids;* Wiley: New York, 1983; Chapter 4. (b) Stauffer, D.: Conialio, A.; Adam, M. *Adu. Polym. Sci.* **1982**, *44*, 103.

40. Daphalapurkar, N. P.; Hanan, J. C.; Phelps, N. B.; Bale, H.; Lu, H. *Mech. Adv. Mat. Struct.* **2008**, *15*, 594-611.

41. (a) Fricke, J. *J. Non-Cryst. Solids* **1988**, *100*, 169-173. (b) Gross, J.; Fricke, J. *Nanostructured Mater.* **1995**, *6*, 905-908. (c) Luo, H.; Churu, G.; Schnobrich, J.; Hobbs, A.; Fabrizio, E. F.; Dass, A.; Mulik, S.; Sotiriou-Leventis, C.; Lu, H.; Leventis, N. *J. Sol-Gel Sci. Technol.* **2008**, *48*, 113-134.

42. Katti, A.; Shimpi, N.; Roy, S.; Lu, H.; Fabrizio, E. F.; Dass, A.; Capadona, L. A.; Leventis, N. *Chem. Mater.* **2006**, *18*, 285-296.

43. Leventis, N.; Sotiriou-Leventis, C.; Chandrasekaran, N.; Mulik, S.; Larimore, Z. J.; Lu, H.; Churu, G.; Mang, J. T. *Chem. Mater.* **2010**, *22*, 6692-6710.

44. Meador, M. A. B.; Fabrizio, E. F.; Ilhan, F.; Dass, A.; Zhang, G.; Vassilaras, P.; Johnston, J. C.; Leventis, N. *Chem. Mater.* **2005**, *17*, 1085-1098.

45. Meador, M. A. B.; Capadona, L. A.; MacCorkle, L.; Papadopoulos, D. S.; Leventis, N. *Chem. Mater.* **2007**, *19*, 2247-2260.

46. Mulik, S.; Sotiriou-Leventis, C.; Churu, G.; Lu, H.; Leventis, N. *Chem. Mater.* **2008***, 20,* 5035-5046.

47. Woignier, T.; Reynes, J.; Hafili-Alaoui, A.; Beurroies, I.; Phalippou, J. *J. Non-Cryst. Solids* **1998**, *241*, 45-52.

48. (a) American Society for Metals, ASM Engineering Materials Handbook, Composites, Volume 1: ASM International: Materials Park, OH, p 178, Table 2, 1998. (b) Luo, H.; Chen, W. *Intern. J. Appl. Ceram. Techn.* **2004**, *1*, 254-260. (c) Luo, H.; Chen, W.; Rajendran, A. M. *J. Am. Ceram. Soc.* **2006**, *89*, 266-273.

49. Hogg, P. J. *Science* **2006**, *314*, 1100-1101.

50. Parker, W. J.; Jenkins, J. J.; Abbott, G. L.; Butler, C. P. *J. Appl. Phys.* **1961**, *32*, 1679-1684.

51. Lee, D.; Stevens, P. C.; Zeng, S. Q.; Hunt, A. J. *J. Non-Cryst. Solids* **1995**, *186*, 285-290.

52. (a) Cowan, R. *J. Appl. Phys.* **1961**, *32*, 1363-1369. (b) Cowan, R. *J. Appl. Phys.* **1963**, *34*, 926-927.

53. Lide, D. R. *CRC Handbook of Chemistry and Physics 84th Edition*; CRC Press: Boca Raton, FL, 2003; pp 12/22612/227.

6. Figures
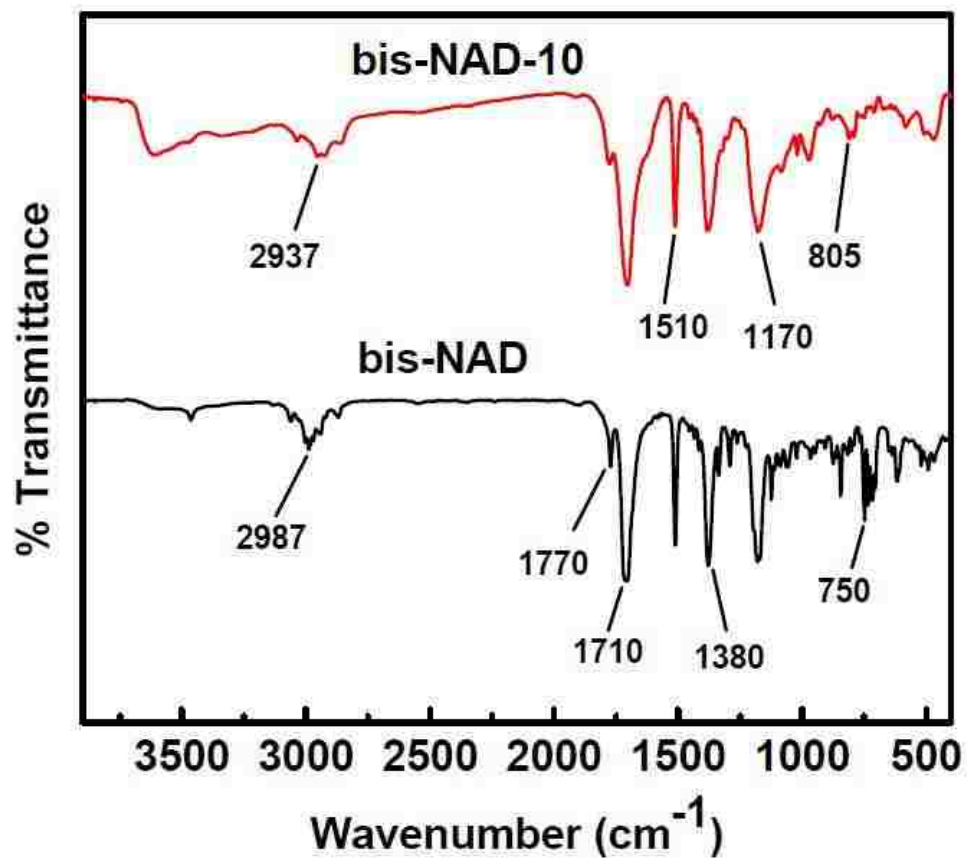
Figure 1. Infrared (IR) data for **bis-NAD** monomer and a representative ROMP-derived polyimide aerogel.
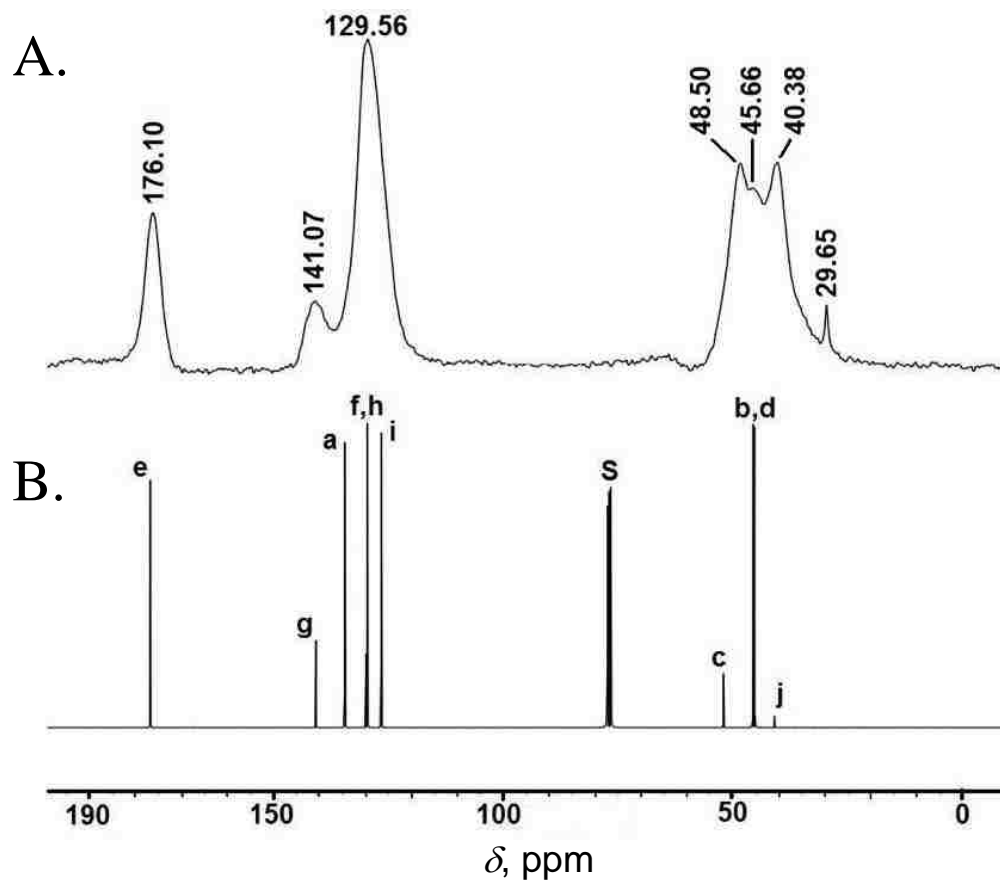
Figure 2. A. Representative CPMAS ^{13}C NMR spectrum of a ROMP-derived polyimide aerogel (case shown: **bis-NAD-10**). The resonance at 29.65 ppm is attributed to residual solvent (acetone). B. Liquid ^{13}C NMR of the **bis-NAD** monomer in CDCl$_3$ (marked "S"). For peak assignment see structure in the text.
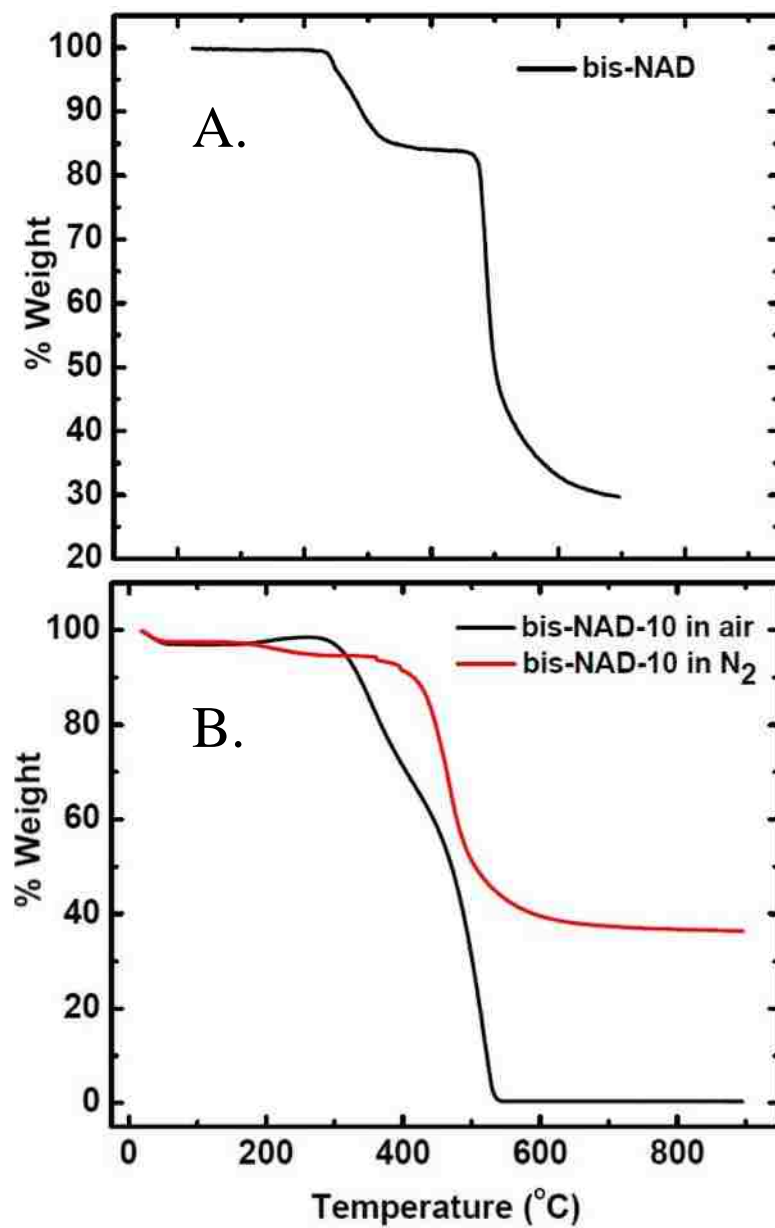
Figure 3. A. Thermogravimetric analysis (TGA) data for the monomer (**bis-NAD**) at 10 ^{o}C min^{-1}. B. TGA data for a representative ROMP-derived polyimide sample as shown at the same heating rate.
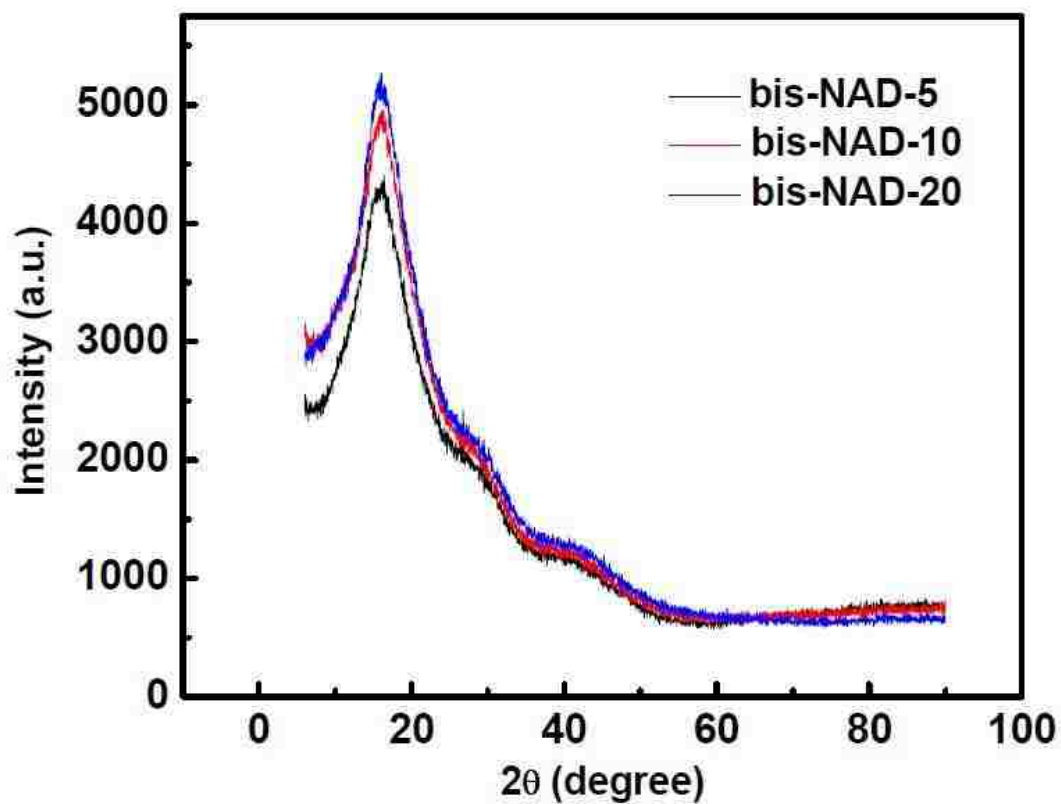
Figure 4. X-ray diffraction (XRD) of three representative ROMP-derived polyimide aerogels as shown.
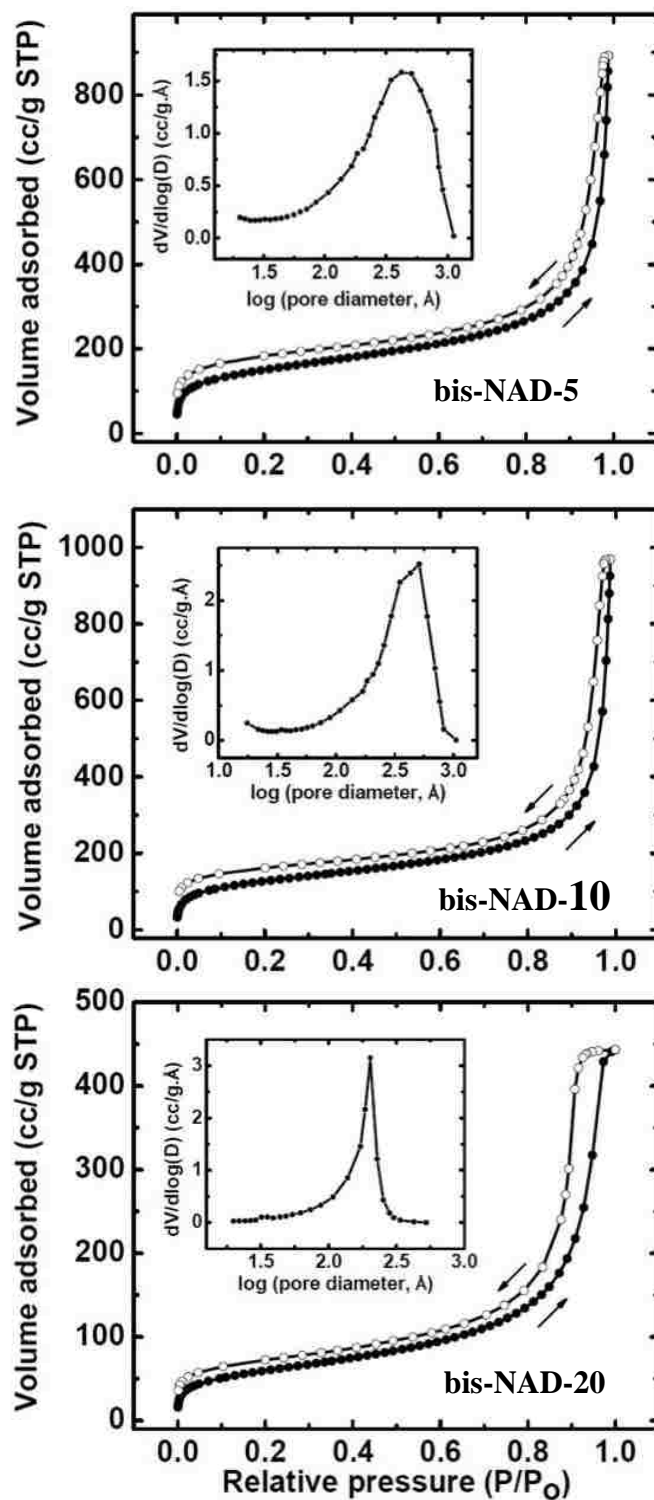
Figure 5. N_2-Sorption isotherms for the **bis-NAD-xx** aerogels as a function of the bulk density (ρ_b). Insets, BJH-desorption plots. Data are summarized in Table 2.
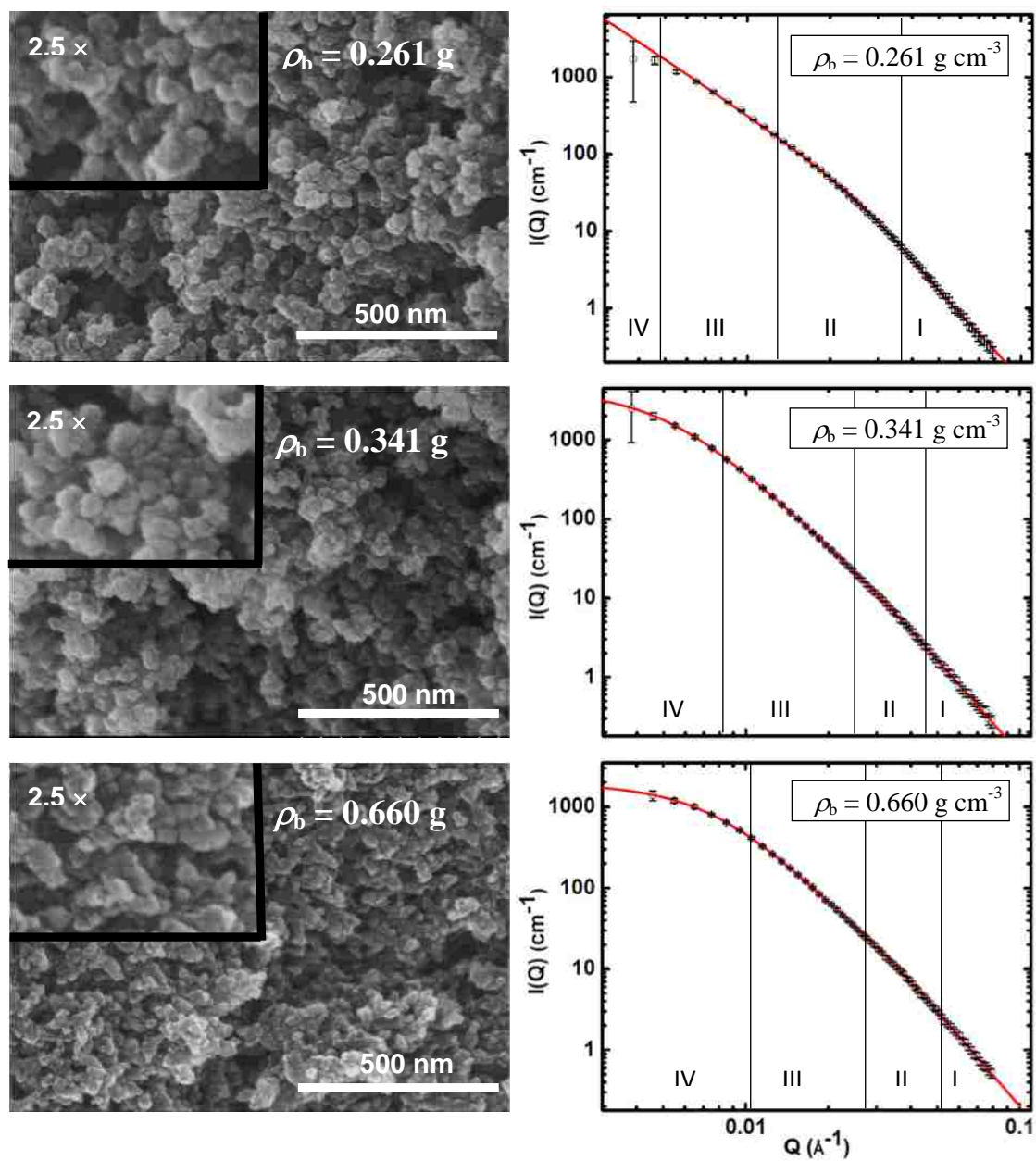
Figure 6. Scanning electron microscopy (SEM) and small angle neutron scattering (SANS) of ROMP-derived **bis-NAD-xx** aerogels as a function of the bulk density (ρ_b). Information from the SANS data and for the meaning of Regions I-IV refer to Table 3.
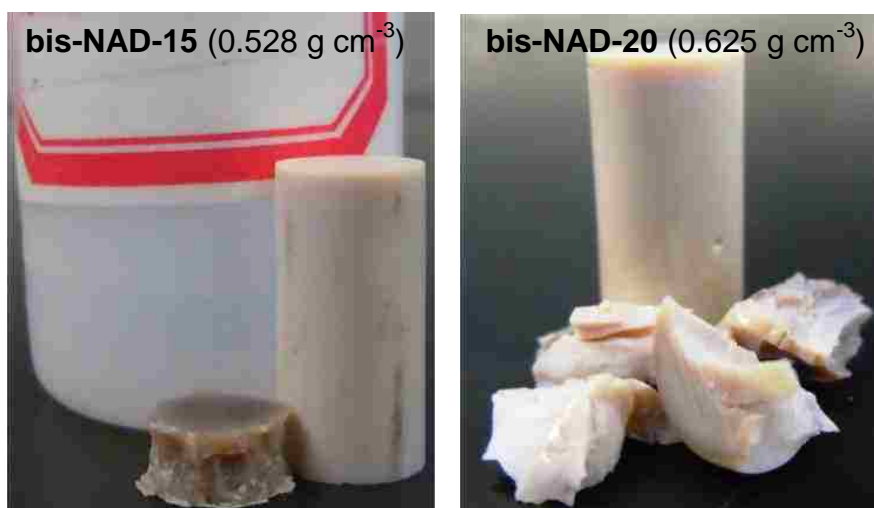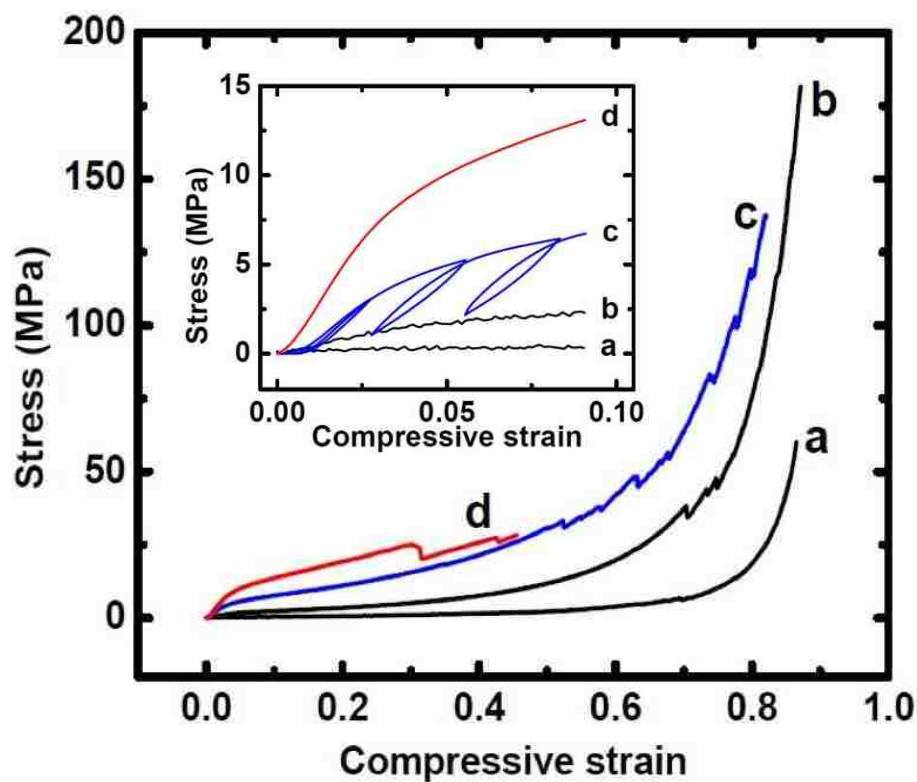
Figure 7. Top: Stress-strain curves under quasi-static compression of the **bis-NAD-xx** aerogels as a function of the bulk density (a: **bis-NAD-5**, ρ_b= 0.24 g cm^{-3}; b: **bis-NAD-10**, ρ_b= 0.39 g cm^{-3}; c: **bis-NAD-15**, ρ_b= 0.53 g cm^{-3}; d: **bis-NAD-5**, ρ_b= 0.63 g cm^{-3}). <u>Inset</u>: Magnified early nearly-elastic region, including loading-unloading data for a **bis-NAD-15** sample. Bottom: Photographs of two samples as indicated, before and after compression, showing the different mode of failure.
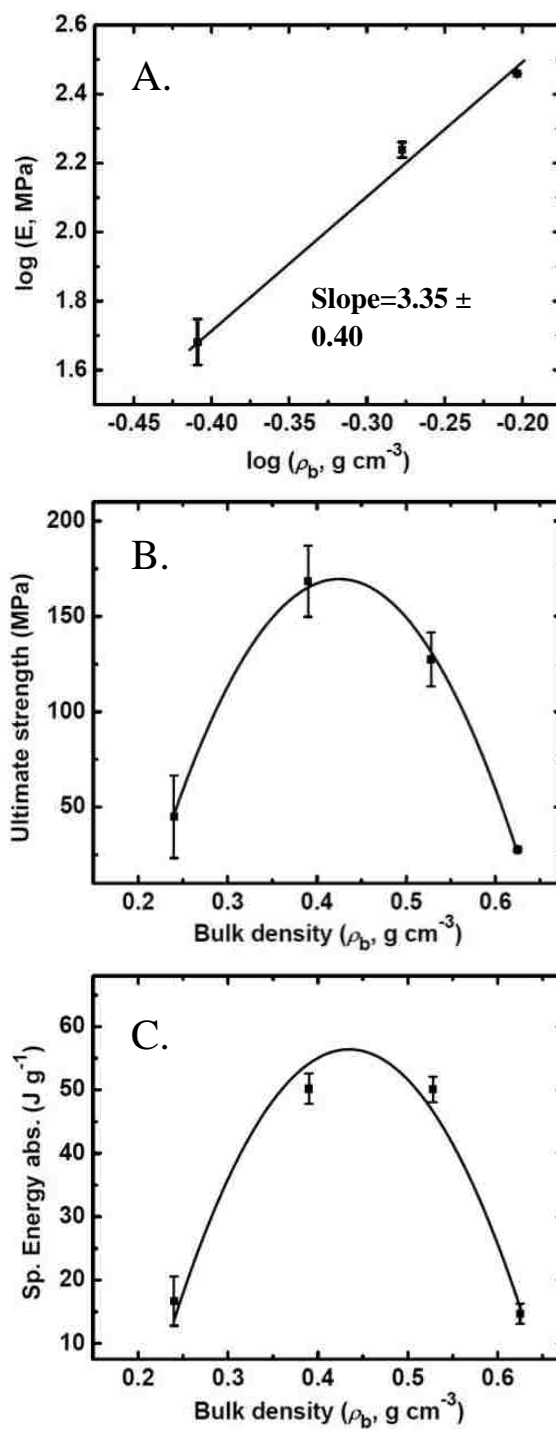
Figure 8. A. log-log plot of the Young's modulus versus bulk density of various **bis-NAD-xx** aerogels. B and C. Variation of the ultimate compressive strength and energy absorption of the same **bis-NAD-xx** aerogels as a function of their bulk density. (Lines have been added to guide the eye.)
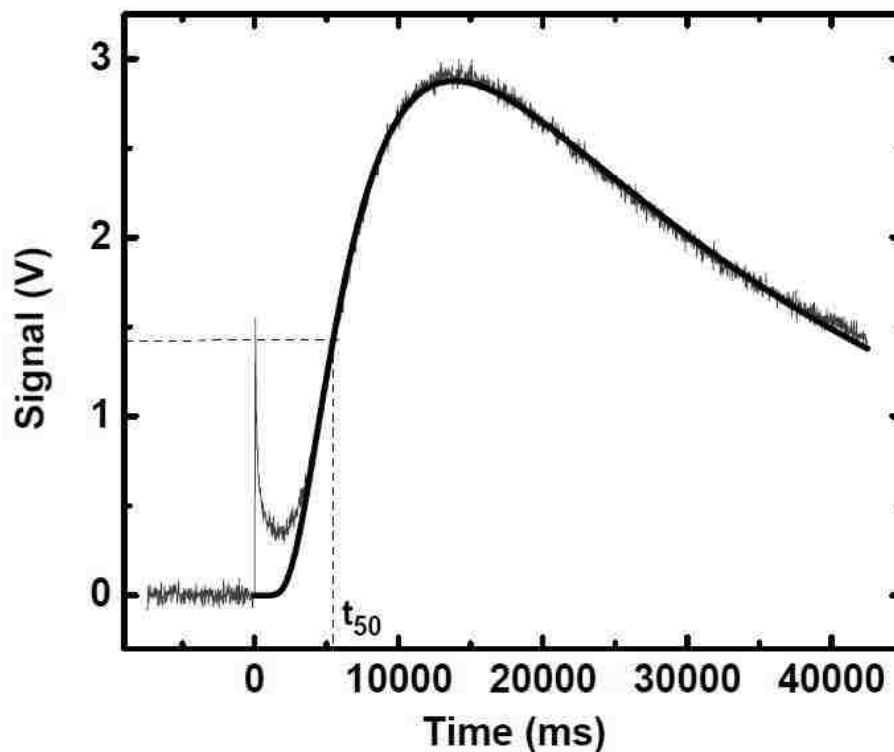
Figure 9. Temperature rise curve of the back face of a **bis-NAD-15** aerogel disk (9.32 mm in diameter, 2.17 mm thick, $r_b = 0.568$ g cm^{-3}) coated with gold and carbon on both faces, following a heat pulse incident to the front face. Dashed reference lines indicate t_{50}, the time for the detector voltage (proportional to temperature) to reach half its maximum value. Data have been fitted to the pulse-corrected Cowan model (see text).

III. The Nanotopology of Bulk Deformation in Polydicyclopentadiene Gels, and how Grafting with PMMA Yields Dimensionally Stable Nanoporous Solids (Aerogels)

Dhairyashil P. Mohite[1], Shruti Mahadik-Khanolkar[1], Huiyang Luo[2], Hongbing Lu[2,*],
Chariklia Sotiriou-Leventis[1,*] and Nicholas Leventis[1,*]

1. Department of Chemistry, Missouri University of Science and Technology, Rolla, MO 65409, U.S.A. Tel.: (573) 341-4391 (N.L.), (573) 341-4353 (C.S.-L.); E-mail: leventis@mst.edu, cslevent@mst.edu

2. Department of Mechanical Engineering, The University of Texas at Dallas, Richardson, TX 75080, U.S.A. Tel.: (972) 883-4647; E-mail: hongbing.lu@utdallas.edu

Abstract: Polydicyclopentadiene (pDCPD) is a material of emerging technological significance from separations to armor. It is a paradigm of ring opening metathesis polymerization (ROMP) and some of its remarkable properties (e.g., strength) have been attributed to crosslinking of the pendant cyclopentenes. pDCPD should be an ideal material for strong nanoporous solids (aerogels), however, problems were encountered even from the wet-gel stage: an excessive swelling in toluene (up to 200% v/v) was followed by de-swelling and severe deformation in acetone, rendering the resulting aerogels unusable. Swelling of a hydrocarbon gel in non-polar toluene and de-swelling in polar acetone is not surprising. However, this conventional view is not sufficient to account for deformation. In this context, *herewith we describe how the nanostructure could play the role of a conduit that transmits and translates molecular forces to the bulk.* For this, we followed two complementary approaches: a bottom-up and a top-down. First, rheometry shows that the pDCPD gel network is formed by mass fractal aggregates (D_f~2.4). Further, based on spectroscopic evidence (IR, solids ^{13}C NMR and several

liquid ^{1}H NMR controls), pDCPD is not crosslinkable via metathesis with the 2nd generation Grubbs's catalyst used here, and *only* 4-5% of the cyclopentene double bonds are engaged in crosslinking, presumably via Wagener-type olefin coupling. Introducing additional crosslinking was deemed appropriate. Control studies confirmed that all double bonds and allylic positions on the polymer are prone to react with radicals. Thus, pDCPD was engaged in the polymerization of methylmethacrylate (MMA) put in the pores of wet-gels, and the network was grafted with polyMMA (PMMA). The uptake of PMMA was varied in the 13-28% w/w range. All resulting aerogels kept the shape and dimensions of their molds. Evidence though suggests (e.g., DSC) that PMMA remains a linear polymer, hence pDCPD/PMMA networks resist deformation, not because of molecular-level crosslinking, but due to a synergism related to the nano-topology of the two components. SEM and N_2 sorption on dry aerogels show that macroscopic deformation of wet-gels is accompanied by coalescence of nanoparticles. Small angle x-ray scattering (SAXS) shows that both deformed (pDCPD) and non-deformed (pDCPD/PMMA) aerogels consist of same-size primary (1°) and *non*-mass-fractal secondary (2°) particles. Putting this information together, the pDCPD network is formed by fractal aggregates of non-fractal 2° particles. Coalescence is driven by non-covalent interactions that squeeze deformable 2° particles of one fractal assembly inside the empty space of another. PMMA fills the space between 1° particles; 2° particles become rigid and can no longer squeeze past one another. With monoliths now available, the nanoparticle interface in pDCPD/PMMA aerogels was probed top-down through thermal conductivity and mechanical testing, using polynorbornene aerogels as a control system. Results point to cross-metathesis as the common mechanism for interparticle

crosslinking. Cross-metathesis effectively extends polymeric chains from one nanoparticle into another, and is reflected on very large polydispersities (8-13).

1. Introduction

Aerogels are low-density open-pore nanostructured solids invented by Kistler in 1931 as a means to study the structure of wet-gels.[1] However, high-porosity related properties, such as low thermal conductivities, low dielectric constants and high acoustic impedance have shifted attention to applications, with main focus on insulation.[2] In the spirit of the original intent, we use aerogels to study the mechanism of structural collapse in polymer gels upon swelling/de-swelling. Owing to its technological significance, the model system of choice is based on polydicyclopentadiene.

Microscopically, aerogels consist of nanoparticles that can be organic or inorganic.[3] Their most widely-studied variety is based on silica and are prepared from wet-gels, which in turn are most commonly synthesized from alkoxides via polymerization-induced phase separation.[4] To prevent collapse by surface tension forces exerted by evaporating solvents on the fine nanostructure, gelation solvents are extracted with liquid CO_2, which is then converted into a supercritical fluid and is vented off. Although silica aerogels have been studied extensively, they are fragile materials and have found only limited applications. Other oxide aerogels have been also developed and evaluated as energetic materials, or as precursors for porous metals and ceramics.[5]

The fragility issue of silica and other oxide aerogels has been addressed by using the nanoporous surface hydroxyl functionality to anchor polymer tethers that bridge skeletal nanoparticles covalently.[6] While the vast porosity is minimally compromised, the

mechanical strength increases many-fold, and the new materials are suitable for applications unrelated to aerogels before, as for example in ballistic protection.[7] Since the exceptional mechanical properties of polymer-crosslinked aerogels are traced to the polymer, purely polymeric aerogels with the same nanostructure and interparticle connectivity should have similar mechanical properties.

Polymeric aerogels were first reported together with their inorganic counterparts,[1] but systematic investigation lagged some 60 years behind, until Pekala reported the bottom-up synthesis (from the monomers) of resorcinol-formaldehyde (RF) aerogels.[8] The record-low thermal conductivity,[9] as well as the facile pyrolytic conversion of RF aerogels to mesoporous monolithic carbons (carbon aerogels),[10] led to rapid development of several other phenolic resin-type aerogels based on melamine-formaldehyde,[11] phenol-furfural,[12] and cresol-formaldehyde.[13] More recently, additional organic aerogels based on polyurethane,[14] polyurea,[15] polybenzoxazine,[16] polyimides,[17] aramids,[18] and acrylic polymers via emulsion gelation[19] have all been successfully prepared via bottom-up synthesis. Several of those materials do possess mechanical properties comparable to those of polymer-crosslinked aerogels as designed. It is noted further that top-down approaches to organic aerogel synthesis, involving phase separation by slow cooling of preformed linear-polymer solutions, or by slow addition of non-solvents, have been also described. Top-down aerogels include Kistler's nitrocellulose,[3] and more recently polystyrene,[20] polyacrylonitrile,[21] and cellulose.[22] Overall, to impart strength, the emerging trend is that bottom-up synthesis works best. [14b,15b,c,17b,18,19] In this context, one also needs to induce early phase separation of small colloidal particles with multiple

surface functional groups for interparticle crosslinking. That is best achieved with multifunctional small-molecule monomers capable of molecular-level crosslinking.[19]

Conceptually, organic aerogels are related closely, and sometimes inspired by monolithic polymeric media developed for chromatographic separations. For this, macroporous polymers with structural rigidity consisting of fused arrays of polymeric microglobules were introduced in the 1950s,[23] and have been often prepared in the form of polymeric beads by suspension polymerization from polystyrene-divinylbenzene (PS-DVB) or acrylic monomers.[24] Closer to the aerogel structure, polymeric monolithic columns as continuous chromatographic supports were introduced in the 1980s from polyacrylamide gels.[25] In the 1990s, interest in monolithic porous polymers increased dramatically and today those materials are produced mainly from PS-DVB and acrylic monomers by free radical polymerization via sol-gel methods akin to those employed for the synthesis of wet-gel precursors of aerogels.[26] Living polymerization methods such as atom transfer radical polymerization (ATRP), stable free radical polymerization (SFRP) and reversible addition-fragmentation chain transfer polymerization (RAFT) have been also used successfully.[27]

Ring opening metathesis polymerization (ROMP) is a more recent living polymerization method[28] that is picking momentum in materials synthesis. It has been applied in the preparation of porous monoliths for chromatographic applications using various norbornene derivatives with Grubbs' or Schrock's catalysts in toluene, 2-propanol, 1,2-dichoromethane or THF.[29] In the same context, homogeneous, as well as porosity-gradient rods of polydicyclopentadiene (pDCPD), dried by solvent evaporation at 80 °C under vacuum, have been also reported via *in situ* phase separation of the

polymer in 2-propanol.[30] Aerogels are a natural extension of those activities, and we are aware of at least three reports on ROMP-derived aerogels from pDCPD for thermal insulation,[31] pDCPD-pNB co-polymers for highly porous films for inertial confinement fusion experiments,[32] and polyimides by ROMP-crosslinking of NB end-capped monomers for mechanically robust high-temperature thermal insulation.[33] Among those possibilities, pDCPD stands out for regular structural applications, because it is synthesized from an inexpensive and readily available monomer, DCPD, it is manufacturing-friendly (large objects can be fabricated via reaction injection molding),[34] and yields crosslinked polymers (Scheme 1) with excellent mechanical properties suitable (in bulk form) for armor.[36]

Scheme 1. ROMP of DCPD to pDCPD and possible crosslinking options
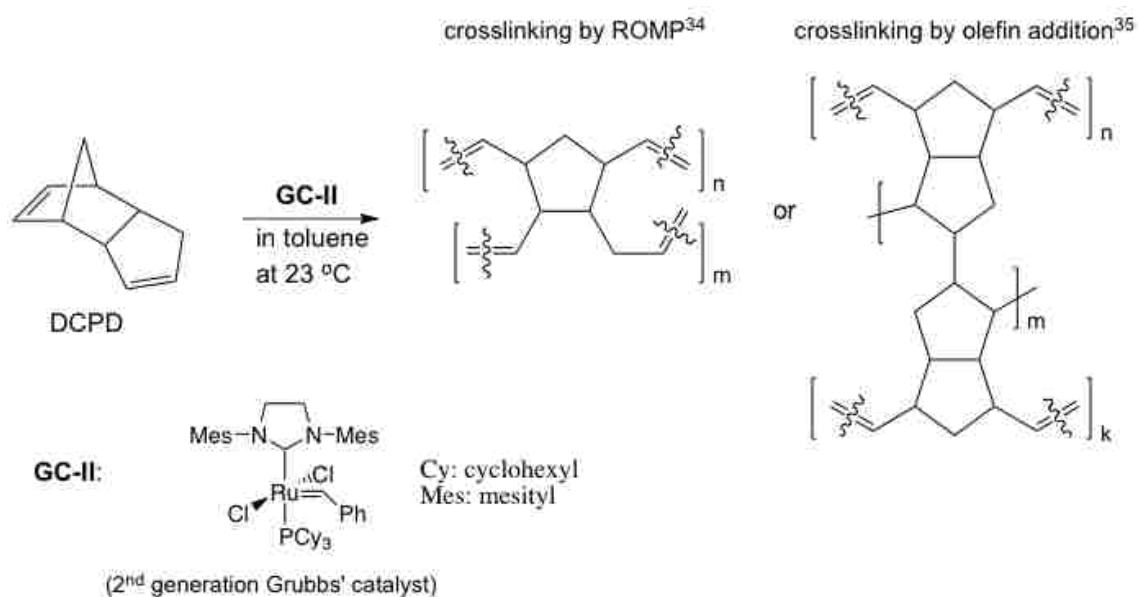
However, during our attempt to prepare monolithic pDCPD aerogels in order to determine their mechanical strength and suitability as strong lightweight materials, we noticed that all wet-gels deformed severely during processing, yielding aerogels

unsuitable for any purpose. Initially, the issue was associated with incomplete crosslinking, and was rectified by grafting polymethylmethacrylate (PMMA) on the pre-formed porous pDCPD network. However, a more detailed investigation of deformation and of the corrective action of PMMA revealed a different mechanism by which the hierarchical nanostructure of pDCPD (primary/secondary particles and higher aggregates) mediates the expression of molecular forces into the bulk. Subsequently, with regular monolithic samples available, we set off on a top-down investigation of the interparticle connectivity from bulk properties such as the thermal conductivity and the mechanical strength. Subsequently, with regular monolithic samples available, we set off on a top-down investigation of the interparticle connectivity from bulk properties such as the thermal conductivity and the mechanical strength. Specifically, the solid thermal conduction of the network is related to the interparticle cross-sectional area per unit volume, while stiffness to chemical bonding. Those properties of pDCPD/PMMA aerogels were studied in parallel with those of pNB aerogels, in essence using the last system as a control. By observing that pNB aerogels, with no chance for crosslinking between polymer strands through a cyclopentane ring, are as strong materials as pDCPD/PMMA aerogels (the stiffness of the two materials scales about as their interparticle surface area), it is concluded that both materials should share cross-metathesis as the common mechanism for interparticle crosslinking, which effectively extends polymer chains from one nanoparticle inside another.

2. Experimental

2.1. Materials. All reagents and solvents were used as received, unless noted otherwise. Dicyclopentadiene (DCPD, only the *endo-* could be detected by ^{1}H NMR – see Appendix I in Supporting Information), norbornene (NB), 2nd generation Grubbs' catalyst **GC-II** ((1,3-bis(2,4,6-trimethylphenyl)-2-imidazolidinylidene) dichloro(phenylmethylene) (tricyclo-hexylphosphine) ruthenium), methyl methacrylate (MMA), 2,2´-azobisisobutyronitrile (AIBN) and 2-propanol were purchased from Aldrich Chemical Co. 5,6-Dihydrodicyclopentadiene (**dhDCPD**) was purchased from TCI America (Portland, OR). Deuterated solvents were purchased from Cambridge Isotope Laboratories (Andover, MA). AIBN was purified by recrystallization from methanol and dried under vacuum at room temperature. HPLC grade toluene was purchased from Fisher.

2.1.1. Synthesis of polydicyclopentadiene (pDCPD-xx)-based aerogels. Two solutions were prepared, one containing DCPD in toluene (Solution A) and a second one with the appropriate amount of Grubbs' catalyst, **GC-II**, in 1 mL of toluene (Solution B). Different sets of samples were prepared by varying the concentration of DCPD: 20, 30 and 40 % w/w of DCPD versus (DCPD+toluene). The resulting aerogels are referred to as **pDCPD-xx** (where **xx** stands for the % w/w concentration of DCPD in the sol). The amount of **GC-II** was varied in roughly an inverse order to DCPD. All formulations and molar concentrations are summarized in Table 1. Solution B was added to Solution A at room temperature, the mixture was shaken vigorously and was poured into molds (either Wheaton polypropylene OmniVials Part No. 225402, 1 cm in diameter, or 8cc Fisherbrand Class B amber glass threaded vials, 1.4 cm in inner diameter, Part No. 03-

339-23C; the latter molds were used for samples intended for compression testing). All solutions gelled within 10-20 minutes. The resulting wet-gels were aged in their molds for 24 h at room temperature. Subsequently, wet-gels were transferred directly into toluene (for this, glass molds were broken with a hammer) and were washed 4×, 8 h per wash cycle, using 4× the volume of the gels. (It is noted that during processing wet-gels swell up to >2× their mold volume. That was accounted for by adjusting the volume of the wash solutions to be always 4× the volume of the wet-gel.) Next, pore-filling toluene was exchanged with acetone (4 washes, 8 h per wash cycle, 4× the volume of the gel per cycle), and wet-gels were either dried in an autoclave with liquid CO_2 taken out at the end as a supercritical fluid (SCF) to yield **pDCPD-xx** aerogels, or were treated with MMA/AIBN as described below.

2.1.2. Synthesis of pDCPD/PMMA aerogel composites (pDCPD-xx-X-MMA-yy). Toluene-washed pDCPD-xx wet-gels (4× as above) were transferred in toluene solutions of MMA and AIBN (1.22 mol percent versus MMA) and equilibrated for 36 h at room temperature with intermittent swirling. The amount of toluene used to dissolve MMA was 4× the volume of the swollen gels after the 4th toluene wash. The amount of MMA dissolved in that volume of toluene was 5× the desirable amount so that after equilibration the mol amount of MMA in the pores relative to the DCPD monomer units, would be at the prescribed level. The compositions of the MMA baths are summarized in Table 1. Subsequently, gels still submerged in their MMA baths were heated at 85 °C for 12 h. At the end, MMA baths were cooled to room temperature and wet-gels were washed with fresh toluene (4×, 8 h each wash cycle, each time using 4× the volume of each gel) to remove unreacted monomer (MMA) and loose PMMA from the pores. Next,

wet-gels were solvent-exchanged with acetone (4 washes, 8 h per wash cycle, 4× the volume of the gel per cycle), and finally were dried with SCF CO_2 in an autoclave to yield **pDCPD-xx-X-MMA-yy** aerogels. **xx** denotes the *weight* percent (% w/w) of DCPD in the initial toluene sol (see above), and **yy** stands for the *mol* percent (% mol/mol) of MMA versus DCPD monomer making up the wet-gels. (It is noted again, the concentration of MMA in the crosslinking baths was higher than the desirable mol:mol ratio of MMA:DCPD, in order to account for the effect of dilution after equilibration by the pore-filling solvent, i.e., toluene.) In that regard, pDCPD gels were treated with 20, 30, 40 and 50 % mol/mol of MMA versus DCPD, and therefore are referred to as **pDCPD-xx-X-MMA-20(30, 40 or 50)**.

2.1.3. Synthesis of polynorbornene (pNB-30)-based aerogels. Four different wet-gels were prepared using a 30% w/w solution of norbornene (NB) in four different solvent compositions zz:ww (50:50, 30:70, 10:90, and 0:100 w/w of toluene:2-propanol). The formulations are summarized in Table 2, and aerogels are referred to as **pNB-30(zz:ww)**. The NB solution in the corresponding toluene/2-propanol mixture was cooled to -5 $^{\circ}$C, and a cold (-5 $^{\circ}$C) solution of **GC-II** (0.0125 mol% versus NB) in toluene (100 μL) was added to it. The mixture was shaken vigorously, and immediately was poured into molds (2.00 cm inner diameter, 25 cm^3 Luer-Lock Norm-Ject polyethylene syringes from Fisher Scientific, Part No. AL20). All solutions gelled within 10-15 min. The resulting wet-gels were aged for 24 h at room temperature in their molds, washed with acetone (4×, 8 h per wash cycle, using 4× the volume of each gel) and dried with liquid CO_2 taken out as a SCF to yield monolithic **pNB-30(zz:ww)** aerogels.

2.2. Methods. Pore-filling solvent exchange with liquid CO_2 was conducted in an autoclave (SPI-DRY Jumbo Supercritical Point Dryer, SPI Supplies, Inc. West Chester, PA). At the end, liquid CO_2 was taken out as a supercritical fluid (SCF).

Control liquid ^{1}H NMR experiments were conducted with a 400 MHz Varian Unity Inova NMR instrument.

Mass-spectrometric analysis was conducted with a Hewlett Packard 5989A Mass Spectrometer connected to a Hewlett Packard 5890 Gas Chromatograph using a 30 m long column (Model DB-5ms from Agilent). Other parameters: Injector temperature: 280 ^{o}C; Detector temperature: 290 ^{o}C; Column temperature ramp rate: 20 ^{o}C min^{-1} from 50 ^{o}C to 290 ^{o}C. Carrier gas: N_2 at 5 psi head pressure.

Chemical characterization of **pDCPD-xx-X-MMA-yy** aerogels was conducted with infrared and solid-state ^{13}C NMR spectroscopy. Infrared (IR) spectra were obtained in KBr pellets, using a Nicolet-FTIR Model 750 Spectrometer. Solid-state ^{13}C NMR spectra were obtained with samples ground into fine powders on a Brucker Avance 300 Spectrometer with a carbon frequency of 75.475 MHz, using magic angle spinning (at 7 kHz) with broadband proton suppression and the CPMAS TOSS pulse sequence for spin sideband suppression. ^{13}C NMR spectra were referenced externally to glycine (carbonyl carbon at 176.03 ppm).

Bulk densities of aerogels (ρ_b) were calculated, whenever possible, from the weight and the physical dimensions of the samples. Skeletal densities (ρ_s) were determined with helium pycnometry, using a Micromeritics AccuPyc II 1340 instrument. Porosities, Π, were determined from ρ_b and ρ_s via $\Pi=100\times[(\rho_s-\rho_b)/\rho_s)]$.

Table 1. Formulations for **pDCPD-xx** and **pDCPD-xx-X-MMA-yy** aerogels

sample	DCPD (mL) [mol]	total toluene (mL) [mol]	DCPD in sol [a] (% w/w) [% mol/mol]	GC-II [a] (mg) [% mol vs. DCPD]	MMA [b] (mL) [mol]	AIBN vs. MMA [c] (% w/w) [% mol]
pDCPD-20	3.05 [0.0227]	13.85 [0.1304]	20.0 [14.83]	9.63 [0.050]	N/A	N/A
pDCPD-20-X-MMA-20	3.05 [0.0227]	13.85 [0.1304]	20.0 [14.83]	9.63 [0.050]	2.40 [0.0227]	2.0 [1.22]
pDCPD-20-X-MMA-30	3.05 [0.0227]	13.85 [0.1304]	20.0 [14.83]	9.63 [0.050]	3.62 [0.0341]	2.0 [1.22]
pDCPD-20-X-MMA-40	3.05 [0.0227]	13.85 [0.1304]	20.0 [14.83]	9.63 [0.050]	4.82 [0.0454]	2.0 [1.22]
pDCPD-20-X-MMA-50	3.05 [0.0227]	13.85 [0.1304]	20.0 [14.83]	9.63 [0.050]	6.03 [0.0568]	2.0 [1.22]
pDCPD-30	4.58 [0.0341]	12.10 [0.1141]	30.0 [23.00]	7.23 [0.025]	N/A	N/A
pDCPD-30-X-MMA-20	4.58 [0.0341]	12.10 [0.1141]	30.0 [23.00]	7.23 [0.025]	3.62 [0.0341]	2.0 [1.22]
pDCPD-30-X-MMA-30	4.58 [0.0341]	12.10 [0.1141]	30.0 [23.00]	7.23 [0.025]	5.43 [0.0512]	2.0 [1.22]
pDCPD-30-X-MMA-40	4.58 [0.0341]	12.10 [0.1141]	30.0 [23.00]	7.23 [0.025]	7.23 [0.0683]	2.0 [1.22]
pDCPD-30-X-MMA-50	4.58 [0.0341]	12.10 [0.1141]	30.0 [23.00]	7.23 [0.025]	9.05 [0.0853]	2.0 [1.22]
pDCPD-40	6.10 [0.0455]	10.40 [0.0978]	40.0 [31.75]	9.63 [0.025]	N/A	N/A
pDCPD-40-X-MMA-20	6.10 [0.0455]	10.40 [0.0978]	40.0 [31.75]	9.63 [0.025]	4.83 [0.0455]	2.0 [1.22]
pDCPD-40-X-MMA-30	6.10 [0.0455]	10.40 [0.0978]	40.0 [31.75]	9.63 [0.025]	7.23 [0.0683]	2.0 [1.22]
pDCPD-40-X-MMA-40	6.10 [0.0455]	10.40 [0.0978]	40.0 [31.75]	9.63 [0.025]	9.65 [0.0910]	2.0 [1.22]
pDCPD-40-X-MMA-50	6.10 [0.0455]	10.40 [0.0978]	40.0 [31.75]	9.63 [0.025]	12.07 [0.1138]	2.0 [1.22]

a **GC-II** was dissolved in 1 mL of the total toluene to make Solution B; DCPD was dissolved in the remaining toluene to make Solution A. b That amount of MMA corresponds to the total amount of DCPD that was used for each sol, and was dissolved in a volume of toluene that was 4 times the volume of the corresponding swollen wet-gels to be crosslinked. Since only the 1/5 of the total amount of MMA eventually enters the gel, the amount of MMA dissolved in toluene was set at five times the desirable amount of MMA in the pores after equilibration. Since the original DCPD in the total sol was divided in several separate molds, the total MMA stock solution was allocated to each wet-gel monolith according to its volume. c AIBN was included in the MMA solution in the prescribed proportion to MMA.

Table 2. Formulations for **pNB** aerogels

sample	NB (g) [mol]	toluene (g) [mL; mol]	2-propanol (g) [mL; mol]	GC-II (%mol vs. NB)	NB (% mol/mol) [a] [M]
pNB-30(50:50)	6.0 [0.0638]	7.00 [8.10; 0.0760]	7.00 [8.90; 0.1167]	0.0125	24.85 [2.59]
pNB-30(30:70)	6.0 [0.0638]	4.20 [4.85; 0.0456]	9.80 [12.45; 0.163]	0.0125	23.40 [2.56]
pNB-30(10:90)	6.0 [0.0638]	1.40 [1.60; 0.0152]	12.6 [16.05; 0.210]	0.0125	22.07 [2.53]
pNB-30(0:100) [b]	6.0 [0.0638]	0.09 [0.10; 0.0009]	14.0 [17.80; 0.233]	0.0125	21.50 [2.50]

a 100×(mol NB/ (mol toluene + mol 2-propanol + mol NB). b Contains 100 μL of toluene needed to dissolve **GC-II**.

Number- and weight-average molecular weights (M_n and M_w, respectively) and polydispersity indexes (M_w/M_n) of the **pNB-30(zz:ww)** aerogels were determined by gel permeation chromatography (GPC).[37] A few mg of each **pNB-30(zz:ww)** aerogel sample was dissolved in THF. GPC was conducted with a Shodex GPC KH-803L column connected to a Schimadzu liquid chromatograph (LC-10AD) equipped with a UV-Vis detector (SPD-10AV). HPLC grade THF was used as eluent at 1 mL min^{-1}. Linear polystyrene standards from Varian (Polystyrene Low EasiVials; Part No. PL2010-0400 and PL2010-0403) were used for calibration.

Surface areas and pore size distributions were measured by N_2 sorption porosimetry, using a Micromeritics ASAP 2020 surface area and porosity analyzer. Samples for surface area and skeletal density determination were outgassed for 24 h at 80 °C (except pNB aerogel samples, which were outgassed at 50 °C) under vacuum before analysis. Average pore diameters were determined by the $4 \times V_{Total}/\sigma$ method, where V_{Total} is the total pore volume per gram of sample and σ, the surface area determined by the Brunauer-Emmett-Teller (BET) method. V_{Total} was either taken from the highest volume of N_2 adsorbed along the adsorption isotherm, or it was calculated via $V_{Total}=(1/\rho_b)-(1/\rho_s)$. Since **pNB-30(zz:ww)** aerogels are macroporous materials, their average pore diameter and pore size distributions were probed with Hg-intrusion porosimetry using a Micromeritics Autopore IV model 9500 instrument operated in the intrusion-only/set-time equilibration (10 s) mode. **pNB-30(zz:ww)** samples were outgassed for 12 h at 50 °C before analysis. Pore sizes were calculated with the Washburn equation assuming cylindrical pores. Plotting the log differential intrusion volume (V) vs. pore diameter (D)

(dV/dlog$D$ vs. D) gives information about the average pore size and pore size distribution.

Scanning electron microscopy (SEM) was conducted with Au-coated samples on a Hitachi Model S-4700 field-emission microscope.

Thermogravimetric analysis (TGA) was conducted under air or N_2 with a TA Instruments model TGA Q50 thermogravimetric analyzer at a heating rate of 10 ^{o}C min^{-1}.

Modulated Differential Scanning Calorimetry (MDSC) was conducted under N_2 with a TA Instruments Differential Scanning Calorimeter Model Q2000 at a heating rate of 10 °C min^{-1} in the modulated T4P mode, using 60 s as the modulation period and 1 °C as the modulation amplitude. The mass of each sample was approximately 6-10 mg. Samples were subjected to one heating scan (0-230 ^{o}C), one cooling scan (230-0 ^{o}C) and a second heating scan (0-380 ^{o}C). Glass transition temperatures were determined from the second heating scan. Heat capacities, c_P, at 23 ^{o}C of powders (4-8 mg), needed for the determination of their thermal conductivity, λ, were measured using the MDSC calibrated against a sapphire standard and run from 0 ^{o}C to 40 ^{o}C at 0.5 ^{o}C min^{-1} in the modulated T4P mode, using 100 s as the modulation period and 0.13 ^{o}C as the modulation amplitude. Raw c_P data were divided by a factor of (0.950 ± 0.014) based on measuring the heat capacities of rutile, graphite and corundum, just before running our samples, and comparing with literature values.

Thermal diffusivity, R, was determined with a Netzsch NanoFlash Model LFA 447 flash diffusivity instrument using disk samples ~1 cm in diameter, 1.8-2.5 mm thick. Before every run the instrument reliability was confirmed with manufacturer provided standards (Pyrex 7740, Pyrocream 9606, 99.8% Alumina and AXM-5Q Poco Graphite).

The rheological behavior of DCPD sols was measured with a TA Instruments AR 2000ex Rheometer using a cone (60 mm diameter, 2° angle) and a Peltier plate geometry with a 1 mm gap between them. The instrument was operated in the continuous oscillation mode and time sweep experiments were performed with a fixed strain amplitude from the moment of addition of **GC-II** in DCPD solution, till gelation. The gel point was determined using a dynamic multiwave method with three superimposed harmonics with frequencies 1, 4, and 8 rad s^{-1}. The strain of the fundamental oscillation (1 rad s^{-1}) was set at 5%.

The structure of the fundamental building blocks of the materials was probed with small-angle X-ray scattering (SAXS), using 2-3 mm-thick disks, 0.7-1.0 cm in diameter. SAXS was carried out with a PANalytical X'Pert Pro multipurpose diffractometer (MPD), configured for SAXS using Cu Kα radiation (λ= 1.54 Å) and a $1/32^o$ SAXS slit and a $1/16^o$ anti-scatter slit on the incident beam side, and 0.1 mm anti-scatter slit and Ni 0.125 mm automatic beam attenuator on the diffracted beam side. The samples were placed in circular holders between thin Mylar^{TM} sheets and scattering intensities were measured with a point detector in transmission geometry by 2 Theta scans ranging from -0.1 up to 5°. All scattering data are reported in arbitrary units as a function of Q, the momentum transferred during a scattering event. Data analysis was conducted according to the Beaucage Unified Model,[38] using the *Irena SAS* tool for modeling and analysis of small angle scattering within the commercial *Igor Pro* application (scientific graphing, image processing, and data analysis software from WaveMetrics).[39]

Quasi-static compression testing at low strain rates was conducted on an MTS-810 servo-hydraulic testing machine, following the testing procedures and specimen

length/diameter ratio in ASTM D1621-04a (Standard Test Method for Compressive Properties of Rigid Cellular Plastics), as described before.[40] The specimens had a nominal diameter of 1.2 cm and a length/diameter ratio of one. The recorded force as a function of displacement (machine-compliance corrected) was converted into stress as a function of strain. Compression experiments at high strain rates (about 1,000 s^{-1}) were conducted on a long split-Hopkinson pressure bar (SHPB) under ambient conditions.[41] The SHPB consists of a steel striker bar, incident and transmission bars, and a strain data acquisition system. Disk-shaped samples (0.2´´-0.25´´ thick, 0.48´´-00.57´´ in diameter) were sandwiched between the incident and transmission bars. The incident bar was made of 304L stainless steel, it was 8,810 mm long and its outer diameter was 19 mm. The transmission bar was made of a solid 7075-T651 aluminum rod, it was 3,660 mm long and its outer diameter was also 19 mm. That modification took advantage of the low Young's modulus of aluminum (~1/3 of steel) in order to reach high signal-to-noise ratios for the transmitted signal,[42] similar to those accessible with hollow transmission steel tubes.[7b] A Cu disk pulse shaper was used to reach a dynamic stress equilibrium state and constant strain rates, removing the dispersion of the incident wave due to the bar geometry, which is necessary for a valid SHPB experiment.[41c]

3. Results and Discussion

3.1. Materials design. Bottom-up synthesis of organic aerogels involves polymerization of monomer(s). However, although many polymeric solutions gel, only a sub-set can be dried into aerogels. Solutions of polymers with progressively increasing molecular weight either build sufficiently high viscosity and stop flowing, or undergo phase separation of colloidal particles due to insolubility of the growing polymer in the

polymerization solvent. Linear polymers formed in true-solvents for the polymer tend to give polymer gels due to high viscosity; if formed in non-solvents for the polymer they may give either precipitates or flocs. Linear polymer gels collapse upon drying in order to maximize the non-covalent interactions between polymeric strands. On the other hand, if phase-separated colloidal particles can develop covalent bonding with one another through their surface functional groups, then the network stores enough chemical energy to resist collapse, and gel can be dried into aerogels keeping approximately the volume of the original wet-gels. Formation of such three-dimensional networks of colloidal particles is more often possible with crosslinked polymers. Therefore, careful choice of monomers is essential.[19]

Reportedly,[34,35] DCPD is a crosslinkable monomer (Scheme 1), hence quite suitable for the synthesis of mechanically strong aerogels. Norbornene, on the other hand, is not a crosslinkable monomer, therefore should not be able to form robust nanostructures. During preparation, pDCPD wet-gels got severely deformed. That was rectified by incorporating PMMA in the pDCPD network; afterwards pDCPD/PMMA and pNB aerogels were similarly strong materials. This defies expectations set forth above, and a detailed investigation led naturally to a comparative study of the two nanoporous materials from molecular to bulk through nano.

3.2. Synthesis of pDCPD and pNB aerogels and the need for crosslinking. Following literature reports,[29,31] ROMP of DCPD was carried out in toluene where the polymer, pDCPD, was expected to undergo early phase separation of small nanoparticles. The concentration of the second-generation Grubbs' catalyst, **GC-II**, was varied slightly in order to keep the apparent gelation time, and therefore the heat release rates about

constant. The process is summarized in Scheme 2. The weight percent of DCPD in the sol (designated in the sample names with extensions –xx: -20, -30, -40) was varied in order to produce variable density aerogels (see Experimental). Attempts to gel lower concentration sols (e.g., pDCPD-05) gave gels (10 min), which dissolved spontaneously (12 h) to free-flowing solutions that eventually turned into thixotropic liquids: they are gel-like, but flow freely upon shaking. This aspect has not been pursued further yet, but the behavior of the pDCPD-05 sols is partly consistent with Wagener's observations, whereas Shrock's metathesis catalyst in low DCPD concentrations yielded soluble polymer.[35] **pDCPD-xx** aerogels obtained with the –xx: -20, -30, -40 formulations were stable and insoluble in all common solvents.

Scheme 2. Synthesis of **pDCPD-xx** and **pDCPD-xx-X-MMA-yy** aerogels
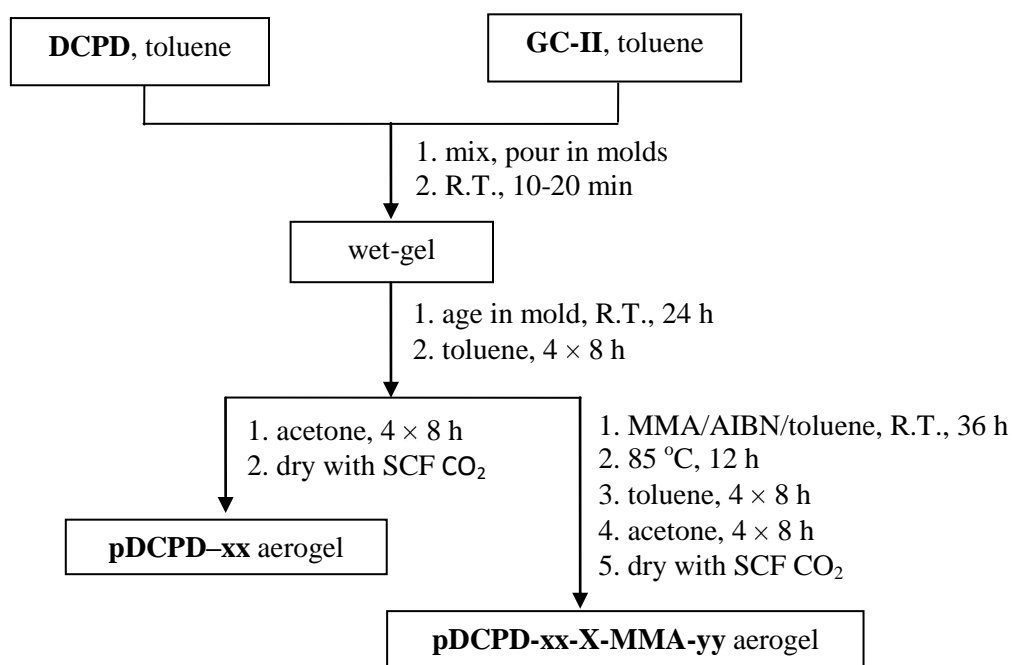
On the other hand, polynorbornene, pNB, is soluble in toluene and ROMP typically proceeds to viscous solutions that may look like gels, but they collapse

completely upon drying (case of linear polymer gels -see Section 3.1). To decrease the solubility of pNB in the polymerization medium and induce phase-separation, we added *i*PrOH, working our way to pure *i*PrOH. The toluene/*i*PrOH (w/w) ratio is designated with extensions (zz:ww) in the sample names. The process is summarized in Scheme 3. For comparison with **pDCPD-xx** aerogels, the concentration of the sol was fixed to pNB-30, which corresponds to about the middle of the concentration range of the pDCPD gels. In typical good solvents for pNB, such as toluene and THF, **pNB-30(zz:ww)** aerogels first swell and eventually dissolve completely with the help of some sonication.

Scheme 3. Synthesis of monolithic polynorbornene **pNB-30(zz:ww)** aerogels
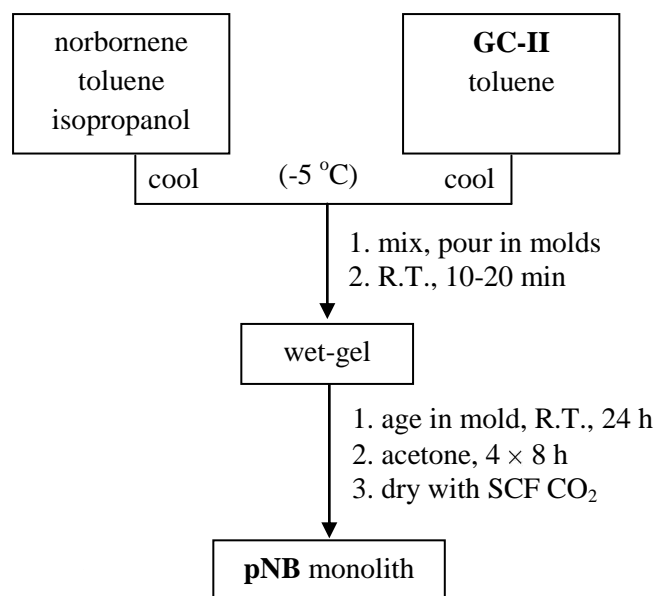
Within the conditions above, in both cases gelation proceeded uneventfully. In the case of pDCPD, the process was monitored with rheometry in the multiwave oscillation mode (see Experimental). Figure 1 shows typical data obtained with oscillation frequency $\omega = 1$ rad s^{-1}. Near the gelation point, the storage modulus (G') crosses over the loss modulus (G''), however the actual gelation point is defined as the common, independent-

of-ω, crossing point of all $\tan\delta$ ($=G''/G'$).[43] That common crossing point is better detected in the plot of the statistical variable log(s/$<\tan\delta>$) versus time (see Inset in Figure 1; s: standard deviation of the three $\tan\delta$ at three different ω at each sampling time during gelation – see Experimental).[44] At the gelation point, $\tan\delta = \tan(n\pi/2)$,[45] whereas the gel relaxation exponent, n, is related via $n=[D(D+2-2D_f)]/2(D+2-D_f)$ to the fractal dimension, D_f, of the particles that form the gel (for three-dimensional non-fractal clusters, $D_f=D=3$).[46] The data are summarized in Table 3 for all three formulations (concentrations) of the DCPD sols. Since in all three cases $D_f<3$, we conclude that the gel network is formed by mass-fractal particles via diffusion-limited growth.[47] In other words, the particles that meet the percolation threshold have internal structure, i.e., they consist of smaller particles and include extra empty space in addition to that expected from closely packed spheres, which is already substantial: 25.95% v/v for cubic or hexagonal arrangement, and 36.3% v/v for random packing.[48]

Table 3. Rheometry data from the gelation of the three DCPD sols as indicated

Sample	gelation point, t_{gel} (s)	tan δ at t_{gel}	n	D_f
pDCPD-20	170	0.300	0.186	2.33
pDCPD-30	354	0.235	0.147	2.37
pDCPD-40	354	0.187	0.118	2.40

pDCPD wet-gels were removed from their molds and washed with toluene (4×), then acetone (4×) and dried with liquid CO_2 taken out as a SCF according to standard procedures (see Introduction). Two important observations were made during those procedures. First, wet-gels swelled significantly during toluene washes. Figure 2A shows

two wet-gel monoliths, one right out of the mold, and one after 4 toluene washes. In turn, Figure 3 shows that swelling, both in linear dimensions and in volume, proceeds linearly with time. (In fact, swelling continued unobstructed even in the toluene/MMA crosslinking baths, and during the additional toluene washes to remove unbound PMMA - see below). Second, in preparation for drying with SCF CO_2, the solvent was changed to acetone. In acetone, wet-gels de-swelled rapidly (within the first wash) and shrunk unevenly, getting deformed completely. Consequently, the resulting aerogels were irregular-shaped objects with bulges and voids (see Figure 2B),[49] unsuitable for practical purposes. Attempts to exchange toluene with acetone progressively did not prevent severe deformation. Also, taking toluene-filled gels right after aging directly from toluene into acetone had the same bad effect.

Volume changes in polymer gels, whether continuous or discontinuous (sometimes accompanied by phase transitions - the subject was not investigated here) are traced to upsetting the fine balance of molecular forces between polymeric strands (ionic, hydrophobic, van der Waals, hydrogen bonding), interaction with the solvent and the stiffness of the network.[50] Therefore, swelling of pDCPD wet-gels is attributed to the flexibility of the polymeric network on one hand, and the affinity of the hydrocarbon backbone for toluene on the other. Conversely, de-swelling is attributed to the prevalence of the hydrophobic/van der Waals interactions between polymeric strands over interaction with polar acetone. However, this view does not account for the nanostructure, hence cannot explain disorderly de-swelling.

The case of pNB is different. The main component of the gelation solvent (*i*PrOH) is polar, with low affinity for the network. pNB wet-gels were placed directly in

acetone, and no swelling or de-swelling was observed. Efforts to adopt lessons learned from pNB into pDCPD were not fruitful: although pDCPD gels made in *i*PrOH did not deform by going to acetone, nevertheless the resulting **pDCPD-30** aerogels were chalky with minimal structural integrity, suggesting that wet-gels were flocks rather than gels.

Initially, the deformation of pDCPD gels was attributed to a lack of quantitative crosslinking between polymeric strands. This was based upon both literature reports, and independent evidence gathered herewith. Indeed, crosslinking in pDCPD has been controversial. As shown by Wagener, the Schrock's Mo-alkylidene catalyst, $Mo(CH-CMe_2Ph)(N-2,6-C_6H_3-iPr_2)(OCMe(CF_3)_2)_2$,[51] which is generally considered more active towards olefin metathesis than Grubbs' catalysts, does not promote metathesis of the pendant cyclopentene ring of pDCPD. Crosslinking (justified by the insolubility of pDCPD) was attributed by Wagener to olefin coupling of cyclopentene rings, induced by the intense heat released from the ROMP of the norbornene moiety (see Scheme 1).[35] The extent of that crosslining though was not quantified. For our purposes, using ^{1}H NMR of 5,6-dihydrodicyclopentadiene (**dhDCPD** – Wagener's control molecule),[35] we have

dhDCPD
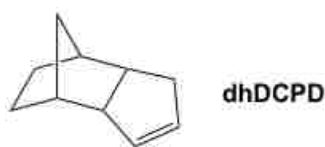
confirmed that nor **GC-II** is able to induce metathesis of the pendant cyclopentene ring, either under ambient conditions, or after 15 h at 70 ^{o}C (see Figure S.1 in Supporting Information). Furthermore, ^{1}H NMR during polymerization of low concentrations of DCPD (corresponding to the pDCPD-05 formulation that would not give stable gels as described above) shows clearly that the cyclopentene double bond is not involved in

reaction quantitatively (see Figure S.2 in Supporting Information). On the other hand, in highly exothermic polymerizations of DCPD at higher concentrations (corresponding to the pDCPD-30 formulation) the vinylic proton resonances from the cyclopentene ring progressively disappear (see Figure S.3 in Supporting Information). It remains, however, ambiguous whether all cyclopentene reacted, as its vinylic protons may be hiding underneath the broad resonance of the *cis*-vinylic protons of the backbone. Turning to FTIR (Figure 4), the absorption bands of the DCPD monomer at 1572 and 1614 cm^{-1} are assigned to the C=C stretching vibrations of the norbornene and cyclopentene double bonds, respectively. (The IR spectra of both DCPD and **dhDCPD** are included in Figure 4 for comparison.) The 1572 cm^{-1} absorption has disappeared from the FTIR spectrum of the **pDCPD-30** aerogels, which shows two characteristic features at 1716 and 1620 cm^{-1}. Consistent with the FTIR spectrum of pNB, the 1716 cm^{-1} absorption is assigned to the *trans* C=C stretch in the polymer backbone, and the 1653 cm^{-1} shoulder to the *cis* configuration.[52] In turn, the 1620 cm^{-1} absorption is assigned to the C=C stretch in pendant cyclopentene rings,[53] indicating that they have not been involved in crosslinking quantitatively.

At that point, the extent of crosslinking was actually quantified via solids CPMAS ^{13}C NMR. Having excluded metathesis-type crosslinking, the only viable possibility is Wagener-type crosslinking. That should decrease the size of the sp^2-C resonance at 131 ppm and add the same amount of carbon in the aliphatic region (30-60 ppm). The fraction, *x*, of the cyclopentene double bonds reacting in Wagener-type crosslinking is given by:

$$(2-x)/(3+x) = [C\text{-alkene}/C\text{-aliphatic}]_{\text{experimental}}$$

From the CPMAS ^{13}C NMR spectrum of the **pDCPD-30** aerogel shown in Figure 5A, [C-alkene/C-aliphatic]$_{experimental}$=0.641, so x=0.047. Therefore, *only* 4.7% of the pendant cyclopentene rings of **pDCPD-30** have been involved in crosslinking.

Based on the above, the immediate consideration was to get the pDCPD-xx networks rigidized at the molecular level by additional crosslinking between polymeric strands through either the pendant cyclopentene rings, or the double bonds of the ROMP-derived backbone. For that purpose, we would have to consider only soluble polymers that could be removed easily if unbound.

Control ^{1}H NMR and GC-MS experiments with DCPD+AIBN and polynorbornene+MMA+AIBN (see Figures S.4-S.6 in Supporting Information) show that allylic positions as well as both the cyclopentene and the backbone double bonds of the ROMP polymer can be engaged in the AIBN-induced free-radical polymerization of MMA, leaving many possibilities open for attachment of the growing polymer (PMMA) on the pDCPD backbone (Scheme 4).

Thus, toluene-washed pDCPD wet-gels were equilibrated with toluene solutions of variable MMA/AIBN concentrations. Subsequently, gels were heated in the equilibration baths to induce polymerization of MMA. The bath solution became viscous, loose PMMA was removed with extensive toluene and acetone washes, and gels were dried with CO_2 (refer to Scheme 2). As mentioned above, swelling continues linearly with time in toluene during and after MMA treatment, followed by rapid de-swelling during acetone washes (Figure 3). However, after MMA treatment de-swelling was orderly: all wet-gels kept their shape, and returned to approximately the size of their molds. The resulting aerogels were regular cylinders (Figure 2B).

Scheme 4. The structure of pDCPD and options for attachment of PMMA on the polymer backbone (For simplicity, only the *trans* backbone structure is shown; arrows indicate positions of possible allyl radical formation.)
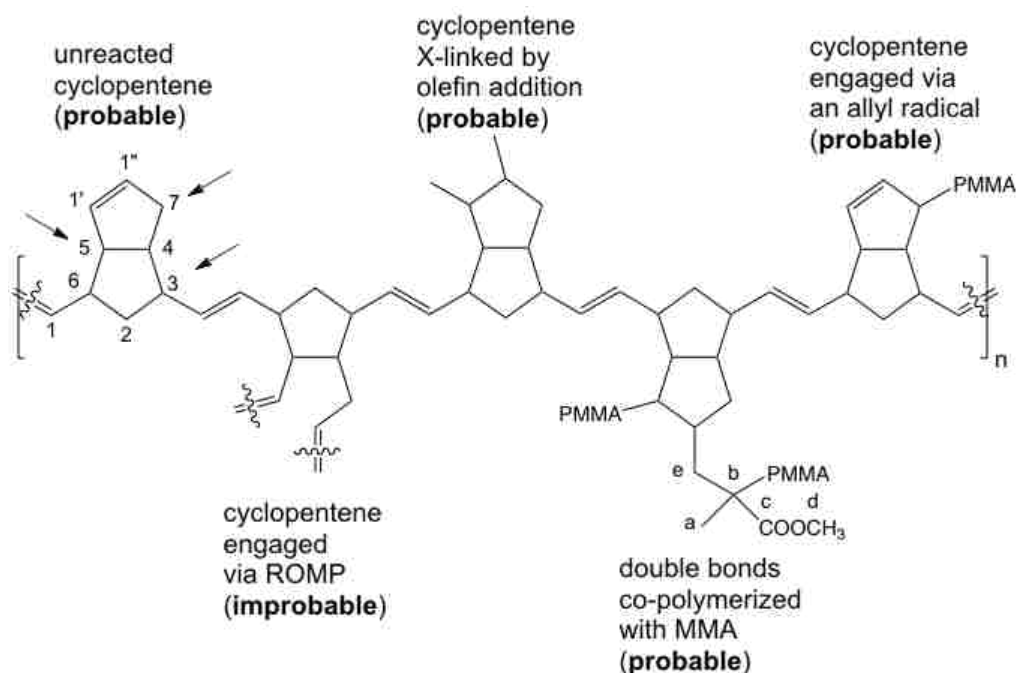
The uptake of PMMA was confirmed by FTIR (Figure 4) and solids CPMAS ^{13}C NMR (Figure 5). In FTIR, apart from the new PMMA-assigned absorptions of the C=O stretch at 1730 cm^{-1} and the C-O stretches in the 1140-1250 cm^{-1} region (traced with dashed lines), the absorption at 1620 cm^{-1}, assigned to the C=C stretch of cyclopentene, is still strong. Solids ^{13}C NMR also shows resonances from both pDCPD and PMMA (Figure 5A; for peak assignment refer to Scheme 4). As described in the Experimental section, the concentrations of the MMA baths were formulated so that after equilibration the mol ratio of MMA to DCPD monomer units inside the gel would be fixed at prescribed values, which are reported with extension -yy in the sample names (**pDCPD-xx-X-MMA-yy**). Thus, it was found that the ^{13}C NMR peak ratio of C=O$_{from\_PMMA}$:C=C$_{from\_pDCPD}$ varies linearly with the MMA:DCPD (mol:mol) in the gel formulation (see Figure 5B). The slope (0.25±0.02) is equal to the slope expected for a

random blend of the two polymers, pDCPD and PPMA, at the prescribed ratios, signifying that: (a) all MMA put in the gels has been attached to pDCPD as PMMA quantitatively (hence cannot be washed off); and, (b) PMMA engages only a small amount of the pDCPD double bonds, below the differentiation limit of solids ^{13}C NMR. Engagement of allylic positions along the pDCPD backbone cannot be inferred, because of overlapping aliphatic carbons. Finally, the linear relationship of Figure 5B allows quantification of the relative amounts of pDCPD and PMMA, based on the initial formulation. The amount of PMMA varies from ~13% w/w in **pDCPD-30-X-MMA-20** to ~28% w/w in **pDCPD-30-X-MMA-50**. (It is noted that in polymer-crosslinked aerogels, the polymer content is higher, in the range of 20-75% w/w. [54])

Overall, spectroscopic data show that neither pDCPD is quantitatively crosslinked within itself, nor PMMA seems to participate in extensive crosslinking. In fact, DSC (see Figure S.7 in Supporting Information) shows glass transitions for both **pDCPD-30** and **pDCPD-30-X-MMA-yy** aerogels, confirming the linear character of both polymers, and suggesting that PMMA is mostly dangling from the pDCPD backbone (as opposed to bridging). Clearly, quantitative crosslinking with PMMA at the molecular level has to be ruled out as causing the dimensional stability gained by inducing polymerization of MMA in the pores of pDCPD wet-gels. Hence, the reasons of the structural integrity gained with PMMA will have to be traced at the next structural level (1-100 nm). That inquiry leads naturally into a detailed investigation of the nanostructure.

3.3. Material properties and nanoscopic characterization of pDCPD and pNB aerogels. Microscopically, by SEM, both pDCPD and pNB aerogels consist of open-pore structures made of three-dimensional networks of interconnected nanoparticles (Figures 6

and 7, respectively). Qualitatively, the particles and pore sizes in pDCPD aerogels are much smaller (in the nm range) than those in pNB (in the μm range). Uptake of considerable amounts of PMMA in pDCPD aerogels (13-28% w/w as concluded above) does not affect the microstructure in an obvious manner. Basically, PMMA is not visible. Upon closer examination (refer to the 2.5× magnified insets in Figure 6), in **pDCPD-30** and **pDCPD-30-X-MMA-20** we see particles (pointed with arrows) fused together to larger entities (circles), while in **pDCPD-30-X-MMA-30** and **pDCPD-30-X-MMA-40** the larger entities in circles become less clattered, and finer structure (arrows) becomes visible more clearly. The same basic structure is visible in pNB aerogels made with higher concentrations of *i*PrOH, signifying the role of particle growth up to the point of the phase-separation in nanostructure formation. In other words, consistent with those results, the more insoluble the polymer, the smaller and more numerous the resulting particles and the smaller the pores. As the solvent becomes more compatible with the polymer [case of **pNB-30(50:50)]** particles are no longer visible, the structure turns bi-continuous, implying spinodal decomposition.[30a]

General materials characterization data for pDCPD and pNB samples are summarized in Tables 4 and 5, respectively. Irrespective of volume changes taking place during processing of wet-gels (swelling/de-swelling), aerogels obtained from lower concentration sols (**pDCPD-20-X-MMA-yy**) shrank 13-17% in linear dimensions relative to their molds. pNB samples shrank more (17-29%), and among those, samples made in 100% *i*PrOH shrank the least. (The last observation stems from the role of the solvent affinity to the polymer backbone for swelling.) Shrinking of pDCPD aerogels decreases with increasing DCPD concentration in the sol, and is less for **pDCPD-30-X-**

MMA-yy samples (0-10%), while **pDCPD-40-X-MMA-yy** samples do not shrink at all; in fact, they are slightly larger than the molds. Variable shrinkage is reflected on the bulk densities, ρ_b, which do not vary as much as one would have expected from the linear increase of the PMMA uptake with the MMA/DCPD ratio (referring to the ^{13}C NMR data in Figure 5B). Measurement of bulk densities of deformed **pDCPD-xx** aerogels was not attempted. The skeletal densities, ρ_s, of **pDCPD-xx** aerogels are in the range expected for polydicyclopentadiene (1.03 g cm^{-3}),[55] hence no close porosity is present. Upon PMMA uptake, ρ_s values increase towards the density of bulk PMMA (1.18 g cm^{-3}). Percent porosities of all X-samples (calculated from bulk and skeletal densities via $\Pi=100\times[(\rho_s-\rho_b)/\rho_s]$) do not vary systematically with PMMA uptake, and range from 57% to 70% v/v. The microstructure of pDCPD aerogels was probed further with N_2 sorption porosimetry (data included in Figure 6), and of pNB aerogels with N_2 sorption as well as Hg intrusion porosimetry (data shown in Figure 7).

The N_2 sorption isotherms of all pDCPD aerogels reach saturation with well-defined hysteresis loops indicating mesoporous materials. Nearly vertical and parallel adsorption and desorption branches indicate aggregates and narrow pore size distributions, which is evident from the BJH-desorption plots (insets in Figure 6 and data in Table 4). Reflecting the macroscopic collapse at the nanoscopic level, the BET surface areas, σ, of the **pDCPD-xx** aerogels are all much lower (38-39 m^2 g^{-1}) than those of the samples that contain PMMA, doubling in the samples with the least amount of PMMA (77-99 m^2 g^{-1} in **pDCPD-xx-X-MMA-20**), and keeping on increasing with more PMMA uptake, reaching 121 m^2 g^{-1} in certain **pDCPD-xx-X-MMA-50** samples.

Table 4. Material characterization data for all pDCPD aerogels

sample	diameter (cm)[a]	shrinkage (%)[a,b]	bulk density, ρ_b (g cm^{-3})[a]	skeletal density, ρ_s (g cm^{-3})[c]	porosity, Π (% void space)	BET surface area, σ (m^2 g^{-1})	average pore diameter, (nm)[d]	average pore diameter, (nm)[e]	particle radius, r (nm)[h]
pDCPD-20	f	f	f	1.055 ± 0.004	f	37.7	32.4	40.4[34.8]	75.4
pDCPD-20-X-MMA-20	0.83$_3$ ± 0.02$_8$	17 ± 3	0.34$_3$ ± 0.01$_3$	1.089 ± 0.003	69	98.7	17.9	26.0[21.9]	27.9
pDCPD-20-X-MMA-30	0.83$_1$ ± 0.02$_1$	17 ± 2	0.37$_1$ ± 0.02$_2$	1.080 ± 0.004	66	86.6	30.2	33.0[17.7]	32.1
pDCPD-20-X-MMA-40	0.84$_0$ ± 0.01$_6$	16 ± 2	0.386 ± 0.017	1.091 ± 0.007	65	105.1	19.2	27.6[19.5]	26.2
pDCPD-20-X-MMA-50	0.87$_1$ ± 0.01$_9$	13 ± 2	0.349 ± 0.018	1.154 ± 0.002	70	121.3	17.3	26.5[17.5]	21.4
pDCPD-30	f	f	f	1.011 ± 0.003	f	38.7	23.2	28.5[12.1]	76.7
pDCPD-30-X-MMA-20	0.90$_5$ ± 0.04$_5$	10 ± 5	0.44$_1$ ± 0.06$_0$	1.095 ± 0.001	60	77.3	19.7	21.8[9.9]	35.4
pDCPD-30-X-MMA-30	0.95$_5$ ± 0.01$_8$	5 ± 2	0.40$_3$ ± 0.03$_2$	1.155 ± 0.002	65	106.0	25.0	23.2[10.7]	24.5
pDCPD-30-X-MMA-40	0.94$_3$ ± 0.02$_0$	6 ± 2	0.43$_6$ ± 0.02$_8$	1.148 ± 0.002	62	93.0	20.9	25.0[10.2]	28.1
pDCPD-30-X-MMA-50	1.00$_7$ ± 0.04$_1$	g	0.39$_5$ ± 0.03$_4$	1.164 ± 0.004	66	120.5	18.4	25.1[12.2]	21.4
pDCPD-40	f	f	f	1.095 ± 0.003	f	37.3	22.1	29.0[13.3]	73.4
pDCPD-40-X-MMA-20	1.022 ± 0.007	g	0.472 ± 0.006	1.092 ± 0.004	57	99.3	23.7	33.5[13.1]	27.7
pDCPD-40-X-MMA-30	1.07$_5$ ± 0.02$_8$	g	0.43$_2$ ± 0.02$_6$	1.136 ± 0.006	62	103.1	16.5	25.0[13.2]	25.6
pDCPD-40-X-MMA-40	1.08$_9$ ± 0.01$_2$	g	0.463 ± 0.008	1.134 ± 0.004	59	111.3	14.9	22.3[10.0]	23.8
pDCPD-40-X-MMA-50	1.09$_2$ ± 0.03$_7$	g	0.47$_0$ ± 0.05$_1$	1.168 ± 0.004	60	100.1	19.4	22.2[12.1]	25.7

a Average of 4 samples. (Mold diameter: 1.0 cm.) b Shrinkage = 100 × (sample diameter – mold diameter)/(mold diameter). c Single sample, average of 50 measurements. d By the $4 \times V_{Total}/\sigma$ method. V_{Total} by the single-point adsorption method. e From BJH desorption plot. The first numbers are peak maxima; numbers in brackets are full widths at half maxima. f Deformed cylinder; not measured. g Those samples did not shrink relative to their molds. h Calculated via $r = 3/\rho_s\sigma$

Table 5. Material characterization data for all pNB aerogels

sample	diameter, (cm) [a]	shrinkage (%) [a, b]	bulk density, ρ_b (g cm^{-3}) [a]	skeletal density, ρ_s (g cm^{-3}) [c]	porosity, Π (% void space)	BET surface area, σ (m^2 g^{-1})	Avg. pore diam. (μm) [d]	Avg. pore diam. (μm) [e]	particle radius, (μm) [f]
PNB-30(50:50)	1.427 ± 0.003	29 ± 1	$0.68_4 \pm 0.01_5$	1.002 ± 0.002	32	1.34	1.39	1.30[1.61]	2.23
								36.6[34.5] [g]	
PNB-30(30:70)	$1.60_9 \pm 0.01_2$	20 ± 1	0.449 ± 0.007	1.047 ± 0.004	57	3.06	1.66	1.70[0.94]	0.94
PNB-30(10:90)	$1.68_4 \pm 0.01_2$	16 ± 1	0.395 ± 0.007	1.010 ± 0.002	61	2.68	2.30	2.15[1.21]	1.11
PNB-30(0:100)	$1.66_2 \pm 0.01_5$	17 ± 1	0.449 ± 0.005	0.976 ± 0.002	54	2.36	2.04	2.50[1.70]	1.30

a Average of 3 samples. (Mold diameter: 2.0 cm.) b Shrinkage $= 100 \times$ (sample diameter – mold diameter)/(mold diameter). c Single sample, average of 50 measurements. d By the $4 \times V_{Total}/\sigma$ method. V_{Total} was calculated via $V_{Total} = (1/\rho_b)-(1/\rho_s)$. e By Hg intrusion, from the log(differential intrusion) versus pore diameter plot. The first numbers are is maxima; numbers in brackets are full widths at half maxima. f Calculated via $r = 3/\rho_s\sigma$. g In nm (sample showed bi-modal pore size distribution).

Hence, it is concluded that PMMA keeps the nanostructure more open, with more surface area accessible, which is the *opposite* from what has been observed in polymer-crosslinked aerogels.[6,7] Further support for this conclusion is provided by average pore diameters. Those were either calculated by the $4\times V_{Total}/\sigma$ method (where the total volume of N_2 adsorbed, V_{Total}, was taken from the maximum adsorption point – the saturation plateau), or were obtained by the BJH method applied on the desorption branch of the isotherms. The two sets of values agree well with one another (Table 4), all falling in the mesoporous range. The average pore diameters of the **pDCPD-20** samples are larger (in the 32-40 nm range, depending on the method), and are reduced to 17-27 nm with PMMA uptake. Hence, again, PMMA prevents collapse and keeps the nanostructure more accessible to the probe (N_2). The same, but less dramatic, are the trends with **pDCPD-30** and **pDCPD-40** aerogels. Finally, particle radii calculated via $r=3/\rho_s\sigma$, are particularly revealing. Those are ~75 nm in all three **pDCPD-xx** aerogels, but they appear much smaller, in the 20-30 nm range, once PMMA is introduced. Clearly, since PMMA is introduced after the **pDCPD-xx** networks are formed, all **pDCPD-xx** aerogels must consist of smaller particles that collapse together in the absence of PMMA.

The case of pNB aerogels is different. N_2 sorption isotherms rise above partial pressure of 0.9, show no hysteresis loops and do not reach saturation, all consistent with macroporous materials. BET surface areas are small, just 1-3 $m^2\,g^{-1}$. Particle radii are in the 1-2 μm regime, consistent with SEM. Average pore diameters by Hg intrusion (see Table 5) are very close to those calculated via $4\times V_{Total}/\sigma$ [V_{Total} from $V_{Total}=(1/\rho_b)-(1/\rho_s)$], all in the micron range, thus confirming that the SEM particles in Figure 7 are dense with no internal structure.[56] (Curiously, the porosity of bi-continuous **pNB-30(50:50)** aerogels

appears clearly bimodal with pores both in the micro and nano-size regimes. That property could be interesting for applications in separation media, provided that the surface area could be increased.)

At this point, the only safe conclusion is that macroscopic deformation of **pDCPD-xx** aerogels is related to changes in the nanostructure. As implied by SEM, and as shown quantitatively by N_2 sorption, the skeletal network of **pDCPD-xx** has internal

Table 6. SAXS data for a selected series of pDCPD aerogels

	Primary Particles			Secondary Particles		
	high-Q	$R_g(1)$ [b]	R_1 [c]	low-Q	$R_g(2)$ [e]	R_2 [c]
	slope [a]	(nm)	(nm)	slope [d]	(nm)	(nm)
pDCPD-30	4.17±0.06	7.28±0.06	9.45±0.08	3.9±0.6	20.4±0.4	26.5±0.5
pDCPD-30-X-MMA-20	3.87±0.06	7.2±0.5	9.4±0.6	3.9±0.6	18.5±0.2	24.0±0.3
pDCPD-30-X-MMA-30	3.80±0.08	6.4±0.2	8.3±0.3	4.2±0.4	16.7±0.1	21.7±0.1
pDCPD-30-X-MMA-40	4.00±0.06	6.7±0.4	8.7±0.5	4.1±0.7	16.2±0.2	21.0±0.3
pDCPD-30-X-MMA-50	3.9±0.1	6.1±0.4	7.9±0.5	4.2±0.5	15.9±0.1	20.6±0.1

Referring to Figure 8: a From power-law Region I. b From Guinier Region II. c Particle radius = $R_g/0.77$. d From power-law Region III. e From Guinier Region IV.

structure not clearly visible in SEM. The obvious question is where PMMA is located on that nanostructure and how it prevents macroscopic deformation. To address this, the network nanostructure was probed with small angle x-ray scattering (SAXS). Typical data are shown in Figure 8. Scattering profiles were analyzed using the Beaucage Unified Model[38] and results are summarized in Table 6. The best fit was obtained using two

power-law regions (I and III) and two Guinier knees (II and IV), which are marked approximately in Figure 8 by vertical lines. In most samples, the slope of the high-Q power-law (Region I) is ~4.0, indicating that the smallest scatterers are smooth with abrupt interfaces. (The high-Q slope of **pDCPD-30**, equal to 4.2, implies a density gradient interface for the smallest particles.) According to SAXS, all samples tested in the **pDCPD-30** series consist of primary particles of about similar radius (R_1~8-9 nm). From the low-Q slopes (>3.0, Region III), we conclude that primary particles assemble into non-mass fractal secondary particles, with radii, R_2, that all fall in the 20.6-26.5 nm range. Three observations can be made by considering all data so far together:

(a) At first approximation the small downward trend in secondary particle size (radii 27--->21 nm, see Table 6) may be ignored, and the secondary particle size can be considered to be about the same among deformed **pDCPD-30** and underfomed **pDCPD-30-X-MMA-yy** samples. That suggests strongly that the collapse measured by N_2 sorption takes place at a length scale that is beyond secondary particles.

(b) The secondary particle radius from SAXS (R_2 – Table 6) and the particle size calculated from skeletal density and N_2 sorption data via $r=3/\rho_s\sigma$ (Table 4) converge as the amount of PMMA increases. For instance, for **pDCPD-30-X-MMA-50**, R_2=20.6 nm and r=21.4 nm. That is consistent with a collapse mechanism that brings secondary particles closer together, but otherwise leaves them intact. Unfortunately, SEM does not have the resolution to discern the smallest of the building blocks under our sample conditions; qualitatively, however, it does support this conclusion as discussed above, and particles shown by arrows are identified as secondary particles.

(c) SAXS clearly shows that secondary particles are not mass fractals (low-Q slopes>3); however, rheology has shown that the network is formed by mass fractal particles (D_f=2.37, Table 3). Therefore, the network is not formed by secondary particles, but by mass fractal aggregates of secondary particles.[57] Matching the length scales we are dealing with, those mass fractal aggregates have to be the globules shown by circles in SEM. Since by incorporating PMMA, secondary particles start becoming visible within those globules, we conclude that collapse takes place at the globule level, leaving secondary particles intact. The question still is how, and why PMMA prevents collapse.

To address this question, first we have to note that PMMA-incorporating wet-gels keep on swelling (linearly with time) in non-polar toluene and de-swell in acetone, hence: (a) the properties of the network are still determined by non-polar pDCPD rather than PMMA; and, (b) PMMA is segregated in places where it makes no difference in terms of the surfaces that come together during particle coalescence. Second, since PMMA is (a) invisible in SEM, but (b) capable to rigidize the aggregates making finer structure visible, it is safe to conclude that it is mostly contained within secondary particles. But, is there enough space within secondary particles to accommodate enough PMMA to make a difference? Yes, there is. Because secondary particles are randomly-packed non-fractal assemblies of primary particles, the empty space within is ~36%.[48] Hence, the density of the composite (pDCPD+PMMA) secondary particles should be equal to the weighted average of the densities of the two components, or about 1.1 g cm^{-3}, which matches quite well with the skeletal densities of the lower PMMA-content samples (Table 4). Then, as outlined in Scheme 5, it is reasonable to speculate that without PMMA secondary particles are squeezable, and by deforming they allow network-forming aggregates to

interpenetrate into the fractal space of one another. Obviously, this is not an orderly process, leading to macroscopic deformation with concurrent reduction in BET surface areas. Also, smaller pores get closed and larger ones are created to accommodate the void space generated by that fusion (hence, the average pore size increases). On the other hand, PMMA-filled secondary particles are more rigid, they cannot be deformed easily, and their fractal aggregates cannot interpenetrate into one another. Hence, wet-gels keep their shape, more internal space becomes available, BET surface areas increase and average pore diameters decrease.

Scheme 5. Mechanism for collapse of **pDCPD-xx** aerogels (A) and prevention by PMMA (B) (Colors are used in particles as a guide to the eye. All particles are the same.)
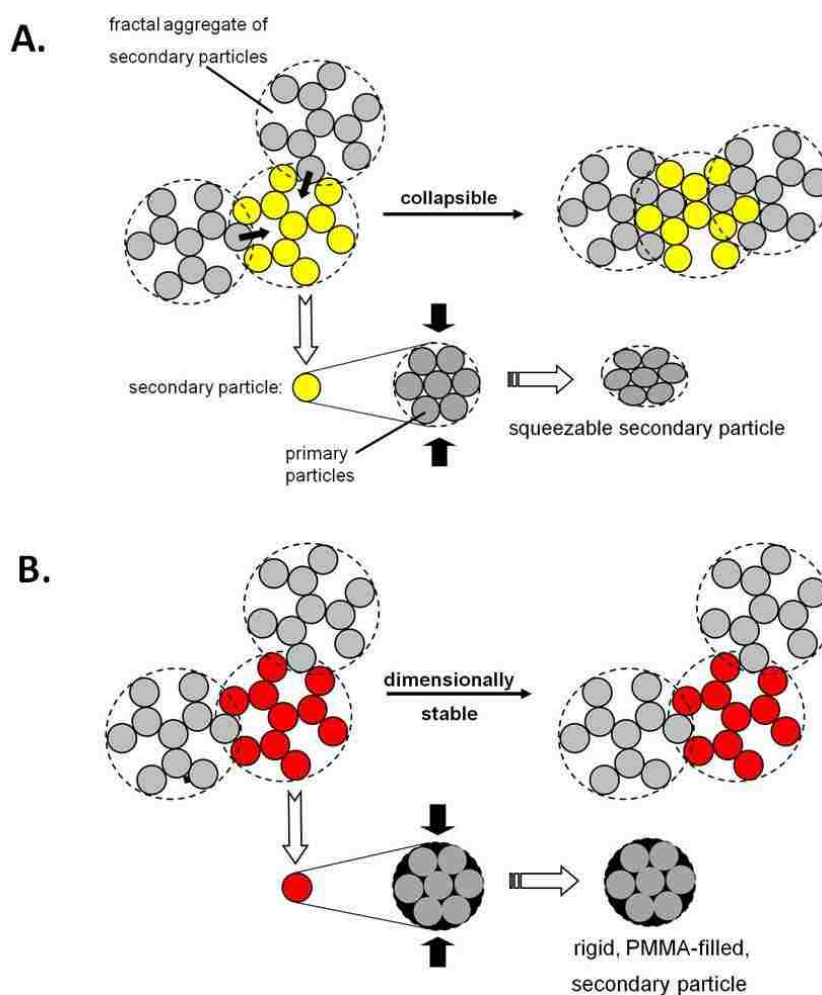
3.4. The interface of skeletal nanoparticles as inferred from the relationship of nanostructure and bulk properties. The primary property of interest in aerogels is their thermal conductivity. In addition, as outlined above, we have been attracted to this area by the possibility of mechanically strong lightweight materials by building chemical energy at the interface of nanoparticles. This section derives clues about the interface of skeletal nanoparticles in pDCPD and pNB aerogels from those bulk properties.

3.4a. Nanoporosity, thermal conductivity and interparticle contact area. Thermal conductivities, λ, were calculated from bulk densities (ρ_b), thermal diffusivities (R) and heat capacities (c_p) using $\lambda = \rho_b \times c_p \times R$. The most dense pDCPD samples were thought to represent the upper limit of λ. Thus, for this study we selected the three **pDCPD-xx-X-MMA-50** aerogels. All four **pNB-30(zz:ww)** samples were also tested in parallel.

Thermal diffusivity, was measured using a heat flash method (see Experimental Section).[58] Disk samples were heated from one side with a heat pulse and the temperature variation was monitored on the other side as a function of time. Coating the samples on both sides with gold and then carbon ensures absorption of the heat pulse and minimizes radiative pathways and pulse "bleed-through."[59] Typical data are shown in Figure 9. The data analysis software employs the pulse-corrected Cowan model to approximate the heat-transfer equation (Fick's First Law).[60] That routine eliminated the early radiative spike seen in Figure 9, and estimated the initial value for the thermal diffusivity from the time it takes for the detector voltage to reach its half-maximum value (marked as t_{50} in Figure 9). Subsequently, a least-squares fitting was performed iteratively within a pre-defined time range ($10 \times t_{50}$), and the result is the value of the thermal diffusivity of the

sample, R. (The value of $10 \times t_{50}$ has been determined to be a suitable estimate of the initial cooling event after the heat pulse.) Table 7 summarizes the data.

First we observe that there is an upwards trend in the λ values of pDCPD aerogels (from 0.039 W m^{-1} K^{-1} to 0.050 W m^{-1} K^{-1}) as we go from **pDCPD-20-X-MMA-50** to **pDCPD-40-X-MMA-50**, mirroring the increase in density (from 0.349 g cm^{-3} to 0.470 g cm^{-3}). More specifically, the thermal conductivity of the **pDCPD-20-X-MMA-50** sample (0.039 W m^{-1} K^{-1}) is similar to that of polyurea-crosslinked silica aerogels (0.041 W m^{-1} K^{-1}) at about the same density (0.451 g cm^{-3}),[61] and compares favorably with the conductivities of glass wool (0.040 W m^{-1} K^{-1}) and styrofoam (0.030 W m^{-1} K^{-1}).[62]

On the other hand, the thermal conductivities of pNB aerogels are higher, in the 0.077-0.081 W m^{-1} K^{-1} range (comparable with sawdust at 0.080 W m^{-1} K^{-1}), except for the most dense sample in the series, **pNB-30(50:50)**, whose λ value is 0.119 W m^{-1} K^{-1}.

At first glance, the difference between the pDCPD and pNB samples could be dismissed based on the conventional line of reasoning according to which mesoporous pDCPD aerogels would be expected to be better thermal insulators. However, this pore-structure based logic is not complete.

Having eliminated radiative heat transfer, thermal conductivity can be considered as the sum of two terms, gaseous heat conduction in the pores, λ_g, and heat conduction through the solid network, λ_s. In other words, $\lambda = \lambda_g + \lambda_s$.

Assuming convective heat transfer in small pores unimportant, values for λ_g can be calculated from Knudsen's equation, $\lambda_g = \lambda_{g,o} \Pi / [1 + 2\beta(l_g/\Phi)]$,[9,63] where $\lambda_{g,o}$ is the gaseous conductivity of the pore-filling gas (for air at 300 K and 1 bar pressure $\lambda_{g,o} = 0.02619$ W m^{-1} K^{-1}),[64] Π is the porosity of the samples (in decimal notation, from

Tables 4 and 5), β is a parameter that accounts for the energy transfer between the pore-filling gas and the aerogel walls (for air β=2), l_g is the mean free path of the gas molecules (for air at 1 bar $l_g \approx 70$ nm) and Φ is the pore diameter, obtained from N_2 sorption or Hg intrusion porosimetry (see Tables 4 and 5). Calculated values for λ_g are cited in Table 7 for all samples. Thus, the expected gaseous heat conduction is very low, 0.001-0.002 W m^{-1} K^{-1} for all the pDCPD samples, and in the range of 0.007-0.014 W m^{-1} K^{-1} for the pNB samples. Clearly, although the pore structure accounts for part of it, it cannot explain the full difference in thermal conductivity of pDCPD and pNB aerogels. Thus, we turn into the solid network.

Conduction through the solid network scales exponentially with bulk density, $\lambda_s = C(\rho_b)^a$, whereas the pre-exponential factor C depends on the particle chemical composition and interconnectivity (contact surface area per unit volume).[9,65] With other organic aerogels, e.g., resorcinol-formaldehyde, exponent 'a' was found equal to 1.2 for smaller-particle systems (obtained with lower resorcinol:catalyst ratios – around 50), and equal to 1.5 for larger-particle aerogels (obtained with higher resorcinol:catalyst ratios – in the range 200-300).[66] Since pDCPD aerogels consist of smaller particles we decided to use a=1.2, and since pNB aerogels consist of much larger particles, we opted for a=1.5. The calculated pre-exponential factors are also cited in Table 7. For pDCPD, C=0.121-0.146 W m^{-1} K^{-1}. For pNB, C=0.209-0.254 W m^{-1} K^{-1}. The values of C are an interplay of two factors: (a) the size of the interparticle necks; and, (b) the number of interparticle contacts. Qualitatively, larger pNB particles (in the micron range) are expected to have larger interparticle necks, but fewer contacts; smaller pDCPD particles (in the few tens of nm range) should have smaller necks, but many more interparticle contacts. However,

although the particle sizes in pDCPD can be 50× smaller than that of pNB, their resistance to heat transfer is *only* up to about 1.5 times higher ($C_{pDCPD}\approx(2/3)C_{pNB}$), meaning that per unit volume the interparticle contact area in pDCPD and pNB aerogels is comparable. This conclusion should be supported by the stiffness of the two materials, provided that the interparticle chemical bonding is similar (refer to the next section).

Overall, from the perspective of the thermal conductivity of aerogels in air, while gaseous thermal conduction is not compromised much by larger pores (after all the thermal conductivity of open air at about ambient conditions is just $\lambda_{g,o}\approx0.026$ W m^{-1} K^{-1}), heat transfer through the network can be detrimental. Results herewith suggest that the benefit may not justify the higher expense typically associated with smaller particles.

3.4b. Mechanical strength and the nanoparticle crosslinking mechanism. Based on the demonstrated possibility of using bulk pDCPD as an anti-ballistic material,[36] and the fact that polymer-crosslinked aerogels can also be used in ballistic protection,[7] it was deemed important to test both pDCPD/PMMA- and pNB-derived aerogels not-only under conventional quasi-static compression, but also under high strain rates using the long split Hopkinson pressure bar (SHPB) at UTD (see Experimental section). Figure 10 shows typical data (stress-strain curves) obtained with the same formulations we tested thermal conductivity with (see Section 3.4a). All experiments were conducted at room temperature. Results under both quasi-static and high strain rate (dynamic) compression of pDCPD/PMMA and pNB samples are summarized in Tables 8 and 9.

All samples show a linear elastic region at small compressive strains ($< 3\%$) and then plastic deformation, followed by densification and inelastic hardening. No buckling was observed under any conditions, and samples can absorb energy up to 80%

compressive strain, where porosity has been decreased due to pore collapse. (Figure S.10 in Supporting Information compares the micromorphology of representative samples (by SEM) before and after compression.) Although a comprehensive data analysis may be complex, some important observations stand out.

First, the Young's modulus, *E*, a measure of stiffness related to the number of interconnected particles per unit volume (or more accurately to the cumulative neck area per unit volume),[66] is not very different between pDCPD/PMMA and pNB aerogels. For example, under quasi-static compression the pDCPD/PMMA samples show a Young's modulus in the range of 279-349 MPa, while at comparable densities pNB samples have Young's modulii in the range of 92-152 MPa. In fact, the ratio of the two value-groups mirrors the ratio of the *C* factors from the solid thermal conduction of those samples (see previous section), meaning that the nature of chemical bridging between nanoparticles in the two kinds of materials, pDCPD/PMMA on one hand and pNB on the other, is similar. This should not be so though, because, all other things been equal, pDCPD is capable of some crosslinking (according to Scheme 1), while pNB is not. Therefore, pNB aerogels should not have been able to carry any significant loads and they should have been much less stiff materials, both of which are not observed. Also, PMMA does not seem to cause and abnormal increase in the stiffness of the pDCPD/PMMA aerogels, therefore it should not be involved in interparticle crosslinking to any appreciable extent, consistent with the conclusions in Section 3.3. With molecular-level crosslinking ruled out, there has to be a common mechanism for holding the two kind of polymeric nanostructures together. Thus, considering that ROMP is a living process, phase-separated nanoparticles of both pDCPD in toluene, and pNB in toluene:*i*PrOH mixtures, are expected to be terminated

Table 7. Thermal conductivity data for selected pDCPD and pNB aerogels

sample	bulk density, ρ_b (g cm^{-3}) [a]	heat capacity, c_p (J g^{-1} K^{-1}) [a,b]	thermal diffusivity, R (mm^2 s^{-1}) [a,b]	thermal conductivity, λ (W m^{-1} K^{-1}) [a,b]	gaseous thermal conductivity, λ_g (W m^{-1} K^{-1}) [c]	solid thermal conductivity, λ_s (W m^{-1} K^{-1}) [d]	C [e] (W m^{-1} K^{-1})
pDCPD-20-X-MMA-50	$0.34_9 \pm 0.01_8$	$1.16_3 \pm 0.07_6$	0.095 ± 0.006	0.039 ± 0.004	0.002	0.037	0.131
pDCPD-30-X-MMA-50	$0.39_5 \pm 0.03_4$	$1.23_5 \pm 0.02_1$	0.101 ± 0.002	0.049 ± 0.004	0.001	0.048	0.146
pDCPD-40-X-MMA-50	$0.47_0 \pm 0.05_1$	1.231 ± 0.007	0.087 ± 0.001	0.050 ± 0.005	0.001	0.049	0.121
PNB-30(50:50)	$0.68_4 \pm 0.01_5$	$1.4_{23} \pm 0.1_{25}$	0.129 ± 0.003	$0.12_5 \pm 0.01_2$	0.007 [f]	0.118	0.209
PNB-30(30:70)	0.449 ± 0.007	$1.45_5 \pm 0.03_5$	$0.12_5 \pm 0.01_0$	$0.08_1 \pm 0.01_2$	0.013	0.068	0.226
PNB-30(10:90)	0.395 ± 0.007	$1.53_1 \pm 0.06_4$	$0.12_7 \pm 0.01_1$	0.077 ± 0.007	0.014	0.063	0.254
PNB-30(0:100)	0.449 ± 0.005	$1.48_0 \pm 0.03_7$	$0.12_1 \pm 0.01_5$	$0.08_0 \pm 0.01_0$	0.013	0.067	0.223

a Average of three samples. b At 23 ºC. c Calculated using Knudsen's equation. d Calculated via $\lambda_s = \lambda - \lambda_g$. e Prefactor related to the interconnectivity of particles. Calculated via $\log C = \log(\lambda_s) - a \log(\rho_b)$, whereas for pDCPD a=1.2 and for pNB a=1.5 (see text). f Bi-modal pore size distribution; this value was calculated from the larger pore sizes (see Table 5).

Table 8. Compression data for selected monolithic pDCPD aerogels under quasi-static conditions (A) and at high strain rates (B)

sample	bulk density, ρ_b (g cm^{-3})	strain rate (s^{-1})	Young's modulus (MPa)	yield strength (MPa)	ultimate strength, *UCS* (MPa)	ultimate strain (%)	Specific energy abs. (J g^{-1})
A. under quasi-static conditions							
pDCPD-20-X-MMA-50	$0.35_4\pm0.01_7$	0.01	278 ± 33	15.0 ± 1.3	461 ± 5	84 ± 1	191 ± 2
pDCPD-30-X-MMA-50	0.386 ± 0.005	0.01	301 ± 21	13.2 ± 0.6	349 ± 11	88 ± 1	86 ± 3
pDCPD-40-X-MMA-50	$0.42_1\pm0.02_4$	0.01	349 ± 16	17.9 ± 4.9	319 ± 31	86 ± 1	85 ± 8
B. at high strain rates (using a SHPB)							
pDCPD-20-X-MMA-50	$0.35_4\pm0.01_7$	1325 ± 124	198	5.7	86	76	16.95
pDCPD-20-X-MMA-50	0.386 ± 0.005	1210 ± 84	346	9.5	155	75	18.87
pDCPD-40-X-MMA-50	$0.42_1\pm0.02_4$	1327 ± 58	385	9.3	97	73	22.75

Table 9. Compression data for monolithic pNB aerogels under quasi-static conditions (A) and at high strain rates (B)

sample	bulk density, ρ_b (g cm^{-3})	strain rate (s^{-1})	Young's modulus (MPa)	yield strength (MPa)	ultimate strength, *UCS* (MPa)	ultimate strain (%)	Specific energy abs. (J g^{-1})
A. under quasi-static conditions							
PNB-30(50:50)	$0.86_9\pm0.01_9$	0.01	1557 ± 89	36.7	$49._4\pm2._1$	$7._1\pm3._4$	$57._2\pm2._5$
PNB-30(30:70)	0.507 ± 0.005	0.01	152 ± 51	2.95	3.2 ± 0.7	$2._9\pm1._1$	$21._9\pm4._8$
PNB-30(10:90)	0.457 ± 0.007	0.01	97 ± 10	1.80	2.1 ± 0.3	4.2 ± 0.1	$1.0_6\pm0.1_4$
PNB-30(0:100)	0.502 ± 0.002	0.01	92 ± 56	2.10	2.6 ± 0.9	$4._4\pm1._1$	$0.8_8\pm0.3_2$
B. at high strain rates (using a SHPB)							
PNB-30(50:50)	$0.86_9\pm0.01_9$	1217 ± 162	1673 ± 270	60.0 ± 0.6	151 ± 18	65 ± 12	$65._8\pm9._7$
PNB-30(30:70)	0.507 ± 0.005	1224 ± 167	$75._0\pm5._9$	5.2 ± 0.3	50 ± 10	75 ± 6	$23._0\pm7._0$
PNB-30(10:90)	0.457 ± 0.007	1150 ± 221	$29._5\pm9._6$	5.0 ± 0.5	$35._1\pm6._9$	71 ± 9	$16._6\pm5._3$
PNB-30(0:100)	0.502 ± 0.002	1078 ± 40	$27._1\pm9._3$	4.1 ± 0.3	$26._9\pm4._9$	70 ± 1	$12._4\pm1._8$

with active catalyst, which can be engaged in cross-metathesis with polymer on the surface of another phase-separated nanoparticle coming in contact with. That process is summarized in Scheme 6, and is expected to have two effects: (a) development of cross-linking between particles by extending the polymeric network of the one inside the other, and (b) a broad polydispersity for the core polymer. The result of (a) would be an increase of modulus and mechanical strength inversely to the interparticle surface area. Indeed, what is observed experimentally is: $E_{pDCPD} / E_{pNB} \approx C_{pNB} / C_{pDCPD}$. The effect of (b) can be also observed experimentally, but only in the case of soluble pNB. In this context, it is known that the *first* generation Grubbs' catalyst yields pNB with high polydispersities (in the range of 2.0-2.5), which have been attributed to cross-metathesis (backbiting and chain transfer reactions).[67] Here, by dissolving **pNB-30(zz:ww)** aerogels in THF we observe much higher polydispersities – in the 8-13 range (for GPC data see Figure S.11 in Supporting Information).

Scheme 6. Interparticle crosslinking mechanism: Cross-metathesis effectively extends the polymer of one pDCPD or pNB nanoparticle into another
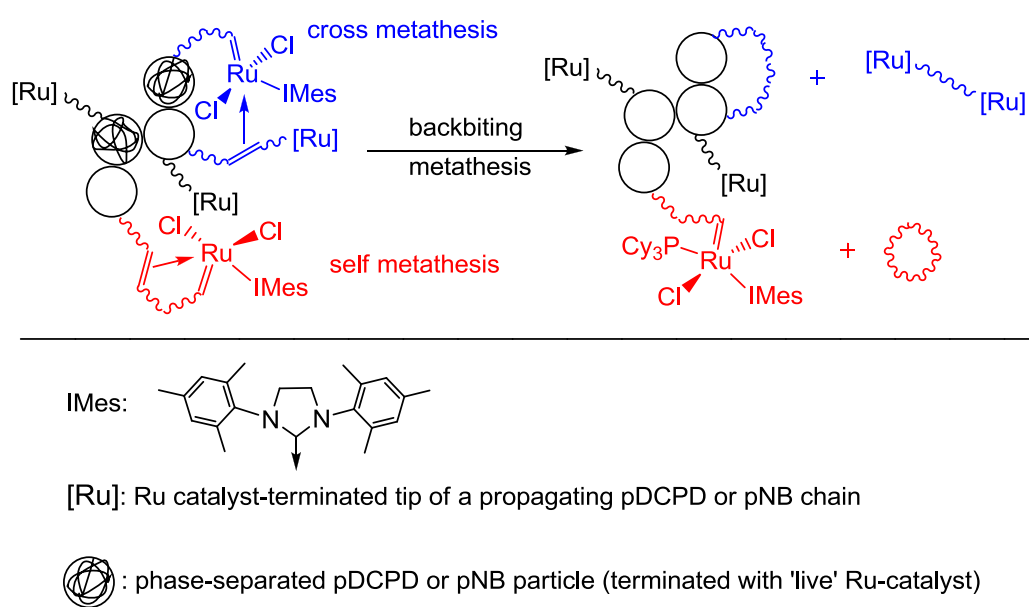
Second, although porous materials in general appear stronger, stiffer and tougher under dynamic loading conditions at higher strain rates,[68] exactly the opposite is true for the **pDCPD-xx-X-MMA-50** aerogels (compare Figures 10A and 10B, and results in Table 8). The case of **pNB-30(zz:ww)** is more complex: with the exception of the **pNB-30(50:50)** samples, which have different micromorphology (Figure 7), all others are stiffer under quasi-static loading (higher Young's modulii), but in general they are stronger and can absorb more energy (tougher) under dynamic loading conditions (see Table 9). The mode of failure is also quite revealing. Under quasi-static compression, **pDCPD-xx-X-MMA-50** samples fail by shattering in fragments, while under dynamic loading they seem to hold themselves together. On the other hand, **pNB-30(zz:ww)** samples shatter under both quasi-static and under dynamic loading conditions.

Analysis of time-dependent structural rearrangement is very complex.[69] However, from a chemical perspective, the comparative behavior of the pDCPD/PMMA versus the pNB samples is consistent with the nanostructure described in Scheme 5, the particle crosslinking mechanism outlined in Scheme 6 and the fewer interparticle contacts identified for macroporous pNB samples.

According to Scheme 6, skeletal nanoparticles in pDCPD/PMMA and pNB aerogels are linked by sharing and entanglement of their core polymeric strands. Those interparticle links are energy-wise flexible, in the sense that various conformations of the entangled polymers may comprise local minima. Thus, at slow strain rates the material is given time to re-organize itself at the nano-level, and take more load. Clearly, this has to be the case of pDCPD/MMA samples that under quasi-static compression take on average ~376 MPa at ~86% strain, but only ~86 MPa at ~72% stain under dynamic

loading. By the same token, at the highest strains (85%), pDCPD/PMMA has reached the point where most void space has been squeezed out (Figure S.10), the rigidity of the PMMA-filled secondary particles takes control, and the material displays brittle-like behavior and shutters.

In terms of ultimate strength, the behavior of pNB aerogels is 'normal,' in the sense that at high strain rates **pNB-30(zz:ww)** aerogels appear stronger. In general, bulk porous materials fail by buckling and shear failure of the walls. When the Young's modulus, or the yield strength of the skeletal material is higher, walls are stiffer and less prone to buckling or forming shear bands, which are incipient to wall collapse. Meanwhile, it is known that in general the Young's modulus of polymers increases with strain rate.[70] Thus, the bulk porous material becomes capable of withstanding higher loads at higher strain rates.[71] Conversely, that is to say that the micron-sized particles of the **pNB-30(zz:ww)** aerogels have a lot of parasitic (or unnecessary) weight: more than enough to support the macroporous structure, which does very little towards carrying high mechanical loads. According to that model, the bi-continuous structure of **pNB-30(50:50)** requires more attention. Overall, due to the non-covalent nature of the interparticle links, both pDCPD/PMMA and pNB aerogels are expected to show significant creep. Future plans include a study of this complex mechanical behavior through bottom-up molecular modeling, and top-down simulations using the material point method (MPM).[72]

4. Conclusion

The pendant cyclopentene rings of polydicyclopentadiene, pDCPD, were found inert to metathesis with the second-generation Grubbs' catalyst, leaving Wagener-type crosslinking through olefin coupling (Scheme 1) as the only alternative. Yet, the extent of crosslinking is very low; only 4-5% of the cyclopentene rings react. Consequently, the resulting deformable nanoparticles are unable to resist hydrophobic/van der Waals interaction-driven coalescence, and under the right conditions (e.g., in polar acetone) merge into one another. Macroscopically, that leads to disorderly shrinkage and produces severely deformed aerogel monoliths, unsuitable for any application. The issue was rectified by employing free radical chemistry in order to graft a small amount of PMMA on the pDCPD backbone (as little as 13% w/w). The resilience of the resulting pDCPD/PMMA nano-composites is not traced to molecular level crosslinking (evidence suggests that PMMA mostly stays as a linear polymer), but instead to a nano-level synergism of the two components, which is derived by their relative topology: PMMA fills the empty space of pDCPD secondary nanoparticles, which can no longer squeeze past one another and the composite material does not deform. That has allowed preparation of large regular monoliths for the study of macroscopic properties (thermal conductivity and compressive strength), which are used as probes of the interparticle connectivity. Specifically, solid thermal conduction is related to the interparticle contact area per unit volume, while stiffness to interparticle bonding. That study was conducted comparatively with polynorbornene (pNB) aerogels, which have no pendant cyclopentene rings, and therefore no chance for crosslinking via either metathesis or Wagener-type olefin coupling. Remarkably, the compressive strengths of pDCPD/PMMA and pNB

aerogels were found similar, pointing to a common mechanism for interparticle bonding. That was assigned to cross-metathesis, which effectively blends the polymer chains of adjacent nanoparticles.

It will be instructive to study the effect of other Grubbs' and Schrock's catalysts on the porous structures/interparticle connectivity of pDCPD and pNB, and to adopt the nanostructure point of view in other nanoporous polymers.

 Supporting Information. Appendix I: ^{1}H NMR and GC-MS controls for probing possible modes of crosslinking in **pDCPD-xx** and in **pDCPD-xx-X-MMA-yy** aerogels (Figures S.1-S.6, Tables S.1 and S.2); Appendix II: Differential scanning calorimetry (DSC) and thermogravimetric analysis (TGA) data (Figures S.7-S.9); Appendix III: SEMs before and after compression (SHPB) of **pDCPD-30-X-MMA-50** and of **pNB-30(0:100)** aerogels (Figure S.10); Appendix IV: Gel permeation chromatography data for the **pNB-30-(zz:ww)** samples (Figure S.11 and Table S.3).

5. References

1. Kistler, S. S. *Nature* **1931**, *127*, 741.

2. (a) Pierre, A. C.; Pajonk, G. M. *Chem. Rev.* **2002**, *102*, 4243-4265. (b) Hüsing, N.; Schubert, U. *Angew. Chem., Int. Ed.* **1998**, *37*, 22-45.

3. Kistler, S. S. *J. Phys. Chem.* **1932**, *36*, 52-64.

4. (a) Gommes, C. J.; Blacher, S.; Goderis, B.; Pirard, J-P. *Nuclear Instruments and Methods in Physics Research B* **2005**, *238*, 141-145. (b) Nakanishi, K.; Tanaka, N. *Acc. Chem. Res.* **2007**, *40*, 863-873.

5. (a) Baumann, T. F.; Gash, A. E.; Chinn, S. C.; Sawvel, A. M.; Maxwell, R. S.; Satcher, J. H., Jr. *Chem. Mater.* **2005**, *17*, 395-401. (b) Leventis, N.; Chandrasekaran, N.; Sadekar, A. G.; Mulik, S.; Sotiriou-Leventis, C. *J. Mater. Chem.* **2010**, *20*, 7456-7471.

6. (a) Leventis, N. *Acc. Chem. Res.* **2007**, *40*, 874-884. (b) Leventis, N.; Sotiriou-Leventis, C.; Zhang, G.; Rawashdeh, A.-M. M. *Nano Lett.* **2002**, *2,* 957-960. (c) Leventis, N.; Sotiriou-Leventis, C. "Methods and Compositions for Preparing Silica Aerogels," U.S. Patent No. 7,771,609 (2010).

7. (a) Leventis, N.; Lu, H. "Polymer Crosslinked Aerogels," in *Aerogels Handbook - Advanced in Sol-Gel Derived Materials and Technologies*, Aegerter, M.; Leventis, N.; Koebel, M. Eds., Springer: New York, NY, **2011**, pp 251-285. (b) Lu, H.; Luo, H.; Leventis, N. "Mechanical Characterization of Aerogels," in *Aerogels Handbook - Advanced in Sol-Gel Derived Materials and Technologies*, Aegerter, M.; Leventis, N.; Koebel, M. Eds., Springer: New York, NY, **2011**, pp 499-535.

8. (a) Pekala, R. W. "Low Density Resorcinol-Formaldehyde Aerogels," U.S. Patent No. 4,873,218, (1989). (b) Pekala, R. W. *J. Mater. Sci.* **1989**, *24*, 3221-3227. (c) Pekala, R. W.; Alviso, C. T.; Kong, F. M.; Hulsey, S. S. *J. Non-Cryst. Solids* **1992**, *145*, 90-98. (d) Pekala, R. W.; Schaefer, D. W. *Macromolecules* **1993**, *26*, 5887-5893.

9. Lu, X.; Arduini-Schuster, M. C.; Kuhn, J.; Nilsson, O.; Fricke, J.; Pekala, R. W. *Science* **1992**, *255*, 971-972.

10. Ritter, J. A.; Al-Muhtaseb, S. A. *Adv. Mater.* **2003**, *15*, 101−114.

11. Pekala, R. W. *Melamine-Formaldehyde Aerogels*, U.S. Patent No. 5,086,085, 1992.

12. Pekala, R. W.; Alviso, C. T.; Lu, X.; Gross, J.; Frickle, J. *J. Non-Cryst. Solids* **1995**, *188*, 34-40.

13. Li, W. C.; Lu, A.-H.; Guo, S.-C. *J. Colloidal Interface Sci*. **2002**, *254*, 153-157.

14. (a) Biesmans, G.; Martens, A.; Duffours, L.; Woignier, T.; Phalippou, J. *J. Non-Cryst. Solids* **1998**, *225*, 64-68. (b) Chidambareswarapattar, C.; Loebs, J. M.; Larimore, Z.; Dharani, L.; Luo, H.; Lu, H.; Sotiriou-Leventis, C.; Leventis, N. *MRS Proceedings* (mrsf11-1403-v17-37) **2012**, Vol.: *1403*, pp. 1-6 (DOI: 10.1557/opl.2012.357).

15. (a) Lee, J. K.; Gould, G. L.; Rhine, W. L. *J. Sol-Gel Sci. Technol.* **2009**, *49*, 209-220. (b) Leventis, N.; Sotiriou-Leventis, C.; Chandrasekaran, N.; Mulik, S.; Larimore, Z. J.; Lu, H.; Churu, G.; Mang, J. T. *Chem. Mater.* **2010**, *22*, 6692-6710. (c) Leventis, N.; Sotiriou-Leventis, C.; Chandrasekaran, N.; Mulik, S.; Chidambareswarapattar, C.; Sadekar, A.; Mohite, D.; Mahadik, S. S.; Larimore, Z. J.; Lu, H.; Churu, G.; Mang. J. T. *MRS Proceedings* (2010 MRS Fall Meeting) **2011**, *1306*, pp. 1-12 (DOI: 10.1557/opl.2011.90).

16. Lorjai, P.; Chaisuwan, T.; Wongkasemjit, S. *J. Sol-Gel Sci. Technol*. **2009**, *52*, 56-64.

17. (a) Rhine, W.; Wang, J.; Begag, R. Polyimide Aerogels, and Metal Carbide Aerogels and Methods of Making Same, U.S. Patent No. 7,074,880, 2006. (b) Chidambareswarapattar, C.; Larimore, Z.; Sotiriou-Leventis, C.; Mang, J. T.; Leventis, N. *J. Mater. Chem.* **2010**, *20*, 9666-9678. (c) Haiquan, G.; Meador, M. A. B.; McCorkle, L.; Quade, D. J.; Guo, J.; Hamilton, B.; Cakmak, M.; Sprowl, G. *ACS Appl. Mater. Interfaces* **2011**, *3*, 546-552. (d) Meador, M. A. B.; Malow, E. J.; Silva, R.; Wright, S.; Quade, D.; Vivod, S. L.; Haiquan, G.; Guo, J.; Cakmak, M. *ACS Appl. Mater. Interfaces* **2012**, *4*, 536-544.

18. Leventis, N.; Chidambareswarapattar, C.; Mohite, D. P.; Larimore, Z. J.; Lu, H.; Sotiriou-Leventis, C. *J. Mater. Chem.* **2011**, *21*, 11981-11986.

19. Sadekar, A. G.; Mahadik, S. S.; Bang, A. N.; Larimore, Z. J.; Wisner, C. A.; Bertino, M. F.; Kalkan, A. K.; Mang, J. T.; Sotiriou-Leventis, C.; Leventis, N. *Chem. Mater.* **2012**, *24*, 26-47.

20. Daniel, C.; Guidiee, S.; Guerra, G. *Chem. Mater*. **2009**, *21*, 1028-1034.

21. Goueree, P.; Tabli, H.; Miousse, D.; Tran-van, F.; Dao, L. H.; Lee, K. H. *J. Electrochem. Soc*. **2001**, *148*, A94-A101.

22. (a) Fisher, F.; Rigacci, A.; Pirard, R.; Berthon-Fabry, S.; Achard, P. *Polymer* **2006**, *47*, 7636-7645. (b) Gavillon, R.; Budtova, T. *Biomacromolecules* **2008**, *9*, 269-277. (c) Surapolchai, W.; Schiraldi, D. A. *Polym. Bull*. **2010**, *65*, 951-960.

23. Cong, Y. U.; Mingcheng, X. U.; Frantisek, S.; Jean, M. J. F. *J. Poly. Sci. Part A: Poly. Chem.* **2002**, *40*, 755-769.

24. (a) Sherrington, D. C. *Chem. Commun.* **1998**, 2275-2286. (b) Santora, B. P.; Gagne, M. R. *Macromolecules* **2001**, *34*, 658-661.

25. Hjerten, S.; Liao, J-L.; Zhang, R. *J. Chromatogr.* **1989**, *473*, 273-275.

26. See for example: (a) Aoki, H.; Tanaka, N.; Kubo, T.; Hosoya, K. *J. Sep. Sci.* **2009**, *32*, 341-358. (b) Vlakh, E.; Tennikova, T. *J. Sep. Sci.* **2007**, *30*, 2801-2813.

27. (a) Wand, A. R.; Zhu, S. *Macromolecules* **2002**, *35*, 9926-9933. (b) Viklund, C.; Nordstrom, A.; Irgum, K.; Svec, F.; Frechet, J. M. J. *Macromolecules* **2001**, *34*, 4361-4369. (c) Liu, H.; Zhuang, X.; Turson, M.; Zhang, M.; Dong, X. *J. Sep. Sci.* **2008**, *31*, 1694-1701.

28. Grubbs, R. H. *Tetrahedron,* **2004**, *60*, 7117-7140.

29. (a) Buchmeiser, M. R. *J. Sep. Sci.* **2008**, *31*, 1907-1922. (b) Gatschelhofer, C.; Mautner, A.; Reiter, F.; Pieber, T. R.; Buchmeiser, M. R.; Sinner, F. M. *J. Chromatogr. A.* **2009**, *1216*, 2651-2657. (c) Sinner, F. M.; Gatschelhofer, C.; Mautner, A.; Magnes, C.; Buchmeiser, M. R.; Pieber, T. R. *J. Chromatogr. A.* **2008**, *1191*, 274-281. (d) Buchmeiser, M. R. Rigid polymers, *J. Chromatogr.* **2003**, *67*, 104-118.

30. (a) Martina, A. D.; Hilborn, J. G.; Mhlebach, A. *Macromolecules,* **2000**, *33*, 8, 2916-2921. (b) Martina, A. D.; Garamszegi, L.; Hilborn, J. G. *J. Poly. Sci. Part A: Poly. Chem.* **2003**, *41*, 2036-2046. (c) Martina, A. D.; Hilborn, J. G. *J. Mater. Res.* **2001**, *16*, 2045-2051.

31. Lee, J. K.; Gould, G. L. *J. Sol-Gel Sci. Technol.* **2007**, *44*, 29-40.

32. Dawedeit, C.; Kim, S. H.; Braun, T.; Worsley, M. A.; Stephan, A. L.; Wu, K. J.; Walton, C. C.; Chernov, A. A.; Satcher, J. H. Jr.; Hamza, A. V.; Biener, J. *Soft Matter* **2012**, *8*, 3518-3521.

33. Leventis, N.; Sotiriou-Leventis, C.; Mohite, D. P.; Larimore, Z. J.; Mang, J. T.; Churu, G.; Lu, H. *Chem. Mater.* **2011**, *23*, 2250-2261.

34. Grubbs, R. H. *Angew. Chem. Int. Ed.* **2006**, *45*, 3760-3765.

35. Davidson, T. A.; Wagener, K. B.; Priddy, D. B. *Macromolecules* **1996**, *29*, 786-788.

36. http://www.nobelprize.org/nobel_prizes/chemistry/laureates/2005/grubbs-slides.pdf (7-11-2012).

37. (a) Harmon, D. J. *J. Polym. Sci.* **1965**, *C8*, 243-251. (b) May, J. A. Jr.; Smith, W. B. *J. Phys. Chem.* **1968**, *72*, 216-221.

38. (a) Beaucage, G. *J. Appl. Cryst.* **1995**, *28*, 717-728. (b) Beaucage, G. *J. Appl. Cryst.* **1996**, *29*, 134-146. (c) Mang, J. T.; Son, S. F.; Hjelm, R. P.; Peterson, P. D.; Jorgensen, B. S. *J. Mater. Res.* **2007**, *22*, 1907-1920.

39. Ilavsky, J.; Jemian, P. R. *J. Appl. Cryst.* **2009**, *42*, 347-353.

40. Leventis, N.; Sotiriou-Leventis, C.; Mulik, S.; Dass, A.; Schnobrich, J.; Hobbs, A.; Fabrizio, E. F.; Luo, H.; Churu, G.; Zhang, Y.; Lu, H. *J. Mater. Chem.* **2008**, *18*, 2475-2482.

41. (a) Gray, G. T. *Mech. Test. Eval*. ASM Handbook **2000**, *8*, 462-476. (b) Gama, B. A.; Lopatnikov, S. L.; Gillespie, J. W. *Appl. Mech. Rev.* **2004**, *57*, 223-250. (c) Frew, D. J.; Forrestal, M. J.; Chen, W. *Exp. Mech.* **2002**, *42*, 93-106.

42. (a) Luo, H.; Roy, S.; Lu, H. *Compos. Sci. Technol.* **2012**, *72*, 159-166; (b) Luo, H.; Roy, S.; Lu, H. *Mech. Time-Depend. Mater. 2012*, in the press.

43. Winter, H. H. *Polym. Eng. Sci.* **1987**, *27*, 1698-1702.

44. Kim, S.-Y.; Choi, D.-G.; Yang, S.-M. *Korean J. Chem. Eng*. **2002**, *19*, 190-196.

45. Raghavan, S. R.; Chen, L. A. ; McDowell, C.; Khan, S. A., Hwang, R.; White, S. *Polymer* **1996**, *37*, 5869-5875.

46. Muthukumar, M. *Macromolecules* **1989**, *22*, 4656-4658.

47. Pope, E. J. A. "Fractal Growth Model of Gelation," in *Chemical Processing of Ceramics*, Lee, B. I.; Pope, E. J. A. Eds., Marcel-Dekker, Inc. New York, N.Y., 1994, Chapter 14, p 337.

48. (a) Feder, J. *Fractals.* Plenum Press, New York, N.Y, 1988. (b) Lee, D. G.; Bonner, J. S.; Garton, L. S.; Ernest, A. N. S.; Autenrieth, R. L. *Wat. Res.* **2000**, *34*, 1987-2000.

49. Similar observations have been mentioned by the authors of reference 31, but did not elaborate.

50. (a) Hirokawa, Y.; Tanaka, T. *J. Chem. Phys.* **1984**, *81*, 6379-6380. (b) Annaka, M.; Tanaka, T. *Nature* **1992**, *355*, 430-432. (c) Ilmain, F.; Tanaka, T.; Kokufuta, E. *Nature* **1991**, *349*, 400-401. (d) Sizuki, A.; Tanaka, T. *Nature* **1990**, *346*, 345-347.

51. Schrock, R. R. *Angew. Chem. Int. Ed.* **2006**, *45*, 3748-3759.

52. Schaubroeck, D.; Brughmans, S.; Vercaemst, C.; Schaubroeck, J.; Verpoort, F. *J. Mol. Cataly. A: Chemical* **2006**, *254*, 180-185.

53. Abadiea, M. J.; Dimonieb, M.; Couvea, C.; Dragutan, V. *Eur. Polym. J.* **2000**, *36*, 1213-1219.

54. For example see: Mulik, S.; Sotiriou-Leventis, C.; Churu, G., Lu, H.; Leventis, N. *Chem. Mater.* **2008**, *20*, 5035-5046.

55. (a) http://www.matweb.com/search/datasheettext.aspx?matid=78164 (07-07-2012).

    (b) http://69.89.19.48/_files/docs/file_39.pdf (07-07-2012).

56. It is noted that the **pNB-30(zz:ww)** samples do not undergo any volume reduction during Hg intrusion, and therefore the method was considered valid. On the other hand, since by N_2 sorption **pDCPD-xx-X-MMA-yy** are mesoporous materials, Hg intrusion was not deemed necessary.

57. It is noted in passing that switching from a non-fractal growth of secondary particles to a fractal one for higher aggregates is not difficult to reconcile: non-fractal growth is kinetically controlled with low sticking coefficients,[47] but as the temperature of the solution increases drastically by the exothermicity of the ROMP reaction, further aggregation turns into diffusion-limited. That implies also that the sticking mechanism of the nanoparticles is not ROMP-based (refer to Section 3.4b).

58. Parker, W. J.; Jenkins, J. J.; Abbott, G. L.; Butler, C. P. *J. Appl. Phys.* **1961**, *32*, 1679-1684.

59. Lee, D.; Stevens, P. C.; Zeng, S. Q.; Hunt, A. J. *J. Non-Cryst. Solids* **1995**, *186*, 285-290.

60. (a) Cowan, R. *J. Appl. Phys.* **1961**, *32*, 1363-1369. (b) Cowan, R. *J. Appl. Phys.* **1963**, *34*, 926-927.

61. Katti, A.; Shimpi, N.; Roy, S.; Lu, H.; Fabrizio, E. F.; Dass, A.; Capadona, L. A.; Leventis, N. *Chem. Mater.* **2006**, *18*, 285-296.

62. http://www.engineeringtoolbox.com/thermal-conductivity-d_429.html (7-15-2012).

63. Reichenauer, G.; Heinemann, U.; Ebert, H.-P. *Colloids and Surfaces A: Physicochem. Eng. Aspects* **2007**, *300*, 204–210.

64. Stephan, K.; Laesecke, A. *J. Phys. Chem. Ref. Data* **1985**, *14*, 227-234.

65. (a) Fricke, J.; Lu, X.; Wang, P.; Büttner, D.; Heinemann, U. *Int. J. Heat Mass Transfer* **1992**, *35*, 2305-2309. (b) Lu, X.; Nilsson, O.; Fricke, J.; Pekala, R. W. *J. Appl. Phys.* **1993**, *73*, 581-584.

66. Lu, X.; Caps, R.; Fricke, J.; Alviso, C. T.; Pekala, R. W. *J. Non-Cryst. Solids* **1995**, *188*, 226-234.

67. Schwab, P.; Grubbs, R. H.; Ziller, J. W. *J. Am. Chem. Soc.* **1996**, *118*, 100-110.

68. See for example: Luo, H.; Zhang, Y.; Wang, B.; Lu, H. *J. Offshore Mech. Arct. Eng.* **2010**, *132*, 021301.

69. See for example: (a) Nesterenko, V. F. *Dynamics of Heterogeneous Materials*, Springer-Verlag New York, Inc., New York, N.Y., 2001. (b) Qiao, P.; Yang, M.; Bobaru, F. *J. Aerosp. Eng.* **2008**, *21*, 235-248.

70. See for example: Chen, W. W.; Song, B. *Split Hopkinson (Kolsky) Bar: Design, Testing and Applications*, Springer, New York, N.Y., 2010.

71. Lu, H.; Tan, G.; Chen, W. *Mech. Time-Depend. Mater.* **2001**, *5*, 119-129.

72. Fu, B.; Luo, H.; Wang, F.; Churu, G.; Chu, K. T.; Hanan, J. C.; Sotiriou-Leventis, C.; Leventis, N.; Lu, H. *J. Non-Cryst. Solids* **2011**, *357*, 2063-2074.
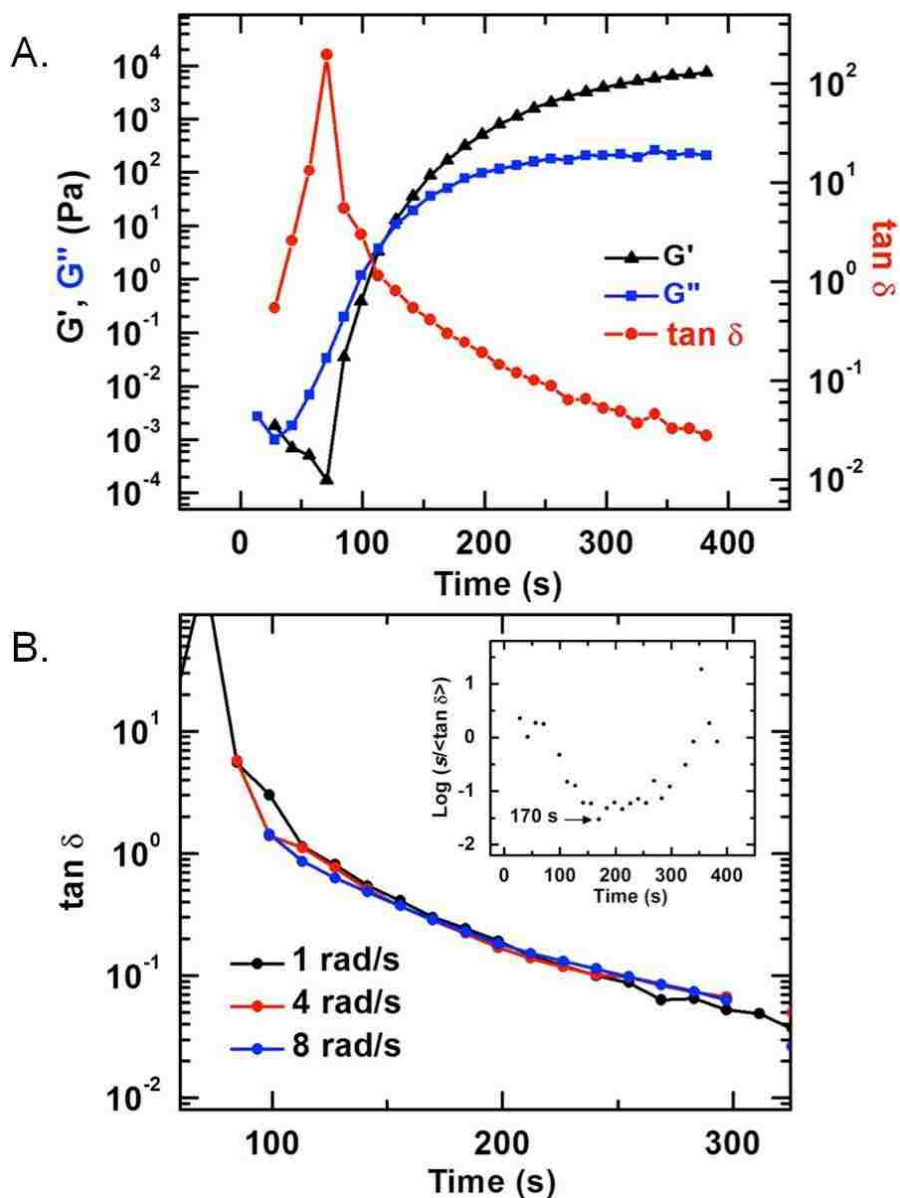
6. Figures

Figure 1. Rheology during gelation of DCPD in toluene using the **pDCPD-20** formulation at 20 °C (see Experimental section). (A) Evolution of the storage (G´) and loss (G´´) modulii versus time from adding the catalyst in the DCPD solution. (Oscillation frequency = 1 rad s^{-1}. For other parameters, see Experimental section.) (B) tan δ versus time from adding the **GC-II** catalyst, close to the gelation point, at three different oscillation frequencies. <u>Inset</u>: Statistical variable versus time (see text). The gelation point is defined at the minimum.

Figure 2. Photographs of: (A) a **pDCPD-30** wet-gel immediately after removed from the mold (left) and of a similar gel swollen after 4 toluene washes (~32 h in toluene baths – right). (B) a **pDCPD-30** aerogel (left-deformed) and of a **pDCPD-30-X-MMA-50** aerogel (right).
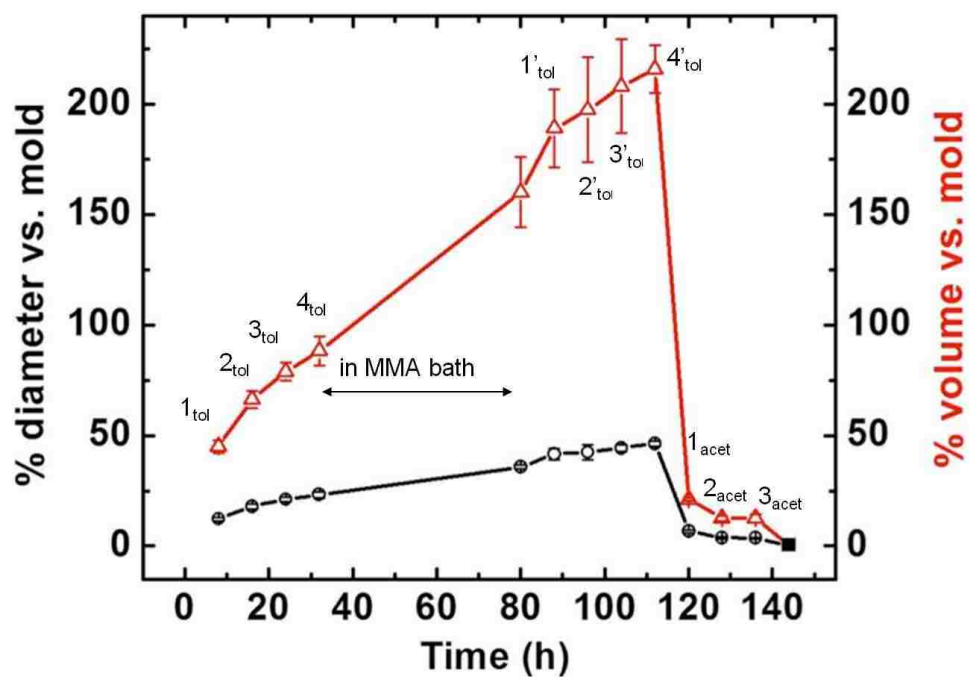
Figure 3. Swelling data for **pDCPD-30** wet-gels in toluene and de-swelling in acetone. Washes and solvents are indicated with numerals and subscripts (<u>tol</u> for toluene and <u>acet</u> for acetone. Note that gels swell about linearly with time, and keep on doing so even during heating in the MMA bath for crosslinking with PMMA. (The specific bath was for the **pDCPD-30-X-MMA-50** formulation – see Experimental section.) The last (filled-square) point at the far right corresponds to the dry aerogel.
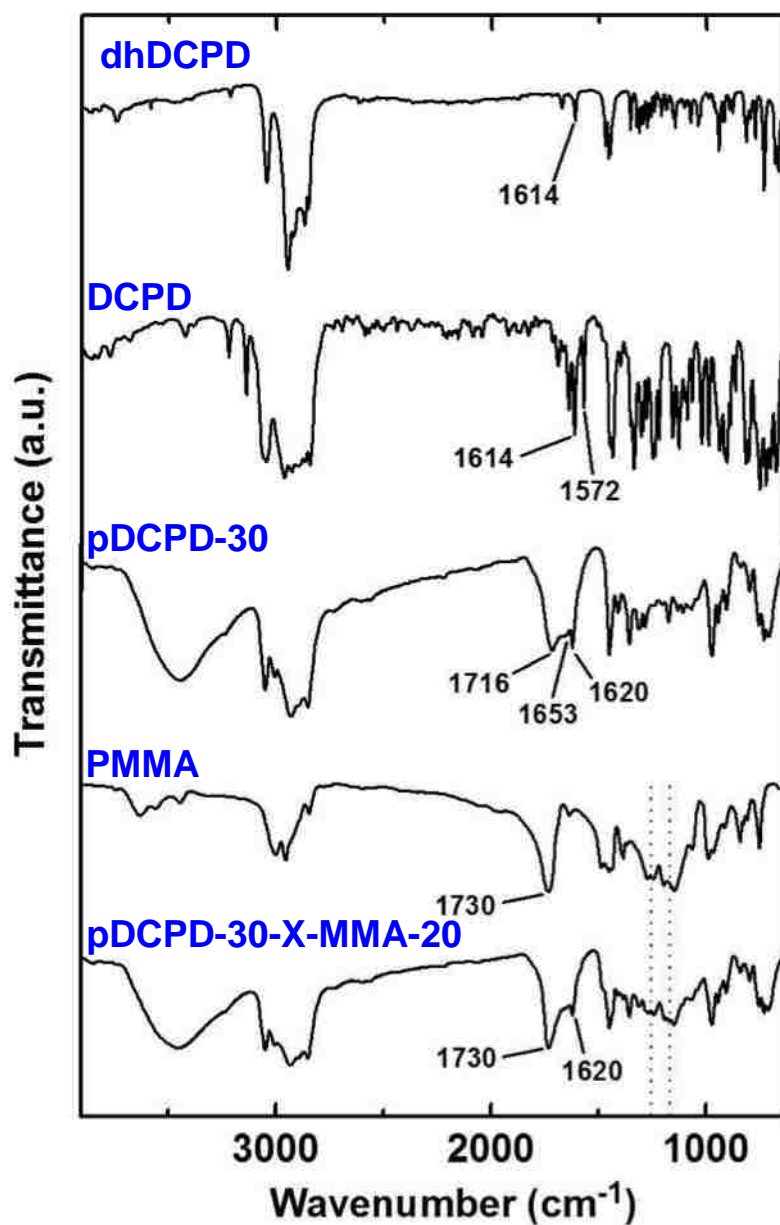
Figure 4. IR data for samples as shown. **dhDCPD** was used as control for identifying the C=C stretching vibration of the cyclopentene ring in DCPD (1614 cm^{-1}). That peak shifts at 1620 cm^{-1} in **pDCPD-30** aerogels and is present even after PMMA uptake (e.g., in the **pDCPD-30-X-MMA-20** aerogel sample shown).
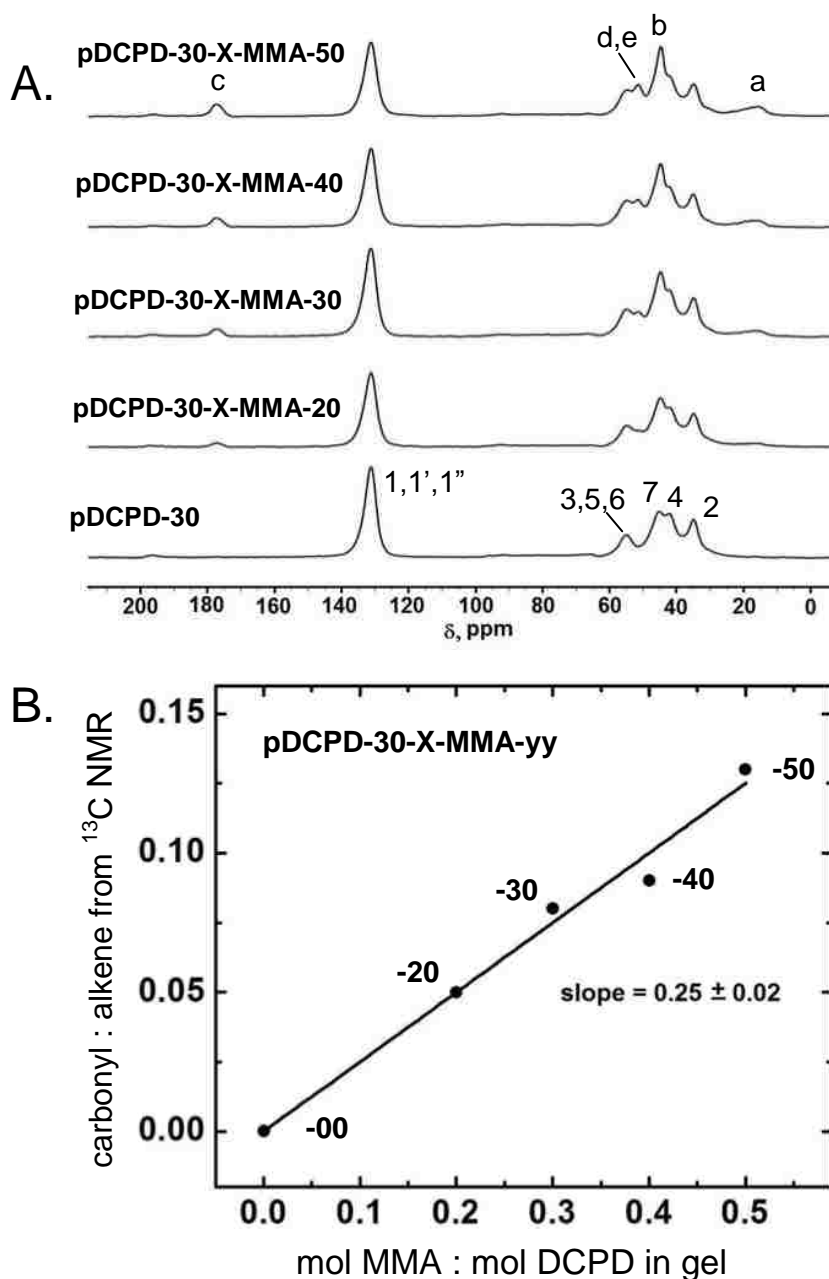
Figure 5. (A) Solid CPMAS ^{13}C NMR data of a native (deformed) **pDCPD-30** aerogel and of similar (non-deformed) samples obtained through treatment with MMA. For peak assignment see Scheme 4. (B) Plotting the integrated peak intensities of the PMMA C=O resonance at 178 ppm (c) over the pDCPD C=C resonance at 131 ppm (1,1',1") versus the mol ratios of the monomers in the gels as formulated and described in the Experimental section.
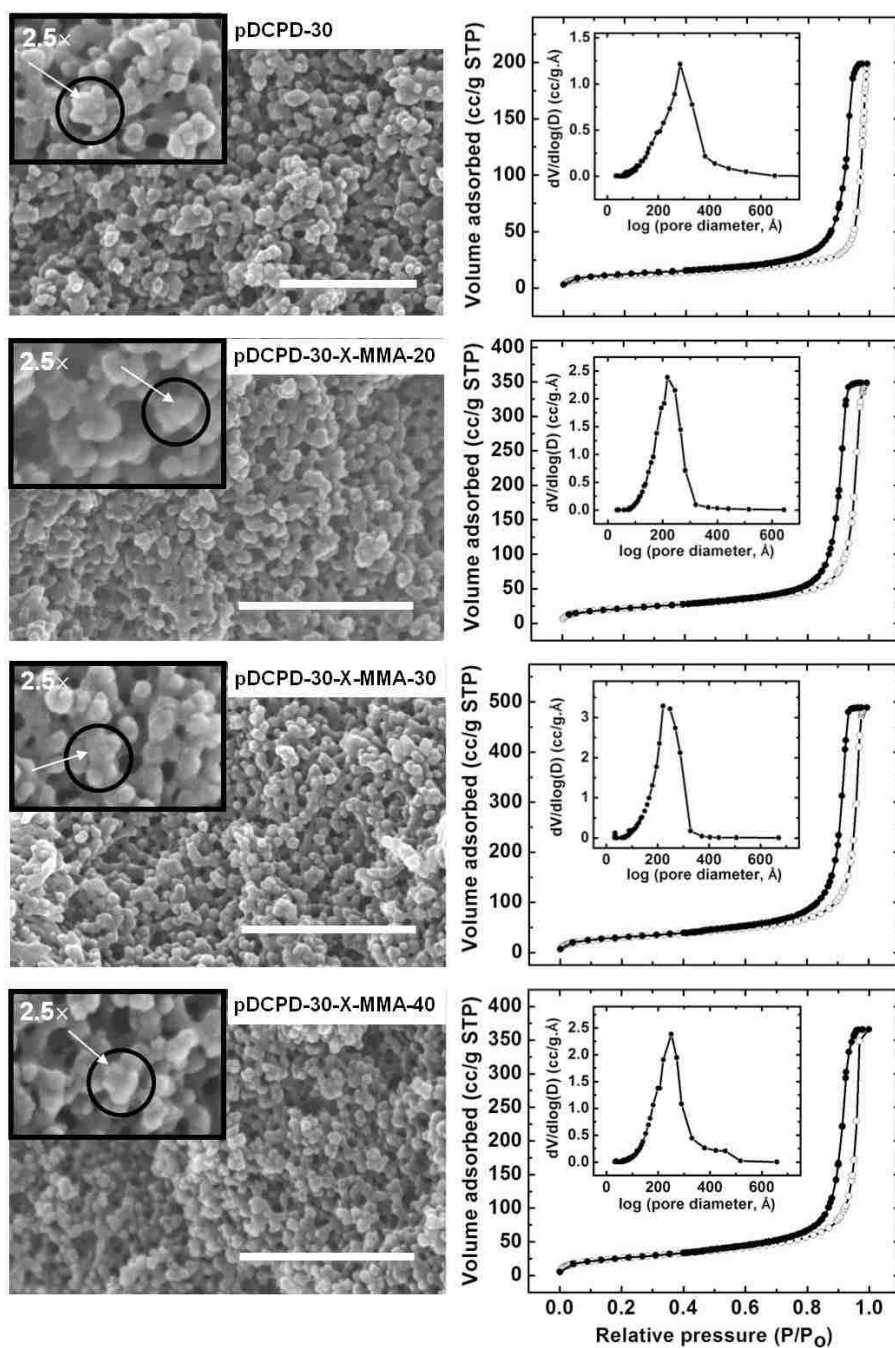
Figure 6. Typical scanning electron microscopy (SEM – scale bars at 500 nm) and N_2 sorption data for the **pDCPD-30** aerogels and the samples obtained after incorporation of PMMA. Insets show the BJH curves obtained from the desorption branch of the isotherms. (For other sample data and N_2 sorption data analysis refer to Table 4.)
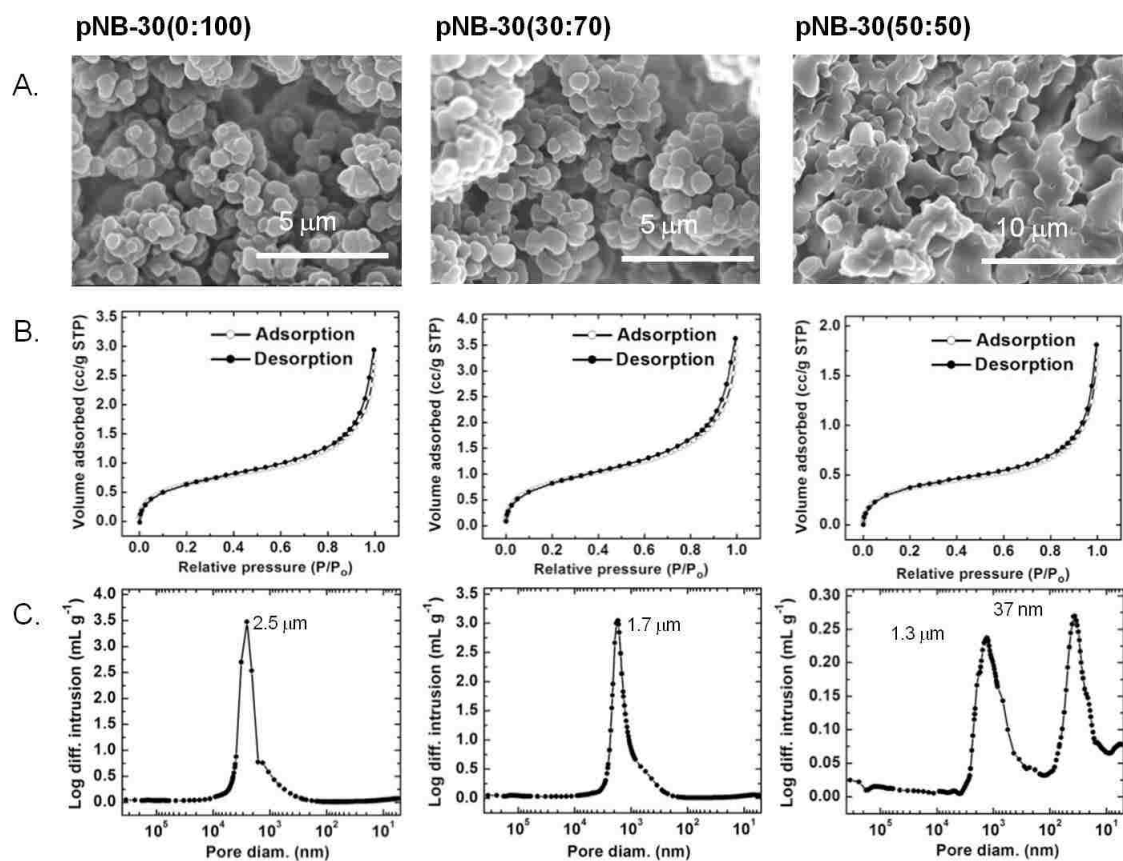
Figure 7. Data for **pNB-30** aerogels obtained using different (toluene:*i*PrOH) ratios. (A) SEM. (B) N$_2$ sorption isotherms. (C) Pore size distributions by Hg intrusion. (For data analysis refer to Table 5.)
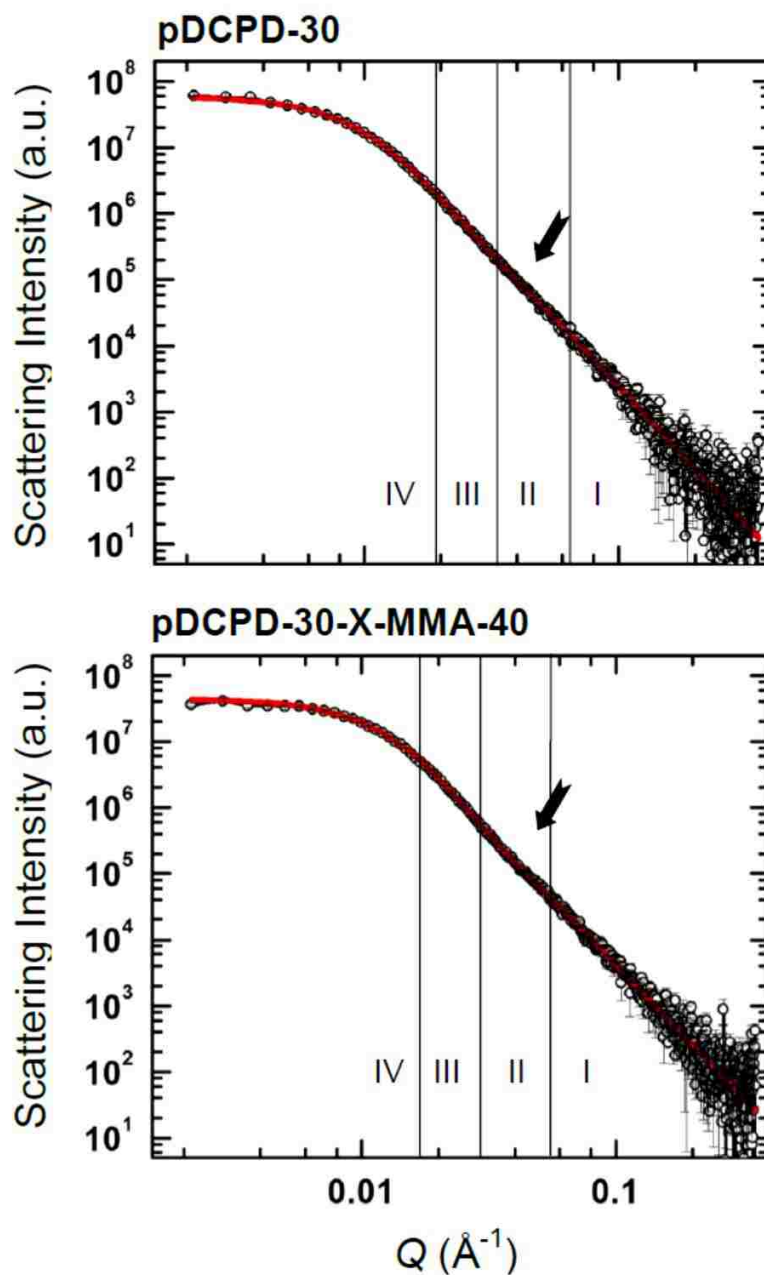
Figure 8. Small angle X-ray scattering (SAXS) data for a typical **pDCPD-30** aerogel sample, and of one derivative sample incorporating PMMA. Data were fitted to the Beaucage Unified Model. Arrows indicate the convex-up deflections that dictated analysis using two power-law and two Guinier regions. Primary particle radii from Guinier Region II. Secondary particle radii from Region IV. Slopes of the narrow low-Q power-law Region III are >3 indicating that secondary particles are closely-packed surface fractals. Results are summarized in Table 6.
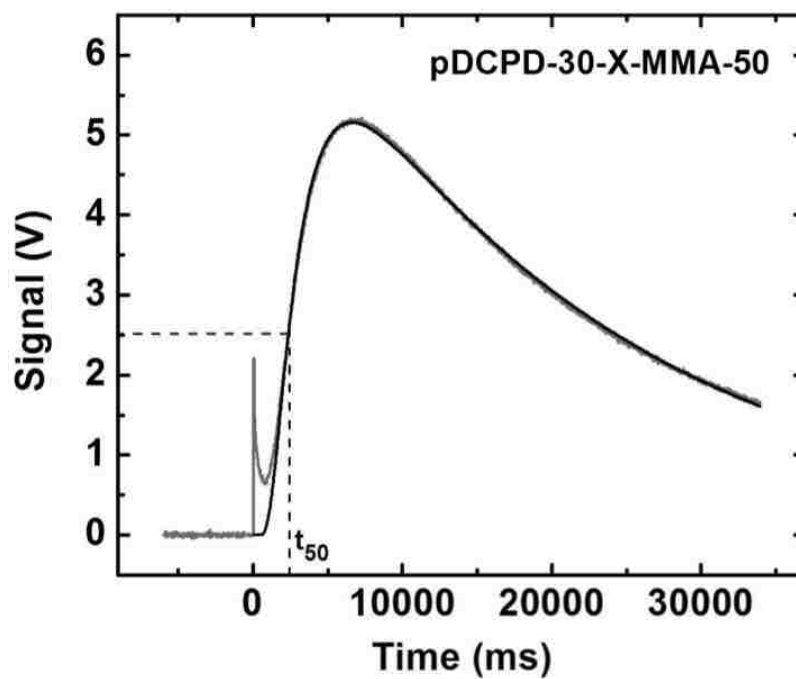
Figure 9. Temperature rise of the back face of a **pDCPD-30-X-MMA-50** aerogel disk (12.5 mm in diameter, 2.30 mm thick, $\rho_b = 0.395$ g cm^{-3}) coated with gold and carbon on both faces, following a heat pulse incident to the front face. Dashed reference lines indicate t_{50}, which is the time required for the detector voltage (proportional to temperature) to reach half its maximum value. Data have been fitted to the pulse-corrected Cowan model (see text).
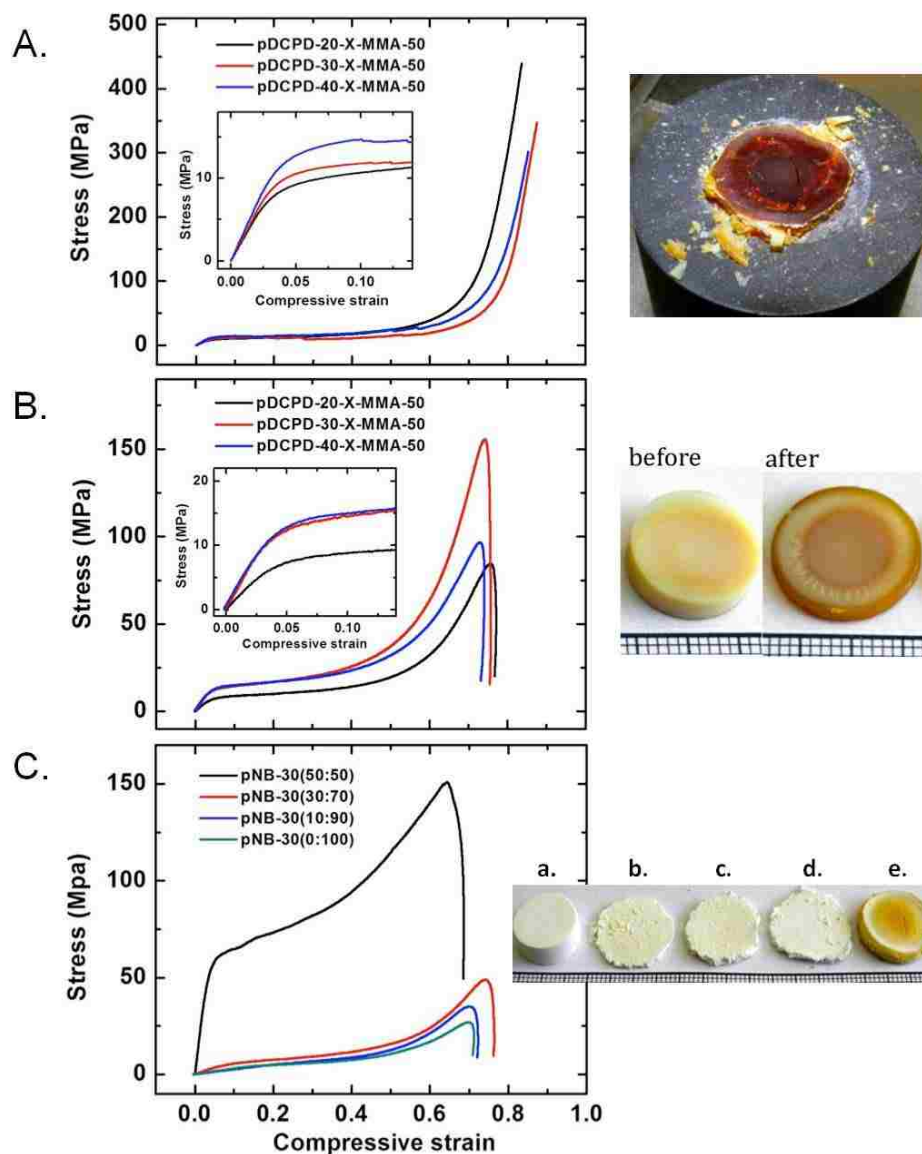
Figure 10. (A) Stress-strain curves of **pDCPD-xx-X-MMA-50** aerogel monoliths under quasi-static (strain rate = 0.01 s^{-1}) compression. <u>Inset</u>: Magnification of the low-strain linear region whose slope gives the Young's modulus. <u>Photograph</u>: a **pDCPD-30-X-MMA-50** sample after failure under quasi-static compression. (B) Stress-stress curves of **pDCPD-xx-X-MMA-50** aerogel monoliths under dynamic compression (strain rates cited in Table 8). <u>Inset</u>: as in part A. <u>Photograph</u>: a **pDCPD-30-X-MMA-50** sample, as shown. (C) Stress-strain curves of **pNB-30(zz:ww)** monoliths under dynamic compression (strain rates cited in Table 9). <u>Photograph</u>: (a.) a representative sample before impact; (b.)-(e.), (zz:ww): (0:100), (10:90), (30:70) and (50:50), respectively.

7. Supporting Information

Appendix I. ¹H NMR and GC-MS controls for probing possible modes of crosslinking in

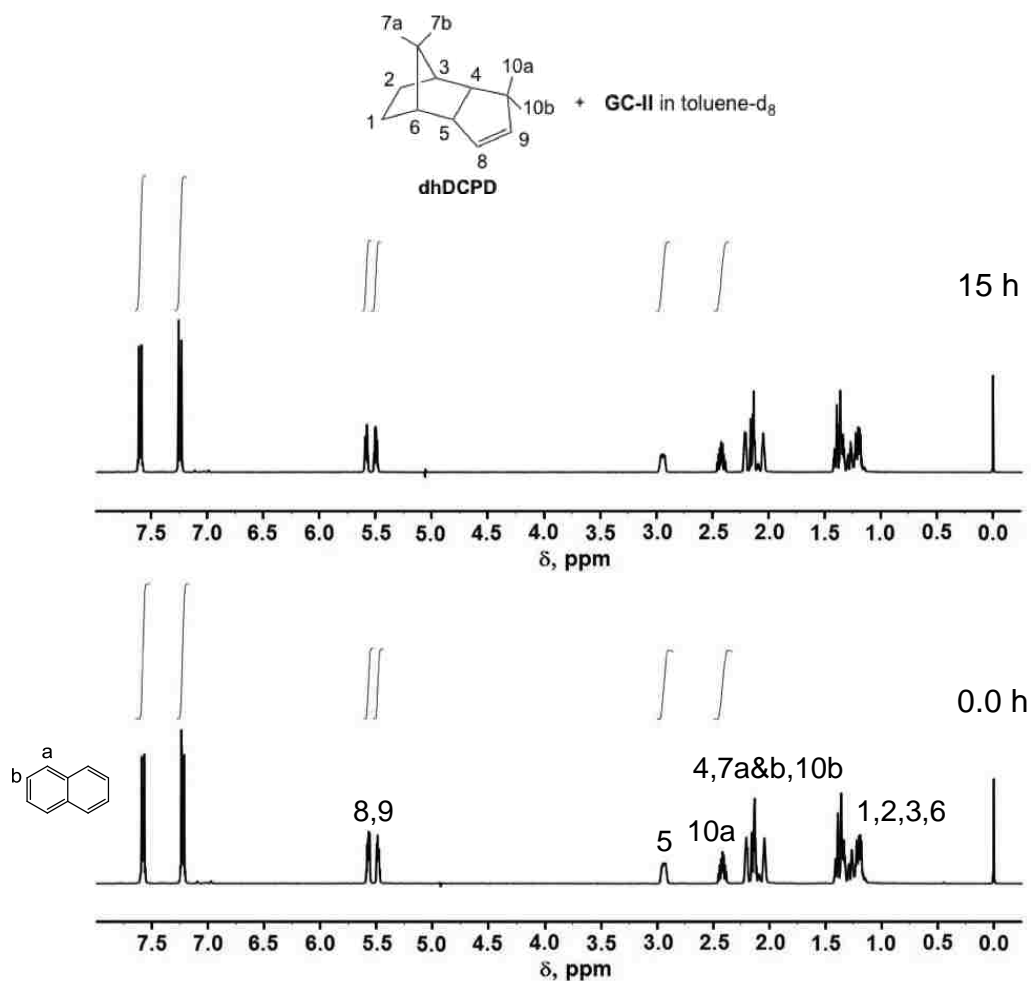**pDCPD-xx** and in **pDCPD-xx-X-MMA-yy** aerogels

Figure S.1 Liquid ¹H NMR as a function of time during attempted ROMP of a 30% w/w **dhDCPD** solution in toluene-d_8 at 70 °C using **GC-II** (0.025 mol% vs. **dhDCPD**). Spectrum at 0 h was taken before the addition of **GC-II**. Naphthalene (50% mol/mol vs. **dhDCPD**) was used as internal standard. Spectra were recorded using the same number of scans (4) and at the same attenuation. Peak assignment by simulation. Signal integration:

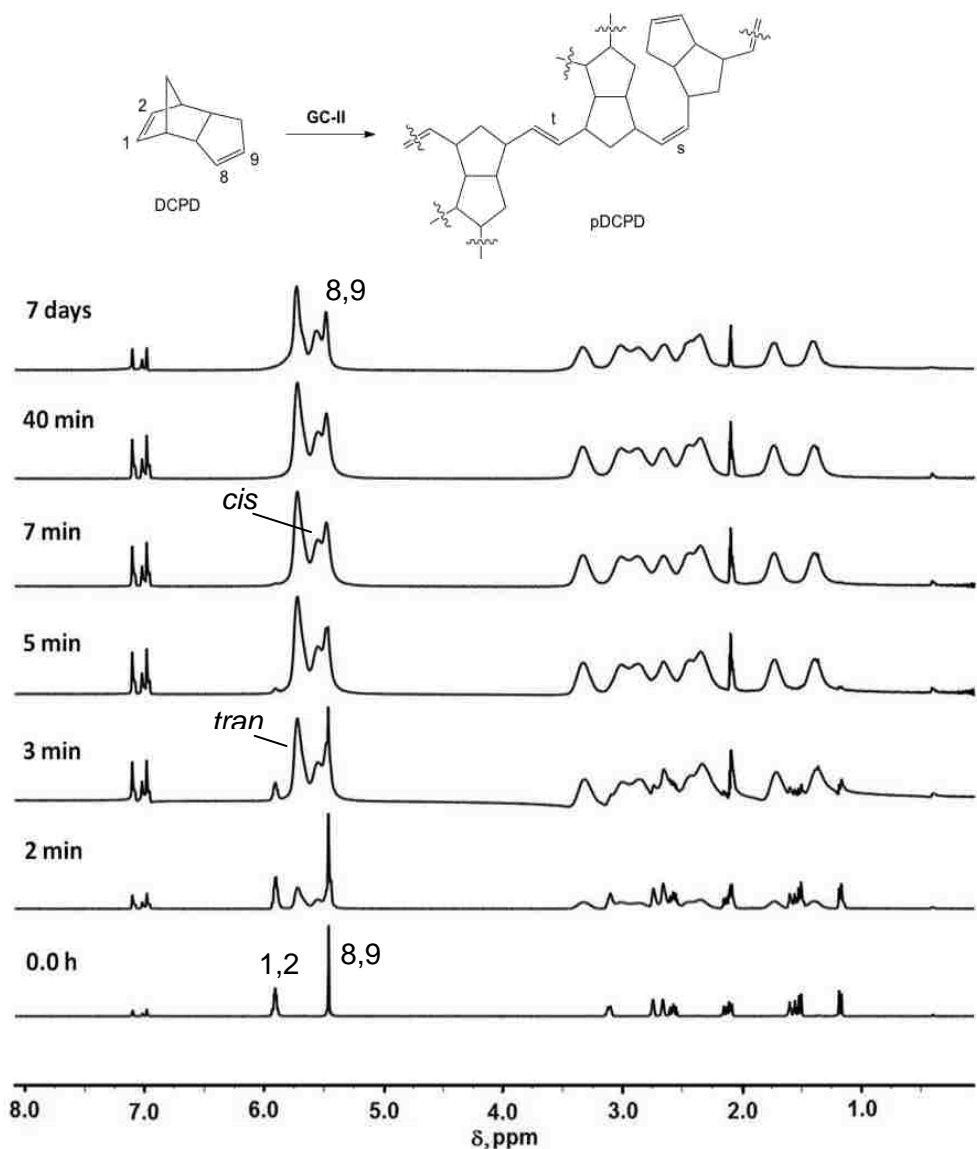| reaction time (h)	vinyl : H_a		allylic : H_a	
	$H_8 : H_a$	$H_9 : H_a$	$H_{10a} : H_a$	$H_5 : H_a$
0 h	0.52	0.52	0.50	0.50
1 h	0.52	0.51	0.50	0.51
2 h	0.52	0.51	0.51	0.52
3 h	0.52	0.51	0.50	0.51
12 h	0.52	0.51	0.50	0.51

Figure S.2 Liquid ^{1}H NMR as a function of time during ROMP of a <u>low-concentration</u> (5% w/w) DCPD solution in toluene-d_8 at room temperature using **GC-II** (0.05 mol% vs. DCPD) as catalyst. Bottom spectrum is before addition of **GC-II**. In the pDCPD structure on top, cyclopentene rings are shown unreacted, consistent with the surviving of resonances '8,9'. The *cis* and *trans* assignment for the backbone double bonds was based on R-S.1 and R-S.2.

R-S.1. Vargas, J.; Martínez, A.; Santiago, A. A.; Tlenkopatchev, M. A.; Gaviño, R.;   Aguilar-Vega, M. *J. Fluorine Chem.* **2009**, *130*, 162-168.

R-S.2. Díaz, K.; Vargas, J.; Del Castillo, L. F.; Tlenkopatchev, M. A.; Aguilar-Vega, M.   *Macromol. Chem. Phys.* **2005**, *206*, 2316-2322.
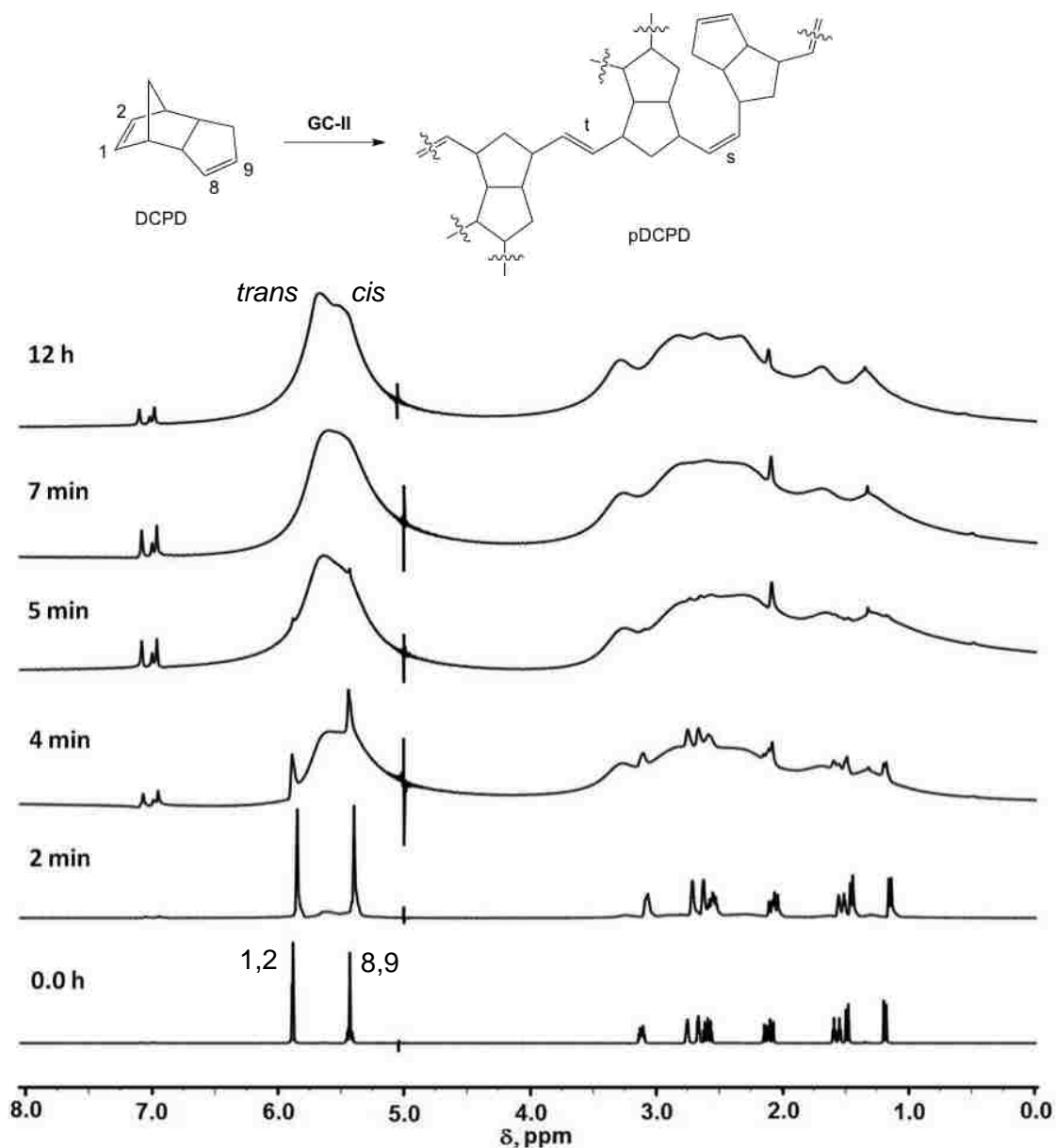
Figure S.3   Liquid ¹H NMR as a function of time towards gelation via ROMP of a <u>high-concentration</u> (30% w/w) DCPD solution in toluene-d_8 at room temperature using **GC-II** (0.025 mol% vs. DCPD) as catalyst. Bottom spectrum is before addition of **GC-II**. With the passage of time, peaks become broader and their intensity decreases, consistent with polymerization. At the end, cyclopentene resonances '8,9' are either buried underneath the polymer resonance, or the 8,9 double bond has reacted. However, based on Figure S.1, that double bond is unreactive towards ROMP. Also, by IR (Figure 4 of the main article) at least some of the cyclopentene double bonds survive through gelation, aging and drying. Therefore, if the cyclopentene double bonds are to participate in crosslinking, that will have to be according to an olefin addition mechanism as suggested by Wagener (and shown in the structure above).
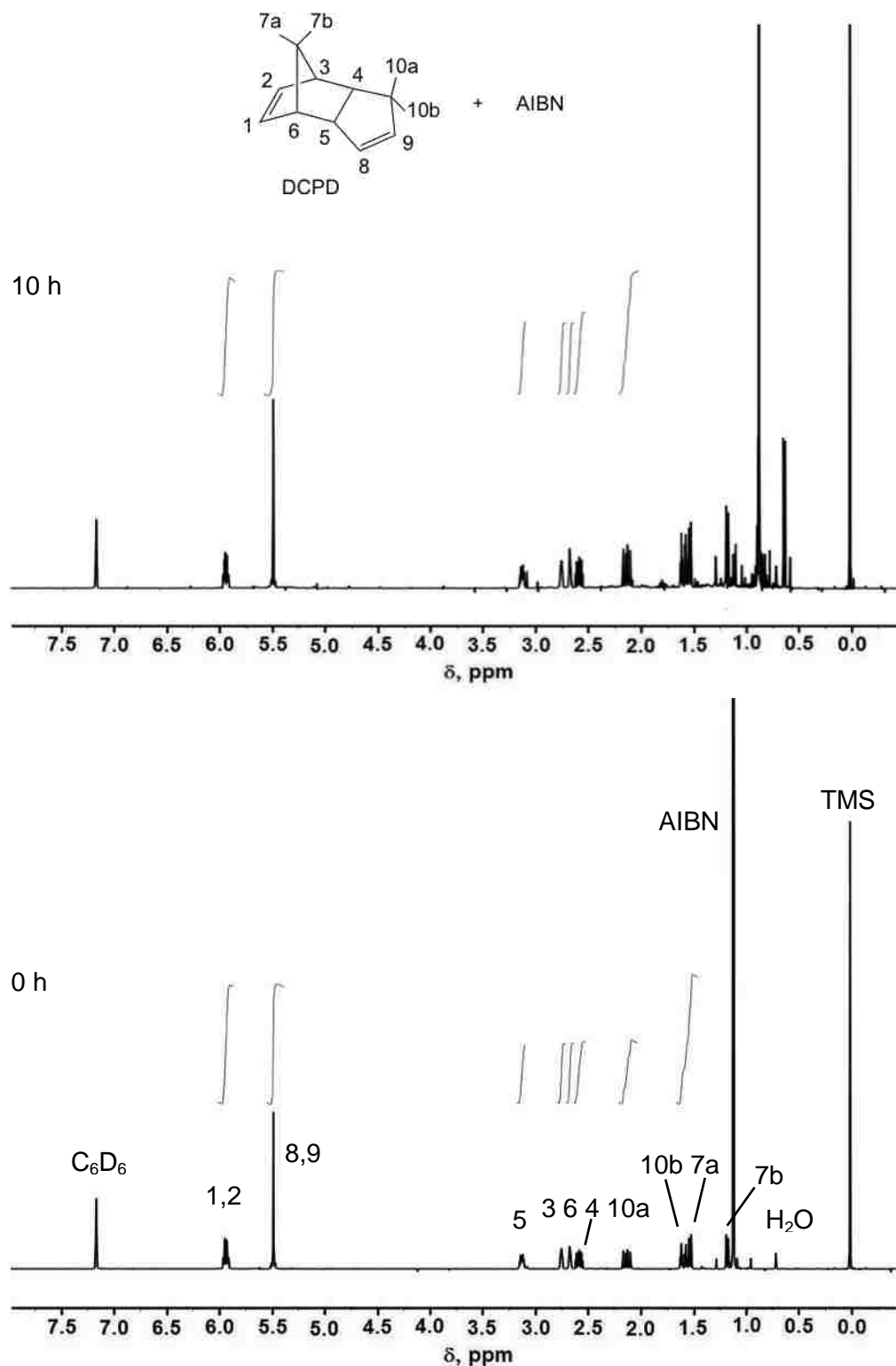
Figure S.4 Liquid ^{1}H NMR of a 35% w/w DCPD solution in benzene-d$_6$ in the presence of AIBN (1:1 mol/mol vs. DCPD). Bottom spectrum is immediately after making the solution at room temperature and top spectrum is after heating the NMR tube at 80 ^{o}C for 10 h. Data summary and conclusions in Table S.1. GC-MS analysis after heating: Figure S.5.

Table S.1   Integration of ^{1}H NMR data of Figure S.4 above, as shown.[a]

reaction time (h)	norbornene vinyl : H$_4$	cyclopentene vinyl : H$_4$	norbornene allylic : H$_4$			cyclopentene allylic : H$_4$	
	H$_{1,2}$: H$_4$	H$_{8,9}$: H$_4$	H$_6$: H$_4$	H$_3$: H$_4$	H$_5$: H$_4$	H$_{10a}$: H$_4$	H$_{10b}$: H$_4$
0	1.96	2.00	0.97	0.98	0.96	1.00	b
2	1.49	1.56	0.89	0.85	0.90	1.41	b
4	1.45	1.55	0.86	0.84	0.86	1.41	b
10	1.44	1.55	0.87	0.87	0.88	1.45 [c]	b

a ^{1}H NMR peak assignment according to R-S.3. Proton H$_4$ is well separated from everything else, and not prone to be involved in radical reactions as it is not in a vinylic nor in an allylic position. Hence, it was used as an internal standard. As it can be seen from the integrals included in the spectra of Figure S.4, as well as from the data summarized in this Table, both double bonds as well as all allylic positions are prone to react. In fact, the vinylic positions are more prone to radical attack. Due to merging of aliphatic protons, product formation is intractable in the ^{1}H NMR of Figure S.4. Therefore, radical addition was confirmed with GC-MS (Figure S.5 below).

b H$_{10b}$ could not be integrated as it merges with H$_{7a}$.

c Ratio increases probably due to overlapping resonances from product protons.

R-S.3. Yang, Y.-S.,; Lafontaine, E.; Mortaigne, B. *J. Appl. Polym. Sci.* **1996**, *60*, 2419-2435.
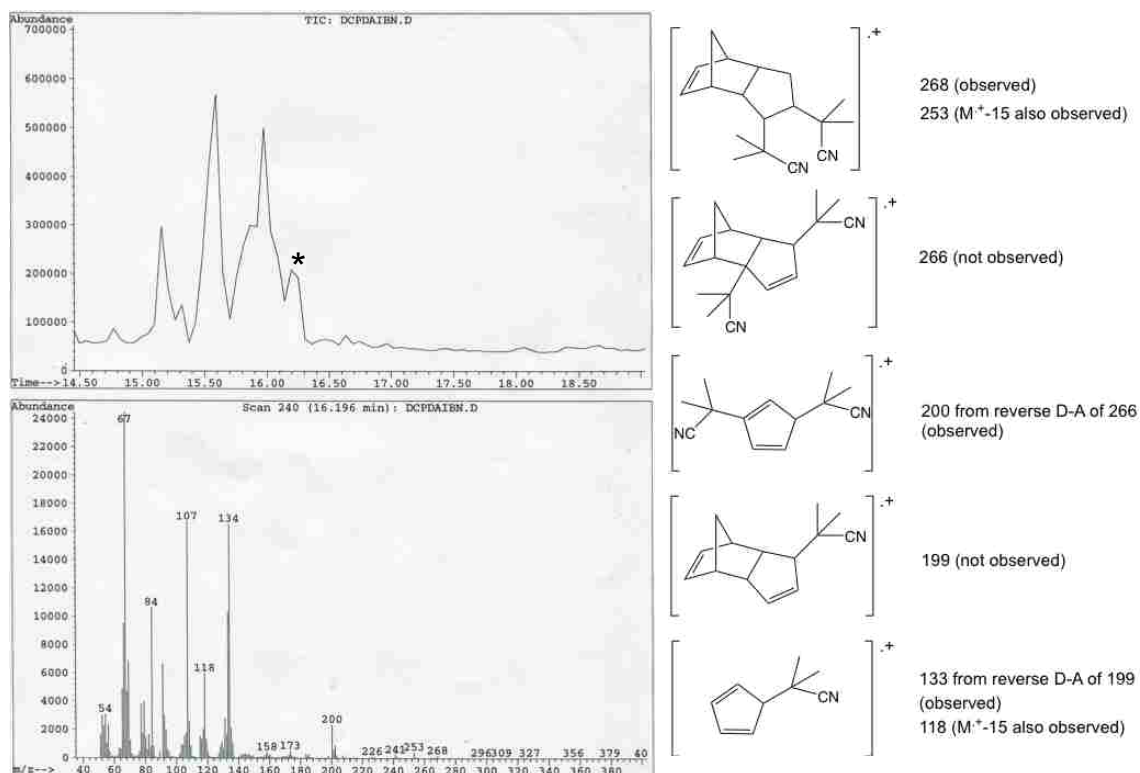
218

Figure S.5 GC-MS analysis of the peak marked with the asterisk of the sample shown in Figure S.4 after the end of the heating period. The other peaks in the cluster show the same spectra with different peak intensities, most probably reflecting different isomers. Addition of the AIBN fragment across the double bond is observed directly (m/z=268). Allylic addition is inferred from the products of inverse Diels-Alder reaction (m/z=200 and m/z=131).

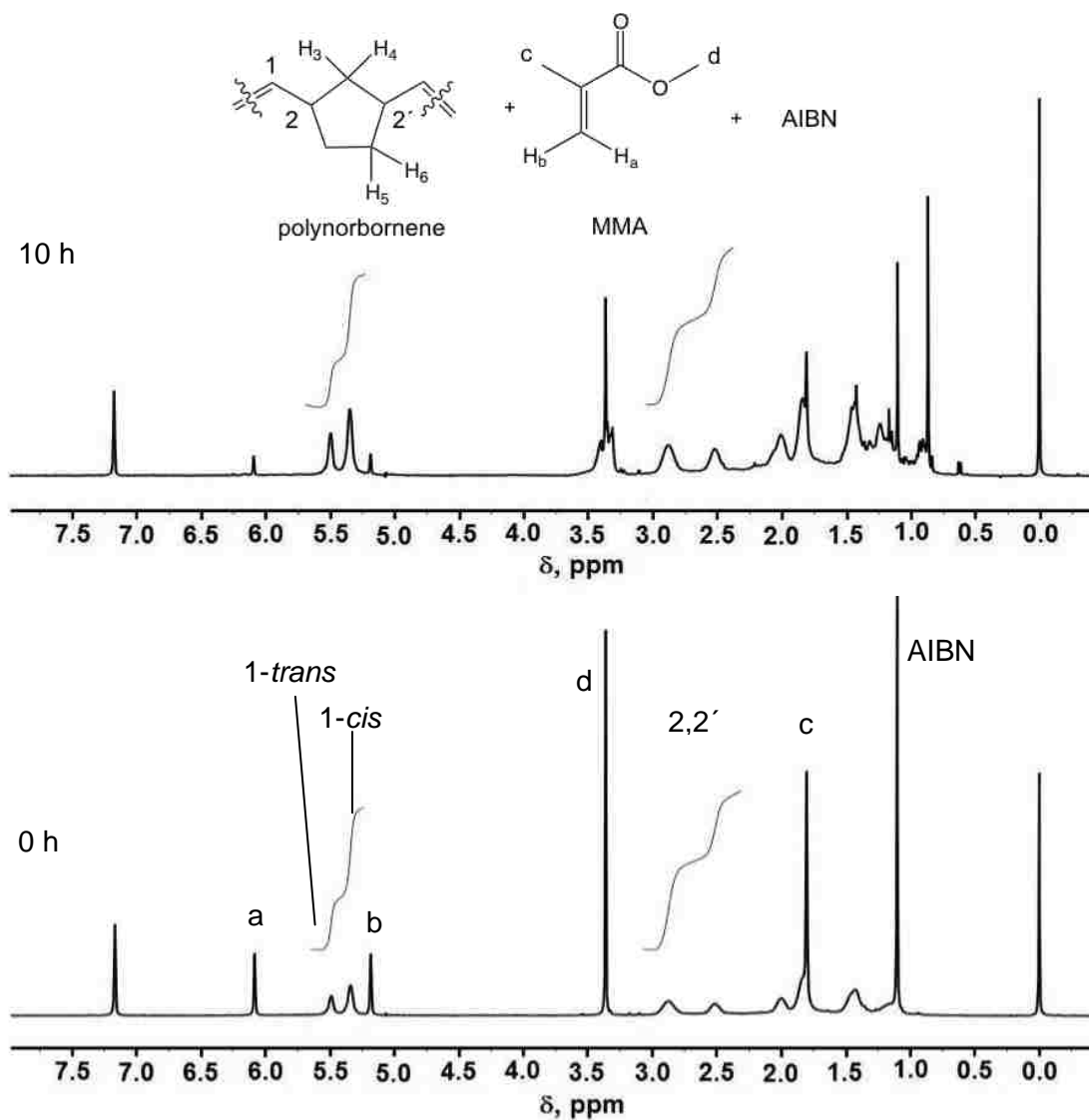**Figure S.6** Liquid ^{1}H NMR of a 5% w/w polynorbornene (pNB) solution in benzene-d$_6$ in the presence of MMA (53% w/w vs. pNB) and AIBN (10% w/w vs. MMA). Bottom spectrum is immediately after making the solution at room temperature and top spectrum is after heating the solution in NMR tube at 80 ^{o}C for 10 h. Peak assignment according to R-S.1 and R-S.2.

Table S.2   Integration ^{1}H NMR data of Figure S.6 above. Vinyl Hs are reacting.

time (h)	Vinyl Hs (*cis+trans*): allylic Hs (2+2´)
0	0.89
2	0.83
4	0.81
10	0.79

Appendix II. Differential scanning calorimetry (DSC) and thermogravimetric analysis
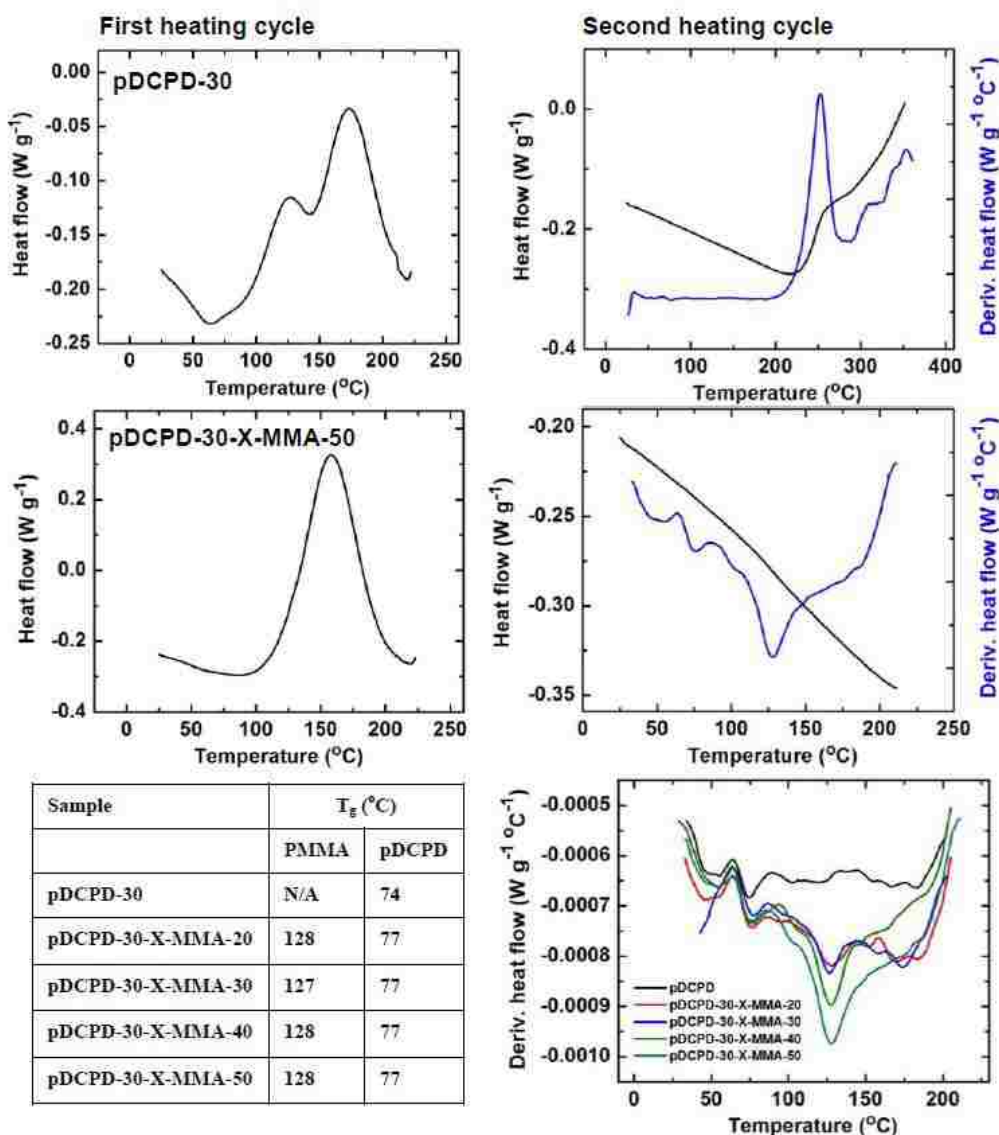
(TGA) data

Figure S.7 DSC data under N_2 (see Experimental section) for selected pDCPD aerogels. Exotherms between 100-200 °C in the first heating cycles are due to crystallization. The exotherm in the second heating cycle of **pDCPD-30** is associated with decomposition (see also TGA data in Figure S.9 [R-S.3]. The glass transition at 77 °C is assigned to linear pDCPD [R-S.4] and it is taken as indication that the polymer is only partially crosslinked.

R-S.3. Dimonie, D.; Dimonie, M.; Munteanu, V.; Iovu, H.; Couve, J.; Abadie, M. J. *Polymer Degradation and Stability* **2000**, *70*, 319-324.

R-S.4   Abadie, M. J.; Dimonie, M.; Couve, C.; Dragutan, V. *European Polymer Journal* **2000**, *36*, 1213-1219.
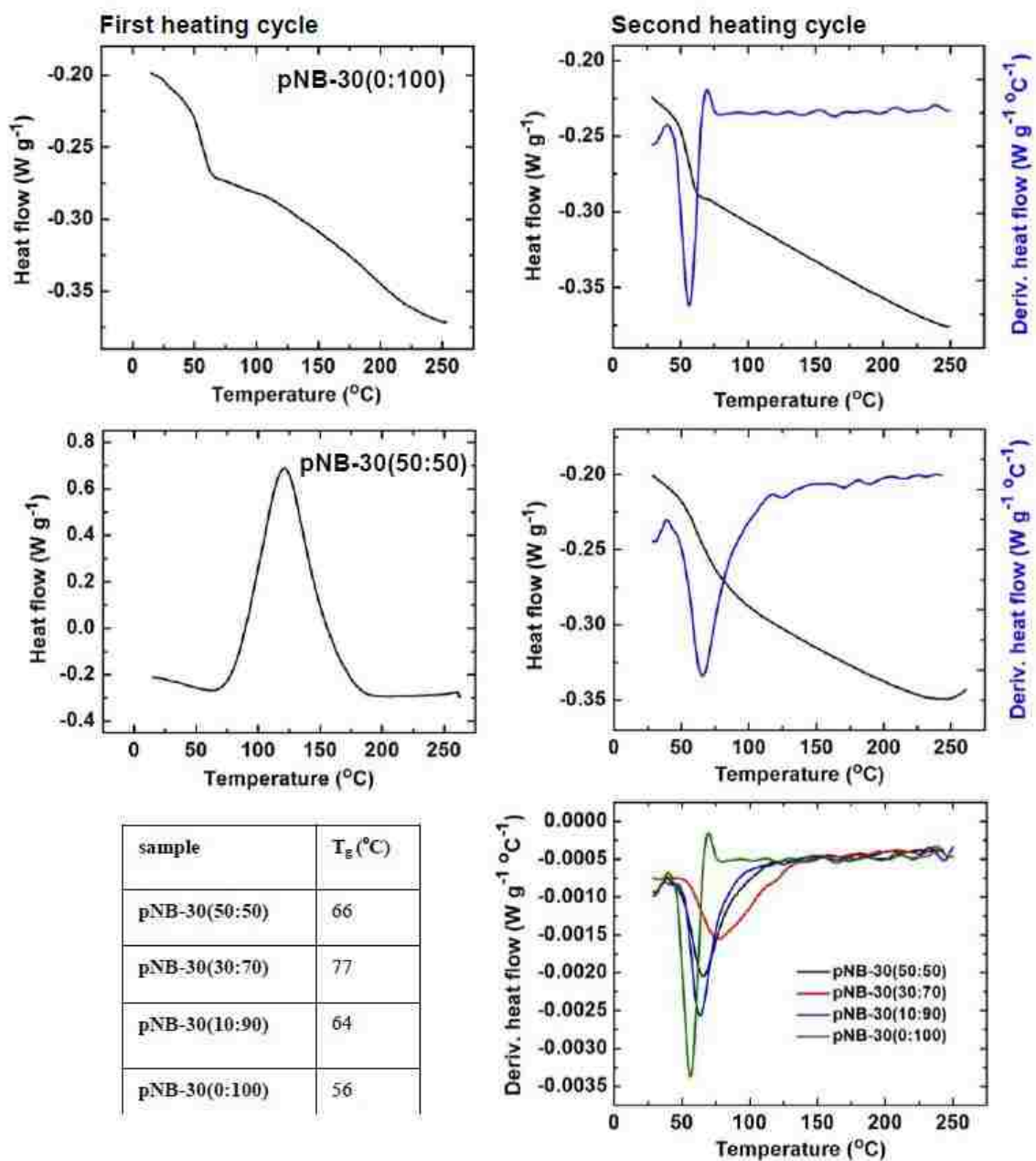
Figure S.8 DSC data under N_2 (see Experimental section) for selected pNB aerogels. Only the **pNB-30(50:50)** sample shows crystallization in the first heating cycle.

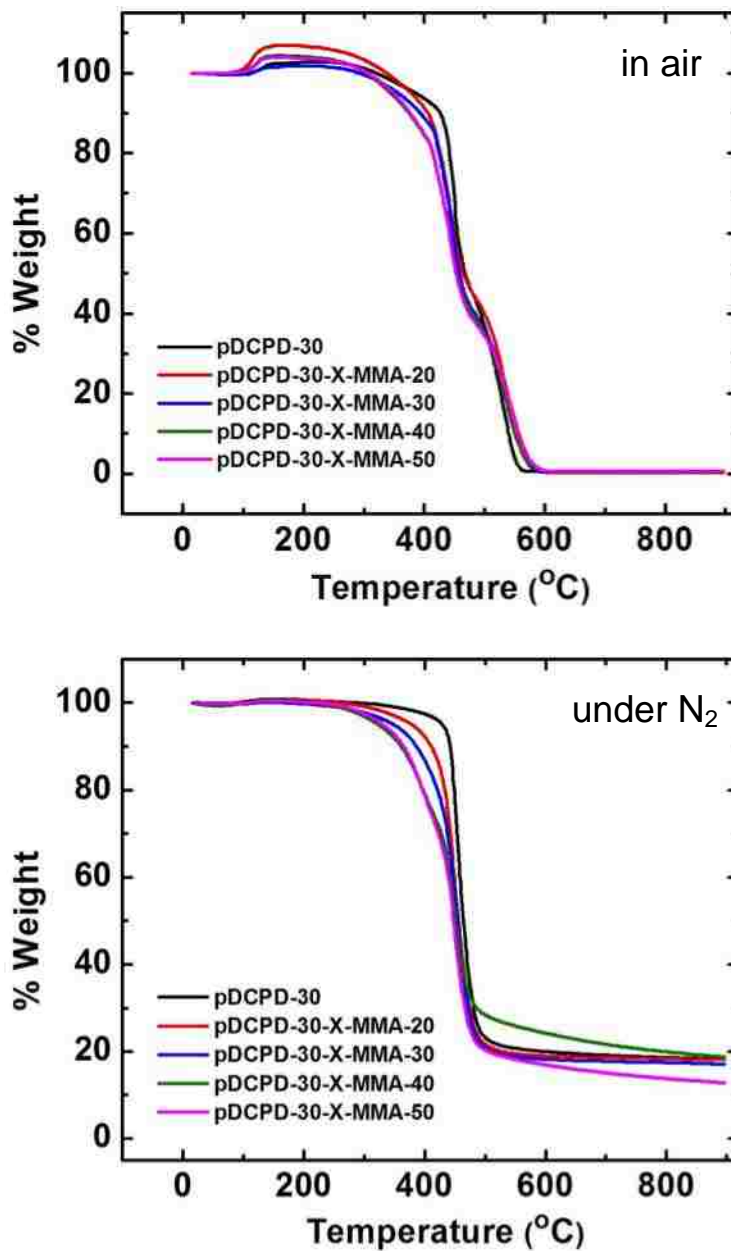| sample	T_g (°C)
pNB-30(50:50)	66
pNB-30(30:70)	77
pNB-30(10:90)	64
pNB-30(0:100)	56

Figure S.9 TGA data for all pDCPD aerogels. (For experimental details see Experimental section.)

Appendix III. SEMs before and after compression (SHPB) of **pDCPD-30-X-MMA-50** and of **pNB-30(0:100)** aerogels.

Before compression
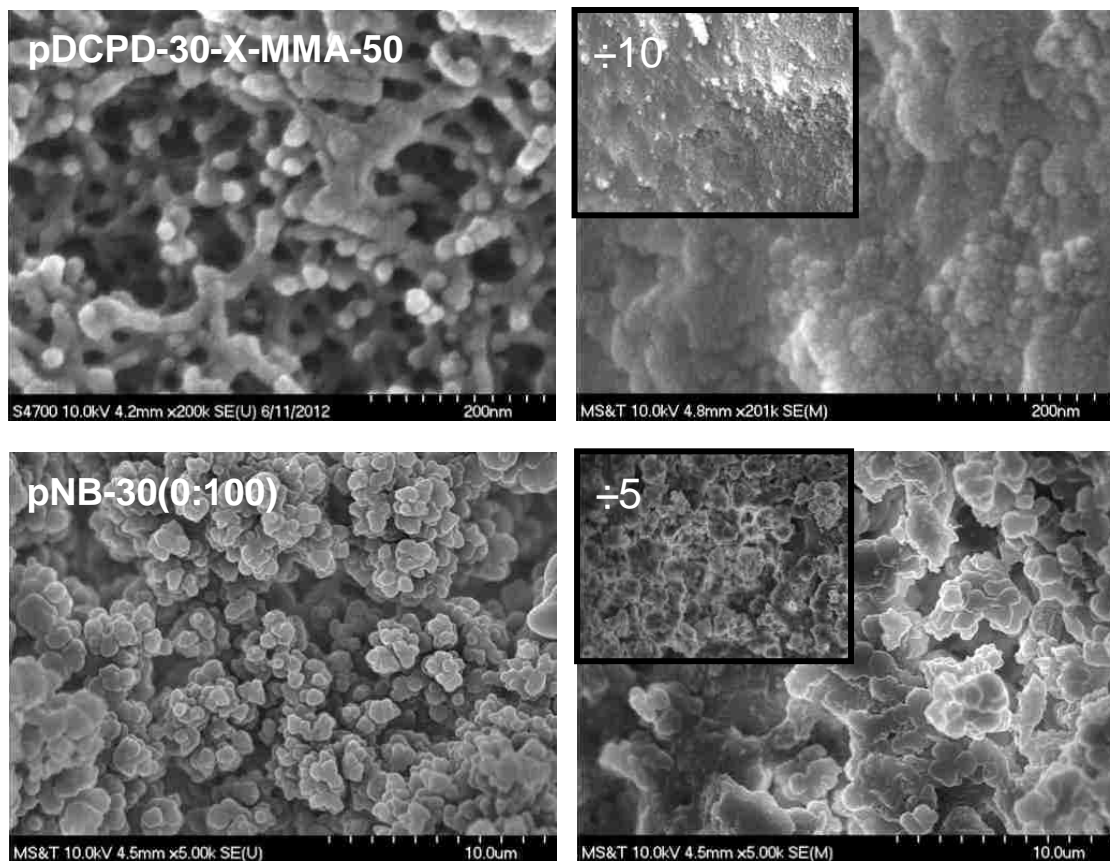## After SHPB compression

Figure S.10 SEM of representative samples before and after compression testing as shown. pDCPD samples loose all their porosity, while pNB samples keep some porosity, but particles are flattened and fused.

Appendix IV. Gel permeation chromatography data for the **pNB-30-(zz:ww)** samples.
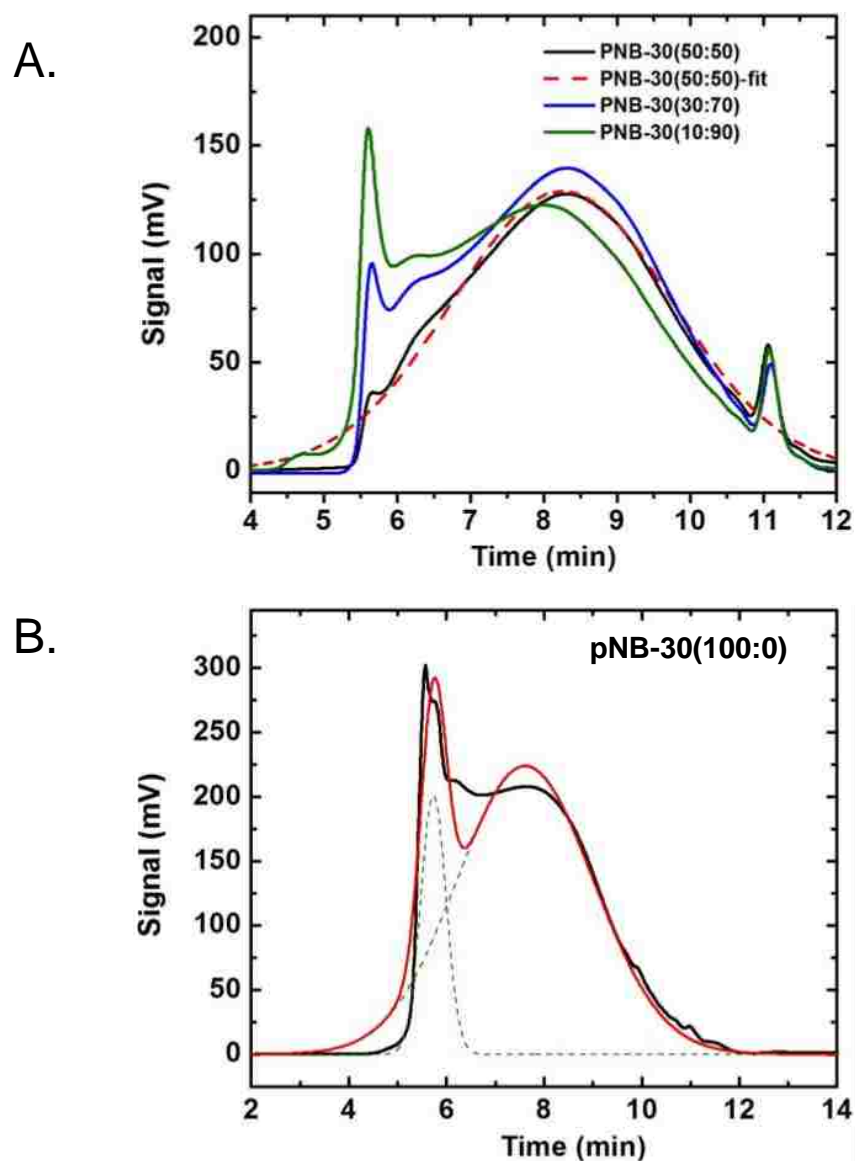

Figure S.11 GPC data of polynorbornene aerogels (A) and a polynorbornene wet-gel right after aging in the mold (B). (Polynorbornene wet-gels were made in toluene, hence the name: **pNB-30(100:0)**. For other pertinent information see Experimental section.) Peaks at low retention times (longer polymers) are cut off abruptly at around 5 min, because of the resolution of the column. Data analysis by fitting as shown by dotted lines. Data for the lower molecular weight polymer are summarized in Table S.3. (In (B), the black line shows the actual chromatogram, the red line is the fitted chromatogram and the red dashed line is the de-convoluted fitted chromatogram.)

Table S.3 GPC data analysis by fitting the broad peak at higher retention times.

sample	N	M_n	M_w	M_w/M_n
pNB-30(100:0) wet-gel$_a$	192	2968	18047	6
pNB-30(50:50)	143	1023	13480	13
pNB-30(30:70)	112	1317	10567	8
pNB-30(10:90)	209	1681	19722	12

a Note, this sample (also shown in Figure S.11B) was made in toluene, which is good solvent for pNB. Therefore, this was not a colloidal gel but rather a linear polymer gel, readily soluble in larger amounts of toluene or THF.

SECTION

2. CONCLUSIONS

Robust silica aerogels are produced by crosslinking with polynorbornene through grafting to ROMP. The exact location and the amount of polymer are correlated with bulk material properties to conclude that the crosslinking polymer follows the hierarchical structure of silica whereas polymer first stays close to the primary particles forming a conformal coating and then almost completely fills secondary particles. A small amount of polymer that coats only primary particles is enough to increase the mechanical strength, making silica aerogels easy to handle robust materials.

Purely organic aerogels with the same nanostructure and interparticle connectivity as that of crosslinked silica aerogels were synthesized via ROMP. Specifically, it is demonstrated that ROMP-derived polyimide aerogels can be prepared in one-step as mesoporous materials over a wide density range with high porosities, high surface areas, high modulus, high strength and high toughness. Combining their mechanical strength with relatively-low thermal conductivity and low speed of sound wave propagation, these materials are reasonable candidates for thermal and acoustic insulation at elevated temperatures. In another venue, dimensionally stable ROMP-derived polydicyclopentadiene (pDCPD) aerogels are synthesized by grafting their nanostructure with polymethylmethacrylate (PMMA) via free radical chemistry. The interparticle connectivity is probed by studying the thermal conductivity and compressive strength of pDCPD-based aerogels to infer that interparticle bonding takes place due to cross-metathesis, which effectively blends the polymer chains of adjacent nanoparticles.

VITA

Dhairyashil Prataprao Mohite was born in the year 1984 in Rethare Bk., Karad, Maharashtra, India. He received his Bachelors degree in Paints Technology from University Institute of Chemical Technology (UICT) at Mumbai, India in 2005. He worked for two years with AkzoNobel Coatings India Pvt. Ltd. as Technical Executive before coming to the United States for his graduate studies. In 2007, he joined Missouri University of Science and Technology to pursue a Ph.D. degree in chemistry. During the course of his Ph.D. work, he has published 7 journal articles, submitted 2 articles and presented his research in 4 national ACS meetings.